THE UNIVERSITY *of* EDINBURGH

THE UNIVERISTY *of* EDINBURGH
School of Engineering
Institute for Infrastructure and Environment

Response on Reinforced Concrete Structural Elements to Ballistic Impact and Contact Detonations

Evangelia Athanasiou

A thesis submitted to the University of Edinburgh, for the Degree of Doctor of Philosophy

November 2017

To my dearly beloved parents George and Anastasia

Declaration

I hereby declare that except where specific reference is made to the work of others, the contents of this dissertation are original and have not been submitted in whole or in part for consideration for any other degree or qualification in this, or any other university. This dissertation is my own work and contains nothing which is the outcome of work done in collaboration with others, except as specified.

Some of the work has been presented in the following Journal papers, peer reviewed conference papers, presentations and extended abstracts:

Journal Papers

- E. Athanasiou, F. Teixeira-Dias, F. Coghe and L. Desmaret, "Response of Reinforced Concrete Structural Elements to Near-field and Contact Explosions", International Journal of Safety and Security Engineering, Vol.6, pp. 418-426, 2016

- E. Athanasiou, F. Teixeira-Dias, F. Coghe, L. Desmaret, J. Pernas-Sanchez, J.Artero-Guerrero, "Near-field Blasts: Experimental and Numerical Assessment of the Response of RC Structures", International Journal of Impact Engineering (at the submission stage)

Peer reviewed conference papers

- E. Athanasiou, F. Teixeira-Dias, F. Coghe and L. Desmaret, "Response of Reinforced Concrete Structural Elements to Near-field and Contact

Explosions", Proceedings of the 14th International Conference on Structures Under Shock and Impact, SUSI, Crete, 2016

- E. Athanasiou, F. Teixeira-Dias, F. Coghe and L. Desmaret, "HESH Projectile Impact on Reinforced Concrete Structures: Numerical and Experimental Analysis", Proceedings of the 2nd International Conference on Structural Safety under Fire and Blast Loading, CONFAB, London, 2017

Presentations and extended abstracts

- 14th International Conference on Structures Under Shock and Impact (SUSI), Crete, 2016

- 4th Infrastructure & Environment Scotland PGR Conference, The University of Edinburgh and Heriot-Watt University, Edinburgh, 2017 (extended abstract submission and winner of the best presentation award)

- 2nd International Conference on Structural Safety Under Fire and Blast Loading (CONFAB), London, 2017

Date: 27/11/2017

Evangelia Athanasiou

Acknowledgements

During my long and challenging research period, many people were willing to give their guidance and a helping hand. I would like to seize the opportunity and recognise in this section the importance of their support and assistance in the completion of the current doctoral research study.

First and foremost, I would like to express my sincere appreciation to my principal supervisor and mentor Dr. Filipe Teixeira-Dias, at the School of Engineering, The University of Edinburgh, for his continuous guidance, inspiration and encouragement all these years. Without his scientific expertise and psychological support, this work would not have been possible. Not only at this moment of writing, that I am emotionally charged, but in my life in general, I will struggle to forget his calm appearance and his presence of mind when difficulties regarding the research work were arisen. Most importantly, I thank him because he believed in me from the very beginning and trusted this research work in my hands, giving myself the chance to unfold my research ambitions.

I am truly grateful for the exceptional support of the department of Weapon Systems and Ballistics (ABAL) at the Royal Military Academy of Belgium. The provided experimental work was significantly important in my research study. Without those results the validation of my numerical simulations would not have been feasible. In particular, I would like to express my gratitude to Major IMM Dr. Frederik Coghe for being alerted every time I had questions regarding the experimental setup of the projects. I cannot also forget his kindness during my one month placement in the Academy for ballistic training. Furthermore, I am very thankful to Dr. Nestor Nsiampa

and Mr. George Kechagiadakis from the same department, for the fruitful discussions, new ideas and guidance regarding the numerical modelling of this research work.

I would like also to thank the UK Engineering and Physical Research Council EPSRC for funding my research during the last 3.5 years. Without the financial support, this research would not have been easily possible.

I am very grateful to Dr. Jose Artero-Guerrero and Dr. Jesus Pernas-Sanchez at the University Carlos III of Madrid for their scientific contribution in my research work, regarding the numerical comparison between two approaches (MMALE and LBE), when near-field blast loading is considered. This work is included in a research paper, nearly to the submission stage. Apart from our common research interests and collaboration, I do not ignore, in the very beginning of my PhD studies, their help and dedication of their valuable time in helping me when numerical issues were arisen. The help that I received was crucial, since, at that period of time, everything seemed to be extremely difficult and almost impossible.

I would like also to acknowledge my friends and colleagues for making my life happier and for their encouragement, especially at the final stage of my thesis writing. In addition, I also am thankful to my good friends Mr Surya Vesavkar, who has supported during the writing up of my Thesis and Dr. Zeynep Karatza for the fruitful discussions and her endless support.

I think that I cannot thank enough my partner in life Dr. Michail Kalloudis. He deserves the best version of myself, because he unconditionally supported me at my worst, especially the last painstaking stages of my PhD. He was the good wizard that was

trying to smooth the difficulties and made me to think positive, no matter if the issues regarding my work remained unsolved. Apart from his crucial psychological support, he used to share with me his own PhD experience and guide me when I asked for his advice and help. Overall, I believe that the most significant lesson I learned through him was to try always as much as I can and that the enemy of the good is the better.

Finally and most importantly I would like to thank from the bottom of my heart my precious family and share how much I needed them especially some “tough” periods during my PhD studies. Words are not enough to express my sincere appreciation to the people that brought me to life and not only gave me endless care and support but helped me to build a personality governed by ethos. It is a fact, that you cannot choose your family, but if I had the option of choice, I would choose the same people without any doubt. My father George, my mother Anastasia and my sweet sister Maria, were standing always next to me and not opposed me, giving me unconditional love and support. My parents had the same target in their common life… to bring up happy, fully-loved, kind and well-educated children. Consequently, I am sure that the best present for them in return, is when their children appreciate those efforts. If at the moment I have achieved some milestones in my life and if I have already finished the writing of my doctoral thesis, I personally feel that I owe everything to them.

Abstract

Concrete is a widely studied material with a composite nature. It is used both in civil and military buildings and infrastructures. An issue of great importance is the protection of people from terrorist attacks that target critical infrastructure. Explosions, detonations and/or projectile impacts are some of the most severe actions a concrete structure can face. Experimental analysis is necessary in order to understand and predict the response of a structure to such dynamic and strain rate sensitive conditions. However, as the cost of performing experiments is significant and numerical simulations offer improved blast and impact analysis capabilities, there is an effort to limit experiments to validation purposes.

In recent years, many researchers have studied the impact loads transferred to reinforced concrete (RC) structures both through direct projectile impacts or blast waves at both near and far field. The aim of the current study is twofold. First, to investigate contact detonations on this type of material (RC), since literature can provide us with limited information. Secondly, to assess the behaviour of the RC structure under combined ballistic impact and contact detonation of a very specific geometry of projectile (HESH) that exists currently on the market and behaves differently from the normal projectiles that consist of one single material.

The author analysed and discussed in depth the response of RC members exposed to contact detonations. More precisely, the effect of the mass of explosive (C4) on pressures, impulses and energy balances. Also, she investigated the kinematic response of RC slabs and the structural role of the reinforcing bars. The driving force of this research was the fact that literature lacks extensive studies on contact detonations on

RC structures. Currently, the majority of studies regarding contact blast are focusing either on innovative types of concrete or normal concrete. However, normal concrete is investigated as a control parameter (to prove the effective resistance of the innovative material) rather than a detailed study on the behaviour of the material.

Thereafter, the author analysed the response of a RC wall under the combined effect of kinetic energy (terminal ballistics) and contact detonation caused by the impact of a 90 mm HESH (High Explosive Squash Head) projectile fired from a distance of 70 m. The aim was to investigate the response of the structural member under the superposition of those two actions and analyse the combined effects of the impact velocity and detonation on the response of the structure.

The numerical modelling is based on a Multi-Material-Arbitrary-Lagrangian-Eulerian approach (MMALE, using LS-DYNA) using the Winfrith concrete constitutive material model to investigate the dynamic response of the RC members under high strain rate conditions. The efficiency of the proposed numerical modelling is validated with experimental results – based on open-arena testing – and provided by the Royal Military Academy of Belgium.

Some of the key findings of this research are that the increase of the amount of the explosive affects the damage failure of the RC members from flexural failure to shear failure. In addition, fitting curves that could be used in design, were proposed, that show the relation between the mass of explosive and the resulting pressures and impulses, within the tested range. In the case of the combined blast and impact scenario, the detonation was found to dominate the structural response of the RC slab.

Table of Contents

List of Figures

List of Tables

Chapter 1. Introduction

1.1 Background

Dynamic loading actions such as earthquakes, winds, blast and impact loading through aircraft crash, dropped bodies and projectiles can be proved significantly harmful for the occupants of nearby buildings.

In recent decades, mostly due to the increasing threat of terrorism, scientific research interest has been focused on the structures subjected to extreme loading conditions of blast and projectile impact. Under those dynamic incidents of short duration and high magnitude, the presence of overloading and large deformations, most frequently leads to the damage of critical infrastructure. Hence, the integrity of structures and the safety of their occupants are issues of great importance, since they can be catastrophically affected by the actions of detonation events and projectile impacts.

Reinforced concrete is a material with a composite nature. It is widely used both in civil and military infrastructures, thus extensive research on this particular material should be carried out. There are several aspects that influence the complex response of concrete, such as, nonlinearity of stress and strain evolution, low tensile resistance compared to its compressive strength, strain softening and stiffness degradation. Thus, modelling of concrete's response and defining the material's failure under multiaxial loading as well as the interaction between the reinforcing bars and concrete is a complicated task that becomes even more complex when dealing with high transient dynamic loading such as blast and impact.

Reinforced concrete slabs and walls are fundamental elements of the critical infrastructure, hence the main focus of this research work is oriented to the dynamic response of those structural members under contact blast and contact blast combined

with soft ballistic impact scenarios. The motivation behind this study was mainly the gap in literature regarding those specific conditions.

In the case of the blast event, the shock wave hits the concrete structure causing triaxial compression. The localised crushing of concrete in the front face is a consequence of concrete's inability to withstand high compressive load. Afterwards, the blast wave hits the back side of the structure and the free surface produces a reflection of the wave. This reflection is responsible for the spalling damage of concrete at the back side. Spalling occurs since concrete material exhibits a low tensile strength and its tensile limit can be easily exceeded.

In the case of projectile impact on a reinforced concrete structure, local and global response takes place. The local response is associated with the crushing of concrete in the front face, radial cracks around the impact zone, scabbing at the back face, shear plugging and perforation while the global response is related with the bending response of the structure. However, these two responses are closely connected since a local shear failure can result in a global failure of the structural component.

Experimental testing is necessary in order to understand and predict the response of a structure to such dynamic and strain rate sensitive conditions. Through the experimental observations it is possible to derive empirical formulae. The main drawbacks of carrying out experiments, apart from their significant cost, are that the empirical predictions are strictly limited to the experimental conditions and also that their focus is restricted to the local response of the material.

On the other hand, the analytical equations (systems of mass and spring) focus on the global rather than the local response of the member. As a result, local failures,

especially under the effect of blast and impact loading, cannot be predicted very accurately.

However, the use of numerical simulations, such as finite element analysis, that focus on both the local and global response of the structural members, can be proved beneficial, especially nowadays that improved blast and impact analysis capabilities exist. The three-dimensional modelling tends to be necessary in particular when the dynamic loading is considered, since it is able to represent more realistically the real loading and structural conditions.

Nuclear power industry and the military sector are contributing significantly to blast and impact research studies. For the time being, several researchers have studied the response of reinforced concrete structures under those loading conditions with the use of experimental and/or numerical approaches.

1.2 Objectives

Even though significant research works have been carried out, limited research has been conducted in order to investigate the detailed response of reinforced concrete structural members under contact detonation events. In addition, there is a lack of literature when the contact blast event is combined with the ballistic impact of a soft projectile. Thus, the author will assess in detail the response of RC slabs under contact detonation in terms of pressures, impulses, energy balances, kinematic response and the role of reinforcing bars, since those findings are not addressed in previous research studies. Also, the author will assess the response of a RC wall, in terms of the same parameters, under the effect of a HESH projectile that does not only impacts the target but detonates in a contact manner when touches the surface of the structural element.

This specific projectile exists currently on the market and behaves differently from normal projectiles that consist of one single material. Since, literature cannot provide us with information regarding this topic, the current work is a unique scientific contribution. Consequently, this doctoral thesis that focuses on the previously mentioned missing components, will aim to develop a three dimensional finite element model which is able to replicate in a realistic manner the response of concrete under those specific conditions. The numerical tool that was employed for the needs of the current study, is the finite element analysis commercial software package LS-DYNA, since it has been proved very efficient in coping with high transient dynamic loading conditions. In order to cover the main objectives satisfactorily, subsequent explorations were performed with respect to the initial target. Their purpose was to:

- Verify the use of a Multi-Material-Arbitrary-Lagrangian-Eulerian (MMALE) approach in the near field through comparison with the totally Lagrangian approach Load-Blast-Enhanced (LBE).
- Validate the efficiency of the numerical modelling along with the selection of Winfrith Concrete constitutive material, with experimental results. The experimental data was obtained from open- arena tests that were carried out by researchers at the Royal Military academy of Belgium. This validation is assessed through the measured diameter of the localised damage zone. Another aim is to explore in both loading scenaria the damage evolution.
- Assess the effect of the mass of the explosive (C4) on pressures, impulses and energy balances. Also, investigate the kinematic response of RC slabs and the structural role of the reinforcing bars. In addition, propose fitting curves where possible.

- Assess the response of RC walls under the combined effect of the impact velocity (terminal ballistics) and contact detonation (contact blast) caused by a High Explosive Squash Head (HESH) projectile, in terms of the previous parameters. In other words, to investigate the dominant event when detonation and ballistic impact are acting at the same time. Examine also, the influence of the increasing kinetic energy on the damage evolution.

1.3 Summary of contents

Chapter 2 refers to the basic theoretical background of detonations. It will also include the fundamental principles regarding the categorisation of the ballistic impact as soft and hard.

Chapter 3 will present the historical background and the governing equations of the Finite Element Method (FEM). The chapter also explains in which way the FEM method is applied through LS-DYNA commercial software package and how the software deals numerically with the blast loading techniques LBE and MMALE.

Chapter 4 refers to the factors that affect concrete's performance under dynamic loading and offers a brief description of the available constitutive material models of concrete in LS-DYNA. In addition, it focuses on the material models used in the current study for simulating the behaviour of concrete and steel (reinforced concrete) under the effect of blast and impact loading.

Chapter 5 presents a significant amount of research papers based on reinforced concrete targets subjected to blast loading and soft projectile impact. It underlines also

the significance of the current work that fills the gap of literature regarding the contact blast and the combined contact blast with ballistic impact.

Chapter 6 describes the on-site experiments that were carried out and the numerical procedure followed in order to replicate the response of the reinforced concrete targets under the described extreme loading conditions. The experimental measurements of damage along with the obtained numerical findings of the same damage will also be referred to but not discussed.

Chapter 7 compares MMALE approach with LBE at the near-field and underlines the necessity of the first approach when dealing with contact detonation scenarios. In this chapter also, the numerical observations of damage will be validated through comparison with the experimental observations along with the relevant discussion. With the numerical models being validated, the pressures, impulses, energy balances and the kinematic response of RC slabs/walls along with the structural role of the reinforcing bars, will be investigated under the effect of the explosive's mass and impact's velocity increase.

The conclusions obtained through the discussion of the results in Chapter 7 will be summarised in **Chapter 8**. In addition, the author will provide some suggestions for future research work.

Chapter 2. Theoretical principles of explosions and terminal ballistics

2.1 Introduction

The present study focuses on the dynamic response of reinforced concrete slabs (RC) under contact detonations of C4 (see Section 6.2.2) explosive as well as the dynamic response of RC walls under the combined effect of the ballistic impact and contact detonation caused by a 90 mm HESH (High Explosive Squash Head) projectile fired from a distance of 70 m. For better understanding of the referred phenomena (blast and ballistic impact), the author decided to include in this chapter basic theory governing the blast waves and hard / soft projectile ballistic impact.

The impact of the HESH projectile, used in the current study, can be considered at the same time as hard and soft. It consists of a thin and low strength steel case (soft impact), that surrounds a steel plug at the back (hard impact), A3 (see Section 6.4.1) explosive material in the middle (soft impact) and wax material in the nose (soft impact). Hence, considering the specific geometry of this projectile (most of the projectile parts result in a soft impact), the author concluded that the literature review should be focused only on deformable (soft) projectiles impacting RC targets.

2.2 Blast loading overview

2.2.1 Behaviour and principles of the High Explosives (HE_s)

An explosion (nuclear, electrical, pressure energy, chemical) occurs due to rapid release of energy from its source, within a small volume, generating an audible sound.

According to Baker et al. [1] the pressure wave created, travels away from the source and is responsible for the damage observed on the structures. There are several types of explosions such as natural explosions (volcano eruptions, meteors and lightning), explosions caused by accident (chemical reactions) and in the end deliberate

explosions (mostly caused for military purposes by explosives and projectiles). The main focus of the current study will be on the deliberate detonations caused by high explosives (HEs) such as Composition 4 explosive (C4) and A3 composition.

An explosive, in general, is supposed to be a material that can be ignited. The detonation can be caused either during its exposure to elevated temperatures or after a mechanical activity that induces elevated heat to the material [2]. If in the one hand the explosive's material condition is elastic after the impact, the propagating waves are named *sound waves*, since they are travelling with *sound velocity*. This velocity is linearly proportional to the pressure (stress) change in the material. If on the other hand the explosive material responds in a plastic manner, the produced waves are named *shock waves* and their velocity accordingly is called *shock velocity*. The shock velocity is higher than the sound velocity and develops in a non-linear manner with the alteration of the material's stress. The shock waves are characterised by an increase in the density, pressure and energy. Thus, an Equation of State (EOS) that relates the pressure with the local energy and density is absolutely essential in order to capture the explosive's shock wave propagation.

High explosives (HE_s) were created to meet the demands of the mining industry. Initially being very sensitive to ignition, they were responsible for many accidents. As a result, high explosives with a controlled detonation governed by the use of an explosive's booster, needed to be developed. In addition, the army has developed an extensive use of those high explosives. Over the years, military sector has dedicated a wide research on the blast loading principles and how this loading affects the nearby structures. The blast loading information included in this study is derived from the

dedicated research of the British and US armies. For the time being, the high explosives which produce high level detonation velocity and pressure when exploded, are safe and do not ignite if the shock wave provided by the booster is kept at low levels.

When the HE is detonated, a chemical reaction takes place, called oxidation. The explosive that is in a burning state is decomposed when oxygen is combined with the molecules of the detonated material. As a result, energy is released, known as *heat of reaction*, evident from the fact that the molecules in the burned stage contain less internal energy compared to the molecules in the unburned stage. If the explosive is fully oxidised, the heat that is exposed to the air is called *heat of combustion* (ΔH_c). Responsible for the oxidation process is in most situations the oxidizer within the explosive material. In some cases, the oxidation is supported by the air in the surrounding environment or by an additive incorporated in the explosive material.

The burning material releases heat at a very fast rate. This phenomenon is known as *thermal explosion* [3]. The energy that is realised under the explosion events is called *heat of detonation* (ΔH_d). The detonation gases (products) formed are mixed with the surrounding air to produce heat at a slower rate, known as the *heat of afterburn* (ΔH_{ab}).

In general, the *heat of combustion* is the sum of the *heat of detonation* and the *heat of afterburn* as shown in the following equation and is supposed to be the maximum heat that is released in an ideal condition,

$$\Delta H_c = \Delta H_d + \Delta H_{ab} \qquad 2.1$$

Deflagration takes place when the propagation wave, due to the chemical reactions, travels within the material at a lower velocity than the sound velocity. On the other hand, when the propagation wave travels within the material with a shock velocity (velocity higher than the velocity of the sound), the condition is known as *detonation.*

The current research study is focused on reinforced concrete elements under the effect of detonation events. When the high explosive is detonated, the reaction that takes place, produces gases with high temperatures and pressures. These gases form the shock waves (detonation waves), which travel within the expanded volume of the explosive material with the shock velocity. For example, the detonation wave in the TNT explosive can have a pressure up to 21 GPa, a temperature up to 3000 °K and a shock velocity up to 6930 m/s, according to the Engineering Design Handbook AMC [3]. The shock wave formed interacts with the neighbouring medium. If the medium is air, the blast wave is called 'air-blast'. If air surrounds the detonation, the blast wave that is produced under the explosion circumstances is unreactive within this medium, meaning that it is weaker and less powerful when is moving away from the detonation source. In addition, the blast wave front (shock front) develops a high pressure compressive wave, named blast wave's 'overpressure' profile. That name was given since the pressure acting on nearby structures is greater than the ambient pressure of the air.

2.2.2 Chapman Jouguet (CJ) state parameters

The inert condition of an explosive is described by its initial density ρ_0, the detonation velocity D_{cj} and the detonation pressure P_{cj}. The last two parameters are called

Chapman Jouguet state parameters. The greater their value is, the more effective the selected explosive is in terms of its detonation. It is a fact that the chemical reaction is governed by the pressure, temperature and confinement conditions. The confinement of the explosive is a very important parameter since it is responsible for the shift from the simple burning condition of the material to the detonation condition [4]. For example, the ignition of black powder does not guarantee any detonation if satisfactory confinement is not provided. Thus, in the military applications, metal cases are commonly used to provide the required confinement. The greater the mass that acts for confinement purposes, the larger the pressure within the detonated material becomes. Consequently, the chemical reaction takes place at a faster rate, so that the density, temperature and pressure are eventually increasing until the detonation boundary is reached.

The way in which the explosive is ignited plays an important role to the denotation velocity achieved. For example, if TNT is ignited with a strong shock, the resultant detonation velocity will be around 6930 m/s, conversely if TNT is ignited using a simple match, the detonation velocity will be around 0.01 m/s.

The detonation pressure P_{cj} and the detonation velocity D_{cj} are related with the density of the unreactive explosive ρ_0 as follows,

$$P_{\mathrm{cj}} = \frac{\rho_0 D_{\mathrm{cj}}^2}{\Gamma + 1} \qquad 2.2$$

where Γ is the ratio between the specific heats at constant pressure and volume, of the gaseous products during detonation. In addition, the Equation of State (EOS) [5], is necessary to be defined, since it describes the expansion of those products.

2.2.3 Energy of the explosive source (TNT equivalent value)

The energy released from a high explosive plays a significant role in causing damage to the structure. To compare the effect caused by different types of explosives, it is common practice to convert its mass into TNT equivalent mass. The main reason of the TNT reference is that the graphs available in the UFC (Unified Facility Criteria) manual [6] are based on the mass of TNT. In other words, the idea is to find the equivalent kilograms of TNT that should be used in order to obtain the same damage when another kind of explosive material is used. The following formula is based on the heat of the detonation that is released both from the TNT explosive and the chosen explosive:

$$M_{\mathrm{TNT}} = \left(\Delta H_{\mathrm{d_{exp}}} / \Delta H_{\mathrm{d_{TNT}}}\right) \times M_{\mathrm{exp}} \qquad 2.3$$

where,

$\Delta H_{\mathrm{d_{exp}}}$ is the heat of detonation of the chosen explosive,

$\Delta H_{\mathrm{d_{TNT}}}$ is the heat of detonation released from TNT,

M_{TNT} and M_{exp} are the equivalent mass of TNT and the mass of the chosen explosive, respectively. The ratio of those energies results in a converting factor that is unique for every explosive.

In the current thesis, Composition 4 (C4) explosive and A3 Composition are going to be used. According to McVay [7] the converting factors used are 1.37 and 1.09 respectively.

2.2.4 Energy distribution of the blast wave

The energy distribution is a very important parameter which affects the explosion procedure. Prior to the explosion event, the chemical energy of the explosive is stored within the explosive in the form of potential energy. Later, when the explosion takes place, it is distributed into kinetic and potential energy. The system becomes unsteady because new material is consumed and the distributed energy is changing forms all the time while dissipating to the surrounding atmosphere.

When idealised conditions are applied such that the explosion produces a spherical blast wave shape, the explosive source contains both the source material and the inert confining material that are not mixed to each other and that the blast wave is the only wave for the energy distribution, then the initial potential energy is converted into the following types:

Wave energy:

The blast wave consists of both potential (internal) E_p and kinetic energy E_k that are given below

$$E_p = \int \rho C_V(\theta - \theta_0)\ \mathrm{d}V \qquad 2.4$$

$$E_k = \int \frac{1}{2}\rho u^2\ \mathrm{d}V \qquad 2.5$$

where V is the atmospheric volume that is confined in the blast wave without considering the confining material or the detonation products, ρ is the density, C_v is

the constant volume specific heat, θ is the temperature and u is the particle velocity. The waste energy after the detonation event, the kinetic and potential energy of the fragments/source material and the radiation caused, will be defined below:

Waste energy (residual energy):

During the blast event the temperature of the atmosphere increases, before it returns to ambient conditions, due to the dissipation of the chemical energy that is released after detonation.

Kinetic and potential energy of the fragments or of the confinement:

The fragments or the confining material will start to accelerate during the detonation as a result of the heat transfer. This induced kinetic energy will decrease and form the potential energy stored in those parts as a consequence of the supplied thermal energy.

Kinetic and potential energy of the source material

During the detonation procedure, the explosive mass will be accelerated. This is the result of the conversion of its potential energy (it stores initially the energy of the explosion), into kinetic energy.

Radiation

Radiation is the consequence of the loss of energy, in a rapid manner, outside the system that experiences the detonation event.

2.2.5 Pressure and impulse of the blast wave

An explosion is categorised as “ideal” when the released energy is so strong that can cause a complete damage on the nearby structure. It is also the result of the detonation that comes from a bare, spherical TNT explosive mass without the case that surrounds it for confinement purposes.

In addition, the term “free air” corresponds to the situations where there are no obstacles in front of the shock wave propagation, hence the radial expansion of the wave is not disturbed.

When the explosive charge is detonated (detonation at its centre) and the blast wave travels through the air, the air next to the shock front is experiencing high levels of compression. On the other side of the air under compression, at a distance which is known as positive wavelength L_w^+, the air is not that compressed compared to the ambient pressures.

The pressure that impacts the nearby structures and is the result of the detonation of the explosive charge can be seen in Figure 2.1. The time t_a is recognised as the time that the shock wave arrives on the surface of the structure and also is the time that the peak incident or side-on pressure P_{so} is achieved [1]. This pressure, is the result of the rapid increase in the atmospheric pressure. After this peak value, the pressure starts to attenuate during a time period t_0, which is considered as the duration of the positive phase of the blast wave curve. Subsequently, the pressure obtains a negative value (a lower value from ambient pressure), which is referred to as the negative incident overpressure P_{so}^-. The time period that the pressure obtains negative values is well

known as negative phase of the blast pressure curve and usually is ignored from the numerical simulations since is not very significant for the design of structures. In most situations the pressure acting on the structure is in the range of MPa and the time duration is measured in ms. The Friedlander equation given below governs the shape of the aforementioned curve,

$$P_s(t) = P_{so}\left[1 - \left(\frac{t - t_a}{t_0}\right)\right] e^{-(t-t_a)/\theta} \qquad 2.6$$

where, t is the time of interest, related to the detonation of the explosive and θ is a constant of time measured in ms.

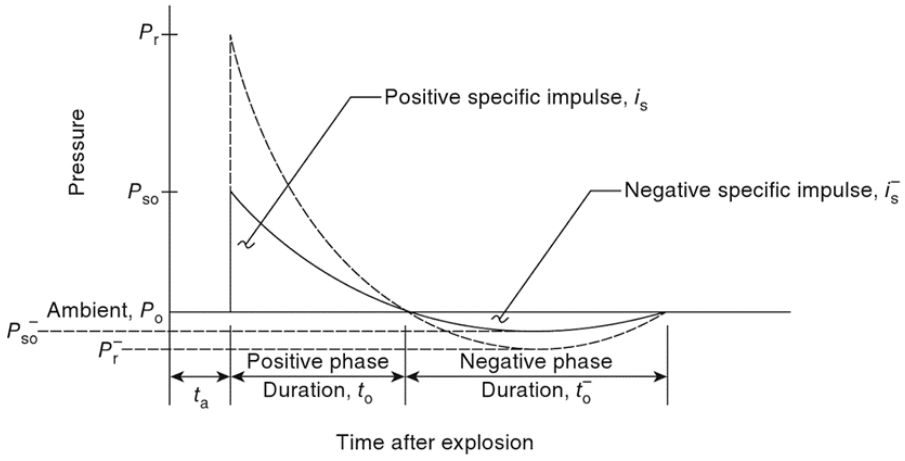

Figure 2.1: Blast wave pressure profile (Figure taken from [1]).

In addition, the area under the pressure curve and during the time t_0 is called positive specific incident impulse i_s. On the other hand, the area under the pressure curve and during the negative phase is referred as negative specific incident impulse i_s^-. In general, the focus and concern about measuring the blast wave parameters is concentrated on the positive phase, since it belongs to the duration where the severe

damage on the structure takes place. Assuming that time t starts at the arrival time t_a, the positive impulse can be given as,

$$i_s = \int_0^{t_0} P_{so}\left[1 - \frac{t}{t_0}\right] e^{-t/\theta} dt \quad 2.7$$

In the case that the shock wave impacts a rigid, large and reflecting area, at a 90° degree angle, it is reflected back, resulting in a reflecting pressure P_r. This pressure can be twice to twelve times greater than the peak overpressure P_{so} (see Figure 2.2). As can be seen, this reflected pressure obtains positive and negative phases as the P_{so} and can be described as follows, assuming that the time of arrival is equal to 0,

$$P_r(t) = P_r\left[1 - \left(\frac{t}{t_0}\right)\right] e^{-t/\theta} \quad 2.8$$

The specific impulse can be given accordingly as,

$$i_r = \theta P_r\left[1 - \frac{\theta}{t_0}\left(1 - e^{-t_0/\theta}\right)\right] \quad 2.9$$

In Figure 2.2 for theoretical peak overpressures varying between 0.001-34.47 MPa and angle of incidence 0<α<90 (degrees), the reflecting pressure can be calculated through the reflecting pressure coefficient $C_{r\alpha}$ as,

$$P_r = C_{ra} P_{so} \quad 2.10$$

Even though the graph in Figure 2.2 is not applied in the current research study (peak incident overpressures exceed 34.47 MPa), the way that the incident peak overpressures, reflected pressures and impulses are developing during the detonation event, remains unchanged.

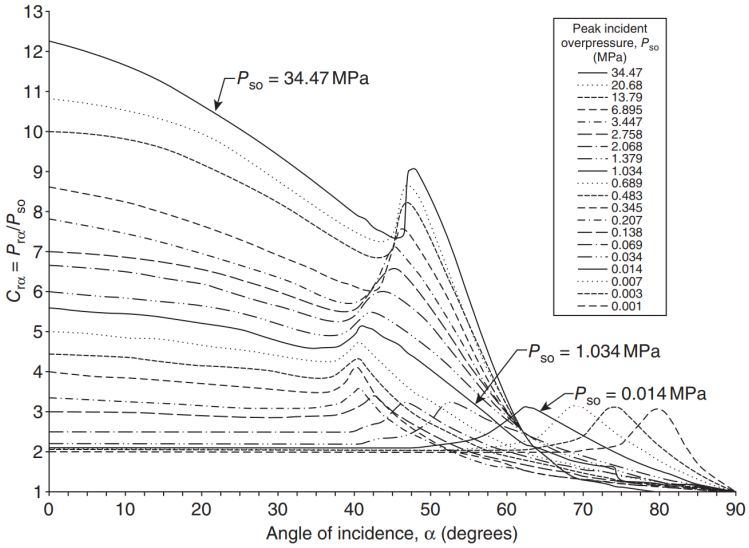

Figure 2.2: Determination of the reflected pressure P_r (Figure taken from [6]).

2.2.6 Confined and unconfined explosion categories

According to the Unified Facility Criteria [6], blast loading can be produced either under confined or unconfined conditions. The local confinement of the explosive which is related with the case that surrounds the charge is a different thing and should not be associated with the current division.

Confined explosions:

Confined explosions take place when the detonation event happens within a close compartment and can be classified as fully vented, partially confined and fully confined. Governed by the compartment's geometry, these internal explosions can result in the formation of shock waves that interact in a complicated manner with the structure boundaries and can cause leakage. Leakage takes place when the reflected and incident waves along with the products of the explosion escape from the closed chamber.

In the case of a fully vented explosion, the detonation takes place in a compartment where one or more boundaries are exposed to the atmospheric conditions. Complexities resulting from the shock waves reflections on the boundaries surfaces as well as leakage are evident.

In partially confined detonations, apart from the complexities in the formation of shock waves and leakage, there is a satisfactory confinement in order to take into account the gas pressure as a result from the detonation products. The level of the gas pressure is governed by the TNT equivalent amount of the explosive charge, the opening area and the free space of the compartment.

In the case of a fully confined explosion, which is a subcategory of the partially confined detonations, there is no leakage and the gas pressure of the detonating products lasts for a long period due to the absence of venting.

Unconfined explosions:

In the current study, the unconfined explosions will be taken into consideration. These are external detonations in which the blast waves are travelling within the air medium. Under those free-air explosion conditions, the shock wave is transmitted without any obstructions between the explosive source and the structure. The distance between the explosive charge and the ground is two to three times the elevation of the structure and there is a sufficient distance between the explosive and the affected target. Thus, the reflection of the blast wave from the ground is combined with the unreflected incident blast wave that propagates toward the target.

In the case of the surface explosions that occur in a very close distance from the ground (usually one or two meters away from the ground surface), the ground can play a

significant role. If it acts as a perfect reflector, then it will result in doubling the energy of the blast wave and causing an enhanced incident pressure. Thus, a factor of 1.8 or 2 can be used in order to define this incident enhanced peak pressure and be able to use the free-air data graphs and calculate the rest of the important blast parameters.

The unconfined contact detonations on reinforced concrete structural elements are going to attract the interest of this particular thesis. Detonations in a contact manner are a particular subcategory of the unconfined explosions. In that type of detonations, the distance between the centre of the explosive charge and the target, (stand-off distance), plays a significant role. The explosive charge is located on the surface of the structure, a fact that results in a direct shock of elevated pressures that is affecting straightaway the structural member and is reflected immediately back, when the target is reached. Consequently, the damage as a result of the induced pressure is restricted to a particular area and can result in fragmentation loading as well.

The fragments can be either classified as primary or secondary and have an important role especially in the case of the contact detonations since they affect the target directly. The primary fragmentation takes place when the explosive is stored within a metal container (casing), which is destroyed after the impact. These fragments of the casing are considered as an additional load that impacts the structural element. On the other hand, secondary fragmentation loading takes place for example when the compartment, inside which the detonation takes place, breaks into pieces or some other times due to debris from the structural elements that are exposed to the detonation event.

Under the above circumstances of the direct loading, the front face of the target (reinforced concrete) is experiencing cratering while spalling occurs at the back face of the structural element. Cratering occurs due to the crushing of concrete in the front face of the impacted area and is associated with the ejection of the material on that side. Spalling on the other hand is related to the ejection of concrete at the back side of the shock loaded surface. Crushing of concrete under an explosion event, either in the far or near field (depending on the distance between the detonation source and the target), takes place in the front face of the target due to the rapid rise of the stresses above the limit of the compressive strength. Afterwards the blast wave hits the back side of the structure and the free surface causes a reflection of this shock wave. When the tensile force exceeds the tensile strength of concrete, the spalling is evident and tensile failure occurs.

In order to be able to recognise the magnitude of the damage caused to nearby structures due to the presence of the unconfined explosions, it is completely necessary to understand the following parameters [8]:

a) Knowledge of the material used as the explosive source along with its unreacted density. This is an important consideration, since in most of the cases the explosive charge is not only TNT explosive and this knowledge helps for calculating the mass of the explosive translated in a TNT equivalent mass.
b) The TNT equivalent mass referred previously, is an important consideration as well. More specifically, the mass of the explosive used should be multiplied by a converting factor in order to obtain the TNT equivalent value. The use of analytical graphs for calculating the important blast parameters (incident

pressure, reflected pressure, impulse etc.) or sometimes the numerical modelling requires the implemented mass in TNT weight.

c) Especially in the field of near-contact detonations the shape of the explosive's geometry contributes in the detonation process.

d) The distance between the centre of the explosive and the impacted structure (standoff distance) is a significant parameter as well, since it affects in combination with the mass of the chosen explosive the magnitude of the damage.

e) The angle of incidence. On the one hand, the normal to the target incident wave can cause the highest blast loads on the structure, on the other hand the oblique incidence is the most common case that a target can face. Thus, the angle specification is of great importance since it influences the values of reflecting impulses and pressures.

f) The height of burst (distance between the ground and the explosive centre), should be also noted. As discussed in a previous section affects the reflection due to the presence of the adjacent ground.

2.2.7 Graphs for determination of the important blast parameters

Scaling laws are extensively used in blast engineering in order to obtain data when moved from smaller to larger scale experiments. Hopkinson – Cranz or "cube root" [1] is the most common law. The aforementioned law is based on the assumption that two explosives of the same kind and of similar geometry can cause a similar blast wave when detonated at a same scaled distance $Z=R/W^{1/3}$, where R is the standoff distance

between the explosive and the target (measured from the centre of the explosive charge) and W is the explosive's equivalent mass in TNT.

In order to be more specific, an explosive charge of diameter d, when placed at a standoff distance R, can cause a blast wave with overpressure P, impulse i and duration of positive phase t_0, while at the same time an explosive charge of diameter λd, placed at λR standoff distance can produce a blast wave with overpressure P, impulse λi and duration λt_0. Under this law only the pressure, density, velocity and temperature are not scaled using the factor λ.

Kingery and Bulmash [9] introduced standard curves (see Figure 2.3) for the airblast that is produced by the explosion of a bare and spherical mass of TNT. These curves were the result of experimental data collection and are included in the Unified Facility Criteria manual [6].

Important blast parameters such as the peak overpressure P_{so} (MPa), the spesific impulse i_s (MPa-ms), the reflected pressure P_r (MPa), the reflected impulse i_r (MPa-ms), the time of arrival t_a (ms), the duration of the positive phase t_0 (ms), the positive wave length L_w^+ (m) and the velocity of the shock front U (m/ms) can be given through logarithmic graphs in those standard curves as a function of the scaled distance Z.

When using those graphs, the explosive charge should be converted into TNT equivalent amount in order to calculate the scaled distance and finally collect the value of the parameters of interest from the curves. As discussed previously, a ground burst can be treated as a free- air burst when multiplying the initial mass of the explosive with a reflecting factor of 1.8 – 2 (2 is used for perfect reflection).

The scaled distance in the aforementioned curves ranges between $0.054 < Z < 39.7$ m/kg$^{1/3}$. On the one hand, the limit of those graphs in terms of scaled distance is at Z=0.054 m/kg$^{1/3}$ (basically represents the radius of the explosive charge under contact detonation event). On the other hand, it is noted, that the curves are not reliable when used for Z lower than 1 m/kg$^{1/3}$. Thus, for contact detonations, where the loading from direct shocks and fragmentation is more significant than in the case of free air detonation, the logarithmic graphs of Kingery and Bulmash are not used.

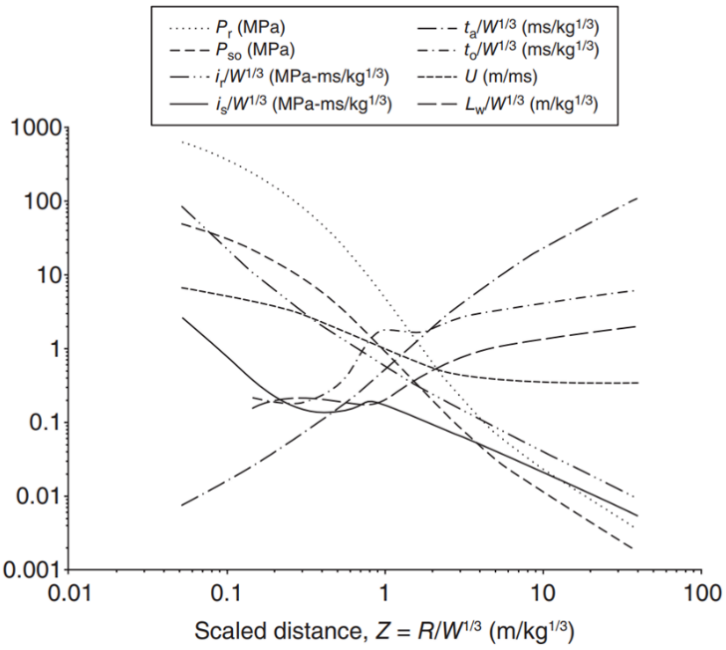

Figure 2.3: Blast wave parameters for the free air detonation of a spherical TNT explosive charge at the sea level (Figure taken from [6]).

Apart from those commonly used curves, some researchers recommended various relationships in order to determine analytically the peak overpressure P_{so}. In all of them the scaled distance, Z, is an important parameter during the calculation process.

Kinney [10], recommends the following formula, related to the chemical nature of the detonations (P_o is associated with the atmospheric pressure),

$$\mathrm{P_{so}} = \mathrm{P_o}\frac{808\left[1+\left(\frac{\mathrm{Z}}{4.5}\right)^2\right]}{\left\{\left[1+\left(\frac{\mathrm{Z}}{0.048}\right)^2\right]\left[1+\left(\frac{\mathrm{Z}}{0.32}\right)^2\right]\left[1+\left(\frac{\mathrm{Z}}{1.32}\right)^2\right]\right\}^{0.5}} \qquad 2.11$$

Brode [11] suggests the following equation depending on the pressure that is applied on the structure under the explosion event caused by a spherical charge. The applied peak overpressure P_{so} is ranging between 0.1 – 10 bars for medium and far field detonations and is greater than 10 bars in the case of the near field. The scaled distance is computed in m/kg$^{1/3}$.

$$P_{\mathrm{so}} = \begin{cases} \dfrac{6.7}{Z^3}+1 & P_{\mathrm{so}} > 10 \text{ bar} \\ \dfrac{0.975}{Z}+\dfrac{1.455}{Z^2}+\dfrac{5.85}{Z^3}-0.019 & 0.1 < P_{\mathrm{so}} < 10 \text{ bar} \end{cases} \qquad 2.12$$

Another proposed equation for the determination of the peak overpressure P_{so} under conditions of a surface detonation, arises from Newmark and Hansen [12],

$$P_{\mathrm{so}} = 6784\frac{W}{R^3}+93\sqrt{\frac{W}{R^3}} \qquad 2.13$$

where P_{so} is measured in bars, W is the weight of TNT explosive mass measured in tonnes and R is the height of burst measured between the centre of the charge and the ground surface.

Mills [13] also suggests the formula below, in which P_{so} is measured in kPa, the mass of TNT is measured in kg and Z in m/kg$^{1/3}$:

$$P_{so} = \frac{1772}{Z^3} - \frac{114}{Z^2} + \frac{108}{Z} \qquad 2.14$$

Blast loading design:

In the design of resilient structures the incident peak overpressure and the reflected pressure are the most important parameters taken into consideration. It is very common to ignore the negative phase of the curve presented in Figure 2.1 and assume a triangular pulse for the positive phase of the same curve (see Figure 2.4). The area under this triangle represents the related specific impulse.

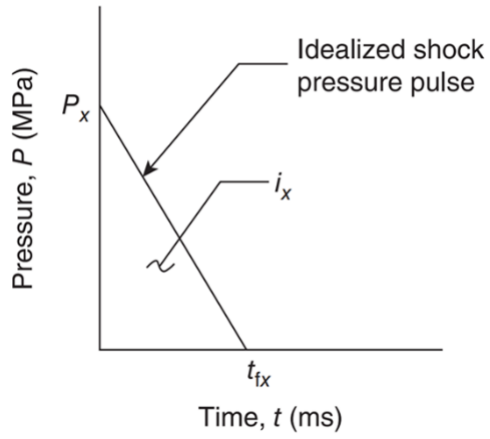

Figure 2.4: Simplification of the pressure curve for design purposes (Figure taken from [6]).

2.2.8 Experimental testing of blast events

In general, three ways (on-site, shock pipe and blast compartment) exist in order to assess experimentally the response of a structure under the effect of blast wave loading.

The on-site experiments require a smooth land in which the blast event would take place without the presence of reflecting areas except for the ground. It is supposed to be the most desired approach especially when the behaviour of the full-scale structure is needed or when the blast forces are needed to be computed in detail.

The shock pipe, is a tube of cylindrical geometry that applies the blast forces on a particular area of the target. The blast pressures are created on the one side of this tube through air under compression or sometimes through a real explosion of a charge and are applied on the other side where the structural element is connected with the tube. It is a good approach when the determination of the blast loading pressure is not required in detail. Although it is supposed to be an economical way compared to the on-site experiments, this method lacks from the consideration of the "clearing effects" [14] that are related to the dimensions of the impacted target.

Finally, the blast compartment is a close space in which the detonation event takes place. Due to the constraints in the available space, there are clear restrictions on the weight of the explosive and on the experimental setup.

In addition, when the experimental testing is carried out, incident and reflecting pressures can be measured by piezo-electric and optical techniques. The shape - transmission of the blast wave front (high speed video) and the temperature increase (heat flux devices) can be measured as well. In terms of the structural behaviour of the impacted member the displacements and strains, shock accelerations, calculation of the mass and the amount of fragments and photographs of the observed response before and after the damage can be collected.

In the current study, on-site tests were carried out and the response of the target was assessed in terms of the diameter of the observed damage.

2.3 Ballistic impact

2.3.1 Soft and hard impact

Impacts can be categorised as soft and hard according to descriptions provided by Eibl [15] and CEB [16]. Impact between two bodies takes place when the one has an initial velocity and collides with the other body that is not moving. This mechanism can be simplified (see Figure 2.5) if idealised with two masses m_1 and m_2, a spring that represents the force applied to m_2 after the impact from m_1 (stiffness equal to k_1) and a spring that shows the motion in terms of deformation as a result of the resistance applied from the impacted mass m_2 (stiffness equal to k_2).

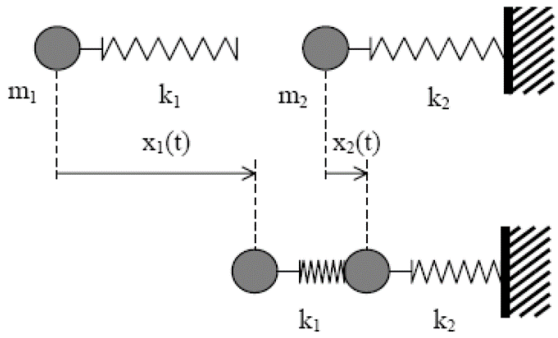

Figure 2.5: Mechanical model of the impact between two bodies, m_1 and m_2 (Figure taken from [8]).

The mechanical model is dominated by the second order differential equations of equilibrium as,

$$\begin{cases} m_1\ddot{x}_1(t) + k_1[x_1(t) - x_2(t)] = 0 \\ m_2\ddot{x}_2(t) - k_1[x_1(t) - x_2(t)] + k_2x_2(t) = 0 \end{cases} \quad 2.15$$

Soft impact

When x_2 (t) << x_1 (t), more precisely when the mass m_2 (target material) is not displaced too much related to the impact of mass m_1 (projectile), then with the substitution of $F(t) = k_1 x_1(t)$, the differential equations will be reduced to the following form,

$$\begin{cases} m_1 \ddot{x}_1(t) + k_1 x_1(t) = 0 \\ m_2 \ddot{x}_2(t) + k_2 x_2(t) = F(t) \end{cases} \quad 2.16$$

This results in two individual equations where the deformation x_1 can be obtained through the first equation and through the second equation, the determination of the response of the structural member is possible to be defined. Hence, there is a "soft impact" when the impacted target stays undeformed after the crashing event. The latter means that the kinetic energy of the projectile is totally converted into its distortion energy (see Figure 2.6).

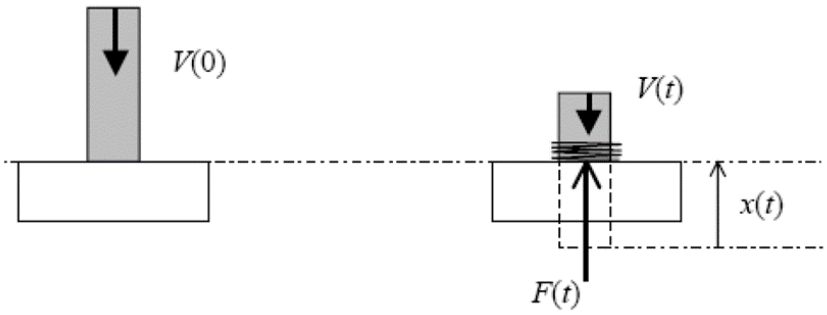

Figure 2.6: Deformation of the projectile under soft impact (Figure taken from [8]).

This uncoupled nature of the equations is very convenient when structures are impacted by an aircraft. According to the experimental studies by Sugano et al. [17], when an aircraft crashes with a reinforced concrete structure, the deformation of the impacted structure is minor compared to the deformation of the projectile. This is

supposed to be a soft impact that results in a total distortion of the striking body. Hence, the benefit of the uncoupled nature of the differential equations is being applied, since the force that impacts the target can be calculated separately from the response of the reinforced concrete target. For the calculation of the impact force, the recommendation by Riera [18] is employed. This has been validated through experimental studies by Sugano et al. [17] and computational work by Wolf et al. [19]. Accordingly, the force F that impacts the target is the superposition of the buckling and the inertia of the mass as follows,

$$F(t) = P_{\mathrm{f}}\big(x(t)\big) + \mu\big(x(t)\big)V(t)^2 \qquad 2.17$$

where P_{f} is the buckling force, μ is the mass per unit length, V is the velocity that impacts the rigid target and $x(t)$ is the crushed length (see Figure 2.6). Researchers proposed enhancements (in the inertia part) on the formula recommended by Riera. More precisely, Sugano et al. [17] introduced the constant of 0.9 as a multiplier of the inertia component in order to account for the effective mass during the impact and the equilibrium between the force F and the force F_{t} coming from the target.

Until recently there was only one equation available in literature that was able to predict the relevant ballistic limit. This minimum impact velocity (m/s) required to perforate the target when soft impact is considered [16], can be given as

$$V_{\mathrm{CEB}} = 50\frac{\left(r_{\mathrm{d}} f_{\mathrm{c,cube}}\right)^{1/6}}{M_{\mathrm{p}}{}^{0.31}}\sqrt{T(3.14d + 7.85T)} \qquad 2.18$$

where, r_{d} is the reinforcement ratio, T is the thickness of the target (m), $f_{\mathrm{c,cube}}$ is the cubic strength of concrete (Pa), M_{p} and d are the mass of the projectile (kg) and its diameter (m) respectively.

Baroth et al. [20], recommended the following formula for the same limit,

$$\mathrm{V} = \sqrt{{V_0}^2 + \frac{2\,P_\mathrm{f}\,x(t)}{M_\mathrm{p}}} \qquad 2.19$$

where, V_0 is the striking velocity of the soft projectile (m/s), P_f is the buckling force (N), $x(t)$ is the crushed length and M_p is the mass of the projectile (kg). According to Bignon and Riera [21], the crushing force P_f for hollow metal cubes can be given as,

$$P_\mathrm{f} = 2\pi e\left(\frac{\sqrt{2(1-\nu^2)}}{eE} + \frac{2}{df_\mathrm{y}}\right)^{-1} \qquad 2.20$$

where E is the modulus of elasticity (Pa), v is the Poisson ratio, e is the projectile's thickness (m), f_y is the yield strength (Pa) and d is the diameter of the projectile (m).

In addition, an estimation for the crushed length $x(t)$ was given by Baroth et al. [22]

$$\mathrm{x}(t) = \mathrm{Max}\left(0, \frac{M_\mathrm{p}}{2P_\mathrm{f}}\left((V)^2 - \frac{\sigma_\mathrm{T} - P_\mathrm{f}/A_\mathrm{p}}{\rho_\mathrm{p}}\right)\right) \qquad 2.21$$

where, M_p is the mass of the projectile, P_f is the crushing force, V is the ballistic limit, σ_T is the compressive strength of the target, ρ_p and A_p are projectile's density and cross section respectively.

Hard impact:

In the case that $x_2(t) >> x_1(t)$, where the mass m_2 (target material) is displaced too much relative to the deformation of mass m_1 (projectile), the impact is considered as a hard impact (see Figure 2.7). In this situation, the system of equations, cannot be treated uncoupled. During this event, the kinetic energy of the missile is transformed into work causing the deformation of the impacted structural component.

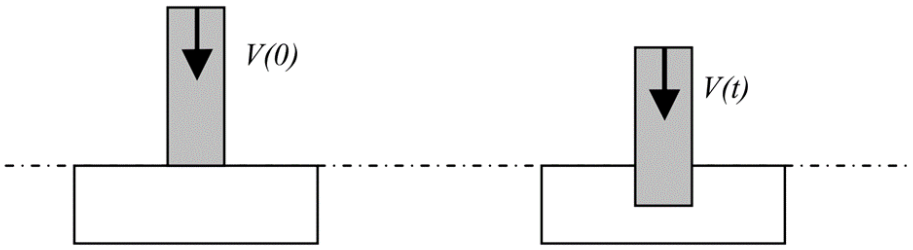

Figure 2.7: Penetration of the target under hard projectile impact (Figure taken from [8]).

The estimation of the depth of penetration (x_p in inches) of the rigid projectile on the surface of a concrete slab can be given through the Petry formula that was developed in 1910 [23],

$$x_p = 12 K_p A_p \log_{10}\left(1 + \frac{V^2}{215000}\right) \quad 2.22$$

where, V is the striking velocity (ft/s), K_p is a coefficient that indicates concrete's penetrability that is related to the strength of concrete material as well as the ratio of the reinforcement and A_p is the projectile's pressure measured in psf. The estimation of this formula was altered in later years by other researchers such as Li et al. [24] in order to consider in a more effective way the concrete strength. Based on Petry formula, Amirikian [25], recommended that the thickness of scabbing h_s is equal to 2.2 x_p and the perforation thickness e is equal to 2 x_p.

A new recommendation for the development of Petry formula was introduced by Chelepati et al. [26]:

$$\frac{x_p}{d} = \frac{1.3310^{-3}}{\sqrt{f_c}}\left(\frac{M}{d^3}\right) d^{0.2}\, V^{1.33} \quad 2.23$$

where, d is the diameter of the missile (m), M is the mass (kg), V corresponds to its impact velocity (m/s) and f_c is concrete's compressive strength (MPa). According to this researcher, the perforation and scabbing thicknesses are $e = 1.3\ x_p$ and $h_s = 2\ x_p$ respectively.

In addition, Forrestal et al. [27] proceeded with a new formulation regarding the depth of penetration. Following his recommendation, Li and Chen [28] taking into consideration experimental studies as well as the contribution of the nose shape recommended the following formula,

$$\frac{x_p}{d} = \sqrt{\frac{\left(1 + (k\pi/4N)\right)}{\left(1 + (I/N)\right)}\frac{4k}{\pi}I} \qquad \text{for} \quad \frac{x_p}{d} \leq k \tag{2.24}$$

$$\frac{x_p}{d} = \frac{2}{\pi}N \ln\left[\frac{1 + (I/N)}{1 + (k\pi/4N)}\right] + k \qquad \text{for} \quad \frac{x_p}{d} > k \tag{2.25}$$

The penetration capacity k (k=0.707+Ψ) is associated with the factor Ψ that governs the nose shape (equal to 0 in the case of a projectile with a flat nose). The parameter N is related to the configuration of the nose and I is associated with the impact of the projectile. These quantities, according to Haldar and Hamieh [29] are the following:

$$\mathrm{N} = \frac{1}{N^*}\left(\frac{M}{\rho\, d^3}\right) \tag{2.26}$$

And

$$\mathrm{I} = \frac{1}{72 f_c^{-0.5}}\left(\frac{MV^2}{d^3 f_c}\right) \tag{2.27}$$

The quantity N^* represents the shape factor of the projectile's nose. This parameter takes lower values when sharper missiles are considered. Li and Chen [28] recommended also the following formula for the determination of the nose coefficient N^*:

$$N^* = \begin{cases} \dfrac{1}{1+4\Psi^2} & \Psi = \dfrac{l_\mathrm{n}}{d} \\ 1 - \dfrac{1}{8\Psi^2} & \Psi = \dfrac{R}{d} \end{cases} \qquad 2.28$$

The first row of the relation above is linked with a projectile of conical nose l_n (length) and the second row of a hemispherical nose R (radius).

The previous predictions are related to the penetration scenario whereby the projectile is trapped within the impacted target. The following predictions are linked with the perforation scenario (the projectile passes on the other side of the target). According to Berriaud et al. [30] the calculation of the perforation limit is the following,

$$\frac{e}{d} = 0.82 \frac{M^{0.5} V_\mathrm{p}^{\,0.75}}{\rho^{0.125} f_\mathrm{c}^{\,0.375} d^{1.5}} \qquad 2.29$$

where, V_p is the ballistic limit (m/s), d is the diameter of the missile (m), M is the mass of the missile (kg), f_c is the compressive strength of concrete (MPa), ρ is the density of concrete material (kg/m^3) and e is the width of the concrete target (m). Rearranging the aforementioned formula, it is possible to determine the ballistic limit V_p:

$$V_\mathrm{p} = 1.3\rho^{1/6} f_\mathrm{c}^{\,1/2} \left(\frac{de^2}{M}\right)^{2/3} \qquad 2.30$$

This determination of the ballistic limit was based on the following ranges: $20 < V_p < 200$ m/s, $30 < f_c < 45$ MPa, $0.3 < e/d < 4$ and density of the reinforcement M_a between 120-300 kg/m^3.

Fullard et al. [31] in order to take into consideration the quantity of the reinforcing bars (reinforcing bars percentage r, considered as a fraction between the area of the rebar and the product resulting from the spacing between the rebars and the concrete's depth, according to CEB [16]) recommended the following enhancement,

$$V_p = 1.3\,\rho^{1/6}\,f_c^{1/2}\left(\frac{de^2}{M}\right)^{2/3}(r+0.3)^{2/3} \qquad 2.31$$

This formulation is valid for the ranges $45 < V_p < 300$ m/s, $15 < f_c < 37$ MPa, $0 < r < 0.75$ and $0.33 < e/d < 5$.

Berriaud et al. [30] enhanced the previous formula taking into consideration the shape of the projectile nose:

$$V_p^{\,2} = 1.9\,f_c\,\rho^{1/3}\left(\frac{de^2}{M}\right)^{4/3}N^2\left[0.35\left(\frac{M_a}{M_{a0}}\right)^{\gamma}+0.65\right]\left(\frac{f_c}{f_{c0}}\right)^{-1/2} \qquad 2.32$$

where, the M_{a0} is the reference density of the reinforcing bars (200 kg/m^3), f_{c0} is the reference compressive strength of concrete (36 MPa), γ is dependent on the layers of the reinforcement (with a value equal to 0.7 when 2 layers are considered and a value equal to 0.1 when 4 layers are taken into consideration) and N factor is dependent on the nose of the projectile (N is equal to 1 and 1.18 when a flat nose or a hemispherical nose, respectively, are being considered). This determination of the ballistic limit is based on the following ranges: $15 < V_p < 300$ m/s, $15 < f_c < 80$ MPa, $0.3 < e/d < 4$ and $0 < M_a < 300$ kg/m^3.

Buzaud et al. [32] agreed that the latest recommendation of the ballistic limit although it is the most accurate compared to the other suggestions, does not take into account the contribution of the shear reinforcement.

Soft compared to hard impact:

Koechlin and Potapov [33], with respect to the previous determinations of soft and hard impact, in which it was stated that the soft impact is the one that causes significant deformation to the projectile and the motion can be decoupled, they stated that the correct criterion for categorising a ballistic impact as soft or hard, should be the absence or the presence of the penetration respectively. Hence, they underlined the necessity of taking into consideration the strength of the interacting materials (both for the target and the projectile) along with the velocity of the missile, in order to predict the impact's category. According to their recommendations and by rearranging Reira's Equation 2.17, the following equation of the line was introduced that results in the criterion shown in Figure 2.8:

$$\frac{\sigma_{\mathrm{p}}}{\sigma_{\mathrm{t}}} + \frac{\rho_{\mathrm{p}} {V_0}^2}{\sigma_{\mathrm{t}}} = 1 \qquad 2.33$$

where σ_{p} is the yield stress of the projectile, σ_{t} the compressive strength of the target, ρ_{p} is the density of the projectile and V_0 is the projectile's striking velocity.

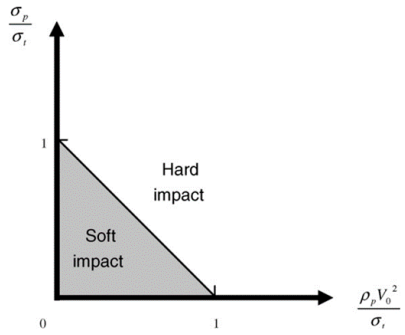

Figure 2.8: Soft and hard impact categorisation (Figure taken from [33]).

2.3.2 Effects of the soft impact on concrete targets

When a soft or a hard projectile impacts a concrete structure, the target will be subjected to a local and global response.

The local response is associated with the local damage around the impact area. More precisely, is related with phenomena such as penetration, spalling, scabbing, radial cracking, cone cracking with plugging and perforation.

Penetration takes place when the projectile is displaced and trapped within the target. The projectile develops a crater around the impact zone and a tunnelling within the target material.

Spalling is the ejection of the material from the front side of the target due to the reflection of the tensile waves.

Scabbing is the ejection of material from the back face of the target, happening due to the impact of the projectile in the front face.

Radial cracking occurs when inclined cracks observed around the impacted area. In some cases (when the impact is severe), these cracks are propagating throughout the thickness of the structural member.

Cone cracking and plugging take place when the radial cracks develop a plug cone that will result in a plugging shear failure.

In a later state, perforation occurs, when the plugging cone fails and the projectile passes through the target with or without residual velocity.

The global response is related with the displacement of the target, evolution of stresses in critical areas and cracking / yielding of concrete and steel material respectively.

Kennedy [23] and more recently Li et al. [24], presented a review of the local damage phenomena observed when a hard projectile impacts a concrete target. Since the current research study is focused on soft projectile impact, according to Jonas et al. [34], the following failure modes occur (see Figure 2.9).

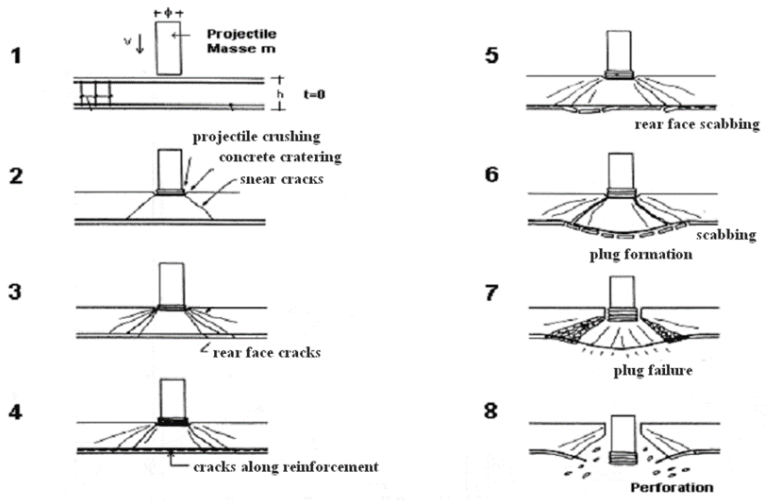

Figure 2.9: Failure modes in concrete material under soft projectile impact (Figure taken from [34]).

In the beginning, the projectile crushes and forms a crater on the impacted front area. Later, radial cracks are propagating through the thickness of the member and along the reinforcement. Consequently, scabbing is started to occur at the back face along with

the formation of the plug. Following the plug's shear failure, the projectile perforates the target.

2.4 References

[1] W. E. Baker, P. Cox, J. Kulesz, R. Strehlow, and P. Westine, "Explosion hazards and evaluation" vol. 5: Elsevier, 2012.

[2] P. W. Cooper, "Explosives Engineering " 1996, VCH Publications, New York, vol. 8, pp. 440.1-1.

[3] U. A. M. Command, "Engineering Design Handbook: Principles of Explosive Behavior," AMC Pamphlet, 1972.

[4] C. L. Mader, "Numerical modeling of explosives and propellants", CRC press, 2007.

[5] E. Lee, H. Hornig, and J. Kury, "Adiabatic expansion of high explosive detonation products," Univ. of California Radiation Lab., Livermore, CA (United States)1968.

[6] DoD, "Structures to resist the effects of accidental explosions", UFC 3-340-02. Washington, DC, USA: US Department of Defence, 2008.

[7] M. McVay, "Spall damage of concrete structures," U.S. Army Corps of Engineers Waterways Experimental Station1988.

[8] N. Uddin, "Blast protection of civil infrastructures and vehicles using composites ", Elsevier, 2010.

[9] C. N. Kingery and G. Bulmash, "Air blast parameters from TNT spherical air burst and hemispherical surface burst", Ballistic Research Laboratories, 1984.

[10] G. F. Kinney, "KJ Graham Explosive Shocks in Air," Springer-Verlag, New York, 1985.

[11] H. L. Brode, "Numerical solutions of spherical blast waves," Journal of Applied physics, vol. 26, pp. 766-775, 1955.

[12] N. Newmark and R. Hansen, "Design of blast resistant structures," Shock and vibration handbook, vol. 3, 1961.

[13] C. Mills, "The design of concrete structure to resist explosions and weapon effects," in Proceedings of the 1st Int. Conference on concrete for hazard protections, 1987, pp. 61-73.

[14] P. Smith, G. Whalen, L. Feng, and T. Rose, "Blast loading on buildings from explosions in city streets," Proceedings of the Institution of Civil Engineers-Structures and Buildings, vol. 146, pp. 47-55, 2001.

[15] J. Eibl, "Soft and hard impact," in Proceedings of the First International Conference on Concrete for Hazard Protection, Edinburgh, 1987.

[16] J. Eibl, "Concrete structures under impact and impulsive loading," CEB-Bulletin d'Information, pp. 1-183, 1988.

[17] T. Sugano, H. Tsubota, Y. Kasai, N. Koshika, S. Orui, W. Von Riesemann, "Full-scale aircraft impact test for evaluation of impact force," Nuclear Engineering and Design, vol. 140, pp. 373-385, 1993.

[18] J. D. Riera, "On the stress analysis of structures subjected to aircraft impact forces," Nuclear Engineering and Design, vol. 8, pp. 415-426, 1968.

[19] J. Wolf, K. Bucher, and P. Skrikerud, "Response of equipment to aircraft impact," Nuclear Engineering and Design, vol. 47, pp. 169-193, 1978.

[20] J. Baroth, L. Daudeville, and Y. Malécot, "About empirical models predicting the missile perforation of concrete barriers," European Journal of Environmental and Civil Engineering, vol. 16, pp. 1074-1089, 2012.

[21] P. Bignon and J. Riera, "Verification of methods of analysis for soft missile impact problems," Nuclear Engineering and Design, vol. 60, pp. 311-326, 1980.

[22] J. Baroth, Y. Malecot, Z. Boukria, M. Briffaut, and L. Daudeville, "Prediction of the perforation of targets impacted by deformable projectiles," International Journal of Impact Engineering, vol. 80, pp. 36-44, 2015.

[23] R. Kennedy, "A review of procedures for the analysis and design of concrete structures to resist missile impact effects," Nuclear Engineering and Design, vol. 37, pp. 183-203, 1976.

[24] Q. Li, S. Reid, H. Wen, and A. Telford, "Local impact effects of hard missiles on concrete targets", International Journal of impact engineering, vol. 32, pp. 224-284, 2005.

[25] A. Amirikian, "Design of protective structures (A new concept of structural behavior)," Bureau of Yards and Docks1950.

[26] C. Chelapati, R. Kennedy, and I. Wall, "Probabilistic assessment of aircraft hazard for nuclear power plants", Nuclear Engineering and Design, vol. 19, pp. 333-364, 1972.

[27] M. Forrestal, B. Altman, J. Cargile, and S. Hanchak, "An empirical equation for penetration depth of ogive-nose projectiles into concrete targets," International Journal of Impact Engineering, vol. 15, pp. 395-405, 1994.

[28] Q. Li and X. Chen, "Dimensionless formulae for penetration depth of concrete target impacted by a non-deformable projectile," International Journal of Impact Engineering, vol. 28, pp. 93-116, 2003.

[29] A. Haldar and H. A. Hamieh, "Local effect of solid missiles on concrete structures", Journal of Structural Engineering, vol. 110, pp. 948-960, 1984.

[30] C. Berriand, A. Sokolovsky, R. Guerand, J. Dulac, and R. Labrot, "Local behavior of reinforced concrete walls under missile impact", in Fourth SMiRT Conference, 1977.

[31] K. Fullard, M. Baum, and P. Barr, "The assessment of impact on nuclear power plant structures in the United Kingdom," Nuclear engineering and Design, vol. 130, pp. 113-120, 1991.

[32] E. Buzaud, C. Cazaubon, and D. Chauvel, "Assessment of empirical formulae for local response of concrete structures to hard projectile impact," in Concrete under severe conditions. Environment and loading, ed, 2007.

[33] P. Kœchlin and S. Potapov, "Classification of soft and hard impacts—Application to aircraft crash", Nuclear Engineering and Design, vol. 239, pp. 613-618, 2009.

[34] W. Jonas, R. Meschkat, H. Riech, and E. Rüdiger, "Experimental investigations to determine the kinetic ultimate bearing capacity of reinforced

concrete slabs subject to deformable missiles," in Structural mechanics in reactor technology. Transactions. Vol. J, ed, 1979.

Chapter 3. Finite Element Modelling

3.1 Introduction

Finite element analysis is shown to be an efficient tool for solving complex problems in the engineering field. This chapter, begins with a brief historical overview of this type of analysis. Later, it covers the basic principles of the method along with the governing equations as well as the implementation of those in the commercial software package LS-DYNA. Furthermore, the author includes information regarding the available type of elements and focuses on the elements used for simulating reinforced concrete. In the end, discusses the available approaches for modelling structures under blast loading.

3.2 Historical Background

Finite element analysis has been applied in engineering problems more frequently in the recent years. This type of numerical analysis can be applied in solid structures, heat transfer problems and fluid mechanics. Even though it is an appealing method for solving complex problems, its use and development started with the introduction of computers. The main disadvantage with the complex problems in engineering field, is that the algebraic equations that govern the behaviour of the problem can be difficult or even impossible to solve analytically. Hence, the use of computers is essential in order to be able to provide an effective solution to these equations. Attention should also be paid to the outcomes of the obtained solution. It is an approximate approach, very close to reality but not the exact approach and also that the solution cannot provide us with more data than the information that exists already in the numerical model [1].

It is complicated to give an accurate date for the origin of the finite element method. The concept can be found in ancient times with the estimation of the π value, where a

circle is characterised as a polygon with finite number of sides [2]. In recent years the concept was applied first in aircraft analysis. Hrennikoff [3] applied the “framework method” where a plane domain is denoted as an assembly of 1D parts (bars). Courant [4] used continuous functions over an area in order to give a rough estimation of an unknown function. He examined, St Venant’s torsion problem by using the minimum potential energy concept along with triangular elements. While significant research has been done by the aforementioned scientists, it is believed that the basic concepts behind the finite element method were formally adopted by Argyris and Kelsey [5], Turner et al. [6] and Clough [7]. The first two authors introduced the use of element matrices in order to efficiently solve complicated structures. But the name “finite element”, was first introduced by Clough. Since this establishment, several books and journals are dedicated to the finite element method and its principles with the work by Zienkiewicz and Taylor [8] being one of the most cited books in relevant literature.

In the finite element field, the body of the structure is an assembly of a number *n* finite parts. This is referred to literature as the “discretisation” of the domain. Each one of these finite parts, named “finite elements”, are attached to each other with common points called “nodes”. The assembly of those elements, forms the well-known domain, named as “finite element mesh". In the case, that the external forces are known and applied to the system, approximate functions in every element predict an approximate solution by calculating nodal displacements. Then, the system’s solution is predicted by collecting the data of all the elements across the domain.

The idea behind the finite element solution process is to represent the real problem, which has a specific geometric domain, material, loading and boundary conditions,

with a mathematical model that corresponds to an idealisation of the real problem. More precisely, the user decides if the problem can be solved in one, two or three dimensions, what material models will be implemented in order to control the stress-strain relationship of the model (constitutive laws) and be in accordance with reality. In addition, the user represents artificially the real boundary conditions and the loading conditions (forces, velocities, pressures etc.) upon the structure. The motion of the deformable body (structure) is governed by differential equations which can be presented through the "principal of virtual work". Finally, the already defined model (structure with a prescribed type of elements and mesh size, external forces, materials and boundary conditions) is being solved by the finite element analysis that gives an approximate prediction of the response. How close is going to be this solution to the real conditions, will determine if it is necessary to make changes in the finite element type, mesh density or in some cases alter the material models of the problem's description [1]. In other words, the "convergence" and "accuracy" of the analysis are strongly dependent upon the user's approximate estimation of the real case, the solution approach of the partial differential equations, the type / size of the elements and the integration points within the elements.

3.3 Principles of the Finite Element Method

The finite element analysis in the beginning was developed for the elastic analysis of solids. The solution of the analysis can be obtained through the displacement method which has been proved to be very efficient. In what follows, this method will be presented along with the description of the "virtual work" principle which governs the equilibrium of a deformable body.

In Figure 3.1 a body in three dimensions can be shown relative to a Cartesian system (*x, y, z*). The motion of a point can be expressed by the three components of displacements:

$$\mathrm{u} = [u, v, w]^{\mathrm{T}} \tag{3.1}$$

The displacements *u*, *v*, *w* follow the same direction with the *x*, *y*, *z* axes. Also, the body is exposed to body forces **b** (per unit volume), surface loads **t** (per unit area) and point loads $\mathbf{P_i}$. Each one of them has three components, one along each direction, that is,

$$\mathrm{b} = \left[\mathrm{b_x}, \mathrm{b_y}, \mathrm{b_z}\right]^{\mathrm{T}} \tag{3.2}$$

$$\mathrm{t} = \left[\mathrm{t_x}, \mathrm{t_y}, \mathrm{t_z}\right]^{\mathrm{T}} \tag{3.3}$$

$$\mathrm{P_i} = \left[\mathrm{P_{xi}}, \mathrm{P_{yi}}, \mathrm{P_{zi}}\right]^{\mathrm{T}} \tag{3.4}$$

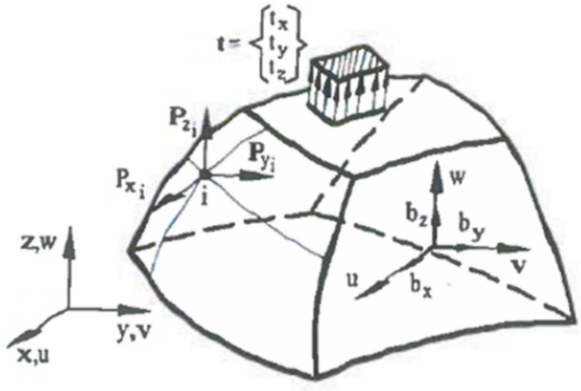

Figure 3.1 Loading and displacements in a 3 dimensional solid (Figure taken from [9]).

The strains of the body are defined as,

$$\varepsilon_x = \frac{\partial u}{\partial x}, \quad \varepsilon_y = \frac{\partial v}{\partial y}, \quad \varepsilon_z = \frac{\partial w}{\partial z} \tag{3.5}$$

$$\gamma_{xy} = \frac{\partial u}{\partial y} + \frac{\partial v}{\partial x}, \quad \gamma_{xz} = \frac{\partial u}{\partial z} + \frac{\partial w}{\partial x}, \quad \gamma_{yz} = \frac{\partial v}{\partial z} + \frac{\partial w}{\partial y} \tag{3.6}$$

If the externally applied loads are known along with the geometry and the configuration of the supports, the aim is often to find the displacements. With the displacements known and through the strain definitions it is possible to determine the strains. When the strains are determined constitutive laws are used to find the stresses. The solution, if based on the displacement method is governed by the principle of virtual work. According to this, the body is in an equilibrium state when for small virtual displacements the internal virtual work is the same as the external virtual work [1], that is,

$$\iiint \delta\boldsymbol{\varepsilon}^{\mathrm{T}}\boldsymbol{\sigma}\ \mathrm{d}V = \iiint \delta\mathbf{u}^{\mathrm{T}}\mathbf{b}\ \mathrm{d}V + \iint \delta\mathbf{u}^{\mathrm{T}}\mathbf{t}\ \mathrm{d}A \tag{3.7}$$

The product of virtual strains $\delta\boldsymbol{\varepsilon}$ and stresses $\boldsymbol{\sigma}$ (specific internal work) is equal to the sum of the products (specific external work) of virtual displacements $\delta\mathbf{u}$ and body forces $\mathbf{b}$ and virtual displacements $\delta\mathbf{u}$ and surface tractions $\mathbf{t}$.

Equation 3.7 ensures equilibrium in static problems. Under some other circumstances, where the applied force is arbitrary and changes during time, d'Alembert's dynamic equilibrium should be considered [10]. In such cases, inertia forces should also be taken into account, in addition to the body forces $\mathbf{b}$. Equation 3.7 can then be rewritten as,

$$\iiint \delta\boldsymbol{\varepsilon}^{\mathrm{T}}\boldsymbol{\sigma}\ \mathrm{d}V = \iiint (\delta\mathbf{u}^{\mathrm{T}}\mathbf{b} - \delta\mathbf{u}^{\mathrm{T}}\rho\,\ddot{\mathbf{u}})\,\mathrm{d}V + \iint \delta\mathbf{u}^{\mathrm{T}}\mathbf{t}\ \mathrm{d}A \tag{3.8}$$

The term $\delta\mathbf{u}^{\mathrm{T}}\rho\ddot{\mathbf{u}}$ represents the inertia forces, with the acceleration being the second derivative of the displacement.

The finite element equations that compute displacements, strains and stresses will be presented in the following lines. The equations are valid for all the three dimensional elements with n number of nodes.

The displacements u, v, w within each element are related to the nodal displacements (U, V, W) through the shape function matrix **N** as,

$$\mathrm{u} = \begin{bmatrix} u \\ v \\ w \end{bmatrix}_{3\times 1} = \begin{bmatrix} N_1 & 0 & 0 & N_2 & 0 & 0 & \cdots \\ 0 & N_1 & 0 & 0 & N_2 & 0 & \cdots \\ 0 & 0 & N_1 & 0 & 0 & N_2 & \cdots \end{bmatrix}_{3\times 3n} \times \begin{bmatrix} U_1 \\ V_1 \\ W_1 \\ U_2 \\ V_2 \\ W_2 \\ \vdots \end{bmatrix}_{3n\times 1} = \mathbf{N}\,\mathbf{U} \tag{3.9}$$

where,

$$N_{\mathrm{i}} = \frac{1}{8}(1+\xi\xi_{\mathrm{i}})(1+nn_{\mathrm{i}})(1+\mu\mu_{\mathrm{i}}) \tag{3.10}$$

Equation 3.10 represents the shape functions in the case of a solid hexahedral element, in which ξ, n, μ are the natural coordinates of the three dimensional element and ξ_{i}, n_{i} and μ_{i} are the natural coordinates of the i$^{\mathrm{th}}$ node depending on its position. The number of shape functions of an element is equal to the number of nodes n.

Using now the strain definitions in Equations 3.5 and 3.6 in combination with Equation 3.9, the relationship between the element strains and the correspondent nodal displacements can be obtained,

$$\varepsilon = \begin{bmatrix} \varepsilon_x \\ \varepsilon_y \\ \varepsilon_z \\ \gamma_{xy} \\ \gamma_{xz} \\ \gamma_{zy} \end{bmatrix}_{6\times1} = \begin{bmatrix} \frac{\partial N_1}{\partial x} & 0 & 0 & \cdots & \frac{\partial N_n}{\partial x} & 0 & 0 \\ 0 & \frac{\partial N_1}{\partial y} & 0 & \cdots & 0 & \frac{\partial N_n}{\partial y} & 0 \\ 0 & 0 & \frac{\partial N_1}{\partial z} & \cdots & 0 & 0 & \frac{\partial N_n}{\partial z} \\ \frac{\partial N_1}{\partial y} & \frac{\partial N_1}{\partial x} & 0 & \cdots & \frac{\partial N_n}{\partial y} & \frac{\partial N_n}{\partial x} & 0 \\ \frac{\partial N_1}{\partial z} & 0 & \frac{\partial N_1}{\partial x} & \cdots & \frac{\partial N_n}{\partial z} & 0 & \frac{\partial N_n}{\partial x} \\ 0 & \frac{\partial N_1}{\partial z} & \frac{\partial N_1}{\partial y} & \cdots & 0 & \frac{\partial N_n}{\partial z} & \frac{\partial N_n}{\partial y} \end{bmatrix}_{6\times3n} \times \begin{bmatrix} U_1 \\ V_1 \\ W_1 \\ \vdots \\ U_n \\ V_n \\ W_n \end{bmatrix}_{3n\times1} \quad 3.11$$

In other words,

$$\varepsilon = \mathbf{B}\,\mathbf{U} \quad 3.12$$

where the nodal displacements **U** are related to the element strains ε through the differential operator **B**. The stresses can now be calculated from the strains through the constitutive law. As an example, if the material response is fully elastic, this relationship follows Hooke's law, yielding

$$\sigma = \mathbf{D}\,\mathbf{B}\,\mathbf{U} \quad 3.13$$

Substituting Equations 3.9, 3.12 and 3.13, into Equation 3.8 leads to

$$\iiint \rho\,\mathbf{N}^{\mathrm{T}}\mathbf{N}\,\mathrm{d}V\ddot{\mathbf{U}} + \iiint \mathbf{B}^{\mathrm{T}}\mathbf{D}\,\mathbf{B}\,\mathrm{d}V\,\mathbf{U} - \iint \mathbf{N}^{\mathrm{T}}\mathbf{t}\,\mathrm{d}A - \iiint \mathbf{N}^{\mathrm{T}}\mathbf{b}\ \mathrm{d}V = 0 \quad 3.14$$

which yields:

$$\mathbf{M}\,\ddot{\mathbf{U}} + \mathbf{K}\,\mathbf{U} - \mathbf{R} = 0 \quad 3.15$$

where **M** is the inertia matrix, **K** is the stiffness matrix and **R** is the vector representing the external applied forces to the structure.

In the current work, the blast loading will represent the external applied force that will result in displacements within the elements of the structural mesh. Following the abovementioned equations, the finite element method will give nodal displacements and finally the response of the structural element in terms of strains and stresses.

3.4 LS-DYNA Finite Element code

LS-DYNA is a commercial finite element analysis software package of general use that was developed by the Livermore Software Technology Corporation (LSTC) [11]. Until now, LS-DYNA has an extensive constitutive model library and offers advanced capabilities when dealing with high transient dynamic problems such as blast loading. Hence, in the current study, it is going to be used as a numerical tool in order to assess the structural response of reinforced concrete targets exposed to contact blast and impact.

The origin of this software goes back to 1976 when Dr. John Hallquist created the three dimensional finite element analysis program DYNA 3D [12] at the Laurence Livermore National Laboratory in order to simulate the blast wave caused by the detonation of a nuclear bomb.

A problem is characterised as nonlinear when the boundary conditions of the structure are changed during the time, or when large deformations take place or materials with nonlinear behaviour are considered. In addition, a problem is said to be transient dynamic when inertia forces are dominant due to the presence of short duration external forces and due to high velocity impacts. Such events, that the physical object resists to any change in its state of motion, could be the crash deformations, explosions and industrial material forming.

The LS-DYNA package applies the Finite Element Analysis method through explicit time integration based on the central difference technique, which will be discussed later in this chapter. In addition, this package simulates the response under blast or impact loading by using mesh dependent approaches such as totally Lagrangian, totally Eulerian or Multi-Material-Arbitrary-Lagrangian-Eulerian (MMALE), which is a combination of the two, or mesh free approaches such as Smooth Particle Hydrodynamics (SPH).

The numerical capabilities of LS-DYNA are being enhanced continuously and this makes it a very powerful and effective tool when dealing with the aerospace, automobile, construction, manufacturing, bioengineering and military sectors, among others.

3.4.1 Solution approach of the second order equilibrium equations

The equation of motion (Equation 3.15) consisting of a set of second order differential equations is computationally demanding especially as the order of matrices is often very high. Finite element packages use either explicit or implicit time integration techniques in order to find a reliable solution. On the one hand, when the analysis is static - inertia forces are not taken into account -, the solution is found using the implicit technique. On the other hand, when the analysis is dynamic - inertia forces are taken into consideration -, either implicit or explicit technique can be applied.

In the explicit analysis the stiffness matrix is updated at the end of each increment due to changes in the geometry and the material condition. After the generation of the new matrix, the incremental loading is being applied. This numerical technique is stable if and only if the size of the time increments is sufficiently small. The time step should

be less than the time a sound wave needs in order to travel within the element (Courrant time step condition).

The implicit numerical technique works in approximately the same way with the explicit. The only difference is that right after every load increment a Newton – Raphson iteration can be applied to enforce equilibrium between the internal and the external forces. Implicit numerical techniques, even though can withstand bigger time-steps and are unconditionally stable, are computationally expensive if compared to the explicit analyses since the stiffness matrix has to be constructed in every iteration.

In this study, the explicit solver is used since it is ideal for dynamic analyses. LS-DYNA's, explicit solver uses the central difference scheme.

According to this time discretisation scheme (central difference), between the time equal to 0 and equal to t_0, the acceleration $\ddot{U}_0$, velocity $\dot{U}_0$ and displacement U_0 are already known. The main aim is to move forward in time and find the acceleration $\ddot{U}_1$, velocity $\dot{U}_1$ and displacement U_1 at time $t_1 = t_0 + \Delta t$, where Δt is the time increment.

Using the Taylor series at time $t = t_0$ and times $t_1 = t_0 + \Delta t$ and $t_{-1} = t_0 - \Delta t$, we get the following displacements U_1 and U_{-1}:

$$U_1 = U_0 + \Delta t \dot{U}_0 + \frac{\Delta t^2}{2} \ddot{U}_0 + \cdots \quad 3.16$$

and

$$U_{-1} = U_0 - \Delta t \dot{U}_0 + \frac{\Delta t^2}{2} \ddot{U}_0 + \cdots \quad 3.17$$

In the same manner it is possible to express the displacement at time $t = t_0$ as

$$U_0 = U_1 - \Delta t \dot{U}_1 + \frac{\Delta t^2}{2} \ddot{U}_1 \quad 3.18$$

When Equation 3.16, is substituted to Equation 3.18, the following relation is adopted for the acceleration at time t_1

$$\dot{U}_1 = \dot{U}_0 + \frac{1}{2}\left(\ddot{U}_0 + \ddot{U}_1\right)\Delta t \quad 3.19$$

Through the above equations, the displacements, accelerations and velocities are specified for time t_1. The same procedure is followed to find the corresponding values for time $t_2 = t_1 + \Delta t$.

As stated above, the explicit time integration method is conditionally stable. This means that in order to maintain the stability of the solution, the time step size should be smaller than a Δt_{cr} value. This value is related to the highest eigen-frequency ω_{max} whose determination is computationally demanding. So,

$$\Delta t \leq \Delta t_{cr} = \frac{2}{\omega_{max}} \quad 3.20$$

ω_{max}, is related to the sound speed c of the material and the minimum element size h_c through

$$\omega_{max} = \frac{2c}{h_c} \quad 3.21$$

In solids, the sound speed $c = (E/\rho)^{1/2}$ is related to the material's density ρ and Young's modulus E.

In addition, the element size is related to the type of element used for the analysis. For three dimensional 8-noded solid hexahedra elements, which are used in the current study, the element size can be given as

$$h_c = \frac{V_{\text{element}}}{A_{\text{element}}} \tag{3.22}$$

where V_{element} and A_{element} represent the volume and the area of the largest side of the element respectively. Using all the equations above, the critical time step [13] then becomes,

$$\Delta t_{cr} = \frac{h_c}{c} \tag{3.23}$$

The above equation is known as Courant-Friedrichs-Lewy (CFL) law. According to this law and for a stable solution, the time step should be lower than the time a wave needs to travel across an element.

For the above reason, the time step used in simulations is always the theoretical value determined previously, decreased by 10 % or more. In some cases, especially when dealing with explosion events it is better to use a value lower than 0.9.

3.4.2 Reinforced concrete: type of elements, integration points, hourglassing

In general, the actual problem can be modelled using finite elements in 1D, 2D or in 3D space. In 2D case, triangular or quadrilateral elements can be used. The most common elements in three dimensions are the tetrahedral (pyramid), pentahedral (wedge) and hexahedral (brick) elements. In the current study, where reinforced

concrete is exposed to blast and impact, the 3D formulation captures this complex phenomenon in a better way. Modelling of reinforced concrete in 2D space can be adequate under situations of static loading. In the case of dynamic loading, such as blast and impact, modelling in 3D offers a better representation of the real conditions and the actual externally applied load. Thus, phenomena such as confinement and dilatation of concrete are taken into consideration easier compared to the 2D. Even though the available element formulations can be explained in detail in Hallquist [13] and Liu et al. [14], only the brick hexahedral elements for modelling the concrete material and the 1D beam elements for modelling the reinforcing bars will be included for discussion herein.

The main reason behind the choice of brick elements in the current study, is that linear tetrahedral elements perform in a poor manner when plasticity, incompressible materials and severe bending are considered. Thus, the severe locking problems that tetrahedral elements can face, forced the use of hexahedral elements. Even if the pyramid elements fit very well in complex geometries, geometrical constraints was not an issue in the current study. The square slab/wall was a simple geometry and brick elements fit adequately within. Figure 3.2 below is an example used in the current study of an 8–noded brick element and 1D beam element.

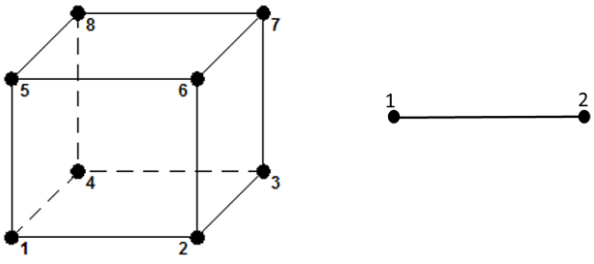

Figure 3.2: Example of a solid brick element and beam element.

The solid elements can be first order 8-noded brick (linear interpolation) or second order 20-noded brick elements (quadratic interpolation). In addition, each of the two categories can be either fully integrated (8 integration points for the 8-noded and 27 integration points for the 20-noded element) or have reduced integration (1 integration point for the 8-noded and 8 integration points for the 20-noded element).

When an element is subjected to bending it is expected to obtain a curved shape due to the applied moment. The main issue with the fully integrated first order elements is that the developed shear stresses can cause shear deformation rather than the expected deformation under the bending conditions. As a result, the elements become too stiff and locked. The referred phenomenon that is responsible for incorrect stresses and displacements is called shear locking (elements are locked due to the incorrect shear stresses). The fully integrated second order elements, are not sensitive to shear locking, but are computationally expensive and thus not preferred.

The reduced integration elements (first order or second order) on the other hand are preferred because can withstand large deformations and are more efficient in terms of the time required for the analysis. Between the first or the second order reduced integration elements (1 integration point scheme), the most computationally efficient choice and widely used in the numerical modelling of structures under blast loading, is the first order elements apart from the fact that they tend to hourglass and special treatments should be applied.

The hourglass effect (Figure 3.3) is a non-physical deformation of the elements causing severe distortion [15]. The control of this numerical issue can be achieved by implementing forces to counteract the hourglassing modes. There are 12 different

hourglassing modes according to Belytschko et al. [15]. The hourglass energy is the dissipation of energy through the work done by the internal forces in order to cancel out the hourglass effect. In addition, internal artificial forces can be applied in different ways either in a viscous or in stiffness form. These forms are known as hourglass formulations.

The stiffness formulation, applies the artificial forces in a proportional way with the displacements at the nodes that are responsible for the hourglassing effect. This formulation that stiffens the behaviour in an artificial way should use an hourglass coefficient low enough in order to reduce the stiffening influence. This formulation usually is applied in cases with low strain rates.

When high impact velocities and strain rates are present, such as in detonation events, the viscous form is preferred, in which the forces are applied proportionally to the velocities at the nodes.

In this study, for the above reasons (high strain rates), when the hourglass control needs to be defined for the solid hexahedral elements, the viscous formulation is selected.

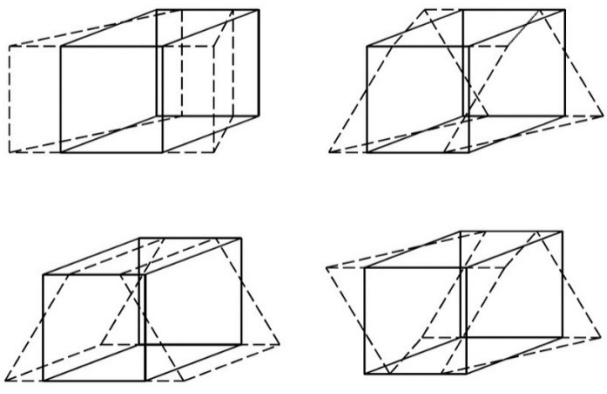

Figure 3.3: Examples of hourglassing modes (Figure taken from [13]).

The reinforcement can be modelled either as 1D truss or 1D beam elements. Truss elements can only take tensile or compressive axial forces, while beam elements are preferred, especially in this study, since can withstand bending and shear.

The reinforcing bars are taken into consideration inside the concrete material using three techniques named as smeared approach, explicit with shared nodes (beams and trusses) and explicit constraint [16]. The least and the most time consuming are the first and the last approach, respectively. In the smeared approach, the reinforcing bars are considered as a volume fraction between the reinforcement amount and the concrete amount. There are several material models for concrete in LS-DYNA that can use this method to account for rebars. The most relevant disadvantages of this method are the absence of graphical presentation of the rebars, since they are integrated entities within the concrete, and also that it is only an adequate technique for small deformation events, where the rebars deform elastically. The explicit approach with shared nodes, requires the nodes of the lagrangian parts (concrete and rebars) to be exactly the same and there is a challenge using this technique due to mesh constraints. In addition, the third approach that governs the movement of concrete and reinforcement mesh as well as the superposition between them is the explicit constraint (Constrained-Lagrange-in-Solid). The two meshes of concrete and rebars are constructed independently and do not have to be identical and share the same nodes. Then, the reinforcing bars are embedded with constrained acceleration and velocity at the nodes. It is also noted that the results are changing not only with the refinement of the concrete slab but with the refinement of rebars as well. Hence, in the current study, the explicit constraint approach was selected and it was also decided to bond the rebars using exactly the same mesh size with the concrete structure.

3.5 Modelling of blast loading

Three dimensional numerical simulations frequently have to cope with large distortions, either during the interaction between two fluids, two solids or during the interaction between fluids and solids. A very important thought, when coding, in order to capture the behaviour of a body under the applied load, is the selection of the suitable "kinematic description". More precisely, this selection governs the link between the moving body and the finite element mesh. Hence, the capability of the numerical technique to capture large deformations and distortions and lead to a reasonable solution.

There are two main kinematic descriptions. The Lagrangian description and the Eulerian description [17].

In the Lagrangian description every material particle of the continuum is linked to a location on the finite element mesh. This means that the mesh and the material are moving (deforming) together. Although the material points and the nodes of the mesh change location during deformation, the relative location of the points (independent of time) to the mesh nodes does not change. Consequently, the mesh does not allow the material to travel within it. An advantage of the Lagrangian technique is that it is straight forward to capture the response between the interfaces of the materials involved in the numerical simulation. In addition, since the boundary nodes are unchanged, this means that the application of boundary conditions can be done with ease. However, although this is the least computational expensive approach, severe mesh distortions due to large deformations can lead to convergence issues.

The Eulerian description is extensively used in fluid dynamics rather than in the continuum solids domain. It is assumed that the material points of the fluid are moving within a fixed in space Eulerian mesh (background mesh). So, as the fluid flows, the relative location of the material points in conjunction with the fixed mesh changes through time. Some of the drawbacks of this description are the difficulty in the application of boundary conditions and the tracking of interface interactions. The advantage of using this description however, is that, as the background mesh remains fixed, there is no much distortion. However, there is a need for a big enough Eulerian domain that is able to hold the material within its space.

There is also another description, called Arbitrary Lagrangian Eulerian (ALE) [18], which is used mainly in the current study and merges the benefits of both previous techniques trying to eliminate their disadvantages.

In this case the nodes of the mesh are moving either together with the body like in Lagrangian or remain fixed in space like in Eulerian or are moving in an arbitrary mode in order to make capable the rezoning (method to correct a distorted mesh). Thus, the numerical simulation can withstand larger element distortions compared to the purely Lagrangian description and can bring a better resolution compared with the purely Eulerian, because of the mesh flexibility. The three different approaches are shown schematically in Figure 3.4.

Following the above kinematic description, in LS-DYNA finite element hydrocode, four different approaches can be used in order to simulate structures under blast loading. These are the mesh dependent i) Load Blast Enhanced (LBE), ii) Multi Material Arbitrary Lagrangian Eulerian (MMALE), iii) the coupling between the two

[19] and iv) the mesh free methods such as Smoothed Particle Hydrodynamics (SPH) [20] that employs particles in the place of finite elements, that are related together through interpolation functions. For the needs of the current research we are going to focus only on the mesh dependent methods such as the LBE and MMALE techniques.

The first, as discussed previously, is a totally Lagrangian approach, where the material and the mesh are moving together. It is considered as the easiest way (in terms of personal and computational effort) to apply the blast load on the structural target, which is modelled with Lagrangian elements. LBE employs the ConWep relationship in order to consider the application of the pressure created during the detonation event. ConWep is based on the empirical equations of Kingery and Bulmash [21]. The pressure applied to the structure can be given below:

$$\mathrm{P}(t) = P_R \cos^2\theta + P_{so}(1 + \cos^2\theta - 2\cos\theta) \qquad 3.24$$

where P_R is the reflecting pressure, P_{so} is the incident pressure and θ is the angle of the shock impact. Even though it is a very straightforward technique and computationally inexpensive, the main disadvantage of using this approach is that it accounts only for a spherical explosive charge. Thus, if complex explosive geometries are being used, LBE cannot reproduces the actual blast wave propagation. In addition, the equations of Kingery and Bulmash are applicable for scaled distances between $0.147 < Z < 40$ [m/kg$^{1/3}$] and as a result cannot be used in the events of contact detonations. Those equations are based on TNT explosive mass. Thus, the explosive amount used, should be converted into TNT equivalent value.

The Lagrangian Eulerian approach (MMALE) is a better representation of the material's behaviour under high deformation. This is because the explosive and the air

are modelled separately. It is also assumed that the explosive can flow within the Eulerian mesh representing the air domain, which covers the whole Lagrangian structure, and finally impacts the target [22].

There is a fluid-structure interaction between the Lagrangian part (target) and the explosive within the Eulerian part (air). The explosive is supposed to be fluid and is not meshed. Only its position, shape and type are specified. The part of the model that represents the shape of the high-explosive could be either a standard 3D shape (sphere, cylinder etc.) or when complex geometries are considered, shell containers could be created in order to host the explosive material.

This technique will help preventing the formation of negative volumes as a result of the unnatural element deformations that may lead to an abrupt termination, numerical instabilities or convergence issues. Comparisons between the referred blast approaches [23] as well some conclusions drawn by Dobrociński [24] underline the necessity of MMALE technique in the close range (contact) detonations and its computational efficiency compared to the SPH approach even though both methods have a good correlation with the experimental data.

This study based on the above considerations, focuses on the MM ALE technique. The LBE is going to be used in the beginning and compared with the selected approach (MMALE) in order to prove that for close range detonations the latter approach is a very efficient numerical methodology.

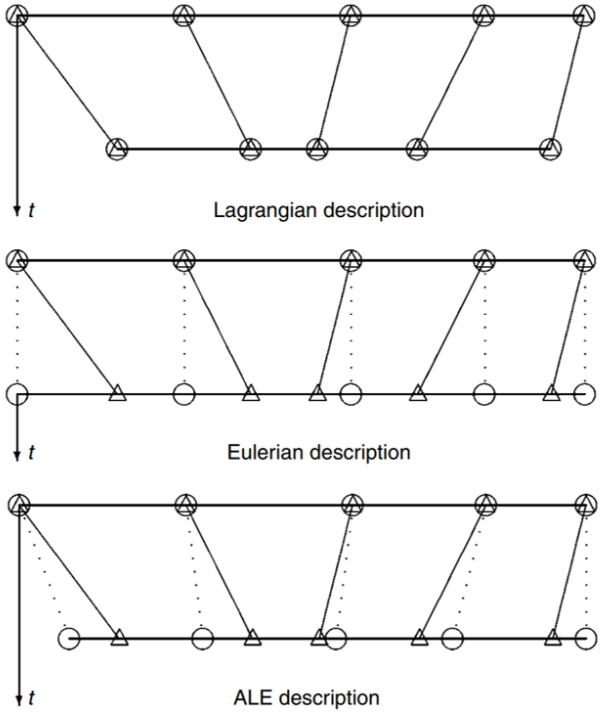

Figure 3.4: Lagrangian, Eulerian, and ALE description (Figure taken from [18]).

3.6 References

[1] K. J. Bathe, "An Introduction to the Use of Finite Element Procedures" Prentice Hall, 1996.

[2] J. N. Reddy, "An Introduction to the Finite Element Method", McGraw-Hill, 1993.

[3] A. Hrennikoff, "Solution of problems of elasticity by the framework method," Journal of applied mechanics, vol. 8, pp. 169-175, 1941.

[4] R. Courant, "Variational Methods for the Solution of Problems of Equilibrium and Vibrations", 1943.

[5] J. H. Argyris and S. Kelsey, "Energy Theorems and Structural Analysis: A Generalised Discourse with Applications on Energy Principles of Structural Analysis Including the Effects of Temperature and Non-linear Stress-strain Relations", Butterworth, 1960.

[6] M. J. Turner, L. J. Topp, H. C. Martin, and R. W. Clough, "Stiffness and Deflection Analysis of Complex Structures", 1956.

[7] R. W. Clough, "The Finite Element Method in Plane Stress Analysis", American Society of Civil Engineers, 1960.

[8] O. C. Zienkiewicz and R. L. Taylor, "The finite element method" vol. 3: McGraw-hill London, 1977.

[9] E. Oñate, "Structural Analysis with The Finite Element Method. Basis and Solids," 2009.

[10] A. K. Chopra, "Dynamics of structures, Theory and Application to Earthquake Engineering", 2001.

[11] J. O. Hallquist, "LS-DYNA keyword user's manual," Livermore Software Technology Corporation, vol. 970., 2007.

[12] J. Hallquist, "Preliminary user's manual for dyna3d and dynap," University of California, Lawrence Livermore Laboratory, Livermore, California, UCID-17268, 1976.

[13] J. O. Hallquist, "LS-DYNA theory manual," Livermore software technology corporation, vol. 3, pp. 25-31, 2006.

[14] G. R. Liu and S. S. Quek, " FEM for 3D solids," Oxford, Butterworth-Heinemann, 2003, pp. 199-232.

[15] T. Belytschko, W. Liu, and B. Moran, "Nonlinear finite elements for continua and structures", 2000, Chichester, New York, John Wiley, vol. 16, p. 650.

[16] L. Schwer, "Modeling rebar: the forgotten sister in reinforced concrete modeling," presented at the 13th International LS-DYNA Users Conference, Detroit, 2014.

[17] L. E. Malvern, "Introduction to the Mechanics of a Continuous Medium", 1969.

[18] J. Donea, A. Huerta, J. P. Ponthot, and A. Rodríguez-Ferran, "Arbitrary Lagrangian–Eulerian Methods", John Wiley & Sons, Ltd, 2004.

[19] Z. S. Tabatabaei and J. S. Volz, "A comparison between three different blast methods in LS-DYNA: LBE, MM-ALE, Coupling of LBE and MM-ALE " presented at the 12th International LS-DYNA Users Conference, Detroit, 2012.

[20] T. Rabczuk, J. Eibl, and L. Stempniewski, "Numerical analysis of high speed concrete fragmentation using a meshfree Lagrangian method," Engineering Fracture Mechanics, vol. 71, pp. 547-556, 3// 2004.

[21] C. N. Kingery and G. Bulmash, "Air blast parameters from TNT spherical air burst and hemispherical surface burst", Ballistic Research Laboratories, 1984.

[22] B. Zakrisson, B. Wikman, and H.-Å. Häggblad, "Numerical simulations of blast loads and structural deformation from near-field explosions in air," International Journal of Impact Engineering, vol. 38, pp. 597-612, 7// 2011.

[23] L. Schwer, H. Teng and M. Souli "LS-DYNA Air Blast Techniques: Comparisons with Experiments for Close-in Charges," presented at the 10th European LS-DYNA Conference, Wurzburg, Germany, 2015.

[24] S. Dobrociński and L. Flis, "Numerical Simulations of Blast Loads from Near-Field Ground Explosions in Air," in Studia Geotechnica et Mechanica vol. 37, ed, 2015, p. 11.

Chapter 4. Constitutive Modelling of Concrete

4.1 Introduction

In previous years the analysis of concrete structures has been mostly limited to the elastic analysis of concrete in conjunction with classical and empirical formulas based on the available experimental results. Although, these methods were very handy and efficient, the growth and improvement of numerical analysis techniques gave the opportunity to structural engineers to perform nonlinear finite element analyses. This was possible by using the finite element method, which is able to predict the nonlinear stress-strain behaviour and failure of materials such as concrete more accurately compared to previous approaches. In past years, due to the lack of computational potential this nonlinear response, was not taken into account or was taken into consideration with limitations in accuracy. In addition, large scale experiments of complex structures were very expensive to conduct and the need for more sophisticated and inexpensive tools was becoming another driving force for assessing their response.

Concrete is a brittle composite material containing coarse and fine aggregates which are connected together with the cement paste. Numerical modelling of concrete is a challenge due to the fact that the behaviour is dependent on its composite nature. More specifically, the type of cement used, the aggregate characteristics as well as the ratio between cement and aggregate, and water and cement can affect its performance. Even though we have to cope with a complex micro structure, this characteristic is often overlooked and the performance of the material is regarded as homogenous and isotropic. This simplifies all the parameters needed to be taken into consideration during the modelling procedure. In general, concrete without the application of any external loading has already developed micro cracks, in particular in interfaces

between the mortar and the coarse aggregates. This happens due to separation, expansion and shrinkage of the mortar. After the application of the load the aforementioned micro cracks become larger due to the interface between cement paste and aggregate, which is considered as the most vulnerable zone within concrete. The latter cracks are increasing as the loading and time progress. Concrete starts to develop a nonlinear response, which may lead to the damage or failure of the material.

In the following sections the response of concrete will be discussed in detail. In addition, the relevant constitutive models implemented in hydrocodes (LS-DYNA etc.) along with the material models used in the current study will be discussed as well. The main aim of the material models is to capture in a realistic way the complex nature of concrete under dynamic loading.

4.2 Nonlinear stress-strain response of concrete under uniaxial and multiaxial loading

According to Kupfer et al. [1], concrete under uniaxial compression adopts the behaviour shown in Figure 4.1 . It has been proven that three stages exist, when the material is under the effect of uniaxial compressive load. In the beginning of the first stage, the performance is linear elastic. The limit of elasticity is assumed to correspond to 30 % of the compressive strength of concrete (f_c'). Right after this point, a deviation from the linear relation is evident. The second stage is the stress – strain relationship from that point up to 75 % of the compressive strength. During this stage cracks develop around aggregates. These cracks, as the load increases, become bigger in size and number and it is the sign that the nonlinear behaviour is starting to take place. Until the upper limit of 75 % of strength is reached, the response of the material is

stable. This point is *onset of unstable fracture propagation.* After that point, the third stage is evident in which the cracks in the mortar are developing at higher rate and lead to further damage. The cracks that follow the path of the compressive load may lead to total failure of concrete.

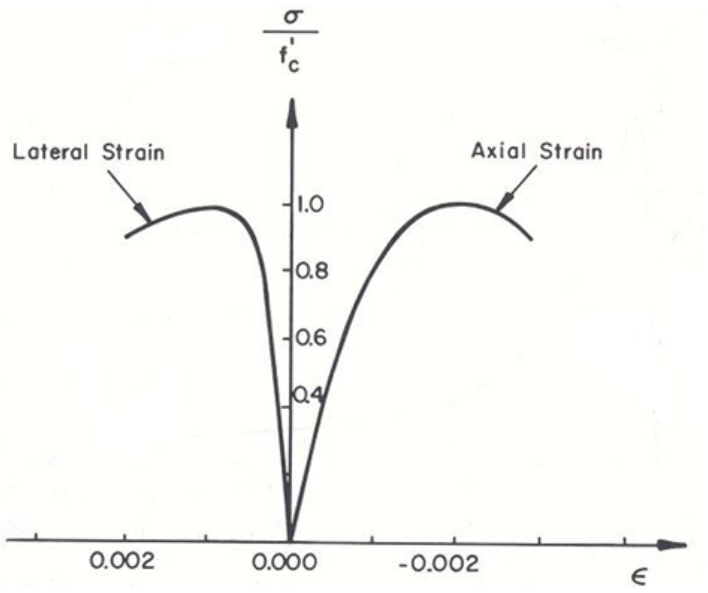

Figure 4.1: Stress strain curve for uniaxial compression of concrete (Figure taken from [1]).

When concrete is subjected to multiaxial loading, the stress-strain relation can be represented in Figure 4.2 [2]. During the experimental procedure the concrete specimens are loaded under σ_1 stress on the axial direction and $\sigma_2=\sigma_3$ on the lateral directions. The σ_1 increases from 3.2 to 23.56 ksi (22 to 162 MPa), while the other two stresses are kept constant and equal to one specific value during each experimental process. More precisely, the lateral stresses are equal to 0, 2, 4, 6, and 8 ksi (0, 14, 28, 41 and 55 MPa). It was noticed, that the concrete specimens under the effect of confined pressure exhibit greater strains compared to the solely uniaxial compression. A comparison between the multiaxial and uniaxial performance of concrete, shows that the confinement of concrete has positive effects in the ductility of the material.

In addition, the three stages of response, that were previously identified in the case of the uniaxial loading (linear elastic, inelastic and damage development) can be detected in the case of multiaxial loading as well.

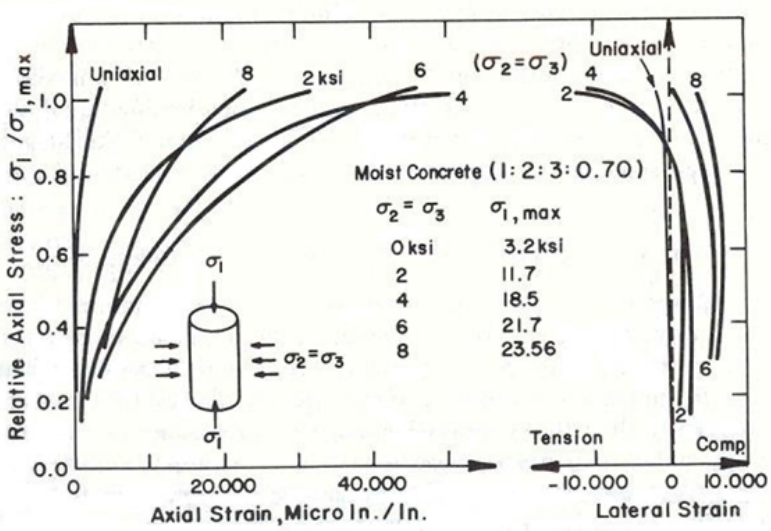

Figure 4.2: Stress strain curves for multiaxial compression of concrete (Figure taken from [2]).

4.3 Factors that affect the performance of concrete

As discussed previously, concrete is a material with complex nature. In order to obtain a reliable numerical response during modelling, the consideration of particular factors that affect the behaviour of concrete, is important. More precisely, uniaxial and multiaxial behaviour of concrete, different response that concrete exhibits in tension and compression, volumetric expansion (dilatation), strain softening, stiffness degradation and tension stiffening, are some of the critical factors that will be presented and described briefly in the following paragraphs.

Concrete exhibits a more brittle behaviour when exposed to uniaxial tension [3] than in compression (see Figure 4.3). The elastic limit of this response is considered to be

between 60 - 80 % of the material's ultimate tensile strength. After this limit micro-cracks begin to develop in a fast manner, being responsible for the brittle nature of concrete. Furthermore, mortar demonstrates a higher tensile strength than the strength of the aggregate – mortar interface. This fact mainly affects the low performance of concrete in tension. Usually, the tensile strength of concrete is around $1/10^{th}$ of its compressive strength.

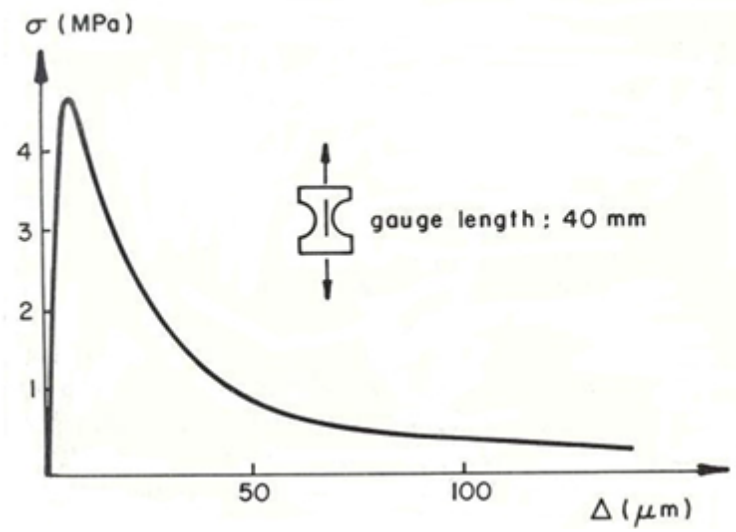

Figure 4.3: Stress- elongation curve for uniaxial tension (Figure taken from [3]).

The volumetric expansion of concrete under biaxial compressive loading is shown in Figure 4.4. Shah and Chandra observed [4], that the composite nature of concrete is responsible for the dilatation of the material. Hence, concrete expands only when the cement paste is mixed with aggregates. Furthermore, the stress at which the initiation of volume expansion takes place is strongly connected with further development of micro-cracks in the mortar.

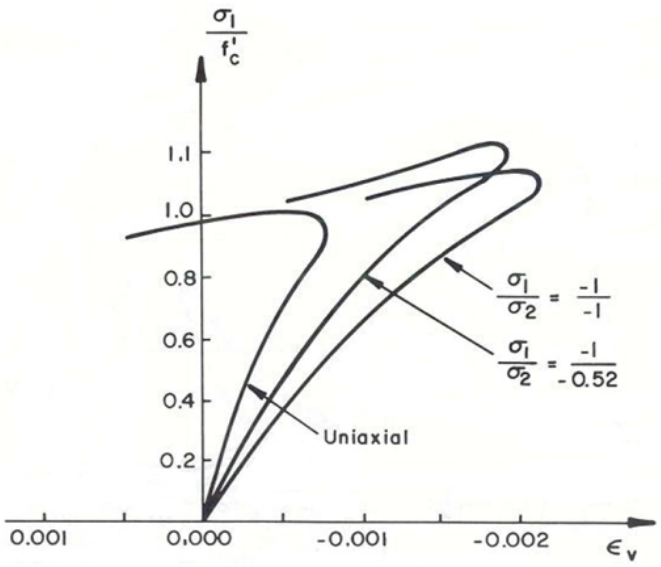

Figure 4.4: Volumetric expansion of concrete under biaxial compressive loading (Figure taken from [1]).

In addition, concrete under uniaxial compressive load demonstrates a strain softening response after the maximum compressive stress is reached [5]. That steep sloping descending part of the stress strain curves can be seen in Figure 4.5.

Experiments by van Mier [6] showed that the aforementioned descending branch is not considered to be a material property but the behaviour of the material under specified loading conditions (structural property). Under compressive tests on specimens with different heights, the softening branches become steeper as the height of the specimen increases (see Figure 4.6).

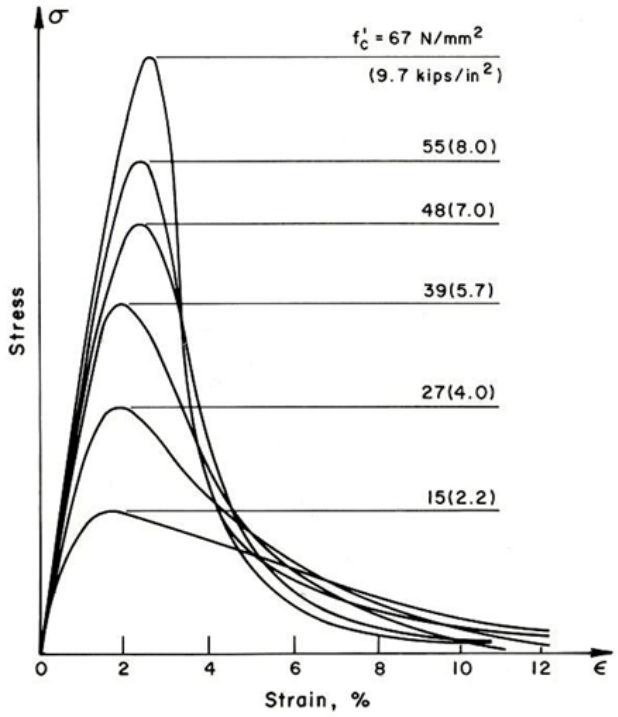

Figure 4.5: Stress strain curves for concrete under compression (Figure taken from [5]).

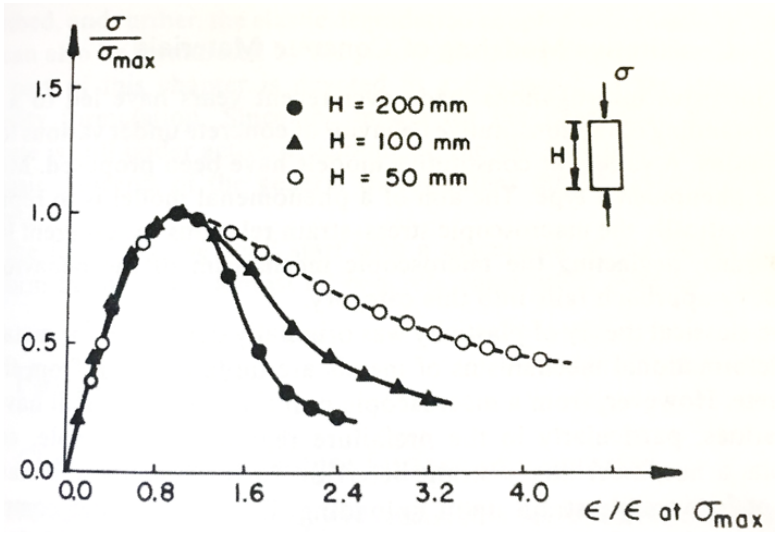

Figure 4.6: Effect of concrete specimen's height in compression (Figure taken from [6]).

Furthermore, as can be seen in Figure 4.7, concrete loses its compressive strength under cycle loading [7]. The unloading and reloading of concrete are curved sections forming loops with gradually decreasing slope. It is considered that each dotted line of every loop represents a slope that decreases with the increase of strains, resulting in a degradation of stiffness. This is closely associated with the damage of the material especially in the post peak regime.

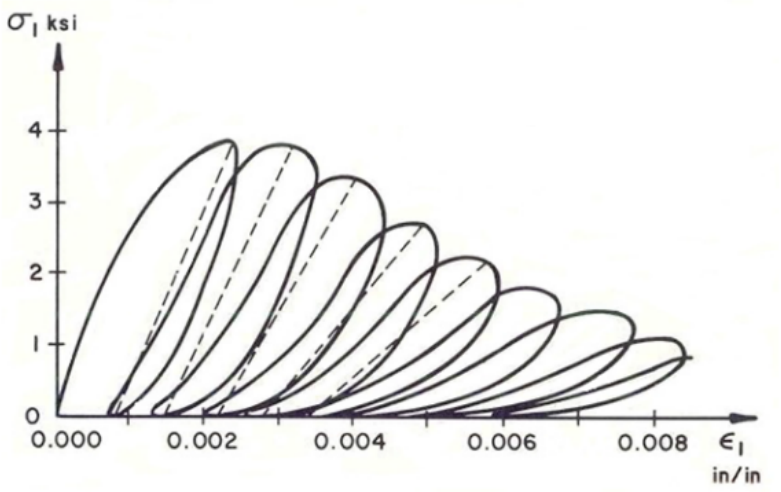

Figure 4.7: Stress strain curve for concrete under cyclic loading (Figure taken from [7]).

In addition, tension stiffening [8] is another factor that influences the behaviour of concrete. This phenomenon depicts the ability of the undamaged concrete, between close cracks, to support low tensile forces.

When a crack develops, the reinforcement is responsible for undertaking the tensile forces. In some regions around the cracks though, where concrete is still intact, tensile forces are undertaken by the undamaged concrete material through the bond between the reinforcement and concrete. As a consequence, the strains of the reinforcement developed in the un-cracked region are smaller than the strains developed in the

cracked region. Hence, the tension stiffening shows the ability of concrete to undertake those tensile forces.

4.4 Strain rate dependency

The type of loading and its position away from the structural target affect the magnitude of the stain rates. Figure 4.8 includes a rough prediction of the strain rates under several loading conditions with the blast and impact loading cases obtaining the highest limits of this range. In order to be able to capture the behaviour of concrete under extreme loading events, the awareness of the strain rate dependency is absolutely necessary. However, existing data needs further development, since most experimental investigations of concrete come out from constant strain rate compressive and tensile tests. In addition, experimental findings are influenced by the design and the content of free water in the concrete mixture. Thus, more research is necessary.

Reinforced concrete structures under the effect of blast loading can be subjected to strain rates of up to 1000 s^{-1}. It has been found that at those high rates the strength of concrete can increase dramatically both for tension and compression. The dynamic increase factor (DIF) is one of the possible ways that represent this sensitivity and is given by the fraction between the dynamic and the static strength of concrete. More precisely, according to Bischoff and Perry [9] concrete under compression can increase its strength by a factor greater than 2. In addition, according to Malvar and Ross [10], McVay [11] and Mellinger et al. [12] the material can increase its tensile strength by a factor of more than 6.

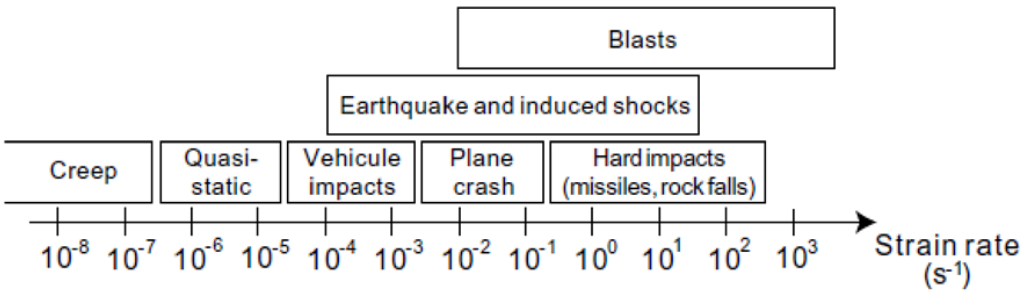

Figure 4.8: Strain rates under the effect of different cases of loading (Figure taken from [9]).

Several experimental techniques were used by researchers [9] in order to study the strain rate sensitivity. Compressive and tensile tests were conducted, for strain rates of up to 10^{-1} s^{-1} with the use of hydraulic testing machines. Very interesting results were found also for strain rates of up to 10^{0} s^{-1}. With the use of drop weight impact tests (masses between 50-100 kg that fall from 2-6 m height), the prediction of the response up to 10^{1} s^{-1} was achieved. In addition, the Split Hopkinson Pressure Bar (SHPB) is becoming a very popular technique for strain rates greater than 10^{2} s^{-1}.

Data available from the conducted tests is summarised in Figure 4.9 and Figure 4.10. In these, the Comité Euro–international du Beton CEB [13] recommendation curves, for both compression and tension, are included as well. These curves have a good correlation with the available experimental studies. It can be seen that there is a clear bilinear behaviour between the enhancement factor and the logarithmic value of the strain rate log($\dot{\varepsilon}$). The value of the strain rate, where the intense change of slope takes place, is $\dot{\varepsilon} = 3 \times 10^{1}$ s^{-1} in compression and $\dot{\varepsilon} \leq 10^{0}$ s^{-1} in tension.

For a better understanding of the strain rate sensitivity, it is worth questioning if what is happening is related to the nature of the material or if it is related to the structural response (not a homogenous stress-strain relationship within the sample). Hence,

experimental efforts should focus on the effect of parameters such as boundary conditions, free water in concrete mixture and the influence of water/cement ratio. For strain rates lower than 10^1 s^{-1}, experiments show that the sensitivity exists because of the free water content [14]. On the other hand, at higher strain rates, the strain rate dependency cannot be clearly identified. Li and Meng [15] for example, concluded after compression SHPB tests, that the phenomenon is due to the inertia confinement. When a compressive static load is applied during an unconfined test, the concrete cylinder expands due to the Poisson's effect. When the same test is conducted under dynamic loading, the radial expansion happens after a time delay, since the mass of the material should be accelerated in that direction. This delayed response, results in the effective inertia confinement and is closely related to the structural response of the material.

The following recommendation of the DIF factor in compression, according to CEB, is widely accepted and depicts in a good manner the material's response in real conditions:

$$\mathrm{DIF} = \frac{f_c}{f_{cs}} = \begin{cases} \left(\dfrac{\dot{\varepsilon}}{\dot{\varepsilon}_s}\right)^{1.026\alpha} & if \quad \dot{\varepsilon} \le 30\ \mathrm{s}^{-1} \\ \gamma\left(\dfrac{\dot{\varepsilon}}{\dot{\varepsilon}_s}\right)^{1/3} & if \quad \dot{\varepsilon} > 30\ \mathrm{s}^{-1} \end{cases} \tag{4.1}$$

where f_c and f_{cs} are the dynamic compressive strength at strain rate $\dot{\varepsilon}$ and the static compressive strength at strain rate $\dot{\varepsilon}_s$, respectively. The ratio of the two strengths is the dynamic increase factor DIF. The strain rate $\dot{\varepsilon}$ varies between 30×10^{-6} and 300 s^{-1}. The static strain rate in compression is $\dot{\varepsilon}_s = 30 \times 10^{-6}$ s^{-1}. In addition, $\log\gamma = 6.156 \times \alpha - 2$, $\alpha = 1 / (5 + 9 f_{cs} / f_{co})$ and $f_{co} = 10$ MPa.

The Dynamic Increase factor in tension can be given as:

$$\mathrm{DIF} = \frac{f_t}{f_{ts}} = \begin{cases} \left(\frac{\dot{\varepsilon}}{\dot{\varepsilon}_s}\right)^{1.016\delta} & \text{if } \dot{\varepsilon} \leq 30 \text{ s}^{-1} \\ \beta\left(\frac{\dot{\varepsilon}}{\dot{\varepsilon}_s}\right)^{1/3} & \text{if } \dot{\varepsilon} > 30 \text{ s}^{-1} \end{cases} \quad 4.2$$

where f_t and f_{ts} are the dynamic tensile strength at strain rate $\dot{\varepsilon}$ and the static tensile strength at rate $\dot{\varepsilon}_s$, respectively. The strain rate $\dot{\varepsilon}$, in this case, varies between 3×10^{-6} and 300 s^{-1}. While the static strain rate in tension is $\dot{\varepsilon}_s = 3 \times 10^{-6}$ s^{-1}. In addition, $\log\beta = 7.11\,\delta - 2.33$, $\delta = 1 / (10 + 6\,f_{cs}/f_{co})$ and f_{co}=10 MPa.

The CEB formulation in tension is valid up to a strain rate of 300 s^{-1}. At this specific strain rate, 30 MPa compressive strength concrete is expected to exhibit an enhancement factor around 3.9 (See Equation 4.2).

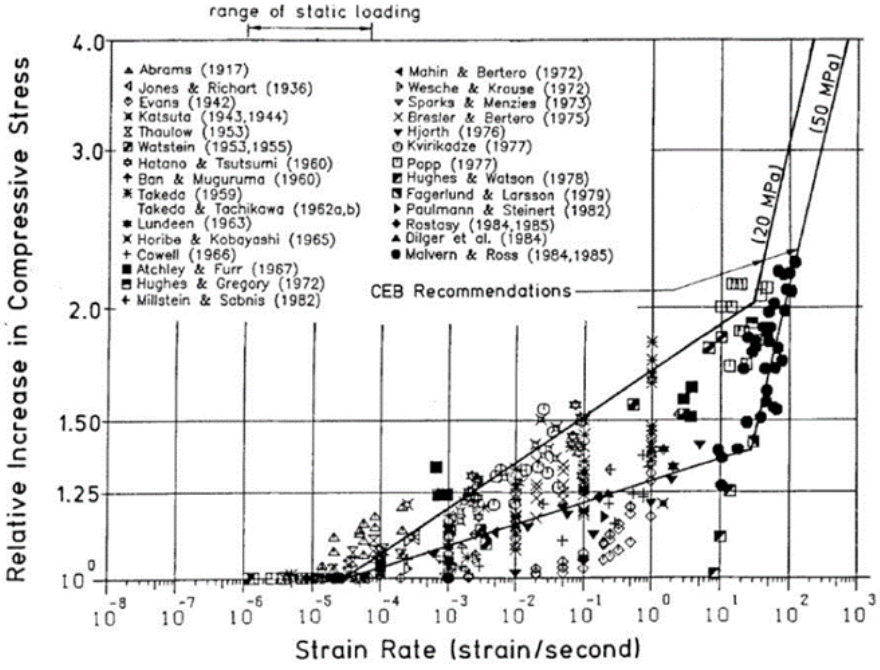

Figure 4.9: Dynamic Increase Factor (relative increase in compressive stress) for concrete in compression (Figure taken from [9]).

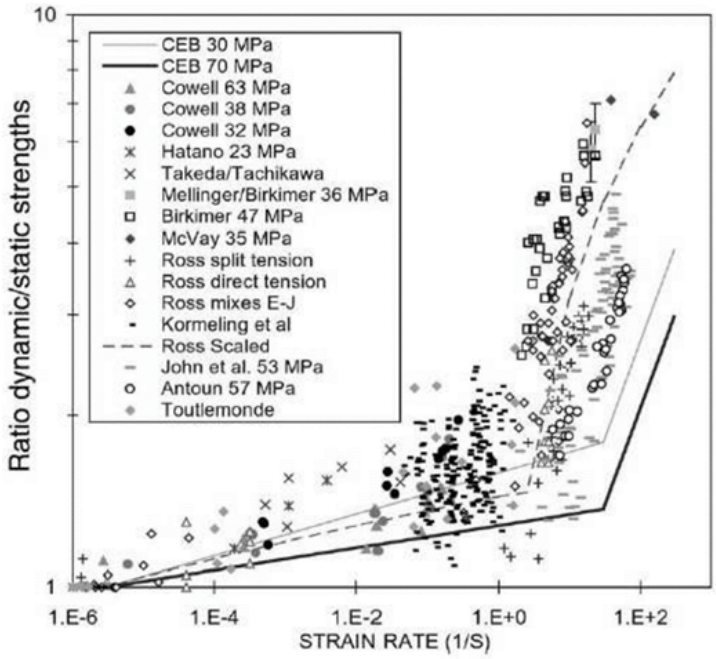

Figure 4.10: Dynamic Increase Factor (ratio dynamic/static strengths) for concrete in tension (Figure taken from [9]).

4.5 Constitutive material models for concrete

In hydrocodes such as LS-DYNA stresses and strains are treated separately in a volumetric and deviatoric part. The volumetric part is governed by the equation of state (EOS) [16] that relates the hydrostatic pressure to the local energy and density. For solid materials, the following EOS relationship is often recommended:

$$p(\rho, E) = A_1\mu + A_2\mu^2 + A_3\mu^3 + (B_0 + B_1\mu)\rho_0 e \qquad 4.3$$

where A_1, A_2, A_3, B_0, B_1 are constants, $\mu = (\rho / \rho_0 - 1)$ is the relative volume, ρ_0 is the initial density and e is the internal energy. For porous materials the following relationship is recommended:

$$p(\rho_p, E, \alpha) = A_1\bar{\mu} + A_2\bar{\mu}^2 + A_3\bar{\mu}^3 + (B_0 + B_1\bar{\mu})\rho_0 e \quad 4.4$$

where $\bar{\mu} = \rho_p \alpha / \rho_0 - 1$, ρ_p is the porous material density and α is the porosity that is described by

$$\alpha = 1 + (\alpha_{ini} - 1)[(p_{lock} - p)/(p_{lock} - p_{crush})]^n \quad 4.5$$

where α_{ini} is the initial porosity of concrete, p_{lock} corresponds to the pressure where α = 1 and p_{crush} is related to the value of pressure where the plastic compaction begins.

The aforementioned formulations are the most typical approach in order to apply the EOS equation in concrete material under shock loading. When concrete is modelled, these equations are implemented separately from the material constitutive models and can be used with no limitations in conjunction with the materials models that will be presented in this section. However, some material models, as the one used in the current research study, take into consideration the volumetric expansion of concrete within the constitutive material model. Hence, there is no need to implement those equations separately.

The strength surface, defined by a strength criterion, governs the deviatoric part and shows the relation between the first stress invariant I_1 and the second invariant of the

deviatoric stress tensor J_2. The third deviatoric stress invariant J_3, that governs the shape of the compressive to tensile meridian, may also be considered [17]. There are several well-known static strength criteria such as Drucker Prager [18], Mohr Coulomb [19], William Warnke [20], Hsieh-Ting Chen [21] and Ottosen [22]. In addition, as previously discussed, the dynamic increase factor (DIF) is a very important consideration when concrete is subjected to dynamic loading [23].

Hence, several material models have been developed and implemented in hydrocodes such as LS-DYNA, trying to take into consideration basic characteristics of material behaviour (e.g. strain hardening, pressure hardening, strain softening, strain rate dependency) but they differ in some of the assumptions [24]. In particular, in some material models the third deviatoric stress invariant J_3 is not considered or the DIF factor is the same in both tension and compression. Each new model tries to recommend better parameters and to improve on existing models. Some of the most used material models for concrete are referred in this section and a more detailed presentation is dedicated to the material model used in the current research work.

The Concrete Damage (CD) model, according to Malvar et al. [25] , [26], is a material model that accounts for damage in concrete by incorporating three surfaces (yield, failure, residual) that are dependent on the third invariant of the deviatoric stress tensor J_3.

The Johnson Holmquist Concrete (JH) model [27], assumes a linear-elastic behaviour before stresses reach their maximum value. If loading continues to be applied, damage will initiate until the total failure of the material. The model does not take into account

the J_3 invariant and even though the strain rate sensitivity is considered, the enhancement factor is the same for tension and compression.

The Riedel-Thoma-Hiermaier (RHT) model developed by Riedel et al. [28] is a further enhancement of the JH model in order to account for the J_3 stress invariant, model appropriately the softening behaviour of the material and consider a different DIF in tension. The model works in a similar manner as the CD model.

The Continuous Surface Cap (CSC) model [29], is comparable to CD and RHT model, since it incorporates strength surfaces as well. In addition, it takes into account the strain rate sensitivity and damage, while it introduces a cap parameter in the failure surface.

Simo et al. [30] and Sandler and Rubin [31] introduced the two invariant Geological Cap (GC) model that supports kinematic hardening. In this model, two stress invariants I_1, J_2 and three surfaces (failure, cap and tensile cut-off) are taken into consideration. One of the model's main disadvantages is that the deviatoric cross section of strength surfaces, is assumed to be circular. This is only true for brittle materials subjected to high pressures, otherwise the shape is triangular. In addition, the softening response of concrete and the effect of confining pressure are not captured satisfactorily with this model.

The Pseudo Tensor Geological (PTG) model [32] consists of two curves in order to capture the shape deformation of the deviatoric part. The upper limit curve depicts the maximum strength, while the lower limit curve describes the residual strength. This model takes into consideration the damage of the material but doesn't account for the strain rate dependency of concrete or the parameter J_3.

In the Soil Concrete (SC) material model [33], the yield function is also governed by the first stress invariant I_1 and the second invariant of the deviatoric stress tensor J_2. In addition, the softening behaviour of the material is not a smooth curve due to the steep change of the scalar factor that controls the softening response.

The Winfrith model [34],[35],[36] was developed by Broadhouse et al. for the demands of the UK nuclear industry in the 1980s and in 1991 was implemented in LS-DYNA. The model considers the third stress invariant of the deviatoric stress tensor J_3, non-compulsory consideration of rate effects, strain softening in tension through crack opening and cracking of concrete in tension with the limit of three orthogonal crack planes on each element. The reinforcing bars can be considered either within the model, as a volume fraction, or explicitly. This material model can capture adequately the response of concrete under tensile cracking and crushing due to compression.

The deviatoric part describing the failure surface of the material can be derived from the Ottosen criterion [22] as:

$$\mathrm{F}(I_1, J_2, \cos 3\theta) = \alpha \frac{J_2}{{f_\mathrm{c}}^2} + \lambda \frac{\sqrt{J_2}}{f_\mathrm{c}} + b \frac{I_1}{f_\mathrm{c}} - 1 \qquad 4.6$$

where λ is related to the third stress invariant and is given by:

$$\lambda = \begin{cases} k_1 \cos\left[\dfrac{\cos^{-1}(k_2 \cos 3\theta)}{3}\right] & \cos 3\theta \geq 0 \\ k_1 \cos\left[\dfrac{\pi}{3} - \dfrac{\cos^{-1}(-k_2 \cos 3\theta)}{3}\right] & \cos 3\theta < 0 \end{cases} \qquad 4.7$$

θ is the lode angle as a function of the J_2 and J_3, α and b are constants that adjust the meridional shape of strength surfaces and are affected by the ratio of the tensile to compressive strengths. In addition, k_1 and k_2 are functions of the same ratio.

The equation of state (EOS) that relates the pressure to the volumetric strain is automatically taken into consideration within the model or can be defined manually. If not defined, the model automatically implements a curve, with the relevant data listed in Table 4.1.

Table 4.1: Numerical values defining the relation between the default pressure and the volumetric strain.

Volumetric Strain	Factor of Pressure P_c
$-P_c/K$	1.00
-0.002	1.50
-0.004	3.00
-0.010	4.80
-0.020	6.00
-0.030	7.50
-0.041	9.45
-0.051	11.55
-0.062	14.25
-0.094	25.05

The first point for the determination of the volumetric strain is derived automatically using $P_c = f_c / 3$ and $K = E / (3\,(1-2\,\nu))$, where f_c, E and ν are the compressive strength, Young's modulus and Poisson's ratio of concrete, respectively.

In addition, Winfrith model follows the enhancement factors recommendations for tension and compression given by the Comité Euro-international du Beton [13], in order to take into consideration the strain rate dependency of concrete when subjected to dynamic loading.

4.6 Material model of concrete in the current study

Most of the referred material models need parameters which are obtained through experimental testing on the behaviour of the material. Consequently, it is not easy and applicable each time a numerical simulation is performed to know in advance all the necessary parameters. Moreover, some material models, such as Concrete Damage Release 3 and Continuous Surface Cap, have the option of automatic generation of parameters. For this reason, many researchers have used these material models in their studies. Moreover, Thiagarajan et al. [37], underlined that CD model exhibits poor performance when the parameters for concrete are automatically created. In addition, according to Kong et al. [38], the model, although it is a very popular choice, needs modifications in order to realistically capture cratering and scabbing on reinforced concrete slabs under the effect of projectile impact.

Other important factors, such as the consideration of the third invariant of the deviatoric stress tensor J_3 and strain rate effects with ideally a different strain rate dependency in tension and compression, are not taken into account in some of the aforementioned models.

In the current study, the Winfrith model is selected for capturing the response of concrete under contact blast and impact events, since it considers all the aforementioned factors.

4.7 Constitutive model of the reinforcing bars

In the current study two material models were used [39] in order to capture the behaviour of the reinforcing bars inside the concrete material. The Piecewise-Linear-Plasticity and the Plastic-Kinematic model describe the plastic behaviour of steel reinforcement adequately and require a simple input of parameters. The first model is applied to the rebars of the contact detonation scenario and the second is applied to the rebars of the combined contact blast and impact event.

The former adopts a linear elastic behaviour before yielding and plastic deformation after yielding. In addition, the rebars exhibit rate effects using a viscoplastic formulation. This model requires the implementation of a curve, describing the variation of the effective plastic strain with the stress. The curve governs the plastic region, consequently, the first value of the curve is the effective plastic strain equal to 0 associated with the yield stress of the material. The material parameters used and the implemented curve will be presented in Section 6.3.7 of the experimental and numerical procedures.

The Plastic-Kinematic model that is used as well, is an isotropic - kinematic material model, depending on the input parameter β. When $\beta = 0$ or $\beta = 1$, pure kinematic hardening (different behaviour in tension and compression) or isotropic hardening (same behaviour in tension and compression) can be achieved, respectively. If $0 < \beta < 1$ the model considers the interaction of both hardenings. In the current study, kinematic hardening is considered. The strain rate sensitivity can be accounted for when employing the Cowper and Symonds model [40], which enhances the static yield stress σ_{stat} as follows:

$$\frac{\sigma_{\mathrm{d}}}{\sigma_{\mathrm{stat}}} = 1 + \left(\frac{\dot{\varepsilon}}{C}\right)^{1/P} \qquad 4.8$$

where, σ_{d} is the dynamic strength, $\dot{\varepsilon}$ is the strain rate and C, P are the Cowper Symonds constant parameters. The bilinear curve of the model is shown in Figure 4.11.

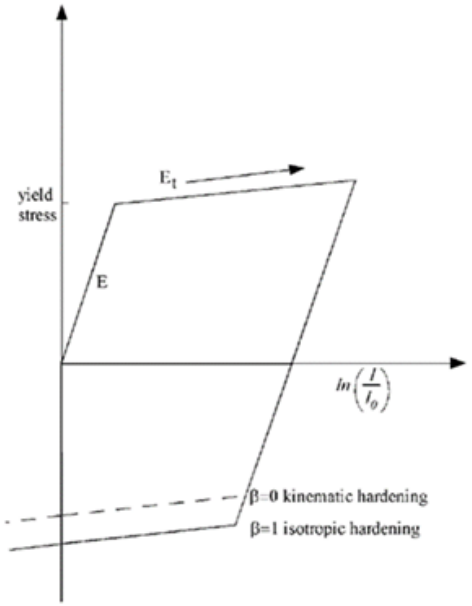

Figure 4.11: Bilinear stress-strain response of steel for the model (Figure taken from [32]).

4.8 References

[1] H. Kupfer, H. K. Hilsdorf, and H. Rusch, "Behavior of concrete under biaxial stresses," in Journal Proceedings, pp. 656-666, 1969.

[2] R. Palaniswamy and S. P. Shah, "Fracture and stress-strain relationship of concrete under triaxial compression," Journal of the Structural Division, vol. 100, pp. 901-916, 1974.

[3] P.E. Petersson, "Crack growth and development of fracture zones in plain concrete and similar materials", Division, Inst., 1981.

[4] S. P. Shah and S. Chandra, "Critical stress, volume change, and microcracking of concrete", in Journal Proceedings, pp. 770-780, 1968.

[5] G. Wischers, "Application of effects of compressive loads on concrete", Betontechnische Berichte, 1978.

[6] J. van Mier, "Complete stress-strain behavior and damaging status of concrete under multiaxial conditions", in RILEM/CEB Symposium on Concrete Under Multiaxial Conditions, 1984.

[7] B. Sinha, K. H. Gerstle, and L. G. Tulin, "Stress-strain relations for concrete under cyclic loading", in Journal Proceedings, pp. 195-212, 1964.

[8] S. M. Allam, M. S. Shoukry, G. E. Rashad, and A. S. Hassan, "Evaluation of tension stiffening effect on the crack width calculation of flexural RC members", Alexandria Engineering Journal, vol. 52, pp. 163-173, 6// 2013.

[9] P. Bischoff and S. Perry, "Compressive behaviour of concrete at high strain rates", Materials and structures, vol. 24, pp. 425-450, 1991.

[10] L.J. Malvar and C.A. Ross, "Review of strain rate effects for concrete in tension", ACI Mat J 1998;95(6):735-91998.

[11] M. McVay, "Spall damage of concrete structures", U.S. Army Corps of Engineers Waterways Experimental Station, 1988.

[12] F. M. Mellinger and D. L. Birkimer, "Measurements of stress and strain on cylindrical test specimens of rock and concrete under impact loading", DTIC Document, 1966.

[13] Comite Euro-International du Beton, "CEB-FIB Model Code", Trowbridge, Wiltshire, UK, Redwood Books, 1990.

[14] P. H. Bischoff and S. H. Perry, "Impact behavior of plain concrete loaded in uniaxial compression", Journal of engineering mechanics, vol. 121, pp. 685-693, 1995.

[15] Q. Li and H. Meng, "About the dynamic strength enhancement of concrete-like materials in a split Hopkinson pressure bar test", International Journal of solids and structures, vol. 40, pp. 343-360, 2003.

[16] W. Hermann, "Constitutive equation for the dynamic compaction of ductile porous materials", J Appl Phys 1969;40:2490-91969.

[17] X. Q. Zhou, V. A. Kuznetsov, H. Hao, and J. Waschl, "Numerical prediction of concrete slab response to blast loading", International Journal of Impact Engineering, vol. 35, pp. 1186-1200, 2008.

[18] P.E. Pinto, "RC elements under cyclic loading, state of the art report", London, Thomas Telford, 1996.

[19] A.C.T. Chen and W.F. Chen, "Constitutive relations for concrete", J Eng Mech Div ASCE 1975;101(EM4):465-811975.

[20] W.F. Chen, "Plasticity in reinforced concrete", New York, McGraw-Hill, 1982.

[21] M.D. Kotsovos and J.B. Newmann, "Generalised stress-strain relations for concrete", J Eng Mech Div ASCE 1978;104(EM4):845-561978.

[22] N.S. Ottosen, "A Failure Criterion for Concrete", Journal of the Engineering Mechanics Division, vol. 103, pp. 527-535, 1977.

[23] J. Eibl and B. Schmidt-Hurtienne, "Strain-rate sensitive constitutive law for concrete", J Eng Mech, vol. 145, pp. 1411-1420, 1999.

[24] Z. G. Tu and Y. Lu, "Evaluation of typical concrete material models used in hydrocodes for high dynamic response simulations", International Journal of Impact Engineering, vol. 36, pp. 132-146, 2009.

[25] L. J. Malvar, J. E. Crawford, J. W. Wesevich, and D. Simons, "A plasticity concrete material model for DYNA3D", International Journal of Impact Engineering, vol. 19, pp. 847-873, 1997.

[26] L.J. Malvar, J.E. Crawford and K.B. Morrill, "K&C concrete material model release III-automated generation of material model input", K&C Technical Report TR-99-24-B1, Glendale, 2000.

[27] T. J. Holmquist and G. R. Johnson, "A computational constitutive model for concrete subjected to large strains, high strain rates and high pressures", in 14th International Symposium on Ballistics, Quebec, 1993.

[28] W. Riedel and K. Thoma, "Penetration of reinforced concrete by BETA-B-500- numerical analysis using a new macroscopic concrete model for hydrocodes", Proceedings of 9th Intrernational Symposium on interaction of the effect of munitions with structures, Berlin-Strausberg, Germany, 1999.

[29] Y. D. Murray, "Theory and evaluation of concrete material model 159", presented at the 8th International LS-DYNA Users Conference, Dearborn, Michigan, USA, 2004.

[30] J.C. Simo, J.W. Ju, K.S. Pister and R.L. Taylor, "An assessment of the cap model: consistent return algorithms and rate-dependent extensions", J Eng Mech 1988;114(2):191-2181988.

[31] I.S. Sandler and D. Rubin, "An algorithm and a modular subroutine for the cap model", Int J Numer Anal Met 1979;3:173-861979.

[32] J. O. Hallquist, "LS-DYNA keyword user's manual", Livermore Software Technology Corporation, vol. 970., 2007.

[33] K. Yonten, T.M. Majid, D. Marzougui and A. Eskandarian, "An assessment of constitutive models of concrete in the crashworthiness simulation of roadside safety structures", Int J Crashworthiness 2005;10(1):5-192005.

[34] B. J. Broadhouse and A. J. Neilson, "Modelling Reinforced Concrete Structures in DYNA3D", Safety Engineering Science Division, AEE Winfrith Technology Centre, U.K, 1987.

[35] B. J. Broadhouse and G. J. Attwood, "Finite element analysis of the impact response of reinforced concrete structures using Dyna3D", Proc. 12th

International Conference on Structural Mechanics in Reactor Technology (SMiRT-12), 1993.

[36] B. J. Broadhouse, "The Winfrith concrete model in LS-DYNA3D," Structural Performance Department, AEA Technology, Winfrith Technology Centre, SPD/D(95)363, U.K, 1995.

[37] G. Thiagarajan, A. V. Kadambi, S. Robert, and C. F. Johnson, "Experimental and finite element analysis of doubly reinforced concrete slabs subjected to blast loads", International Journal of Impact Engineering, vol. 75, pp. 162-173, 2015.

[38] X. Kong, Q. Fang, Q. M. Li, H. Wu, and J. E. Crawford, "Modified K&C model for cratering and scabbing of concrete slabs under projectile impact", International Journal of Impact Engineering.

[39] J. O. Hallquist, "LS-DYNA theory manual," Livermore software technology corporation, vol. 3, pp. 25-31, 2006.

[40] N. Jones, "Structural impact, 1989," Paperback edition, 1997.

Chapter 5. Literature Review on Reinforced Concrete Slabs and Walls under Blast Loading and Soft Projectile Impact

5.1 Blast loading

The last 20 years significant research studies (numerical and experimental) were performed on the dynamic response of reinforced concrete subjected to blast loading.

Low and Hao [1] carried out a reliability analysis of normal designed reinforced concrete slabs under the effect of blast loading. The slab were simplified into a Single Degree of Freedom problem (SDOF) and Monte Carlo simulation was adopted in order to validate the SDOF system. It was stated that the reflected pressures vary significantly as the scaled distance Z changes, a finding, that includes many uncertainties especially due to the fact that the blast experiments are not straightforward to be carried out. It was found that concrete's Young modulus affects considerably the failure propagation, the yield stress of the reinforcing bars does not contribute significantly while concrete's crushing strength has the minimum effect. In addition, the parametric studies showed that the length of the slab slightly affects the response while the thickness and the ratio of the reinforcing bars strongly affect the response of them under those circumstances. Yao et al. [2], performed an experimental and numerical assessment of the response of reinforced concrete under blast loading (0.5 $m/kg^{1/3}$ scaled distance). Their numerical simulations used the CONWEP approach and the Concrete Damage R3 material model. The results showed the strong correlation between the reinforcement ratio and the blast resistance. More precisely the damage mode, the deflections and the spallation were decreased with the increase of this ratio. In addition, it was stated that when the mass of the explosive increases, the damage mode moves from inelastic response to failure under spallation. Finally, the authors developed a formula (for the particular range of stand-off distance), in

which the deflection thickness ratio was related to the reinforcement ratio and the scaled distance. Du and Li [3], performed a numerical study on the behaviour of a reinforced concrete slab under the detonation of 1000 kg of TNT and 10 m away from the concrete target. The authors used the Lagrangian CONWEP approach along with the Johnson-Holmquist material model for concrete. Even though the results needed an experimental validation, they stated that the compressive strength of concrete along with the depth of the slab and the reinforcement fraction can influence the blast resistance.

Wu et al. [4] performed an experimental investigation of impulses and reflected pressures that act on the surface of reinforced concrete targets and compared the obtained data with empirical data. The test included cylindrical and spherical explosives that detonated at standoff distances ranging between 0.75 - 3 ($m/kg^{1/3}$). The results showed, that on the one hand the shape of the explosive doesn't contribute significantly to the predicted pressures. On the other hand, the mass of the explosive and the orientation of the charges are very important parameters. In addition, the authors performed a numerical parametric study, which showed that the aspect ratio of the explosive charge along with the point of detonation, contribute significantly to the reflected pressures. Shi et al. [5] conducted an experimental study on the spallation of reinforced concrete slabs within a scaled distance equal to 0.4 $m/kg^{1/3}$. On this study, they investigated pressures, accelerations and displacements on the impacted targets. They also stated after observing the results that the spalling damage is significantly affected by the height/diameter ratio of the TNT cylindrical explosive (increases when the ratio increases) and that the shape of the explosive from cylinder to other

configurations enhances the damage as well. Jia et al. [6], performed a numerical analysis using CONWEP approach in order to investigate the damage modes on two-way reinforced concrete slabs, with the scaled distance ranging between 1.08 to 2.92 $m/kg^{1/3}$. They proposed a criterion regarding the damage prediction of the slabs and stated that the mass of the explosive is responsible for further development of damage. In addition, according to their findings the damage increases when the charge is closer to the boundary and that the boundary conditions affect the resistance of the impacted structural element.

Li and Hao [7] conducted a numerical study on the spallation of reinforced concrete slabs under blast loading (scaled distance equal to 0.6 $m/kg^{1/3}$) along with the use of Concrete Damage R3 material model and validated those results with existing experimental data. The main reason was the calibration of this particular model in order to be implemented for their numerical study regarding the spallation of reinforced concrete columns. According to them, this is possible, considering the fact that the spallation is a localised damage that is affected by the concrete properties, thickness and reinforcing confinement.

Alia and Souli [8], used the relative new (at this period) ALE technique for simulating a free air blast as well as the blast pressure applied to a rigid wall from a standoff distance equal to 1.2 m. They mentioned the benefits from using this technique instead of a totally Lagrangian approach and also stated that ALE formulation predicts the reflected pressures (case of the wall) in a very good manner, when compared to their experimental observations. Chafi et al. [9], using ALE approach studied the free air blast produced by the detonation of C4 and TNT explosive. Comparing the numerical

pressures under several stand-off distances, found a good correlation with the existing experimental data. Following this study, they applied the same formulation (ALE) in order to investigate the performance of a steel plate under the detonation of TNT (0.781 g) explosive. Even though, the results, as the stand-off distance was increasing, regarding the peak pressure, the evolution of pressure and the deflections, referred to a steel target, it is considered as a good research attempt to validate the efficiency of ALE technique. Tai et al. [10], also studied the behaviour of concrete slabs under the effect of air blast loading and in various stand-off distances (with the smallest being 0.5 m) using ALE approach and Johnson Holmquist concrete material model. These authors concluded that the mesh refinement, the amount of explosive, the standoff distance and the reinforcement ratio affect the response of the concrete targets. Wang et al. [11] conducted an experimental and numerical study to investigate the damage mode of one-way reinforced concrete slabs under blast loading at the near- field explosion regime (scaled distance ranging between 0.5 to 0.7 $m/kg^{1/3}$). The ALE numerical approach was selected as well, along with RHT concrete material model. The authors underlined that the amount of explosive is an important parameter of the damaged mode observed, since the slabs experiencing punching shear as the explosive amount was increasing. They stated also that the outcomes should be verified in two-way slabs in the future.

Kandil et al. [12] studied the importance of the strain rate sensitivity in the dynamic response of reinforced concrete slabs under blast loading. The targets were exposed to blast loading through the detonation of ANFO explosive at two different scaled distances (0.90 and 1.06 $kg/m^{1/3}$). In their numerical approach, they used CONWEP

along with two different material models Kinematic Hardening cap model (without strain rate consideration) and Piecewise linear Isotropic Plasticity model (with inclusion of strain rates). Their numerical results were compared with experimental data and revealed the necessity of strain rates consideration for capturing the experimental damage. Zhou et al. [13], implemented a new plastic damage material model in AUTODYN library which took into consideration a modified strain rate sensitivity in tension and compression. They employed a Langrangian-Eulerian approach for modelling the response of reinforced concrete slabs under blast loading and concluded that there was a good correlation between experiments and numerical simulations in terms of the predicted damage and applied pressure. In addition, Zhou and Hao [14], studied the response of a reinforced concrete wall under blast (between 10-5000 kg of CompB) and at standoff distances in the range of 2-20 m. Using the plastic damage model obtained in their previous study and applying a 2D numerical simulation, they compared the numerical pressures and impulses with empirical predictions achieving a good correlation. As a second step, they applied this pressure as an external load to the wall in order to investigate its dynamic behaviour and to derive curves that showed the critical relation between stand-off distance and mass of the explosive.

Lu and Xu [15] proposed a numerical model in order to capture the response of concrete materials exposed to blast loading. The model takes into consideration the strain rate dependency (with their enhancements) and the damage parameter as a result of the integration of the crack function during time. Their research contribution is in accordance with the experimental data obtained from other researchers and applicable

for all the strain rate regime between 1-1000 1/s. The same authors [16] conducted a research study where they focused on the spallation of reinforced concrete under blast loading at several stand-off distances. They used CONWEP method along with pseudo-tensor concrete/geological model, in which they implemented their recommendations (taken from their previous study) regarding the strain rate. The aim of their study was to propose criteria on how the standoff distance along with the mass of the explosive affects the stages of the spallation. Xu and Lu [17] as well, proposed a formula in order to calculate the velocity of the fragments in the case that the detonation takes place within a closed reinforced concrete storage place. According to them, the new model is in a good agreement with the existing experimental data, but there is a need for further enhancement.

Jinwon Shin et al. [18] studied incident and reflected overpressures along with the obtained impulses under close-in explosion events (without modelling contact detonations) taking place on a rigid structure. They carried out 1D analysis for the blast incident in order to obtain the pressures and impulses and later map the validated results in 2D and 3D. They underlined the necessity of a fine mesh during their simulations and stated that the Friedlander equation cannot be used in the near field regime.

Schenker et al. [19] conducted a full-scale detonation of protected (aluminium foam) and unprotected concrete walls from a 20 m distance away from the target. They measured the velocity, acceleration and displacement history on the surface of the structural elements (protected and not protected) under two different concrete types (normal and high strength concrete). In the case of the normal concrete target, the

accelerations, velocities and displacement histories on unprotected slabs were greater than those of the protected slabs. In addition, a 2D numerical simulation using LS-DYNA showed a good correlation between the pressure history that was measured experimentally and calculated numerically. Wu et al. [20], carried out an experimental study on two reinforced concrete slabs (retrofitted with carbon fibre reinforced polymer plates and un-retrofitted) in order to investigate the fragmentation size and shape factor of the fragments, due to the detonation of 2.1 kg of TNT from a stand-off distance of 0.6 m. In addition, the energy study, showed that the retrofitted specimen dissipated more energy during the spallation process compared to the un-retrofitted. Since the obtained results, came from two blast tests only, the authors suggested further investigation.

Thiagarajan et al. [21] performed an experimental and numerical study in which high strength and normal strength concrete with steel bars of conventional reinforcement and high strength low alloy vanadium reinforcement were exposed to blast loading produced by 9000 kg of TNT. The obtained experimental reflected pressures were used to validate the numerical models that were simulated with two different material models (Winfrith Concrete and Concrete Damage R3). They concluded that the high strength concrete performed in a better way, in terms of deflection, compared to the normal strength concrete and that the high strength reinforcement is more efficient in the case of concrete material with normal strength. In addition, Winfrith model can be applied to a large variety of concrete strengths and they also stated that Concrete Damage R3 exhibited a poor performance when the parameters for concrete were automatically created. Li et al. [22] by using CONWEP approach and elastic-plastic

hydrodynamic material model for concrete (scaled distance 0.41-3.05 m/kg$^{1/3}$), conducted an experimental and numerical study comparing the performance of ultra-high concrete slabs (concrete with high resistance in tension and compression) with normal concrete (concrete with normal resistance). The maximum deflection and the residual deflection of the slabs were investigated, but the authors underlined that even though there is a good correlation between experimental and numerical observations, the numerical modelling needs further research since doesn't take into account the strain rate effects.

The previous research papers focused on useful outcomes regarding the behaviour of concrete material under blast loading in the near or far field. Research studies [1]-[7], showed that parameters such as the thickness of the target, boundary conditions, the ratio of reinforcing bars, the compressive strength of concrete, the mass of the explosive as well as its orientation, aspect ratio and distance from the boundaries, affect considerably the response of the targets under blast loading. However, the yield stress of reinforcing bars, the length of the target and the shape of the explosive, do not contribute significantly. In addition, research studies [8]-[11], verify the benefits of using ALE technique instead of a totally Lagrangian approach, when pressures on the surface of concrete targets are numerically predicted. Also, the importance of the strain rate sensitivity [12]-[17], is highlighted when the dynamic response of reinforced concrete targets is considered. Furthermore, some other researchers [19]-[22], state that retrofitted concrete has a better response if compared with unretrofitted. Protective materials such as aluminium foam, carbon fibre reinforced polymer plates, as well as ultra-high strength concrete can enhance the performance of the target under

such dynamic and strain rate sensitive conditions. The author decided to include those papers in order to give the background research studies on reinforced concrete under blast loading in the near or far field. However, when the field of contact detonations is considered the response of the target is different, since the failure becomes more localised. Thus, further research needs to be conducted on the contact regime, which is the concern of the current doctoral thesis, since literature lacks such studies. The knowledge of the previous papers will strengthen the author's theoretical background in order to model efficiently and understand in depth the response of RC members under contact detonation events.

Moving to the limited research studies dedicated to contact detonations, Gebbeken and Ruppert [23] stated the significance of the strain rate sensitivity when simulating those events with hydrocodes. The authors mentioned that especially in cases such as contact detonations, that belong in the high strain rate regime, the formulation recommended by CEB approaches its limit. Thus, is not straightforward to expand those curves in a linear manner. The purpose of their study was to recommend a formula that predicts the increase of concrete strength under those circumstances. In addition, they proposed a new material model for concrete that took into consideration two damage parameters due to the excess of concrete's compressive stress and due to compaction. Finally, they performed a 2D simulation (applied their model in AUTODYN) in a concrete plate subjected to 650 g TNT (contact detonation). However, this numerical attempt needed additional mesh studies and also didn't take into account the necessity of simulating concrete in 3D space. Zhou and Hao [24] performed a 2D numerical mesoscale simulation of concrete under contact detonation. The heterogeneous nature of concrete

showed that aggregates in the concrete mixture influence the fragmentation and damage on concrete. The cracks mainly developed in the mortar that surrounds the aggregates. The size of the fragmentation given by the mesoscale modelling and by the consideration of a homogenous concrete material are linked with statistical formulae. It was found that the size of fragmentation ranges between 0 and 80 mm. It was also stated that a 3D modelling of concrete is important to be performed in the future along with further experimental tests on the ejection velocity and size of fragments (for better calibration of their modelling).

Rabczuk et al. [25] modelled with a good correlation between numerical and experimental results, a reinforced concrete slab under contact detonation, using SPH approach. He found that the increase of the slab thickness led to a decrease of the maximum pressure applied to the structural elements and stated also that the meshfree SPH is able to predict the fragmentation of concrete material. Although the results seem convincing, the author doesn't refer to the mass of the explosive being responsible for the damage caused but mentions only that in severe damage scenarios (caused by the increasing mass of the explosive) the calculations should be enhanced. In a later work, the same authors [26] enhanced their previous work by studying not only the previous mentioned contact blast scenario but also high impact velocity events. They proposed a new fracture model that takes into consideration the effects of inertia, the hydrostatic compaction of concrete material and the anisotropic nature of the material in tension. In order to carry out the numerical analysis, applied a mesh free method very similar to SPH, in which the fragments were a result of the disconnection of the particles. In the case of the contact detonation of concrete slab

(previous mentioned research work), they noticed, that there was a good fragmentation prediction and the experimental measurements of pressures are in accordance with the numerical. On the other hand the authors stated that their 3D modelling needs further enhancement in the future. On the other hand, Dobrocinski and Flis [27] underlined the necessity of ALE technique in the close range (<3 radius of charge) and contact detonation regime, highlighting its computational efficiency compared to the SPH approach. In addition, was mentioned that the CONWEP approach is not valid for scaled distances below 1 $m/kg^{1/3}$ even though that the method compared to the other approaches needs the least simulation time.

Morishita et al. [28] experimentally investigated reinforced concrete slabs under contact detonation in terms of concrete strength and reinforcing bars ratio. It was found that those parameters do not have a substantial influence in the formation of cratering and spalling. Yuan et al. [29] examined numerically the contact detonation of reinforced concrete slabs (plain and reinforced) under 1, 5, 8, 10 and 15 kg of TNT using 3D ALE approach and pseudo-tensor concrete/geological model. They observed that cratering, spalling, perforation and punching shear are dependent on the explosive's mass. In addition, they underlined the necessity of the reinforcing bars in the protection of the shear resistance of the slabs and in the decrease of the fragmentation size. Although this study is very convincing, lacks experimental validation.

Beppu et al. [30] conducted an experimental study on reinforced concrete under contact detonation of 46 g of C4. Their aim was to investigate its performance when was strengthened with FRP laminates from carbon and aramid. The experimental

damage of the strengthened concrete was compared to the damage obtained by the un-strengthened concrete. It was found that fragments were avoided due to the external sheets and also that the aramids sheets prevented totally the spall damage in comparison with the carbon sheets. In addition, the increase of the tensile stiffness of the external sheets, resulted in a decrease of the height of diagonal cracks. Thus, the punching shear capacity of reinforced concrete with external sheets was greater than the capacity of the un-strengthened concrete. Remennikov et al. [31] proposed an analytical model that predicted the breach mode on walls (including reinforced concrete) under contact detonations. This model was validated using the experimental results of the contact detonation conducted by Beppu et al. [30] and was able to predict the necessary charge size in order to breach the structural element as well as the crater size. However, the authors underlined that the analytical model needs a better calibration in the future.

Li et al. [32], tested ultra-high performance concrete slabs under contact detonation and compared them with normal concrete. In their experiments the spallation and cratering of concrete was being tracked and measured, showing that normal concrete specimens exhibited a lower resistance compared to the ultra-high strength specimens. It was evident also that the theoretical predictions for the spallation of the material gave a good prediction for normal concrete (under contact detonation) but underestimated the prediction in the case of ultra-high performance concrete slabs. They also investigated the size of fragmentation for both types of reinforced concrete. The same authors [33] on this study investigated experimentally the damage observed (crater and spall diameters) on reinforced concrete and ultra-high performance

concrete slabs under the contact detonation of 1kg of explosive material. Later on this study performed numerical simulations using SPH approach and two different material models for normal concrete and ultra-high strength concrete (concrete damage model R3 and elastic-plastic hydrodynamic material model, respectively). After the validation of the models in terms of damage, they concluded the better response of ultra-high performance concrete slabs. More recently, these authors [34] by using a coupled SPH and Finite Element approach along with Concrete Damage R3 material model for concrete, performed an experimental and numerical work for the contact detonation of an innovative steel wire mesh reinforced concrete slab, which exhibited adequate spalling and perforation resistance. In addition, it was found that the reduced spacing between the steel wire mesh resulted in a decreased spallation and perforation. Also, the authors stated that the method gave sensible results in terms of the velocity of fragments.

As it is observed from the previously referred research studies, literature lacks extensive studies on contact detonations of RC structures. More specifically, the 2D numerical attempt of Gebbeken and Ruppert [23] that presents the failure modes of concrete under contact detonation, needs additional mesh studies, since the mesh size influences the results. Also, additional numerical results obtained by a 3D model are also needed. In addition, the 2D numerical simulations performed by Zhou and Hao [24] focused on the heterogeneous nature of concrete rather than the consideration of a homogenous material (widely considered in research studies for simplicity). According to them, a development of a 3D model is needed. Taking into account the complexities of 3D modelling in combination with the additional modelling of

parameters if a heterogeneous material is considered, the good performance of the model is a big challenge. Rabczuk et al. [25] and [26], found that SPH approach predicts in a good manner the fragmentation of concrete and focused on the relation between target's thickness and the applied pressures. However, they stated that their 3D model needs further enhancement in the future. Dobrocinski and Flis [27], by comparing LBE, SPH and ALE in terms of predicted pressures, found that ALE exhibited the best performance, but the study needs further clarication. Morishita et al. [28] performed only experimental studies in order to investigate the influence of concrete strength and ratio of the reinforcing bars. On the other hand, Yuan et al. [29] examined numerically only, the damage modes of RC members without experimental validation. A fact that raises issues regarding the efficiency of the proposed model. Furthermore, in the research studies [30]-[34], the authors examined experimentally and numerically the damage modes on strengthened concrete with carbon and aramid FRP laminates, ultra-high performance concrete and steel wire mesh reinforced concrete. They concluded the efficiency and better performance of those types of concrete when contact detonations are considered.

As can be seen, research papers focused either on experimental investigations of the observed damage modes or on numerical analysis that needed enhancements. In addition, the majority of studies regarding contact blast is focusing on innovative types of concrete. However, normal concrete is investigated as a control parameter (to prove the effective resistance of the innovative material) rather than a detailed study on the behaviour of the material. As a result, the current doctoral thesis, which is an experimental and numerical assessment, not only will verify the use of the ALE

approach and discuss the damage modes observed but will assess in detail the response of RC members in terms of pressures, impulses, energy balances, kinematic response of the target and the structural role of reinforcing bars.

5.2 Soft ballistic impact

Since the 17th century, several researchers focused on the influence of impact in structural elements. The majority of those studies belonged to the military sector and were dedicated to the hard impact of projectiles. Lately, the interest was increased, regarding the local effects of the impacted structure due to the soft impact. Thus, soft impact tests either in laboratories (small scale) or open-arena tests (full scale) were carried out in order to predict the behaviour of the structures under those circumstances and establish relevant empirical formulae. The most important soft impact tests that were performed between 1970 and 1993 are illustrated herein (Meppen, Kojima, Ohno and Sugano tests). In addition, some recent papers regarding soft projectile impact on concrete material are also included.

The Meppen tests [35], [36], [37], [38] were carried out at a military location near Meppen (Germany) and were sponsored by the German Federal Ministry of Research and Technology. During the experimental study, 21 reinforced concrete slabs were tested under soft projectile impact in order to develop the methods that were employed during the crash of an aircraft. The impact velocities were ranging between 220 and 250 m/s and the targets were investigated in terms of reinforcement ratios and slab thicknesses. Based on the findings the response of the reinforced concrete slabs was affected more by the thickness rather than the reinforcing bars ratio.

According to Kojima tests [39], 12 single, double reinforcement and with the occurrence of steel lining at the rear side of the slab, were tested under soft and hard missile impact. The impact velocities were ranging between 100 and 200 m/s. It was found that the increase of the thickness of the slabs as well as the impact velocity results in an increase of the resistance of the slabs and the damage respectively. When soft impacts are considered, rupture of the rebars, depth of penetration and spalling area are smaller than in the case of hard impact. It was also found that the soft missiles experienced plastic buckling while the hard were undeformed. Since the deformation of the soft missiles was taking place for a longer period, their impact force on the target was smaller. In addition, the reinforcing lining at the back face found to be beneficial in terms of scabbing and perforation. In the case of soft impact the resistance provided by the single reinforced slabs is similar to the double reinforced concrete slabs and that the current formulae predicting the critical slab thickness are conservative.

In addition, Ohno [40], performed experimental studies on reinforced concrete slabs using deformable projectiles (200 m/s impact velocity). They found that when the axial strength of the missiles decreases, the length of the axial deformation due to impact increases and that the length of the axial deformation remains the same in cases that the missile fails to perforate the target. They also found that the empirical formulae for the perforation prediction are conservative for the case of soft impact and recommended reduction factors. The nose shape factor, when the same axial strength is considered, didn't affect the thickness of perforation but on the other hand the thickness of scabbing increases with the decrease of that factor.

Sugano [41], [42] carried out a series of experiments in order to investigate the local damage on the surface of reinforced concrete structures under the impact of aircraft missiles. These series of experimental investigations, included reduced scale, intermediate and full-scale tests on deformable and rigid missiles with an impact velocity ranging between 100 to 250 m/s. The experiments showed that the results obtained from the full-scale tests are comparable with the results from the reduce scale tests. The existing empirical equations for the local damage on targets are adequate for the case of rigid missiles. On the other hand, the authors agreed with the previous studies that the application of reduction factors (case of deformable projectiles) is necessary in order to account for the decrease of the local damage due to projectile's deformation.

All the aforementioned series of tests were focused mainly on soft projectile impact with velocities lower than 500 m/s. Forrestal et al. [43] conducted experimental work on the penetration of concrete targets due to the impact of ogive nose steel projectiles. The results showed that under high impact velocities of 1000 m/s, the projectiles were severely damaged.

Liu et al. [44] investigated numerically the penetration of deformable projectiles within concrete material under several impact angles ($0 < \theta < 90^{\circ}$) and impact velocity in the range of 540 m/s. A totally Lagrangian approach for modelling both the projectile and the target was employed and the numerical results were verified with experimental work. It was observed that a rapid dilation of concrete takes place, due to the high speed of the projectile and that the travelling velocity of the projectile decreases when the depth of penetration increases. It was also found that the angle of impact is

inversely proportional with the depth of penetration and that ricochet of the projectile occurs when the angle is 45°.

Pontiroli et al. [45] conducted an experimental and 3D Lagrangian simulation in order to investigate the impact of a soft projectile on thin reinforced concrete slabs. The two striking velocities were 108 and 70 m/s. It was shown experimentally that the slabs were perforated under the impact of 108 m/s. The damage mode included the development of a plugging cone, scabbing and failure of the rebars at the back face. In the case of 70 m/s impact velocity there was no perforation and failure of the reinforcing bars. Moreover, the formation of plugging cone and scabbing at the rear side were evident. Overall, the numerical simulations, correlated well with the experiments in terms of the evolution of the projectile's velocity, the damage mode and the displacement of concrete target.

Sovják et al. [46] experimentally investigated the response of Ultra-High Performance Fibre Reinforced Concrete Slabs (UHPFRC), conventional Fibre Reinforced Concrete (FRC) and normal strength concrete (NSC) under deformable projectile of 710 m/s impact velocity. Assessment of the depth of penetration, the crater diameter and mass loss among the different categories revealed that the UHPFRC (unperforated) exhibited the best resistance under the projectile impact. The authors also stated that the increase of the fibre ratio does not affect considerably the response of UHPFRC slabs and recommended also an optimum amount of fibre ratio.

Heckötter et al. [47] used experimental data provided by Iris [48] regarding soft impact on reinforced concrete targets with striking velocities between 108-136 m/s. The aim of the study was to validate the numerical results obtained using SPH approach and

RHT model for concrete material. The authors also indicated that there is a need of further experimental studies in higher impact velocities.

At the moment being, there is a considerable amount of research regarding hard impact of rigid projectiles on reinforced concrete targets. However, the research studies dedicated to deformable projectiles that impact reinforced concrete targets especially under high velocities, are limited.

5.3 Combined blast and impact loading

A small number of researchers have studied the response of reinforced concrete structures under the combined effect of blast loading due to the detonation of a charge and impact loading due to the explosive's fragmentation. Hader [49], performed experimental studies where he found that the damage caused by explosive charges with casing is more severe than the damage caused by uncased charges. Nordstrom [50] tested reinforced concrete slabs under blast pressures and fragments of different velocities, densities and sizes. The fragments were placed in the form of ball bearings under the explosive charge. The energy absorption capacity of the slabs was measured and compared with the density and velocity of the fragments. Leppänen [51] studied experimentally and numerically the response of concrete blocks under the combined effect of fragments (around 1650 m/s) and the blast caused by the detonation of 1.3 kg of octol and hexotol explosive from a distance of 0.6 m. The author used a Lagrangian approach and RHT constitutive concrete model in order to predict the response. The numerical results obtained only from fragment impacts and from the combination between fragments and blast, showed that the spallation was well predicted in the front

face, but the damage was different within the concrete material and was increasing when the two events were merged together. Thus, the author concluded that for design purposes is possible to differentiate the loading between the blast and the impact (global and local damage). In a later study, the same author [52], used SPH approach along with the same material model for concrete in order to study the efficiency of the technique when fragment and blast impact are considered. Also Nyström and Gylltoft [53] used RHT model and a similar approach for investigation of the same subject. More recently, Linz [54], carried out experimental and numerical work on the same topic in order to assess the damage in terms of penetration depth and radius of crater that is observed on the surface of reinforced concrete slabs. The authors detonated 9 kg of TNT from a standoff distance of 2.1 m in combination with the applied load due to the impact of steel balls that represented the fragments (1750 m/s). Their numerical approach was Lagrangian and Concrete Damage R3 was employed for modelling the concrete material.

However, although separate blast and impact scenarios have been investigated in detail, literature lacks extensive numerical and experimental studies on the combination of those two events.

5.4 Importance of the present study

As mentioned previously, literature lacks detailed studies of contact detonations on reinforced concrete structures. There is also a limited source of papers regarding the soft projectile impact. In addition, a few researchers decided to combine together the blast along with the impact field. However, those combined studies were focused only

on merging the detonation event with the impact due to the fragments coming from the explosive's detonation.

Hence, in this particular thesis, the author investigates contact detonations on reinforced concrete (RC) slabs [55] and assesses the behaviour of RC walls under the combined effect of contact detonation and soft projectile impact.

One of the main objectives of the study was to analyse and discuss in depth the response of RC members exposed to contact detonations. More precisely, to investigate the effect of the mass of explosive (C4) on pressures, impulses, energy balances and on the kinematic response of RC slabs along with the structural role of the reinforcing bars.

Thereafter, the author analysed the response of a RC wall under the combined effect of kinetic energy (terminal ballistics) and contact detonation caused by the impact of a 90 mm HESH (High Explosive Squash Head) soft projectile fired from a distance of 70 m. The aim, on this case, was to investigate the response of the structural member under the superposition of those two actions, analyse and discuss the effects of the impact velocity and detonation on structure's response when acting together.

The numerical modelling was based on a Multi-Material-Arbitrary-Lagrangian-Eulerian approach (MMALE, using LS-DYNA) and the use of Winfrith concrete constitutive material model, in order to investigate the dynamic response of the RC members under high strain rate conditions. Prior to the numerical application of this approach, a comparative study between MMALE and LBE validated not only the accuracy but the necessity of the first technique when dealing with the near-contact

field. The efficiency of the proposed numerical modelling in both cases (contact blast and combined contact blast with ballistic impact) was validated with experimental results – based on open-arena testing – and provided by the Royal Military Academy of Belgium.

Hence, the current research work can be used on its own or as a detailed control study for further research on other novel concrete materials. In addition, validates the use of MMALE approach and Winfrith material in predicting contact detonation events.

5.5 References

[1] H. Y. Low and H. Hao, "Reliability analysis of reinforced concrete slabs under explosive loading," Structural safety, vol. 23, pp. 157-178, 2001.

[2] S. Yao, D. Zhang, X. Chen, F. Lu, and W. Wang, "Experimental and numerical study on the dynamic response of RC slabs under blast loading," Engineering Failure Analysis, vol. 66, pp. 120-129, 8// 2016.

[3] H. Du and Z. Li, "Numerical analysis of dynamic behavior of RC slabs under blast loading," Transactions of Tianjin University, vol. 15, pp. 61-64, 2009.

[4] C. Wu, G. Fattori, A. Whittaker, and D. J. Oehlers, "Investigation of air-blast effects from spherical-and cylindrical-shaped charges," International Journal of Protective Structures, vol. 1, pp. 345-362, 2010.

[5] Y. Shi, L. Chen, Z. Wang, and X. Zhang, "Field tests on spalling damage of reinforced concrete slabs under close-in explosions," International Journal of Protective Structures, vol. 6, pp. 389-401, 2015.

[6] H. Jia, L. Yu, and G. Wu, "Damage assessment of two-way bending RC slabs subjected to blast loadings," The Scientific World Journal, vol. 2014, 2014.

[7] J. Li and H. Hao, "Numerical study of concrete spall damage to blast loads," International journal of impact engineering, vol. 68, pp. 41-55, 2014.

[8] A. Alia and M. Souli, "High explosive simulation using multi-material formulations," Applied Thermal Engineering, vol. 26, pp. 1032-1042, 7// 2006.

[9] M. S. Chafi, G. Karami, and M. Ziejewski, "Numerical analysis of blast-induced wave propagation using FSI and ALEmulti-material formulations," International Journal of Impact Engineering, vol. 36, pp. 1269-1275, 2009.

[10] Y. S. Tai, T. L. Chu, H. T. Hu, and J. Y. Wu, "Dynamic response of a reinforced concrete slab subjected to air blast load," Theoretical and Applied Fracture Mechanics, vol. 56, pp. 140-147, Dec 2011.

[11] W. Wang, D. Zhang, F. Lu, S.-c. Wang, and F. Tang, "Experimental study and numerical simulation of the damage mode of a square reinforced concrete slab under close-in explosion", Engineering Failure Analysis, vol. 27, pp. 41-51, 1// 2013.

[12] K. S. Kandil, M. T. Nemir, E. A. Ellobody, and R. I. Shahin, "Strain Rate Effect on the Response of Blast Loaded Reinforced Concrete Slabs", World Journal of Engineering and Technology, vol. 2, p. 260, 2014.

[13] X. Q. Zhou, V. A. Kuznetsov, H. Hao, and J. Waschl, "Numerical prediction of concrete slab response to blast loading", International Journal of Impact Engineering, vol. 35, pp. 1186-1200, Oct 2008.

[14] X. Zhou and H. Hao, "Numerical prediction of reinforced concrete exterior wall response to blast loading", Advances in Structural Engineering, vol. 11, pp. 355-367, 2008.

[15] Y. Lu and K. Xu, "Modelling of dynamic behaviour of concrete materials under blast loading", International Journal of Solids and Structures, vol. 41, pp. 131-143, 2004.

[16] K. Xu and Y. Lu, "Numerical simulation study of spallation in reinforced concrete plates subjected to blast loading", Computers & Structures, vol. 84, pp. 431-438, 1// 2006.

[17] K. Xu and Y. Lu, "Debris velocity of concrete structures subjected to explosive loading", International Journal for numerical and analytical methods in geomechanics, vol. 30, pp. 917-926, 2006.

[18] J. Shin, A. S. Whittaker, D. Cormie, and W. Wilkinson, "Numerical modeling of close-in detonations of high explosives", Engineering Structures, vol. 81, pp. 88-97, 2014.

[19] A. Schenker, I. Anteby, E. Gal, Y. Kivity, E. Nizri, O. Sadot, et al., "Full-scale field tests of concrete slabs subjected to blast loads", International Journal of Impact Engineering, vol. 35, pp. 184-198, 2008.

[20] C. Wu, R. Nurwidayati, and D. J. Oehlers, "Fragmentation from spallation of RC slabs due to airblast loads", International Journal of Impact Engineering, vol. 36, pp. 1371-1376, 2009.

[21] G. Thiagarajan, A. V. Kadambi, S. Robert, and C. F. Johnson, "Experimental and finite element analysis of doubly reinforced concrete slabs subjected to blast loads", International Journal of Impact Engineering, vol. 75, pp. 162-173, 2015.

[22] J. Li, C. Wu, and H. Hao, "An experimental and numerical study of reinforced ultra-high performance concrete slabs under blast loads", Materials & Design, vol. 82, pp. 64-76, 10/5/ 2015.

[23] N. Gebbeken and M. Ruppert, "A new material model for concrete in high-dynamic hydrocode simulations", Arch Appl Mech 2000;70:463-782000.

[24] X. Q. Zhou and H. Hao, "Mesoscale modelling and analysis of damage and fragmentation of concrete slab under contact detonation", International Journal of Impact Engineering, vol. 36, pp. 1315-1326, 12// 2009.

[25] T. Rabczuk, J. Eibl, and L. Stempniewski, "Numerical analysis of high speed concrete fragmentation using a meshfree Lagrangian method", Engineering Fracture Mechanics, vol. 71, pp. 547-556, 3// 2004.

[26] T. Rabczuk and J. Eibl, "Modelling dynamic failure of concrete with meshfree methods", International Journal of Impact Engineering, vol. 32, pp. 1878-1897, 2006.

[27] S. Dobrociński and L. Flis, "Numerical Simulations of Blast Loads from Near-Field Ground Explosions in Air", in Studia Geotechnica et Mechanica vol. 37, p. 11, 2015.

[28] M. Morishita, H. Tanaka, T. Ando, and H. Hagiya, "Effects of concrete strength and reinforcing clear distance on the damage of reinforced concrete slabs subjected to contact detonations", Concrete Research and Technology, vol. 15, pp. 89-98, 2004.

[29] L. Yuan, S. Gong, and W. Jin, "Spallation mechanism of RC slabs under contact detonation", Transactions of Tianjin University, vol. 14, pp. 464-469, 2008.

[30] M. Beppu, T. Ohno, K. Ohkubo, B. Li, and K. Satoh, "Contact explosion resistance of concrete plates externally strengthened with FRP laminates", International Journal of Protective Structures, vol. 1, pp. 257-270, 2010.

[31] A. Remennikov, I. Mentus, and B. Uy, "Explosive breaching of walls with contact charges: theory and applications", International Journal of Protective Structures, vol. 6, pp. 629-647, 2015.

[32] J. Li, C. Wu, H. Hao, Z. Wang, and Y. Su, "Experimental investigation of ultra-high performance concrete slabs under contact explosions", International Journal of Impact Engineering, vol. 93, pp. 62-75, 7// 2016.

[33] J. Li, C. Wu, and H. Hao, "Investigation of ultra-high performance concrete slab and normal strength concrete slab under contact explosion", Engineering Structures, vol. 102, pp. 395-408, 2015.

[34] J. Li, C. Wu, H. Hao, and Y. Su, "Experimental and numerical study on steel wire mesh reinforced concrete slab under contact explosion", Materials & Design, vol. 116, pp. 77-91, 2/15/ 2017.

[35] W. Jonas, R. Meschkat, H. Riech, and E. Rüdiger, "Experimental investigations to determine the kinetic ultimate bearing capacity of reinforced concrete slabs subject to deformable missiles", in Structural mechanics in reactor technology. Transactions. Vol. J, ed, 1979.

[36] W. Nachtsheim and F. Stangenberg, "Impact of deformable missiles on reinforced concrete plates-comparisonal calculations of Meppen tests", in Structural mechanics in reactor technology. Vol. J (b), ed, 1981.

[37] W. Nachtsheim and F. Stangenberg, "Interpretation of results of Meppen slab tests—comparison with parametric investigations", Nuclear engineering and design, vol. 75, pp. 283-290, 1983.

[38] E. Rüdiger and H. Riech, "Experimental and theoretical investigations on the impact of deformable missiles onto reinforced concrete slabs", in Transactions of the 7. international conference on structural mechanics in reactor technology. Vol. J, 1983.

[39] I. Kojima, "An experimental study on local behavior of reinforced concrete slabs to missile impact", Nuclear engineering and design, vol. 130, pp. 121-132, 1991.

[40] T. Ohno, T. Uchida, N. Matsumoto, and Y. Takahashi, "Local damage of reinforced concrete slabs by impact of deformable projectiles", Nuclear engineering and design, vol. 138, pp. 45-52, 1992.

[41] T. Sugano, H. Tsubota, Y. Kasai, N. Koshika, C. Itoh, K. Shirai, et al., "Local damage to reinforced concrete structures caused by impact of aircraft engine missiles Part 2. Evaluation of test results", Nuclear Engineering and Design, vol. 140, pp. 407-423, 1993.

[42] T. Sugano, H. Tsubota, Y. Kasai, N. Koshika, H. Ohnuma, W. Von Riesemann, et al., "Local damage to reinforced concrete structures caused by impact of aircraft engine missiles Part 1. Test program, method and results", Nuclear Engineering and Design, vol. 140, pp. 387-405, 1993.

[43] M. Forrestal, D. Frew, S. Hanchak, and N. Brar, "Penetration of grout and concrete targets with ogive-nose steel projectiles", International Journal of Impact Engineering, vol. 18, pp. 465-476, 1996.

[44] Y. Liu, A. Ma, and F. Huang, "Numerical simulations of oblique-angle penetration by deformable projectiles into concrete targets", International Journal of Impact Engineering, vol. 36, pp. 438-446, 2009.

[45] C. Pontiroli, A. Rouquand, L. Daudeville, and J. Baroth, "Soft projectile impacts analysis on thin reinforced concrete slabs: Tests, modelling and simulations", European Journal of Environmental and Civil Engineering, vol. 16, pp. 1058-1073, 2012.

[46] R. Sovják, T. Vavřiník, P. Máca, J. Zatloukal, P. Konvalinka, and Y. Song, "Experimental investigation of ultra-high performance fiber reinforced concrete slabs subjected to deformable projectile impact", Procedia Engineering, vol. 65, pp. 120-125, 2013.

[47] C. Heckötter and A. Vepsä, "Experimental investigation and numerical analyses of reinforced concrete structures subjected to external missile impact", Progress in Nuclear Energy, vol. 84, pp. 56-67, 2015.

[48] A. Vepsä, A. Saarenheimo, F. Tarallo, J. Rambach, and N. Orbovic, "IRIS_2010–Part II: Experimental data", SMiRT-21 Transactions, New Dehli, India, SMiRT-21, 2011.

[49] H. Hader, "Effects of Bare and Cased Explosives Charges on Reinforced Concrete Walls", Basler Ernst and partners, Zurich, Switzerland,1983.

[50] M. Nordstrom and R. Forsén, "Damage to reinforced concrete slabs due to fragment loading with different fragment velocities, fragment area densities and sizes of fragments", WIT Transactions on The Built Environment, vol. 8, 1970.

[51] J. Leppänen, "Experiments and numerical analyses of blast and fragment impacts on concrete", International Journal of Impact Engineering, vol. 31, pp. 843-860, 8// 2005.

[52] J. Leppänen, "Concrete subjected to projectile and fragment impacts: Modelling of crack softening and strain rate dependency in tension", International Journal of Impact Engineering, vol. 32, pp. 1828-1841, 2006.

[53] U. Nyström and K. Gylltoft, "Numerical studies of the combined effects of blast and fragment loading", International Journal of Impact Engineering, vol. 36, pp. 995-1005, 2009.

[54] P. Del Linz, S. C. Fan, and C. Lee, "Modeling of Combined Impact and Blast Loading on Reinforced Concrete Slabs", Latin American Journal of Solids and Structures, vol. 13, pp. 2266-2282, 2016.

[55] E. Athanasiou, F. Teixeira-Dias, F. Coghe, and L. Desmaret, "Response Of Reinforced Concrete Structural Elements To Near-field And Contact Explosions", International Journal of Safety and Security Engineering, vol. 6, pp. 418-426, 2016.

Chapter 6. Experimental and Numerical Procedures of Contact Blast and Ballistic Impact on Reinforced Concrete

6.1 Introduction

In this research study, LS-DYNA is used along with the Winfrith Concrete material model to simulate the response of reinforced concrete targets under contact detonation and impact. In the beginning of the study, a two-layer reinforced concrete slab (0.85 × 0.85 × 0.07 [m^3]) is exposed to several detonations using Composition 4 (C4) explosive. The aim is to achieve a contact explosion between the target (reinforced concrete slab of 45 MPa compressive strength) and the explosive, since literature can provide us with limited information regarding such close range blast incidents. The slab and the high explosive are explicitly modelled using the Multi-Material-Arbitrary-Lagrangian-Eulerian approach (MMALE) and the obtained numerical results are validated using experimental data. The experimental results, used for validation, are analysed in terms of the obtained diameter of the crater, diameter of spall as well as the presence or absence of perforation.

Following this study, using the same material model for concrete and adopting the same technique, the response of a double reinforced concrete wall of 35 MPa compressive strength with overall dimensions of 2.5 × 2.5 × 0.2 [m^3] is examined under the combined effect of kinetic energy and contact explosion caused by a 90 mm High Explosive Squash Head (HESH) projectile shot from a distance of 70 m. The numerical and experimental studies presented herein combine the effects of a ballistic impact (kinetic energy) along with the blast wave (detonation energy). More precisely, damage is caused by the combined effect of the impacted kinetic energy (stage 1) and the blast wave that is released after the delayed detonation of the high-explosive (stage 2) on the already damaged surface of the reinforced concrete structure. The HESH

projectile contains A3 explosive and hits the target at impact velocities of 600, 800 and 1000 m/s. In addition, the mechanical response of the target is investigated by analysing the post-impact damaged region (hole). The aim is to study the effect of the impact velocity along with the contact blast energy after the delayed detonation of the fuse.

The outcomes of this particular thesis are a result of both an experimental and numerical assessment. For the needs of this study the experiments were carried out at the Royal Military Academy of Belgium by researchers, who were in collaboration with the University of Edinburgh. The author was not involved in those experiments and was only responsible for the numerical modelling of this project, using the experimental data for validation.

6.2 Experimental setup for the contact detonation of the reinforced concrete slab

6.2.1 Description of the test

In the present research five reinforced concrete square-shaped slabs with dimensions $0.85 \times 0.85 \times 0.07$ [m^3] were tested at the laboratories of the Royal Military Academy of Belgium under contact explosion.

The charge that was chosen as the plastic high explosive was Composition 4 (C4), which is a high explosive extensively used in industrial and military applications. The explosive was placed at zero standoff distance, at the centre of the front face of the slabs (see Figure 6.1).

These identically designed reinforced concrete slabs, were simply supported above rigid supports (in the form of table structures) and tested under the detonation of 10, 15, 25, 50 and 75 g of C4. The configuration of the experiment is shown in Figure 6.2. Except for the design of slabs that remained unchanged throughout the experiment, the only parameter that was changing was the mass of the high explosive. The goal was to determine the amount needed in order to cause a total perforation of the reinforced concrete targets as well the target's response due to the increase of the mass of explosive. Furthermore, the diameter of the damage in the forms of the crater (front face) and spall (back face) was measured for all the tested slabs (perforated and unperforated specimens).

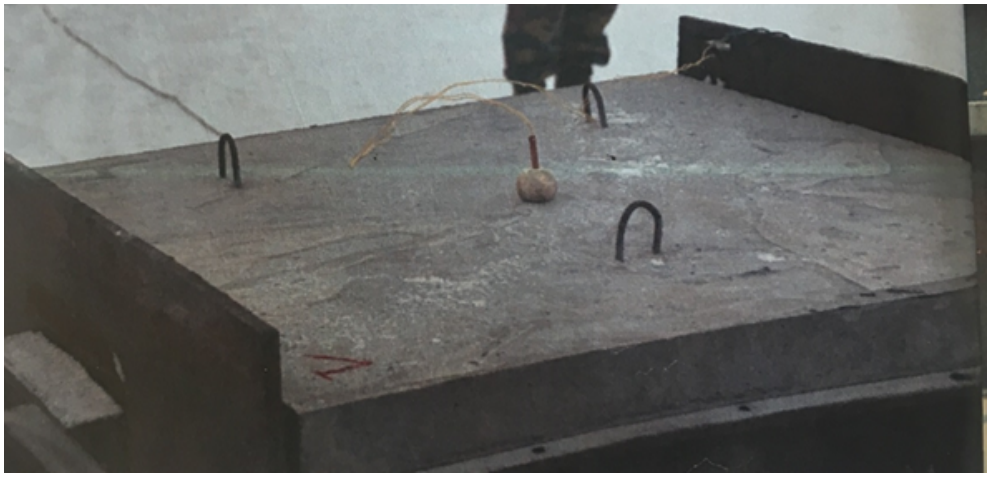

Figure 6.1: Placement of Composition 4 (C4) explosive.

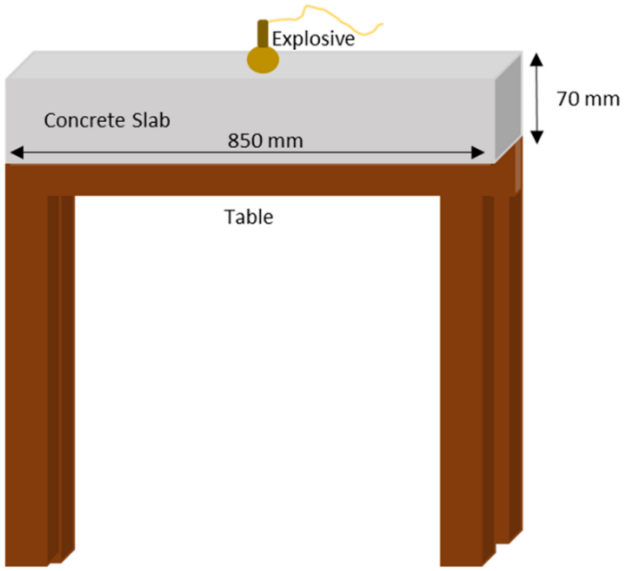

Figure 6.2: Experimental setup of the reinforced concrete slabs.

6.2.2 Selection of the materials

Concrete:

Concrete is a material with a composite nature consisting of gravels, sand, cement and water. Gravels and sand are the aggregates that are mixed together using a binder, which is usually the cement paste (cement powder and water). The way that the materials are mixed together determines the behaviour of concrete. In other words, the type of the cement used, the maximum nominal size of the aggregates, the maximum water/cement ratio (*w/c*) plays an important role in the durability of concrete. In the current study, the aim was to manufacture a concrete mixture with standard characteristics, widely used in the building construction.

According to European standards [1], concrete can be classified in three categories depending on its density. These are lightweight concrete ($800 < \rho < 2000$ kg/m^3), normal concrete ($2000 < \rho < 2600$ kg/m^3) and heavy concrete ($\rho > 2600$ kg/m^3). The

most common concrete that is used in construction is the one with density equal to 2300 kg/m^3. The size of the aggregate is specified through the sieve analysis and should not exceed the 1/4 of the depth of the concrete member (in our case 14 mm). On the one hand, the increase of the size of aggregates results in an increase of the workability of concrete. On the other hand, the smaller the diameter of the aggregate size, the bigger the surface area which is connected with the mortar and leads to a stronger concrete. The optimum value of water / cement ratio (*w/c*) determines the strength as well. The increase of this ratio results in a decrease of the compressive strength of concrete. In addition, Portland cement is manufactured from chalk or limestone and clay or shale. The amount of the aforementioned materials as well as the procedure used for manufacturing, determines the type of the cement. In general, five types of Portland cement exist, and for the needs of this study, cement type I of 52.5 strength class, was used.

Furthermore, when the concrete mixture is prepared, it does not exhibit immediately its ultimate performance. This is because it needs a prescribed drying time of 28 days (maturation time), after which the preferable compressive resistance is adopted. Afterwards, its characteristics do not change much and the performance is stabilised. For that reason, the value of the compressive strength used in our calculations is the value adopted after the prescribed maturation time. The average compressive strength of concrete $f_{cm}(t)$ after t days can be given as follows:

$$f_{cm}(t) = \beta_{cc}(t) f_{cm}(28) \tag{6.1}$$

where $f_{cm}(28)$ is the compressive strength at 28 days and $\beta_{cc}(t)$ is a coefficient depending on the age of the concrete and the type of cement that reaches unity after

28 days. In addition, good storage conditions of concrete during this period of time is a very important factor that affects the final performance of the material. The temperature of the room should be kept constant (around 20 ºC) and the moisture content should be high enough in order to prevent premature evaporation. Figure 6.3 shows the mixture of concrete material, that is used for this study, the moment when is poured into the wooden mould.

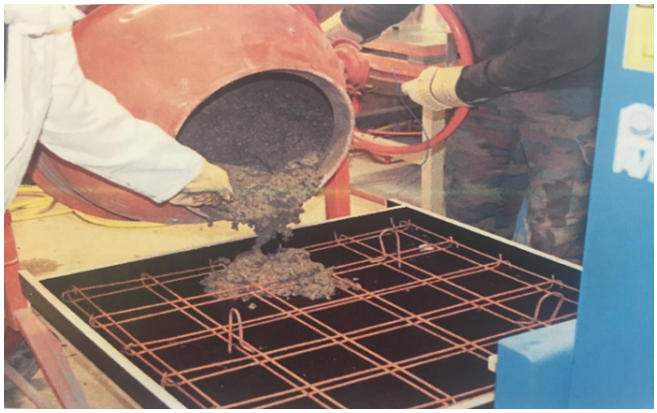

Figure 6.3: Concrete mixture during the preparation of the reinforced concrete slabs.

Reinforcement of the concrete:

There are several ways in order to strengthen the concrete. Some of the preferred approaches are pre-stressed concrete, fibre reinforced concrete and steel reinforced concrete. In the first approach, the concrete undertakes a compressive load prior to the actual loading with the intention of remaining compressed. In the second approach fibres made from metals, glass and polypropylene are mixed with the concrete. While in the third technique, the implementation of a mesh of steel bars is used. The third approach, is supposed to be the most popular choice.

The main reason of the reinforcement implementation is the fact that concrete exhibits a low tensile strength compared to its compressive strength. In order to enhance the tensile performance of concrete, especially in important locations that suffer from tension, the use of reinforcement is necessary. Thus, concrete is benefitted from materials that exhibit a higher tensile strength. In the current study, steel bars were used as a tensile strengthening medium. In Figure 6.4 the steel mesh of reinforcing bars, is shown, prior to the pouring of the concrete mixture.

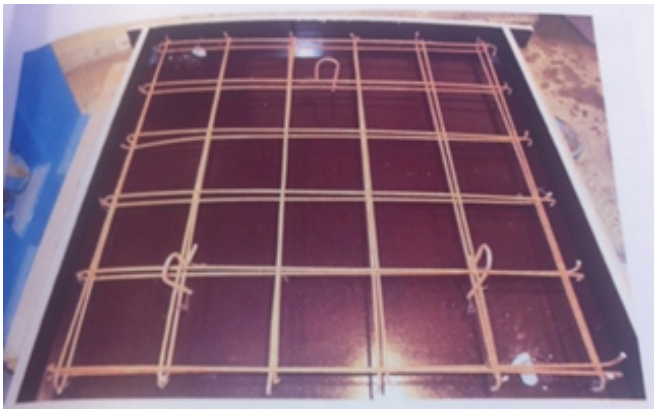

Figure 6.4: Mesh of the steel reinforcing bars (inside a wooden frame) before the preparation of concrete slabs.

Explosive C4:

The high explosive that was chosen for the contact detonation was the M112 Composition 4 (C4) [2]. This particular high explosive is widely used in the military field and it is mainly known as C4. The name M112 represents a block of 570 g of C4 with dimensions of 27 × 52 × 286 [mm^3], usually wrapped with a paper in olive green colour and yellow letters. Its chemical name is cyclotrimethylene - trinitramine ($C_3H_6N_6O_6$) and it is commercially known as RDX (Royal Demolition Explosive or

Research Development Explosive). The main inspiration behind this plastic explosive is the beneficial combination of the explosive material and the plasticiser. Because of that, the application can be done in an easy, quick and secure manner. In addition, this flexible material is resilient under conditions of high temperature and intensive shocks. The shape and the packaging of C4 are shown in Figure 6.5.

Figure 6.5: Composition 4 (C4) explosive.

The only way to detonate the secondary explosive C4 is through an electric detonator which contains a very sensitive primary explosive. The detonator provides a 0.48 current supply and causes the detonation of this primary explosive. As a result of this initial detonation, the C4 will detonate after the activation of its chemical reaction. The velocity of this particular expansion is 8050 m/s resulting in a strong blast wave. In order to be able to quantify the pressure magnitude of each explosive, for practical reasons we usually convert its released energy into TNT equivalent energy. In general, C4 is more powerful than TNT. More specifically, in our experimental investigation, the actual amounts of C4 that were placed above the slabs were equal to 10, 15, 25, 50 and 75 g. For practical and modelling purposes the actual masses of the explosive were multiplied by a converting factor of 1.37, according to McVay [2], in order to obtain

the TNT equivalent mass. The aforementioned amounts, as discussed previously, corresponded to an equivalent mass of 13.7, 20.55, 34.25, 68.50 and 102.75 g of TNT.

6.2.3 Design of reinforced concrete

The primary goal of the design, was to construct five identically reinforced concrete slabs of 0.85 × 0.85 × 0.07 [m^3] with the same characteristics in terms of strength.

Concrete mixture:

The materials that were used for the concrete mixture were the following: sand (0.2 – 0.4 mm), gravel (6.3 – 14 mm) and cement (CEM I 52.5). According to the Standards [1], one volume of cement should be combined with 2 and 3/4 of the volume gravel, 1 and 1/2 of the volume sand and 2/3 of the volume water. The theoretical amounts of the components are specified in Table 6.1, both for the specimens such as the testing slab (0.050575 m^3) and the testing cube (0.0033 m^3).

Table 6.1: Theoretical amounts of components needed per concrete slab and cubic test.

1 slab = 0.050575 m^3	**1 test cube = 0.0033 m^3**
57.8 kg gravel	3.77 kg gravel
36.125 kg sand	2.35 kg sand
8.06 kg cement	1.17 kg cement
9.03 l water	0.58 l water

In practice, in order to take into consideration the fluidity tests and probable losses, the actual amounts of the components used per concrete slab were the ones in Table 6.2.

Table 6.2: Materials used for the concrete mixture per slab.

Material	Mass/Volume
Gravel	62.25 kg
Sand	50 kg
Cement	25 kg
Water	9.5 l

Flow table tests:

The flow table test on fresh concrete mixture was carried out according to the British Standard BS 12350-5 [3]. This test is necessary since it gives a warning for concrete's cohesion levels. It needs a flow table, a tamping rod and a metallic cone (placed in a central position above the table and filled with concrete material in two layers, each of which when placed is compressed 10 times using the rod). The procedure ends when the cone is removed from the concrete material and the diameter of the flow is measured. This test is preferred over the standard slump tests when concrete is too liquid and cannot keep its form when the cone is removed. The results from the flow table test are presented in Table 6.3 and show that the average class of consistency is F3.

Table 6.3: Flow table test results.

Concrete mixture	Diameter [mm]	Class of Consistency
1	425 - 420	F3
2	525 - 490	F4
3	520 - 455	F3
4	500 - 475	F3
5	520 - 485	F4

Compression tests:

The compressive strength test was carried out according to the British Standards BS 12390 – 3: 2001 [4]. During this procedure a compressive load F (N) is applied on the specimen's top surface until its failure. The maximum load that the material can undertake, divided by the area A [mm^2] of the top surface gives the maximum compressive strength of concrete material in MPa. The results from the tests can be summarised in Table 6.4 showing that the average class of resistance is C45/55.

Table 6.4: Compression tests results.

Specimen	Strength (MPa)	Class of resistance
1	57.79	C45/55
2	51.73	C40/50
3	52.44	C40/50
4	64.45	C50/60
5	61.24	C50/60

Density tests

With the aim of defining the density of concrete slabs, the concrete specimens were positioned in a water basin. The obtained results in Table 6.5, led to an average density value of 2370 kg/m^3.

Table 6.5: Density test results.

Slab Nº	Density [kg/m^3]
1	2385
2	2374
3	2377
4	2384
5	2385

Reinforcement placement:

The concrete slabs were reinforced with a two-layer steel mesh having a 20 mm concrete cover from the top and from the bottom. Each layer consisted of 6 × 6 steel bars with a 5 mm diameter and 150 mm spacing from centre-to-centre. The reinforcement yield strength (f_y) was 469 MPa, its density (ρ) was 7890 kg/m^3 and the elastic modulus (E) was 205 GPa. Figure 6.6 represents the dimensions of the slabs as well the detailed placement of the reinforcement.

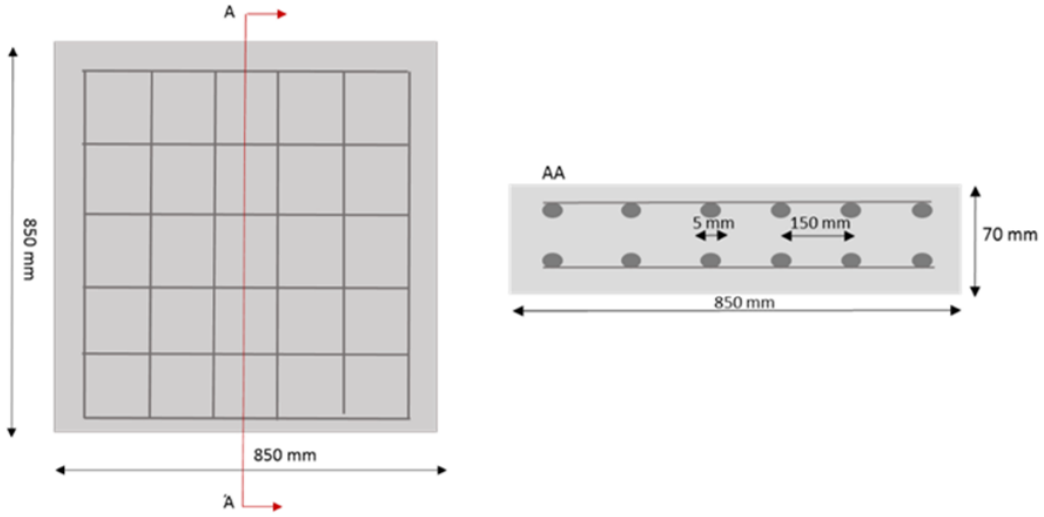

Figure 6.6: Placement of the reinforcing bars.

Final characteristics of the reinforced concrete slabs:

Table 6.6 summarises the final material properties of the concrete and reinforcing steel. More specifically, f_c is the compressive strength, f_t is the tensile strength, f_y is the yield strength, ρ is the density and E is the elastic modulus. In addition, Figure 6.7 shows the concrete slabs at their final preparation stage.

Table 6.6: Material properties for concrete and steel material.

Material	f_c (MPa)	f_t (MPa)	f_y (MPa)	ρ (kg/m^3)	E (GPa)
Concrete Slab	45	5	-	2370	33.5
Steel rebars	-	-	469	7890	205

Figure 6.7: Final preparation stage of the concrete slabs.

6.2.4 Methodology and experimental measurements

The five reinforced concrete slabs had identical characteristics and the tests were conducted in order to replicate the response of a standard wall of a building under a contact detonation event. In the beginning of the experiments, the C4 explosive was placed on top of these slabs and detonated. Afterwards, photos of the damaged slabs, both from the front and the back faces were taken. Finally, measurements of the diameter of the crater and spall as well as of the depth of the crater and spall were collected (see Table 6.7).

Measurement of the diameter of the crater (front face) and the spall (back face):

The obtained diameters of the damage, both from the front and the back face of the tested slabs were obtained from the average value between the maximum *x* (horizontal diameter) and *y* (vertical diameter) presented in Figure 6.8.

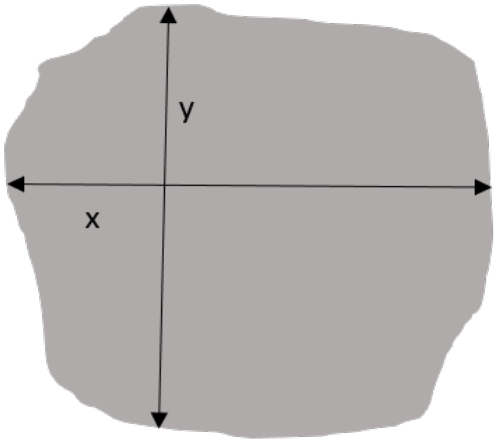

Figure 6.8: Spall and crater measured diameters.

Measurement of the depth of the crater and spall:

The depth of the crater and spall was obtained using a ruler and a batten as shown in Figure 6.9.

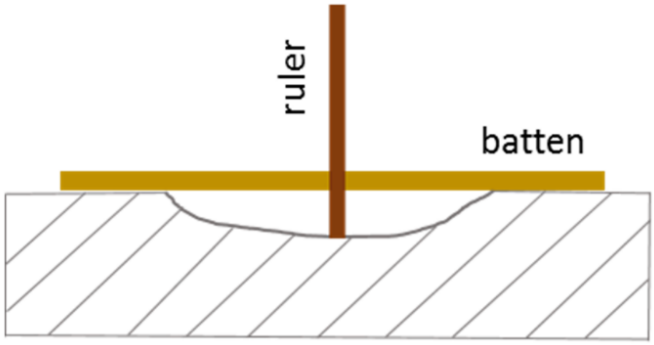

Figure 6.9: Spall and crater measurement method.

Table 6.7: Experimental results of the diameter of damage observed on crater and spall.

	FRONT FACE		BACK FACE	
C4 mass [g]	Crater Diameter [mm]	Depth of crater [mm]	Spall diameter [mm]	Depth of spall [mm]
75	200	perforation	255	perforation
50	165	perforation	240	perforation
25	135	perforation	230	perforation
15	130	20	215	22
10	90	10	175	10

6.3 Numerical modelling for the contact detonation of the reinforced concrete slab.

6.3.1 General approach

The commercial explicit FEA package LS-DYNA was used for capturing the behaviour of the real contact detonation scenario, because of its potential in modelling highly transient problems. For dynamic phenomena such as blast loading, LS-DYNA utilizes explicit time integration based on the central difference technique (see Section 3.4.1). The numerical approach adopted for the modelling of the current situation is the Lagrangian Eulerian MMALE, since it has been proved more robust in the near – contact detonation field compared to the purely Lagrangian LBE (CONWEP). Additionally, in the results and discussion chapter and prior to the analysis of the results obtained using the MMALE technique, a numerical comparison between the two approaches is performed, in order to validate this selection. MMALE allows the explosive to behave like a fluid as it moves within the air domain. As a result, the

approach will prevent the formation of severely distorted elements, which will result, in their turn, in numerical instabilities and failed solution. The discretisation shown in Figure 6.10 (left) was achieved using two-plane symmetry (i.e. 1/4 of the slab, 425 × 425 × 70 [mm^3]) since it was computationally expensive to model the slab as a whole.

The five numerical models (one for each detonation scenario) that were constructed, consisted of a Lagrangian concrete slab (1/4 of the structural element), reinforcing bars within the slab (3×3 in two layers), the Eulerian air domain (1/4 of the structural element), the explosive charge (1/8 of the explosive) and the rigid supports.

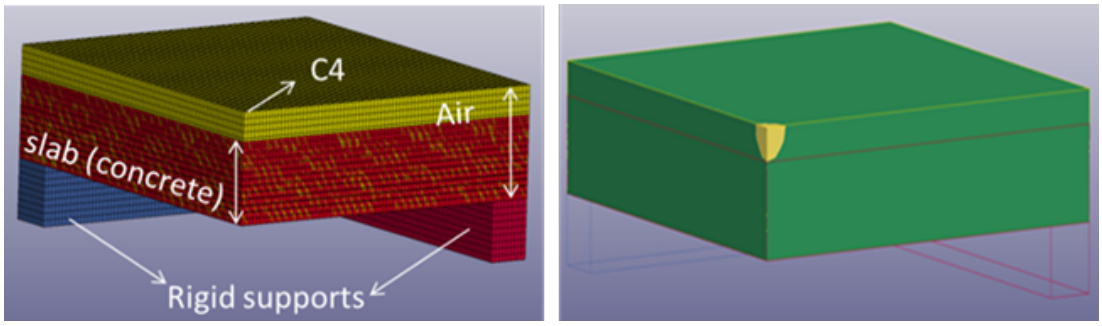

Figure 6.10: LS-DYNA finite element discretisation model (left), location, shape and distribution of the explosive charge (right).

The concrete slab was the Lagrangian part and modelled with solid hexahedra elements (h_c =5.53 mm). Within this slab the consideration of the rebars was implemented through beam elements of the same mesh size (h_c=5.53 mm). The air was modelled using the same mesh size in a box with dimensions of 425 × 425 × (70 + R) [mm^3], where R was the radius of the equivalent TNT charge. Knowing the mass of TNT each time (the C4 masses were converted into TNT equivalent masses according to Section

6.2.2) and its density (ρ = 1600 kg/m^3), the radius of the five different amounts of explosive was determined assuming a spherical volume.

As now for the location of the TNT equivalent mass, MMALE technique utilises the INITIAL-VOLUME-FRACTION-GEOMETRY card in order to define the position, the shape and distribution of TNT and air at the initial stage (see Figure 6.10 right). The shape of the explosive was selected to be a sphere (standard option available) and filled with the explosive material. In the same figure, the green colour represents the air domain that is the background mesh that covers the spherical explosive charge (in yellow) and the slab. In addition, the INTITIAL-DETONATION card was used in order to specify the time (equal to 0 ms in the beginning of the simulation) and the location of the detonation (in the centre of each spherical charge).

6.3.2 Contact algorithms

According to the different approaches that exist (see Section 3.4.2), in order to take into account the reinforcing bars within the concrete, the penalty approach, CONSTRAINED-LAGRANGE-IN-SOLID was the one used in the current research study. Even though the two meshes of concrete and rebars do not have to be identical and share the same nodes, it was decided to connect them using exactly the same mesh size with the concrete slab and a shared location. This alternative technique is called “collocation meshing”, according to Schwer [5]. The inputs of the referred approach are two parts: the “slave” (reinforcement) and the “master” (concrete) which are coupled together with constrained acceleration and velocity at the nodes. This type of contact does not take into account the bond-slip between concrete and steel material. According to literature, in the case of high rate loading originated from explosive

sources, the bond-slip can be neglected. Hence, this contact is recommended when blast and impact studies are considered. The same penalty method was implemented for the interaction between the Eulerian domain (explosive and air) and the Lagrangian domain (RC slab), given that MMALE technique was employed (see Section 3.4.1). According to this interaction, the top surface of the Lagrangian part (slab) is assumed that is penetrating into the ALE fluid. In addition, this type of contact is necessary for fluid-structure-interaction problems in order to obtain the interface forces and calculate the applied blast pressures.

6.3.3 Boundary conditions

The explosive was placed at the front face of the slab, only the $1/8^{th}$ was modelled due to symmetry (with respect to a horizontal plane) and no boundary conditions were needed to be defined for the explosive, since was a volume fraction of the air mesh (Eulerian domain). The concrete slab (Lagrangian mesh) and the surrounding air (Eulerian mesh) follow the boundary conditions shown in Figure 6.11 where X, Y, Z are the translational constraints in x, y, z directions and Rx, Ry, Rz are the rotational constraints about the x, y and z axes. The proposed boundary conditions maximise the computational efficiency of the model without compromising the quality of the obtained results. In addition, boundary non-reflecting conditions were chosen for the two sides of air that were away from the boundaries of symmetry, in order to avoid the reflected stress wave to enter the model.

Since the slabs were left above steel frames, two solid meshes were created, using hexahedra elements like the configuration shown in Figure 6.11. The height of the

supporting structures was 50 mm while the other two dimensions were 425 and 50 mm. An automatic surface-to-surface contact was defined between the slab and the supports, while the bottom was fixed. Automatic contacts check for penetration on either side of elements and are recommended in crash simulations, since the orientation of the parts relative to each other cannot always be predicted as the model undergoes large deformations. The material for the supports was chosen to have a density ρ (7830 kg/m^3), Young's modulus E (207 GPa) and Poisson's ratio v (0.3).

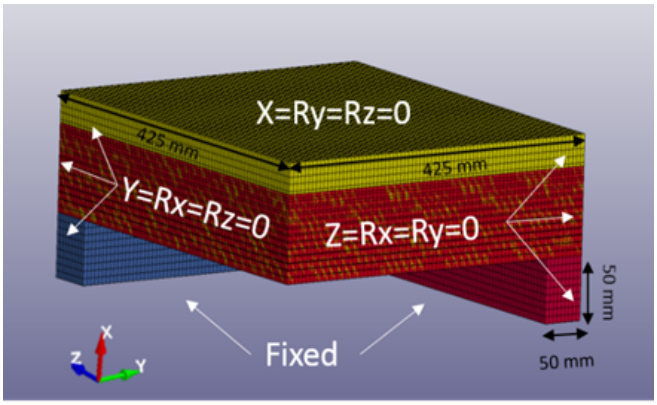

Figure 6.11: Boundary conditions of the 1/4 of the numerical model.

6.3.4 Damage criteria and mesh sensitivity study

An erosion algorithm was implemented and used in order to model the physical damage, following the method analysed by Xu and Lu [6] and Luccioni and Araoz [7]. This is a numerical technique where elements which have reached a limit strain value are deleted from the model. The purpose of doing this is that in conditions of large deformations, such blast wave, the Lagrangian mesh can experience non-physical deformations. In order to avoid this from happening, erosion algorithms bring a solution to the problem through element deletion. In addition, when concrete is the

impacted material, the erosion criteria aim to capture the physical erosion that takes place. There is a wide range of criteria based upon strain and stress limitations. The strain based are the most frequently selected [7] compared to the stress-based criteria and some of them will be presented herein.

Instantaneous geometric strain:

The erosion initiates when instantaneous geometric strain is greater than a particular limit of effective strain:

$$\varepsilon_{\text{eff}} = \frac{2}{3}\sqrt{(\varepsilon_1^2 + \varepsilon_2^2 + \varepsilon_3^2) + 5(\varepsilon_1\varepsilon_2 + \varepsilon_1\varepsilon_3 + \varepsilon_2\varepsilon_3) - 3(\varepsilon_{12}^2 + \varepsilon_{23}^2 + \varepsilon_{13}^2)} \quad 6.2$$

$$(\varepsilon_{\text{eff}})_{\text{lim}} \leq \varepsilon_{\text{eff}} \quad 6.3$$

The geometric strain is the derivative of the displacement field. Hence, it depends only on the field and not on any material properties.

In addition, this technique does not take into consideration the sign of the strains, consequently should not be applied in frictional materials with different behaviour in tension and compression such as concrete.

Maximum principal strain:

The erosion initiates when the maximum principal strain is reached. This value is lower than the instantaneous geometric strain and represents the limit of concrete in tension and spalling of the material under impact and blast loading.

$$(\varepsilon_1)_{\text{lim}} \leq \varepsilon_1 \quad 6.4$$

Maximum shear strain:

The erosion starts when the maximum shear strain is obtained

$$(\gamma_1)_{\text{lim}} \leq \gamma_1 \tag{6.5}$$

This approach works like the previous erosion techniques but it is particularly focused on localised shear failure of concrete. The difficulty regarding this limit is the estimation of the strain threshold in order to obtain representative results.

Effective plastic strain:

This criterion uses the following limitation:

$$\left(\varepsilon_{\text{eff}}^{p}\right)_{\text{lim}} \leq \varepsilon_{\text{eff}}^{p} \tag{6.6}$$

where

$$\varepsilon_{\text{eff}}^{p} = \int \dot{\varepsilon}_{\text{eff}}^{p}\, \mathrm{d}t \tag{6.7}$$

and

$$\dot{\varepsilon}_{\text{eff}}^{p} = \frac{\sqrt{3J_2} - \sigma_y}{3G} \tag{6.8}$$

This is a criterion that takes into consideration plastic deformation and permanent deflections. It can be used in hydrocodes where the deviatoric and hydrostatic parts of stresses are treated separately. In literature this particular criterion is not used when concrete is exposed to blast loading.

The stress-based erosion criteria are the following:

Principal stress:

By using this criterion, erosion begins when the maximum principal stress is reached. Usually when the material fails under tension, such as concrete, the limit can be related to the tensile cut off.

Effective stress:

This is an erosion criterion typically selected for metals and not for materials with brittle nature like concrete, in this criterion the erosion starts when the effective stress is adopted.

Furthermore, erosion can be taken into consideration when using a damage constitutive model, where the damage is related with the stiffness reduction of the material. The main disadvantage of the latter approach, although more straightforward, is that the damage is affected by the chosen constitutive model. For that reason the results are strongly influenced by the damage definition. More precisely, the adopted damage parameters are determined after a sequence of experimental and numerical observations. Thus, they are based on certain conditions and may not be able to represent correctly the damage in a different situation.

As was mentioned previously, a wide range of erosion criteria exist and it is a known fact that numerical results are strongly influenced by the erosion criteria. In addition, most of these criteria which are based upon strain limitations are strongly mesh sensitive. The principal strain erosion criterion is widely used, as discussed previously [7], since it predicts adequately the spalling of concrete material under impact and blast loading. Hence, in the current study four different mesh sizes (3.59, 4.7, 5.53 and 6.35 mm) were numerically tested under three principal strain erosion limits (0.001, 0.0015

and 0.002) in the case of 50 g of C4 explosive. In total twelve numerical simulations were performed (12 pairs). For every mesh size and principal strain limit, the errors $(d_{crater}^{exp} - d_{crater}^{num}) / d_{crater}^{exp}$ obtained from the diameter of damage at the crater d_{crater} and the errors $(d_{spall}^{exp} - d_{spall}^{num}) / d_{spall}^{exp}$ from the diameter of damage at the spall d_{spall}, were averaged in order to find the average errors shown in Figure 6.12. It can be seen that apart from the fact that the finest mesh (3.59 mm) was computationally expensive, exhibited also the highest levels of average errors. The mesh discretisation that exhibited the lowest errors (between 9.7 % - 10.7 %) among the others, following also the most stable trend was the one with a size of 5.53 mm. The latter explains the reason why the mesh size h_c = 5.53 mm along with the principal strain ε_1=0.001 were used in the current study.

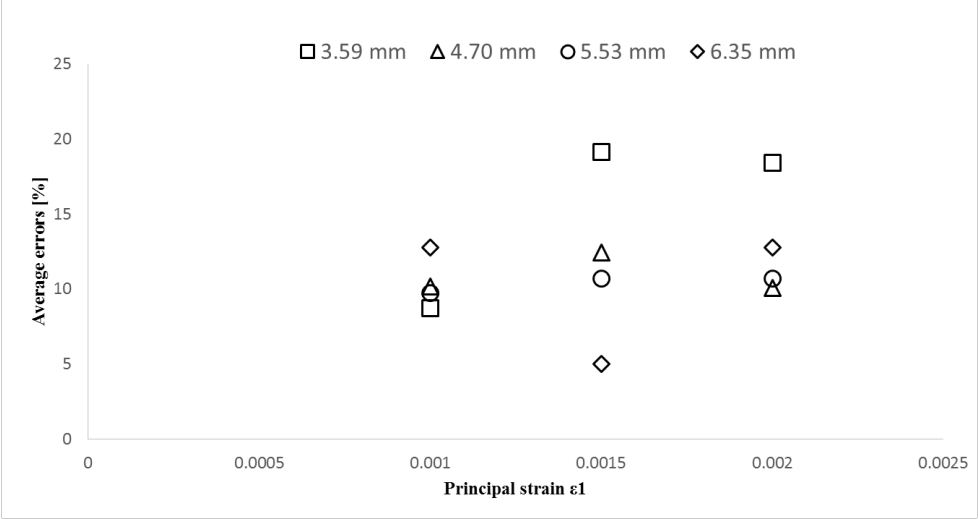

Figure 6.12: Mesh convergence study for several principal strains erosion limits.

6.3.5 Equation of State and material model for the explosive

The Jones-Wilkins-Lee (JWL) equation of state [8], [9] was adopted to model the high explosive charge. In addition, the high explosive material model that was used,

determines the detonation time of the charge when the position, the detonation velocity D, the initial density of the explosive ρ_0 and the Chapman- Jouguet pressure P_{cj} of detonation are known for the particular explosive. These are constant values that govern the robustness of the chosen explosive. Once the detonation is achieved, the pressure that is related with the released energy is given by the following equation:

$$p = A \times \left(1 - \frac{\omega}{R_1 v}\right) e^{-R_1 v} + B \times \left(1 - \frac{\omega}{R_2 v}\right) e^{-R_2 v} + \frac{\omega E_0}{v} \qquad 6.9$$

where A, B, ω, R_1, R_2 are material constants, E_0 is the initial internal energy per unit volume (energy density) and $v = \rho_0/\rho$ is the relative volume. The numerical values for TNT that were used in LS-DYNA, both for the material and the Equation of State description, are shown in Table 6.8.

Table 6.8: Material and EOS parameters for TNT.

ρ_0 (kg/m^3)	D (m/s)	P_{cj} (MPa)	A (MPa)	B (MPa)	R_1 (-)	R_2 (-)	ω (-)	E_0 (MPa)
1630	6930	21000	3.71×10^5	3.23×10^3	4.15	0.95	0.3	7000

6.3.6 Equation of State and material model for the air

The equation of state used for modelling the air is based on the following general linear polynomial equation [10]:

$$p = C_0 + C_1\mu + C_2\mu^2 + C_3\mu^3 + (C_4 + C_5\mu + C_6\mu^2)E_0 \qquad 6.10$$

where E_0 is the initial energy density, $\mu = \rho/\rho_0$ -1 is the fraction of air densities in current and initial conditions and C_0-C_6 are coefficients. When air is assumed to be an ideal gas the aforementioned coefficients take values equal to zero except for C_4=C_5=γ-1. In this case, the ideal gas law (gamma law) is applied, where γ is the fraction between the specific heats at constant pressure and volume. A value of γ = 1.4 (valid at low overpressures) has been proved to be adequate in this case. Taking into account the above considerations the general linear polynomial in Equation 6.10 yields,

$$p = (\gamma - 1)\frac{\rho}{\rho_0} E_0 \qquad 6.11$$

In this work, for the material model used for simulating the air around the slab and the explosive, the material NULL of the LS-DYNA library was employed. The latter material model allows the Equation of State (EOS) to be applied without finding the deviatoric stresses and permits air to behave like a fluid. Table 6.9 summarises the material properties of the air as well as the constant parameters of the Equation of State.

Table 6.9: Material and EOS parameters for air.

ρ_0 kg/m^3	C_1 (-)	C_2 (-)	C_3 (-)	C_4 (-)	C_5 (-)	C_6 (-)	E_0 MPa
1.23	0	0	0	0.4	0.4	0	0.258

6.3.7 Equation of State and material model for the reinforced concrete slab

The material model that was used in order to present numerically the concrete slab was the Winfrith concrete model, which was one of the available models for simulating concrete in LS-DYNA library (see Section 4.5). The reason for this selection was stated in chapter 4 (see Section 4.6) as well.

The reinforcing bars that exhibit rate effects (viscoplastic formulation), were assumed as beam elements. The model which represents "plasticity" in LS-DYNA library, was adopted for simulating this part of the structure. In addition, this model (see Section 4.7), needs the implementation of a stress-strain curve which describes the variation of the effective plastic strain along the stress values. The aforementioned curve, shown in Figure 6.13, illustrates the performance of steel in the plastic region where only permanent deformations are evident.

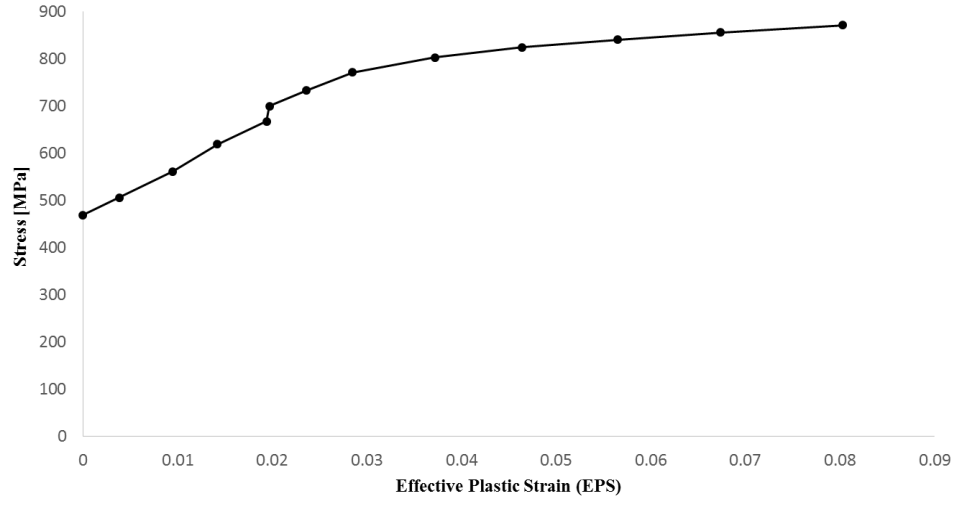

Figure 6.13: Variation of the Effective Plastic Strain (EPS) along the stress evolution (Figure taken from [5]).

6.3.8 Numerical results

The results obtained from the numerical simulations are summarised in Table 6.10 (see also Table 6.7). These are the diameter of the crater and the spall both for the front and the back face of the tested slabs. In addition, the depth of the crater and spall in the case that no perforation was evident, was measured from the deleted elements of the surface in the front and at the back side, respectively. The numerical results are compared and discussed with the experimental in Chapter 7 of the Results and Discussion.

Table 6.10: Numerical results of the diameter of damage observed on crater and spall.

	FRONT FACE		BACK FACE	
C4 amount [g]	Crater Diameter [mm]	Depth of crater [mm]	Spall diameter [mm]	Depth of spall [mm]
75	199	perforation	210	perforation
50	177	perforation	210	perforation
25	144	perforation	199	perforation
15	122	17	177	33
10	100	10	166	10

6.4 HESH projectile impact – Experimental setup

6.4.1 Description of the test

This particular experiment was performed in order to investigate the behaviour of a doubly reinforced concrete wall with overall dimensions of 2.464 × 2.464 × 0.2 [m^3] and concrete of 35 MPa compressive strength under the combined effect of contact

detonation and kinetic energy of a High Explosive Squash Head – High Explosive Plastic (HESH – HEP) projectile. The current work is considered as a continuation of the previous contact detonation event, since the contact detonation is combined with the effects of kinetic energy.

The 90 mm MK8 HESH-T M691A2 projectile [11] had a thin walled steel cylindrical body (2.123 kg) composed of a short ogive nose and a plug (1.101 kg) at the base, which controls the detonation of the fuse. The explosive charge (1.22 kg), used as a filler between the plug and the nose was Composition A3 [12], which consisted of approximately 90% RDX and 10 % wax. In addition, the nose of the projectile was filled with wax (0.015 kg) in order to prevent premature detonation. This round was US Army Safety Certified in December 2002 and was designed against reinforced concrete structures, bunkers and light armored vehicles. The shape of this specific type of projectile is shown in Figure 6.14. The description of the geometry and the material specifications used, are discussed in the numerical modelling section.

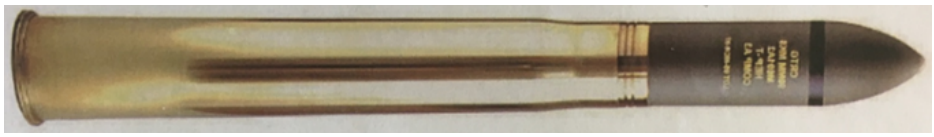

Figure 6.14: 90 mm MK8 HESH-T M691A2 projectile.

The launching equipment (see Figure 6.15) that was used to fire the abovementioned projectiles against the walls, was the 90 mm F4 gun [13]. Compared to the previous series of 90 mm F1 and 90 mm F3, the latest model exhibits better efficiency and lighter establishment. The barrel and the breech are made of steel and the 35° angle of the breech helps loading. In addition, the breech is assembled by several parts, a design

that allows easy maintenance without taking apart the whole gun. The specifications of the 90 mm F4 gun can be found in Table 6.11

Figure 6.15: The 90 mm F4 gun.

Table 6.11: Specifications of the 90 mm F4 gun.

Specification	Value
Main weapon caliber (mm)	90
Length (mm)	5740
Barrel length (calibers)	52
Recoil stroke (mm)	550
Weight (kg)	602
Recoiling mass (kg)	420
Muzzle velocity (m/s)	1275
Firing range (m)	1660

The projectiles were fired from a distance of 70 m, in a total number of 8 shots, one on each quarter of the reinforced concrete walls that were positioned vertically to the ground. Two of the shots were fired with a velocity of approximately 600 m/s, four of 800 m/s and two of 1000 m/s. In addition, the projectiles were detonated on the surface of the RC walls after a detonation delay of 150 μs (for the 600 and 1000 m/s) and 250

μs (for the 800 m/s). The conditions of the experiments were kept the same for all the sets of shots and the only changing parameter was the velocity of the projectiles and the detonation delay. The aim was to investigate the evolution of damage as the impact velocity was increasing.

Figure 6.16 shows the reinforced concrete walls before and after impact and Table 6.12 summarises the velocities along with the detonation delay time of the fuse. The detailed experimental measurements of damage and the presentation of the material parameters of the RC wall and the parts of the HESH projectile are included in Sections 6.4.3 and 6.5, respectively.

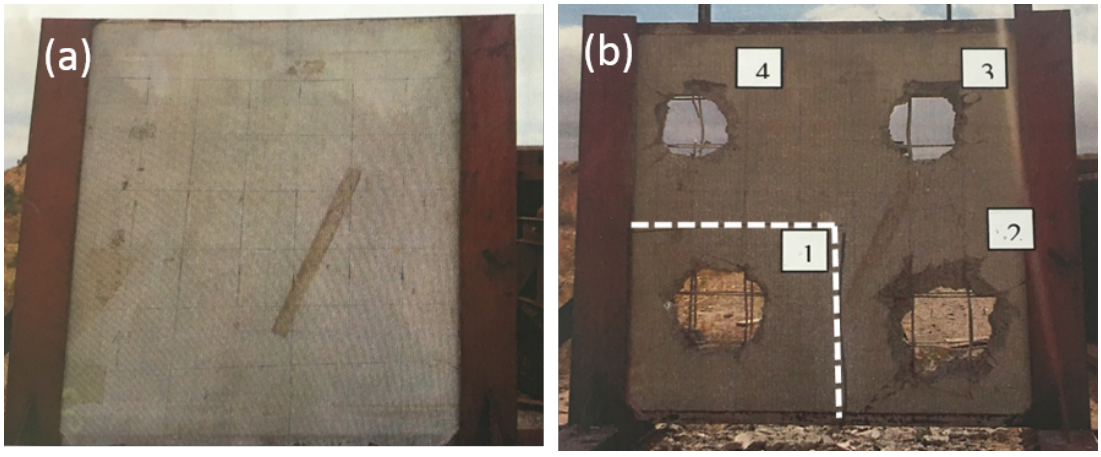

Figure 6.16: Reinforced concrete wall before (a) and after (b) the shots.

Table 6.12: Summary of the prearranged parameters of the projectile.

Parameter	Values	Units
Detonation delay time	150, 250, 150	μs
Impact velocity	600, 800, 1000	m/s

6.4.2 Design of reinforced concrete

Concrete mixture:

The concrete mixture for the aforementioned walls followed the Standards [1], using Type I category of Portland cement. Table 6.13 summarises the material properties of the concrete mixture.

Table 6.13: Concrete mixture for the double reinforced concrete target.

Materials	Density/Volume
Cement	158 kg/m^3
Fly Ash	53 kg/m^3
Fine Aggregate 1	322 kg/m^3
Fine Aggregate 2	322 kg/m^3
Coarse Aggregate	840 kg/m^3
Water	12 l

The concrete had an average 28-day compressive strength f_c = 35 MPa, a tensile strength f_t = 3.5 MPa, a density ρ = 2314 kg/m^3 and an elastic modulus E = 29.58 GPa.

Reinforcement placement:

The reinforcing bars (A615, Grade 40) that were placed in two layers, had a nominal diameter of 12 mm. The mechanical properties of the rods comprised an elastic modulus E = 210 GPa, a density ρ = 7896 kg/m^3, a minimum tensile strength f_t = 413 MPa and a minimum yield strength f_y = 275 MPa. In addition, the rebars had a spacing of 300 mm from centre to centre, the gap between the two layers was 127 mm and were embedded 38 mm from the outer surface of the concrete wall. The configuration

of the concrete wall, as well the placement of the reinforcing bars, is shown in Figure 6.17.

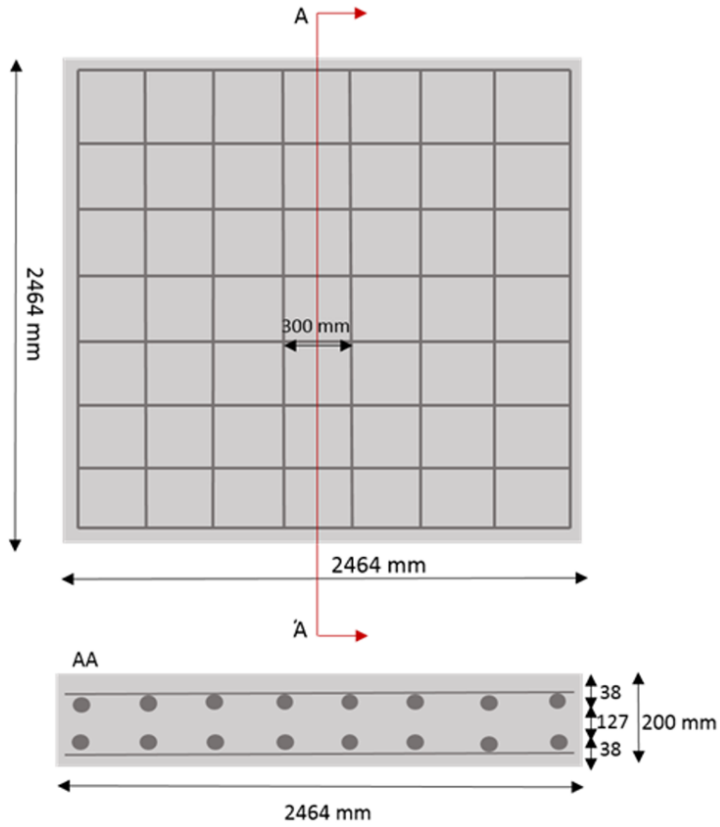

Figure 6.17: Placement of the reinforcing bars.

Final characteristics of the double reinforced concrete walls:

The mechanical properties both for concrete and steel material are summarised in Table 6.14:

Table 6.14: Material properties for concrete and steel.

Material	f_c (MPa)	f_t (MPa)	f_y (MPa)	ρ (kg/m^3)	E (GPa)
Concrete Slab	35	3.5	-	2314	29.58
Steel rebars	-	410	275	7896	210

6.4.3 Methodology and experimental measurements

The two double reinforced concrete walls were hit by 90 mm MK8 HESH-T M691A2 projectiles under three different velocities (600, 800, 1000 m/s). The projectiles were detonated after they touched the concrete surface, resulting in a contact detonation event. Velocity measurements of the projectiles at the initial and at the impact stage, measurements of the average diameter of the obtained holes and photos of the damaged walls both from the front and the back faces, were collected.

A 35 GHz Doppler radar was used by MECAR [11] in order to collect velocity measurements. Also, two high-speed Photron cameras [14] were employed in order to capture high-speed imaging. In addition, a FARO laser scanner [15] was used for a fully virtual reconstruction of the scene. The high-speed cameras were placed at a 90-degree angle from the shooting direction and captured the event at the front and the back face of the concrete wall. Even though a high standard equipment was used, the actual penetration of the projectile could not be recorded due to the debris of concrete material after impact.

The experimental measurements obtained from the on-site investigations are listed in Table 6.15. These are the initial velocity V_{ini} and the impact velocity V_{imp} which is

slightly lower due to the deceleration of the projectile caused by aerodynamic effects. The average impact velocity V_{ave} is the actual impact velocity of the projectiles. Furthermore, in order to experimentally measure the dimensions of the holes caused by the impact and detonation, both the horizontal ($H_{orizontal}$) and vertical ($V_{ertical}$) diameters of the holes were measured and averaged to get the average hole size A_{veg1} (similarly to previous scenario). The value used for the validation of the numerical modelling results, was the average of the A_{veg1} values obtained from the same velocity impacts. Thus, according to Table 6.15, the average diameters of the hole A_{veg2} obtained from the 600, 800 and 1000 m/s are 347, 420 and 497 mm, respectively. Although, three different velocities were tested on site, only the two of them (600 and 1000 m/s) are tested numerically and discussed. The reason of this was that under those two velocities the detonation delay remained the same (150 μs) and the only difference between the models was the kinetic energy of the impact.

Table 6.15: Experimental measurements of the impact velocity and perforation diameter.

Experimental measurements							
Impact Velocity				**Diameter of Hole**			
t_{det} [μs]	V_{ini} [m/s]	V_{imp} [m/s]	V_{ave} [m/s]	$H_{orizontal}$ [mm]	$V_{ertical}$ [mm]	A_{veg1} [mm]	A_{veg2} [mm]
150	1011	989	988	480	480	480	497
150	1014	986		460	570	515	
250	818	799	802	440	450	445	420
250	825	805		400	390	395	
250	822	797		400	440	420	
250	830	806		430	410	420	
150	628	607	605	320	330	325	347
150	619	602		330	410	370	

Hence, it was feasible to investigate the effect of the impact velocity since the detonation delay could influence the evolution of damage as well. More precisely, a delayed detonation results in a deeper penetration of the projectile, thus the response of the RC member in terms of damage changes.

6.5 HESH projectile impact – Numerical modelling

6.5.1 General Approach

The numerical modelling of the above experiments followed the MMALE approach described in Section 6.3.1, due to the very demanding and highly deformation nature of the problem, in which the formation of negative volumes was a possibility if severely distorted elements were evident. The MMALE technique proved, once again, an efficient numerical tool, in order to capture the extreme loading scenario of the impact and contact blast. The numerical model of the impacted system consisted of the reinforced concrete wall, the air around the wall and the HESH projectile. This numerical configuration as well the modelling procedure, will be presented step by step in this section. The specific geometry of the projectile is shown in Figure 6.18 and the cross sections (1 – 13) are listed in Table 6.16 and Table 6.17.

In Table 6.16, the points of the curved segments of the 2D projectile geometry (coordinates) are specified. Each line of the table represents a point that is a part of an arch with a prescribed angle, center (X, Y) and radius.

In addition, each line of Table 6.17 represents one of the linear segments of the 2D geometry that needs the coordinates of two points in order to be defined.

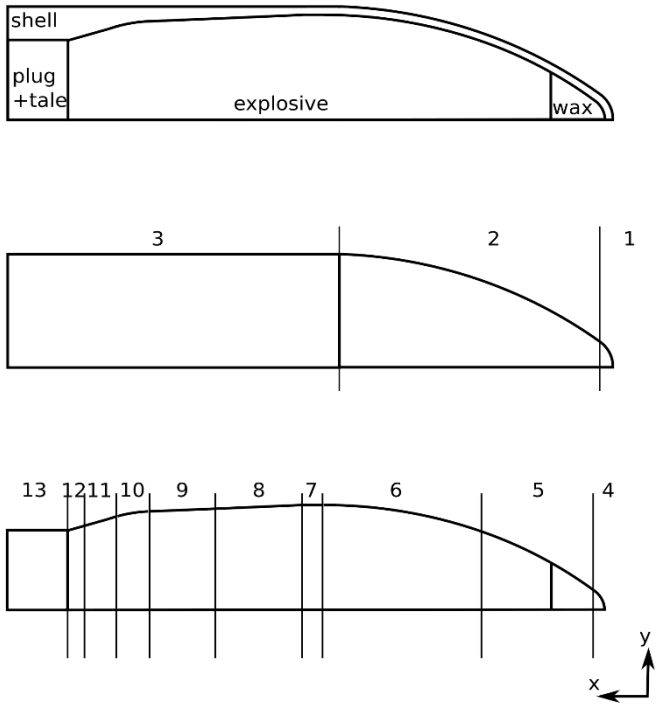

Figure 6.18: 2D geometry of the 90 mm HESH along with the cross sectional points.

Table 6.16: Coordinates of the curved segments.

Cross section	Start angle (◦)	End angle (◦)	Center_X (mm)	Center_Y (mm)	Radius (mm)
1	0	53.403	-12.5	0	12.5
2	53.403	87.943	-108.96	-129.89	174.29
4	0	52.531	-12.7	0	10.2
5	52.531	70.547	-102.19	-116.76	157.31
6	70.547	90	-108.31	-134.1	175.7
10	90	106	-170.72	-10.814	50

Table 6.17: Coordinates of the linear segments.

Cross section	Start point X (mm)	Start point Y (mm)	End point X (mm)	End point Y (mm)
3	-102.7	44.285	-226.6	44.285
7	-108.31	41.6	-116.52	41.6
8	-116.52	41.6	-148.7	40.195
9	-148.7	40.195	-172.9	39.138
11	-184.5	37.249	-189.1	35.93
12	-189.1	35.93	-203.15	31.9
13	-203.15	31.9	-226.6	31.9

As can be seen from the 2D drawing in Figure 6.18, the plug, the A3 explosive and the wax are surrounded by the thin steel case. Hence, following this specific geometry, the 2D numerical mesh surface was developed. The four individual parts are shown in Figure 6.19.

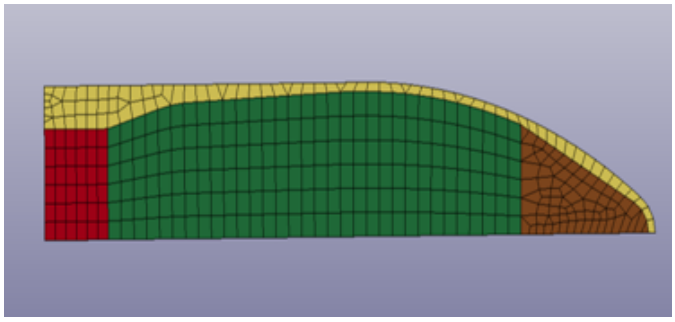

Figure 6.19: 2D finite element mesh of the projectile.

The plug (red), the wax (brown) and the steel case (yellow) were modelled with elements of 4 mm average size. The explosive (green) was meshed with elements of 5 mm average size. This 2D shell element configuration was revolved 360° degrees around the horizontal axis, in 80 segments, in order to create the 3D bullet

configuration that can be seen in Figure 6.20. During this step the creation of four shell element containers (one for each part) was developed. Since MMALE technique was applied along with a very specific 3D geometry, the creation of those shell 'boxes' was completely necessary in order to define a Lagrangian surface boundary of spatial region inside of which a particular material would fill up. Since we had four containers, the filling procedure was repeated four times, one for every material (plug, explosive, wax and steel case). In addition, according to this approach, the fillings (different projectile parts) were supposed to be fluids that flew within the Eulerian background mesh.

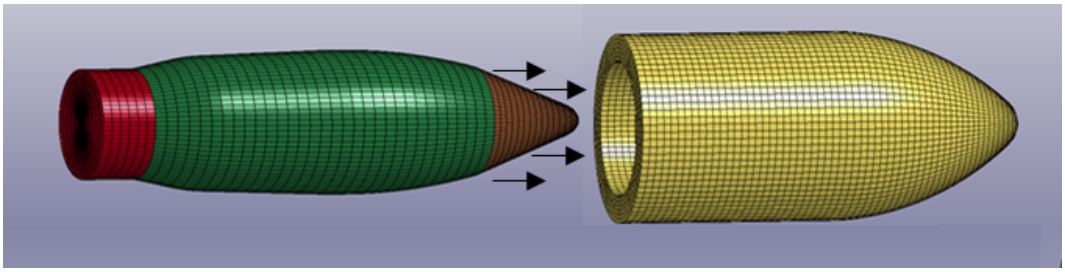

Figure 6.20: 3D finite element mesh of the projectile.

After a mesh study that will be discussed in Section 7.3, uniform hexahedral elements with h_c = 15 mm mesh size were used to model the concrete wall. In addition, only one quarter of the structure was modelled (1232 × 1232 × 200 $[mm]^3$), due to the particular conditions of the experiment (4 shots one after the other, in the 4 quarters of the structural element, as shown in Figure 6.16 (b)).

The reinforcing bars were placed in two layers, with 4 rebars on each layer (4 × 4) due to symmetrical conditions and using a uniform mesh size of 15 mm beam elements.

The spacing between them followed the description presented in the experimental setup (see Figure 6.17).

The air domain, which represented the Eulerian background mesh, was a box with dimensions 1232 × 1232 × 438 [mm]^3 and element size h_c = 15 mm.

The distance that was applied between the target and the bullet was 2 mm. Thus, the value of the air height (438 mm) was determined as the sum of the depth of the wall (200 mm), the distance between the projectile and the wall (2 mm), the length of the projectile (227 mm) and the cover between the back of the bullet and the air (9 mm). Figure 6.21(assuming 4 simultaneous shots) shows the FE discretisation of the model containing the wall and the projectile (a) and the wall with the air domain (b).

The time needed for the detonation due to the physical fuse delay, t_{physical}, was the sum of the time needed for the projectile to travel within the 2 mm distance (d) at an average velocity V_{ave} and the time needed for the shock wave to travel within the projectile's length L (227 mm) at an average speed (S) of approximately 6000 m/s.

This physical delay time (t_{physical}) according to Hallquist [16] was calculated as 50 μs through the following Equation,

$$t_{\text{physical}} = \frac{d}{V_{\text{ave}}} + \frac{L}{S} \qquad 6.12$$

Hence, a simulation delay of 100 μs, led to a detonation time (t_{det}) after 150 μs. In addition, a delay equal to 200 μs, resulted in a detonation time after 250 μs.

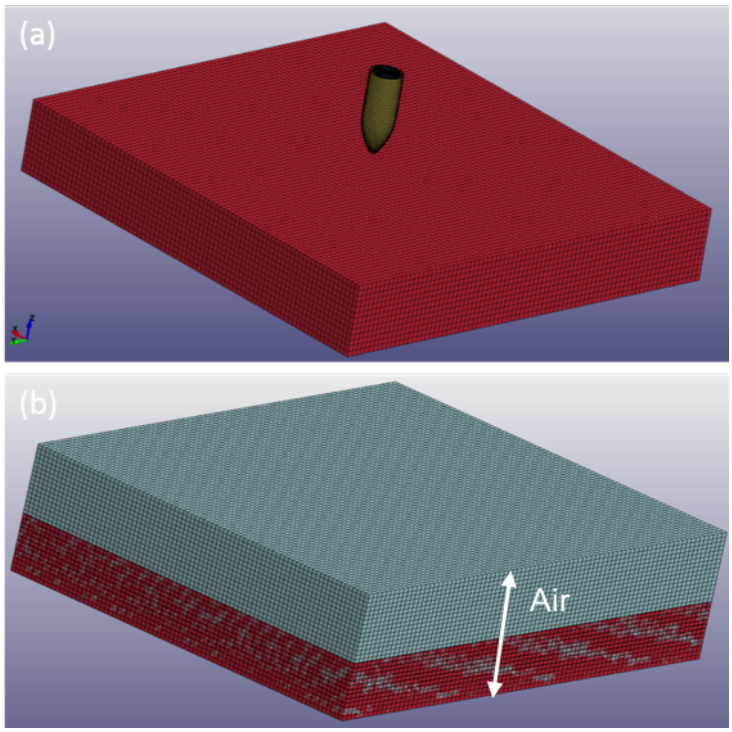

Figure 6.21: Finite element discretisation of the model, reinforced concrete wall and projectile (a), reinforced concrete wall and air domain (b).

6.5.2 Boundary conditions

As discussed previously, the reinforced concrete wall, for economical reasons, was hit by the HESH projectiles with 4 shots, one after the other, resulting in the condition shown in Figure 6.16 (b). The wall was positioned vertically to the ground, was fixed on the two sides and free on the other two. However, the experimental aim was to investigate the response of the RC wall when the impact of the HESH was in the centre. The author, after performing numerical simulations of the projectile in the centre of the structural element, realised that the correlation with the experimental data was not good at all. That happened because during the actual experiments (4 shots on each wall), the wall was losing gradually its strength after each shot, resulting in a weaker

condition with greater damage (holes). As a result, it was decided to model only the 1/4 of the RC wall using the boundary conditions that are shown in Figure 6.22 and the whole projectile (assuming 4 shots simultaneously). Additionally, the air domain had non-reflecting boundary conditions.

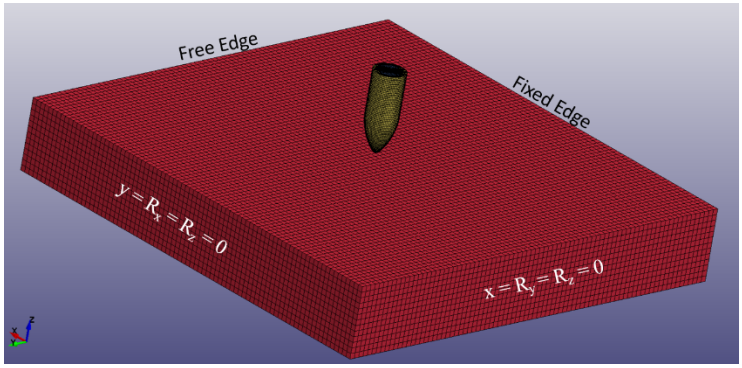

Figure 6.22: Implemented boundary conditions.

6.5.3 Contact Algorithms and Damage criteria

Since the conditions were kept the same as those of the previous numerical approach, the same contact definition (CONSTRAINED-LAGRANGE-IN-SOLID) was used for the coupling between the reinforcing bars and the concrete wall as well as for the coupling between the air domain and the Eulerian parts with the surface of the Lagrangian wall. In addition, the same erosion criterion of the maximum principal strain (ε_1) was used as an erosion limit. That was equal to 0.002 for the case of 600 m/s and equal to 0.0002 for the case of 1000 m/s impact velocity. This difference, in the selected limit value, existed due to the strain rate sensitivity of the impact and blast scenario that was being modelled. More specifically, when the impact velocity was increased, the strain rate increased as well. Hence, concrete's dynamic strength was numerically enhanced through the implementation of the Dynamic Increase Factors

(see Section 4.4). Consequently, there was a need of a smaller principal strain limit in order to be able to capture the damage of concrete.

6.5.4 Equation of State and material models for the projectile parts and air

Material model for plug:

Although the real projectile is fin-stabilised, the tail was not modelled since it was considered that it did not have a significant contribution to the impact. Nonetheless, in order to ensure the correct inertia, the mass of the plug (booster and fuse) was increased accordingly. The plug does not undergo large deformations but behaves like a piston, pushing the explosive after impact and spreading it on the surface of the RC wall. Thus, an elastic material model was adequate to capture this response. In Table 6.18, the material properties for the plug are summarised.

Table 6.18: Specified material properties for the plug.

Property	Value	Unit
Density ρ	14689	kg/m^3
Young's Modulus E	2×10^5	MPa
Poisson ratio v	0.3	-

Equation of State (EOS) and material model for wax:

The wax had a density ρ = 904 kg/m^3 and was located in the nose of the projectile in order to prevent premature detonation. Due to its low stiffness and strength, the constitutive model that was used to describe its behaviour was the "null" material model. It was the same material model that was used to model the air in the contact

detonation scenario, but with different properties (ρ = 904 kg/m^3). This model allows the hydrostatic pressure to be considered without the calculation of the deviatoric stresses. In addition, the EOS that was used to relate the pressure to the internal energy and density was the Gruneisen EoS [16], since it is widely used for solid materials. The cubic relation between the particle velocity v_p and shock velocity v_s leads to the following two relations under compression and expansion, respectively:

$$p = \frac{\rho_0 C^2 \mu \left[1 + \left(1 - \frac{\gamma_0}{2}\right)\mu - \frac{\alpha}{2}\mu^2\right]}{\left[1 - (S_1 - 1)\mu - S_2 \frac{\mu^2}{\mu + 1} - S_3 \frac{\mu^3}{(\mu + 1)^2}\right]^2} + (\gamma_0 + \alpha\mu)E \qquad 6.13$$

$$p = \rho_0 C^2 \mu + (\gamma_0 + \alpha\mu)E \qquad 6.14$$

Assuming a linear relation between the velocities v_s and v_p (v_s=C+$S_1 v_p$), C is the bulk sound speed and the intercept of this curve, S_1, S_2 and S_3 are coefficients of the slope of the curve and due to the assumption of the linear relationship $S_1 \neq 0$ and $S_2 = S_3 = 0$, γ_0 is the Gruneisen gamma coefficient, α is the first order volume corrector to γ_0 and $\mu = (\rho/\rho_0)$-1. Table 6.19 summarises the parameters that were used for wax.

Table 6.19: Material and EoS parameters for wax.

Property	Value	Unit
Density ρ	904	kg/m^3
C parameter	2908	m/s
S_1 parameter	1.56	-
Gruneisen coefficient γ_0	1.18	-

Equation of State (EoS) and material model for explosive:

The Jones-Wilkins-Lee (JWL) EoS ([8], [9]) was used in this problem as well, in order to represent the energy released during the detonation. In addition, the High-Explosive-Burn material model was also used in order to capture the behaviour of the A3 high-explosive. This material model relates the initial density ρ_0 of the explosive, the detonation velocity D and the Chapman-Jouguet pressure P_{cj}. The specific properties for A3 explosive [12] that were used in the current study are listed in Table 6.20 (see also Equation 6.9).

Table 6.20: Material and EoS parameters for A3 explosive.

Property	Value	Unit
Density ρ_0	1563	kg/m^3
Velocity D	8300	m/s
Chapman-Jouguet pressure P_{cj}	3×10^4	MPa
Parameter A	6.11×10^5	MPa
Parameter B	1.065×10^4	MPa
Parameter R_1	4.4	-
Parameter R_2	1.2	-
Parameter ω	0.32	-
Energy density E_0	8440	MPa

Equation of State (EoS) and material model for steel case:

The Johnson Cook material model [17] was used to model the steel case that surrounds the plug, the explosive and the wax. This constitutive model accounts for strain hardening, strain rate effects and thermal softening. Hence, it is an ideal option when dealing with strain rate sensitive dynamic events where the temperature changes

significantly during the impact. The equivalent stress σ_y is related to the yield stress, the strain rate and the temperature as:

$$\sigma_y(\varepsilon_p, \dot{\varepsilon}_p, T) = \left[A + B(\varepsilon_p)^n\right]\left[1 + C\ln(\dot{\varepsilon}_p^*)\right]\left[1 - (T^*)^m\right] \quad 6.15$$

where

$$\dot{\varepsilon}_p^* = \dot{\varepsilon}/\dot{\varepsilon}_0 \quad 6.16$$

and

$$T^* = \frac{T - T_r}{T_m - T_r} \quad 6.17$$

ε_p is the equivalent plastic strain, $\dot{\varepsilon}_p^*$ is the dimensionless plastic strain rate for $\dot{\varepsilon}_0 = 1\ s^{-1}$ (reference strain rate), T^* is the homologous temperature, calculated with the room temperature T_r and the melting temperature T_m, A is the initial yield stress, B is the hardening constant, n is the hardening exponent, C is the strain rate constant and m is the thermal softening exponent. The material parameters used in this particular model are listed in Table 6.21 and the Gruneisen EoS parameters in Table 6.22. Both the material and EoS parameters were obtained and provided by MECAR [11].

Table 6.21: Material parameters for the steel case.

Property	Value	Unit
Density	8436	kg/m^3
Specific heat C_p	452	J/kg °C
Initial yield stress A	225	MPa

Hardening constant B	669	MPa
Hardening exponent n	0.5159	-
Strain rate constant C	0.296	-
Thermal exponent m	1	-
Melting temperature T_m	1811	°C
Room temperature T_r	28	°C
Reference strain rate	1	s^{-1}
Shear modulus G	80769	GPa

Table 6.22: EOS parameters for the steel case.

Property	Value	Unit
C parameter	5788	m/s
S_1 parameter	1.49	-
Gruneisen coefficient γ	2.17	-

Equation of State (EoS) and material model for air:

The material model used for the Eulerian background mesh of air (ρ = 1.23 kg/m^3) was the same that was used to model the air in Section 6.3.6. The same linear polynomial EoS, assuming that the air behaves as an ideal gas was used.

6.5.5 Equation of State and material model for the reinforced concrete wall

The Winfrith material model that was used to capture the behaviour of concrete under the contact detonation event, was employed for the current investigation as well (see Section 4.5). In addition, the reinforcing bars with a yield strength of 275 MPa, were

modelled using the plastic – kinematic constitutive model which was described in Section 4.7.

6.5.6 Numerical results

The numerical results, in terms of damage, obtained from the finite element analysis are listed in Table 6.23. These are the diameter of the hole formed in the centre of the detonated RC walls after the impact of the HESH projectile at two striking velocities. The discussion and the comparison of those with the relevant experimental findings will follow in Chapter 7.

Table 6.23: Measurements of the diameter of the hole from the numerical results.

t_{det} [μs]	V_{ave} [m/s]	D_{hole} [mm]
150	988	436
150	605	300

6.6 References

[1] EN, 206-1 "Concrete Specification, Performance, Production and Conformity", 2000.

[2] M. McVay, "Spall damage of concrete structures", U.S. Army Corps of Engineers Waterways Experimental Station,1988.

[3] BS, 12350-5 "Testing fresh concrete-Part-5, Flow table test", British Standard, 2000.

[4] BS, "Testing hardened concrete", British Standard, 2009.

[5] L. Schwer, "Modeling rebar: the forgotten sister in reinforced concrete modeling", presented at the 13th International LS-DYNA Users Conference, Detroit, 2014.

[6] K. Xu and Y. Lu, "Numerical simulation study of spallation in reinforced concrete plates subjected to blast loading", Computers & Structures, vol. 84, pp. 431-438, 1// 2006.

[7] B. Luccioni and G. Araoz, "Erosion criteria for frictional materials under blast loads", 2011.

[8] B. Zakrisson, B. Wikman, and H.-Å. Häggblad, "Numerical simulations of blast loads and structural deformation from near-field explosions in air", International Journal of Impact Engineering, vol. 38, pp. 597-612, 7// 2011.

[9] Y. S. Tai, T. L. Chu, H. T. Hu, and J. Y. Wu, "Dynamic response of a reinforced concrete slab subjected to air blast load", Theoretical and Applied Fracture Mechanics, vol. 56, pp. 140-147, Dec 2011.

[10] A. Alia and M. Souli, "High explosive simulation using multi-material formulations", Applied Thermal Engineering, vol. 26, pp. 1032-1042, 7// 2006.

[11] MECAR. Available: http://www.mecar.be

[12] E. Lee, M. Finger, and W. Collins, "JWL equation of state coefficients for high explosives", 1973.

[13] Army-Guide. Available: http://www.army-guide.com

[14] Photron. Available: http://www.photron.com

[15] FARO. Available: http://www.faro.com

[16] J. O. Hallquist, "LS-DYNA theory manual," Livermore software technology corporation, vol. 3, pp. 25-31, 2006.

[17] G. R. Johnson and W. H. Cook, "A constitutive model and data for metals subjected to large strains, high strain rates and high temperatures", in Proceedings of the 7th International Symposium on Ballistics, 1983, pp. 541-547.

Chapter 7. Results and Discussion

7.1 Numerical validation for blast pressure modelling in the near-field zone

In this section, the numerical methodology (ALE) is studied. The work is the product of collaboration with the Department of Continuous Mechanics and Structural Analysis of the University Carlos III of Madrid and is focused on the reliability of the use of ALE approach in the case that near-field blast phenomena are considered (scaled distance $Z < 0.198$ m/kg$^{1/3}$). To this end, experimental near blast tests are reproduced and LBE and ALE approaches are compared, focusing on the capabilities of these methods in the near-field.

The experimental tests used to validate the numerical models were carried out by Huffington and Ewing [1]; in this test campaign an effort to obtain blast data for small scaled distance (Z) was done. The authors used an impulse plug technique [1] comparing the impulse transmitted by Pentolite spheres at different Z values. The authors vary the scaled distance from 0.079 to 0.198 m/kg$^{1/3}$. For each scaled distance different mass to stand-off distance combinations are tested in order to study its influence. A summary of the tested groups at different scaled distances can be found in Table 7.1. Each group was tested at least 3 times in order to achieve a good repeatability.

The range of scaled distances that Huffington studied is very close to a contact explosion scenario. In the current doctoral thesis that contact detonations are considered, the scaled distance is determined by the mass of explosive (density) and is equal to 0.057 m/kg$^{1/3}$. Thus, the validation of the use of ALE approach in the

previously referred close range (Huffington's data) means that the method is applicable to contact detonations as well.

Table 7.1: Groups of tests (Table taken from [1]).

Group	Mass [g]	Stand-off distance [mm]	Scaled distance [m/kg$^{1/3}$]
G1	484.81	155.80	0.198
G2	897.25	191.14	0.198
G3	237.23	98.47	0.158
G4	488.27	124.89	0.158
G5	892.77	152.90	0.158
G6	239.02	73.90	0.118
G7	483.70	93.726	0.119
G8	891.24	114.80	0.119
G9	240.84	49.276	0.078
G10	483.70	62.484	0.079
G11	896.15	76.454	0.079

The aforementioned experimental tests, conducted by Huffington, are modelled using LBE and ALE approaches in LS-DYNA. The LBE approach (Section 3.5) reproduces the effect of a spherical charge by using analytical equations. Thus, only the stand-off distance and the explosive mass are needed to be specified. The impulse generated by the explosive is measured on a rigid plate and the scaled distance is evaluated from the surface of the plate. For the ALE approach (Section 3.5) the plate is not necessary. Instead, the impulse is measured in a tracer point. The air surrounding the explosive and the tracer should be modelled and non-reflecting boundary conditions should be specified as well. The rectangular domain is meshed using a characteristic element

length of 4.59 mm. In both numerical investigations Pentolite explosive is used in order to be consistent with Huffington's experiment. Furthermore, in the numerical simulations the symmetry of the problem is explored and only 1/4 of the domain is used. Summarizing, eleven different stand-off/mass combinations are simulated for each approach (LBE and ALE). Figure 7.1 shows the impulses as a function of the scaled stand-off distance for the experimental results (Huffington's data, see Table 7.1) and the ones numerically obtained from both techniques (LBE and ALE). The experimental results show a downward trend of the impulse generated by the blast as the scaled distance increases. This trend is well captured by the numerical simulations. As expected, the LBE for values of scaled distance lower than 0.17 gives more dispersion than the ALE approach, since the values of impulse predicted by this last technique are always closer to the experimental data.

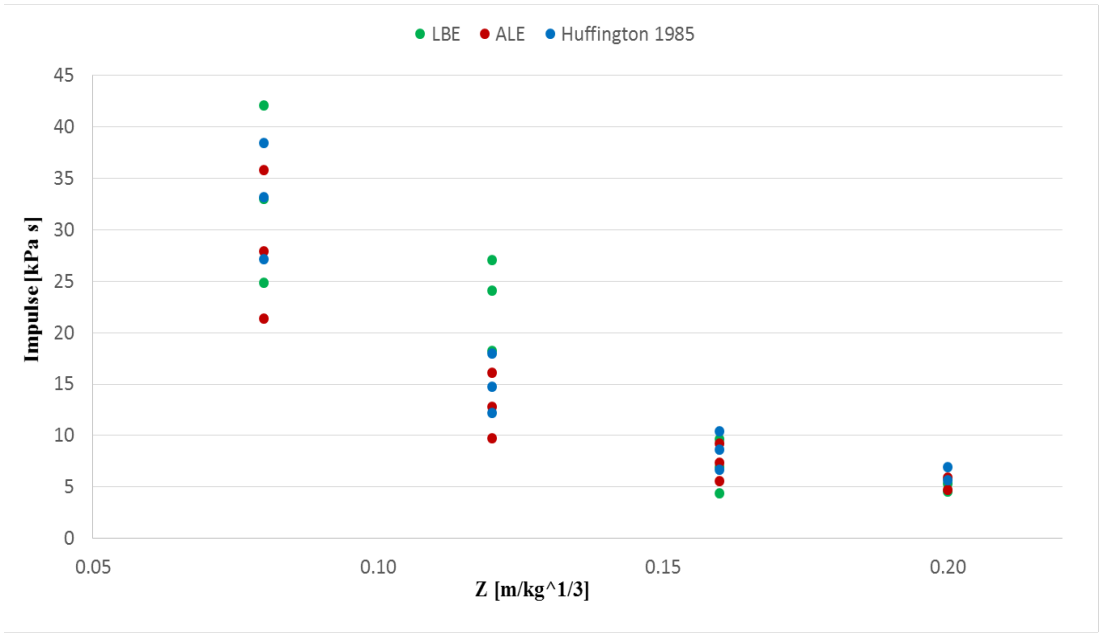

Figure 7.1: Impulse as a function of explosive scaled stand-off distance.

The impulses of Figure 7.1 are normalised by the relevant cubic root of the mass (see Table 7.1) in order to make the values independent of the explosive's mass. Figure 7.2

shows the experimental values of the normalised impulses, in comparison with the normalised numerical values predicted by LBE and ALE. A similar negative trend is shown for the scaled impulse as the scaled stand-off distance is increasing; the values collapse to an almost single point for all the techniques. Again, the values predicted by the ALE are the closest to the experimental results. Figure 7.3 summarises the errors in the predictions. The results reveal that the errors obtained by ALE are smaller and more stable. In addition, deeper analyses of the error relative to experimental measurement predictions are performed by groups and not by scaled distances. It can be noted, in Figure 7.4, that there are 3 groups (G6, G7, G8) in which the error predicted by LBE is higher. That corresponded to values lower than Z=0.17.

Once the impulse is compared with the experimental values, it can be concluded that the numerical simulations are reproducing the physics of the problem in terms of impulse, but the predictions of the ALE are closer to the values registered in the tests.

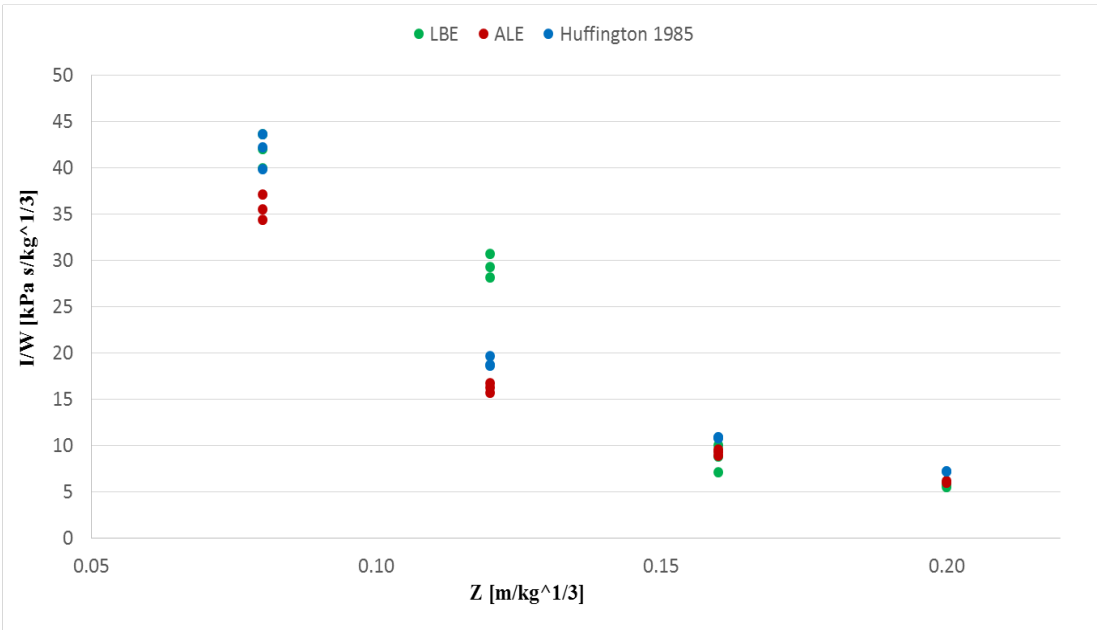

Figure 7.2: Scaled impulse as a function of explosive scaled stand-off distance.

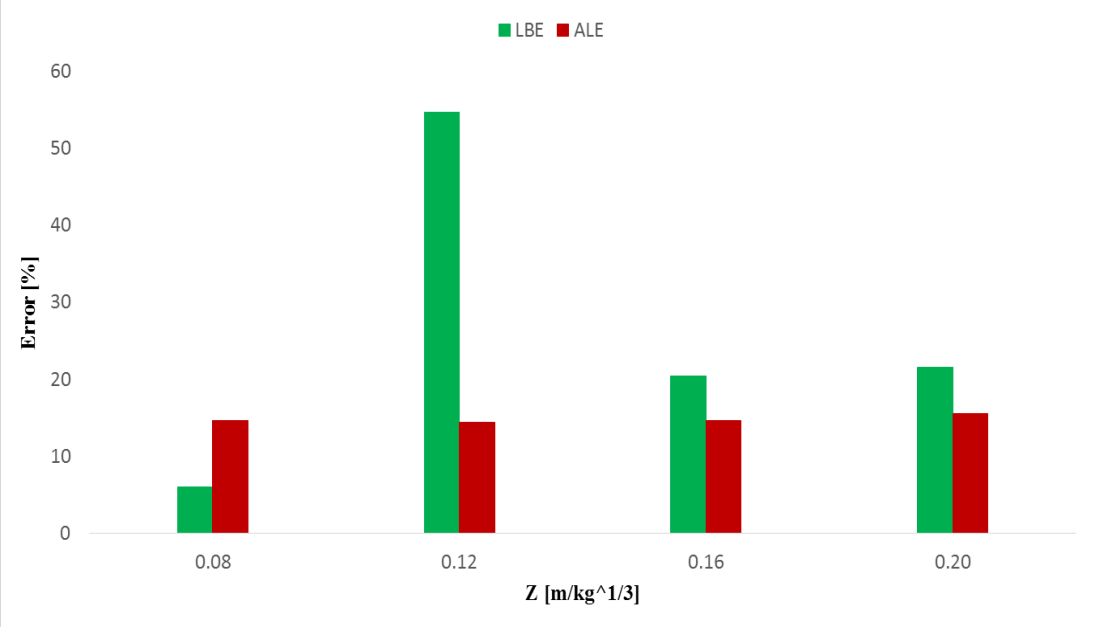

Figure 7.3: Error in the predicted scaled impulse as a function of explosive scaled standoff distance.

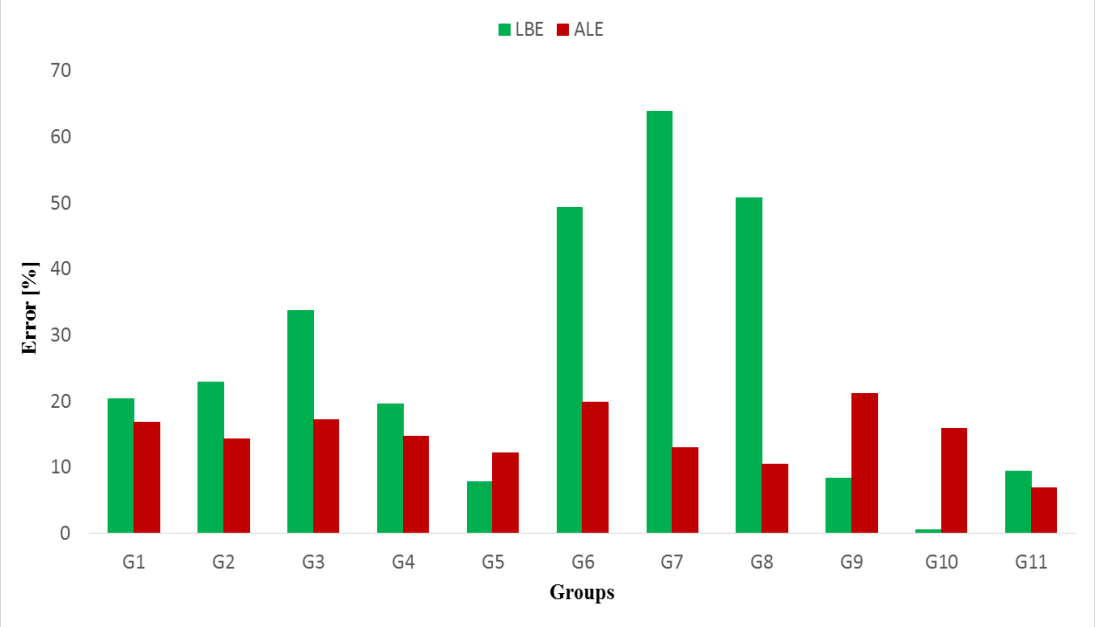

Figure 7.4: Error in the predicted scaled impulse as a function of explosive mass-standoff distance combination.

The pressure pulse produced by the explosive is presented in Figure 7.5, in order to extend this study and the validation of ALE method. There are no experimental results so only LBE and ALE approaches are compared. LBE approximations for smaller Z, underpredict the maximum pressure in comparison with the ALE approach. This underprediction increases as the scaled distance decrease. Moreover, the impulse obtained by the two approaches remains similar due to the fact that LBE not only underestimates the pressure but overestimates the time duration of pressure as well. All these results are expected because LBE approach employs CONWEP relationship based on Kingery and Bulmash empirical equations [2] that are not designed for this range of Z.

In summary, both numerical approaches are compared with experimental results and analysed. As a result, the most convenient numerical approach for small stand-off distances is the ALE, which predicts good results in terms of impulse and pressure peaks.

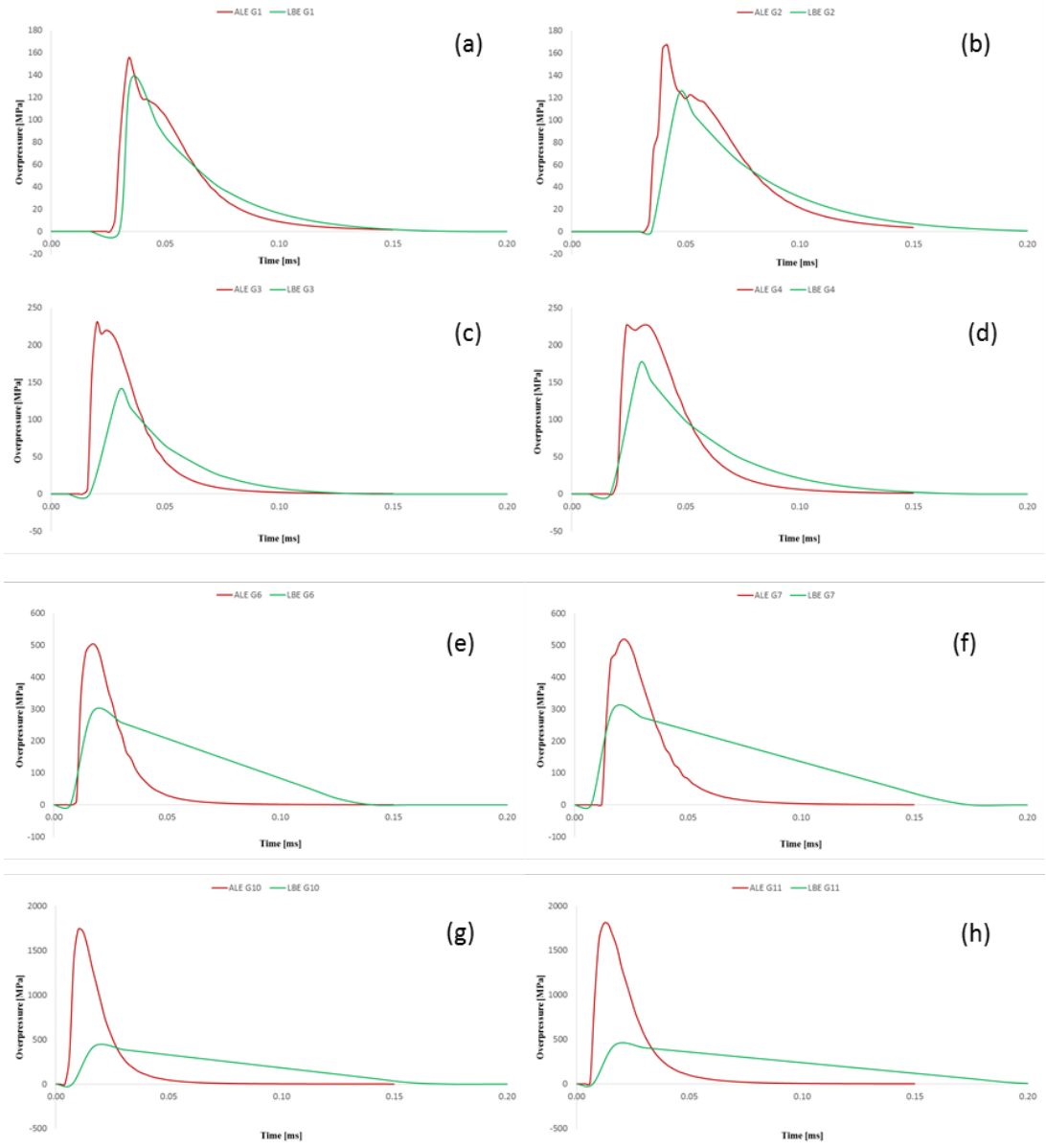

Figure 7.5: Pressure contour generated by the blast: Z = 0.2 (a), (b), Z = 0.16 (c), (d), Z = 0.12 (e), (f), Z = 0.08 (g), (h).

7.2 Validation of the numerical damage obtained under contact detonation of the reinforced concrete slabs

Five reinforced concrete slabs are tested at the Royal Military Academy (Belgium) under the contact detonation of 75, 50, 25, 15 and 10 g of C4. The slabs have identical

mechanical properties and the tests are conducted in order to replicate the response of a standard wall of a building under a contact detonation event.

The C4 explosive is placed and detonated on top of the slabs. Upon detonation, photos of the damaged slabs, both for the front and the back faces are taken. Following this, measurements of the diameter of the crater (front face) and spall (back face) are obtained. These diameters are taken as the average value between the maximum horizontal diameter and the vertical diameter of the total damage caused due to the contact detonation. This particular experimental data of the diameter of damage is then compared with the obtained measurements of the numerically predicted damage (see Table 7.2).

Table 7.2: Numerical and experimental measured diameters of the damaged slabs.

Front Face diameter (Crater)				**Back Face diameter (Spall)**			**Average $Error_F$ and $Error_B$**
C4 [g]	**Experimental [mm]**	**Numerical [mm]**	**$Error_F$ [%]**	**Experimental [mm]**	**Numerical [mm]**	**$Error_B$ [%]**	**[%]**
10	90	100	10.6	175	166	5.2	7.9
15	130	122	6.4	215	177	17.7	12.1
25	135	144	6.5	230	199	13.4	10.0
50	165	177	7.0	240	210	12.4	9.7
75	200	199	0.5	255	210	17.5	9.0

The numerical simulations were carried out using h_c= 5.53 mm and ε_1= 0.001, as discussed previously (Section 6.3.4). The obtained numerical results of the damage (in Table 7.2), prove that the simulations using the MMALE approach can predict well the experimental data. The average errors of damage between the actual and the numerical results, obtained from the front and the back side of the slabs, listed in Table

7.2 and shown in Figure 7.6, indicate that the errors are lying in the range of 7.90 - 12.1 %. Furthermore, the experiments show that increasing the amount of explosive, the damage increases as well. This observation agrees with the numerical results. By comparing on each detonation the error obtained separately from the front ($Error_F$) and the back face ($Error_B$) of the slabs, it should be also noted that the numerical modelling predicts more accurately the damage on the crater rather than the spall damage.

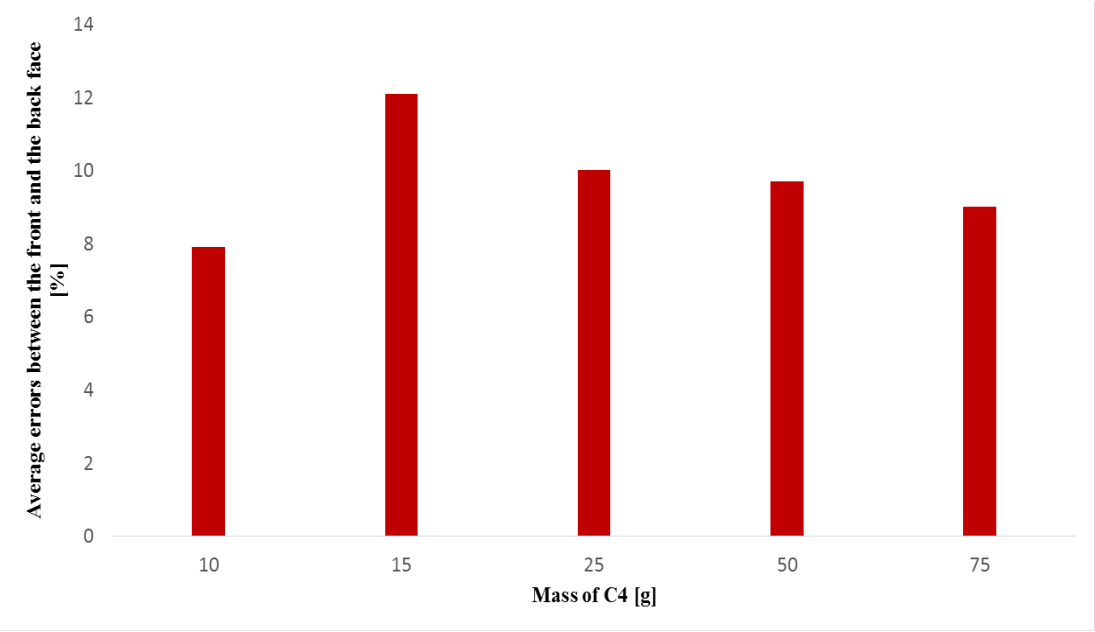

Figure 7.6: Average errors between experimental and numerical results.

The numerical and experimental damage on the reinforced concrete slabs is presented also in Figure 7.7 to Figure 7.11. The different colours in the images taken from the numerical simulations represent the nodal displacements of the finite elements around the damage.

More precisely, the slab under the detonation of 10 g of C4 exhibits both for experiments and numerical simulations the damage shown in Figure 7.7. The spallation that occurs in the experiments – very shallow penetration of 10 mm from

the top and the bottom of the slab – matches the numerical spallation. Also, the errors of damage for the front and the back side of the slab (10.6 and 5.2 %, respectively) reinforce this agreement.

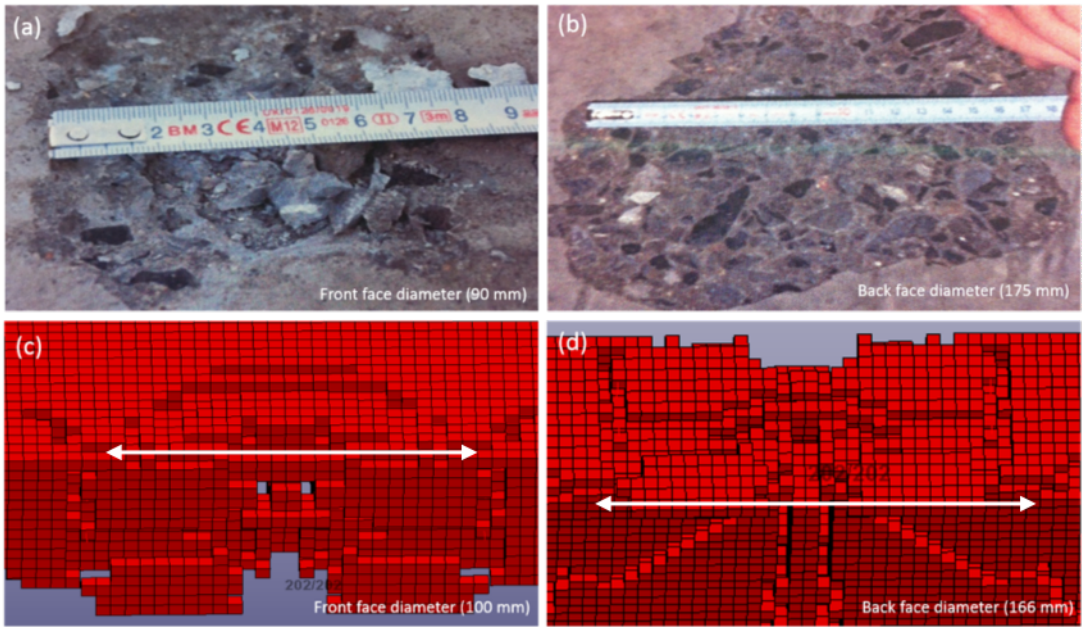

Figure 7.7: Damage caused by the detonation of 10 g of C4: (a) experimental: front face, (c) numerical: front face, (b) experimental: back face and (d) numerical: back face.

The slab under the detonation of 15 g of C4 (Figure 7.8), as expected, shows an even greater penetration. The experimental penetration is measured as 20 and 22 mm for the front and the back sides of the tested slab, respectively, while the numerical penetration is measured as 17 and 33 mm for the same sides. Although the error obtained in the front face is comparatively low (6.4 %), the numerical simulations for the back face underestimate the damage, with an error of 17.7 %.

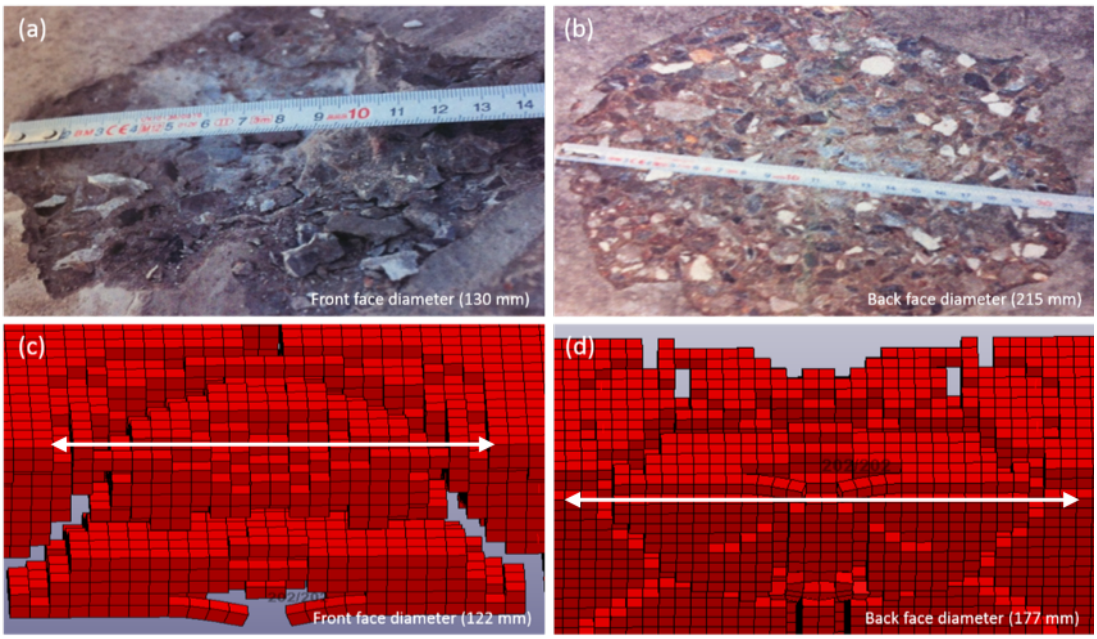

Figure 7.8: Damage caused by the detonation of 15 g of C4: (a) experimental: front face, (c) numerical: front face, (b) experimental: back face and (d) numerical: back face.

The case of the 25 g of C4 explosion, see Figure 7.9, reaches the threshold of the total perforation. Comparison between experimental and numerical results shows that the analysis predicts the damage in the front and at the back face of the slab with errors of 6.5 and 13.4 %, respectively. Evidence of total perforation can be observed in Figure 7.10 as well, which represents the case of the detonation under 50 g of C4. The numerical result of the damage in the front side is predicted with an error of 7 % while the error obtained at the back is slightly higher (12.4 %), but again is considered to be acceptable by the author.

Finally, the slab under the detonation of 75 g of C4 (Figure 7.11) shows a high consistency between the numerical damage and the experimental. In both detonations the presence of total perforation as well as the development of a greater diameter of damage, compared with the previous cases, is evident. In the front face of the slab, the predicted damage is close to the experimental with a given error of 0.5 %. This result

has the best performance among all the numerical models. At the same time, at the back, the numerical prediction of the spall damage is the same with the spall damage obtained by the 50 g, leading to an underestimated spall damage (error of 17.5 %). One possible explanation for the error level could be the occurrence of the "venting" phenomenon. More precisely, the numerical formation of the hole (under 25, 50 and 75 g of C4) results in the loss of the detonation energy. Thus, the numerical damage at the back face is not increasing, as expected, even though the amount of the explosive increases. Overall, the numerical predictions under the detonation of 75 g of explosive exhibit the second best correlation after the case of 10 g of C4.

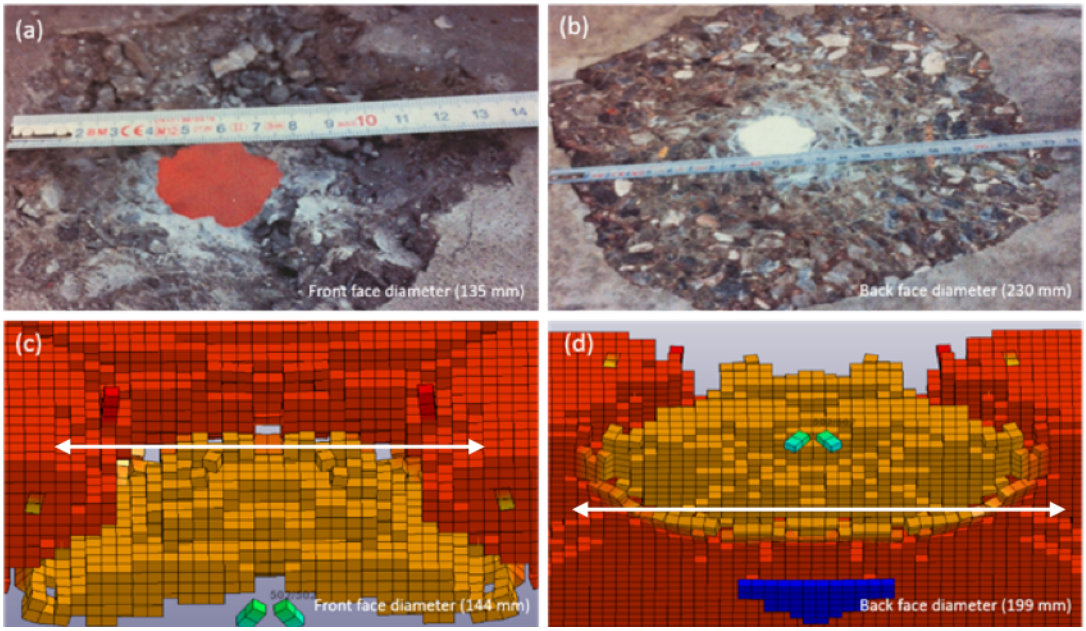

Figure 7.9: Damage caused by the detonation of 25 g of C4: (a) experimental: front face, (c) numerical: front face, (b) experimental: back face and (d) numerical: back face.

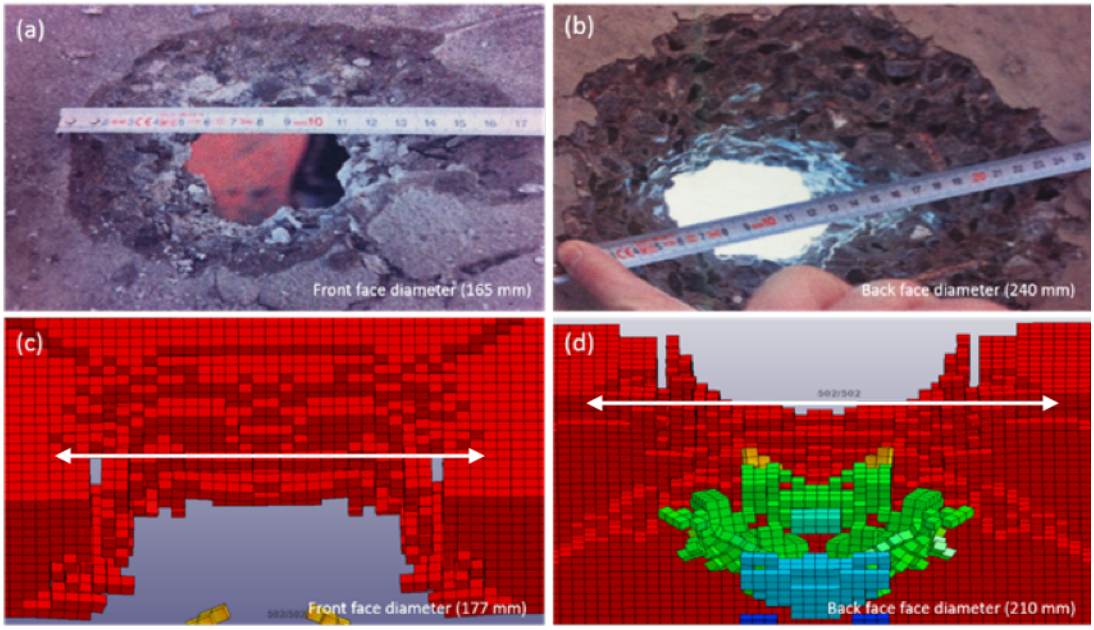

Figure 7.10: Damage caused by the detonation of 50 g of C4: (a) experimental: front face, (c) numerical: front face, (b) experimental: back face and (d) numerical: back face.

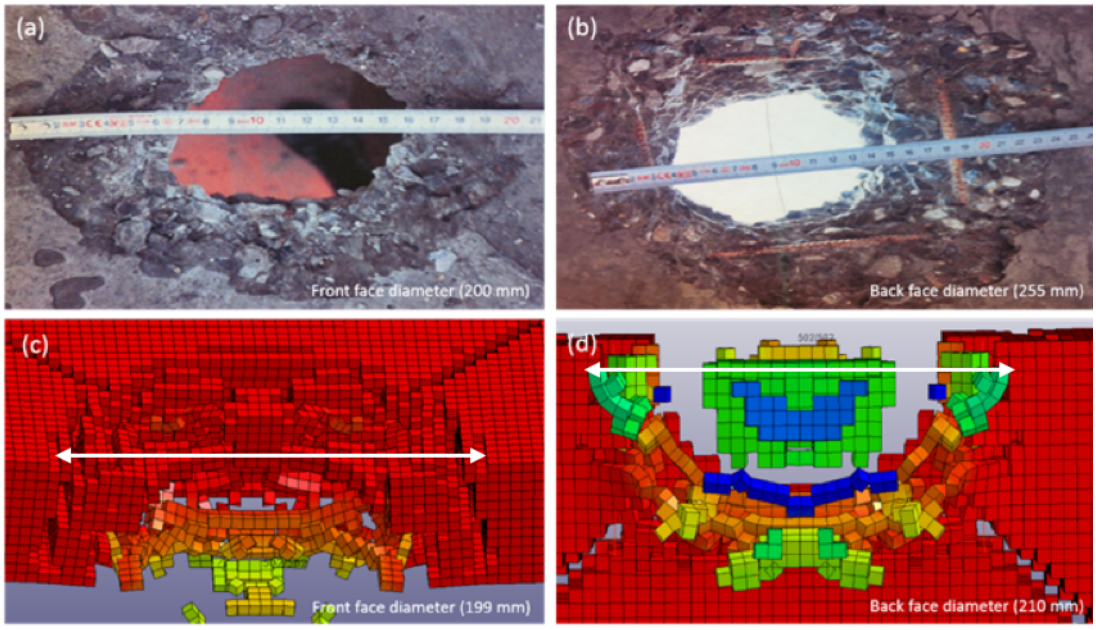

Figure 7.11: Damage caused by the detonation of 75 g of C4: (a) experimental: front face, (c) numerical: front face, (b) experimental: back face and (d) numerical: back face.

The crack pattern (numerical) is also analysed. In Figure 7.12, we can observe the cracking patterns in the front face of all the tested RC slabs. As the amount of C4

increases, diagonal cracks start from the centre of the specimens and expand to the corners. These cracks follow the yield lines (highly stressed areas) of a simply supported two-way slab. Under 10 g, the cracks are initiated around the crater. When the explosive is increased to 15 g the first circular cracks become evident, showing that the slab undertakes the load and deforms in a flexible manner. The progression of those into clear diagonal cracks, a fact that indicates the failure of the structural member, is present in the case of the 25 and 75 g of C4 where the slab is completely perforated. The cracks are approximately 11 mm deep and this is measured from the deleted elements along the diagonal line. Hence, when the mass of explosive increases above 15 g, the cracks are propagating from the detonation area to the corner of the slab. Overall, a reasonable numerical prediction is achieved, given that the RC slabs are simply supported. The only exception is the detonation of 50 g, in which, the diagonal cracks do not expand as far as the corner. This behaviour can be explained due to the fact that the 50 g of C4 are the "venting" balance between the 25 and 75 g of C4.

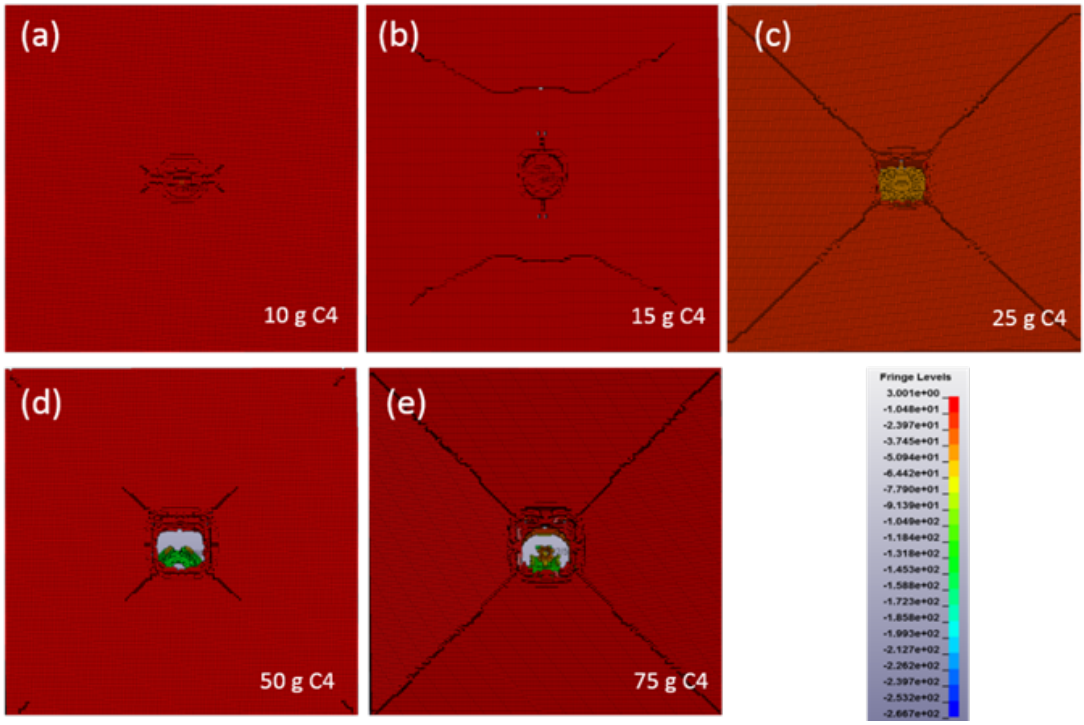

Figure 7.12: Damage in the front face of the tested slabs: (a) 10 g C4, (b) 15 g C4, (c) 25 g C4, (d) 50 g C4 and (e) 75 g C4.

The crack pattern along with the damage at the back face of all the tested slabs is shown in Figure 7.13. The incident wave, as a compressive load, attacks the front face of each slab. At the same time and due to contact conditions, the compressive wave is reflected directly on the opposite side. Thus, the reflected wave, that acts as a tensile load causes a bending failure at the back face of the slabs due to the lower tensile strength of concrete. It is also noted that when the amount of the explosive is increased, the slabs moved from bending failure to punching shear failure. More precisely, since the diameter of the hole at the front is smaller than the diameter at the back face, the concentrated forces from contact explosion induce a cone shaped perforation through the thickness of the slabs (shear effect). In addition, 11 mm deep diagonal cracks can be observed, along with the formation of short radial cracks around the impacted area that are increasing in number as the amount of the explosive increases.

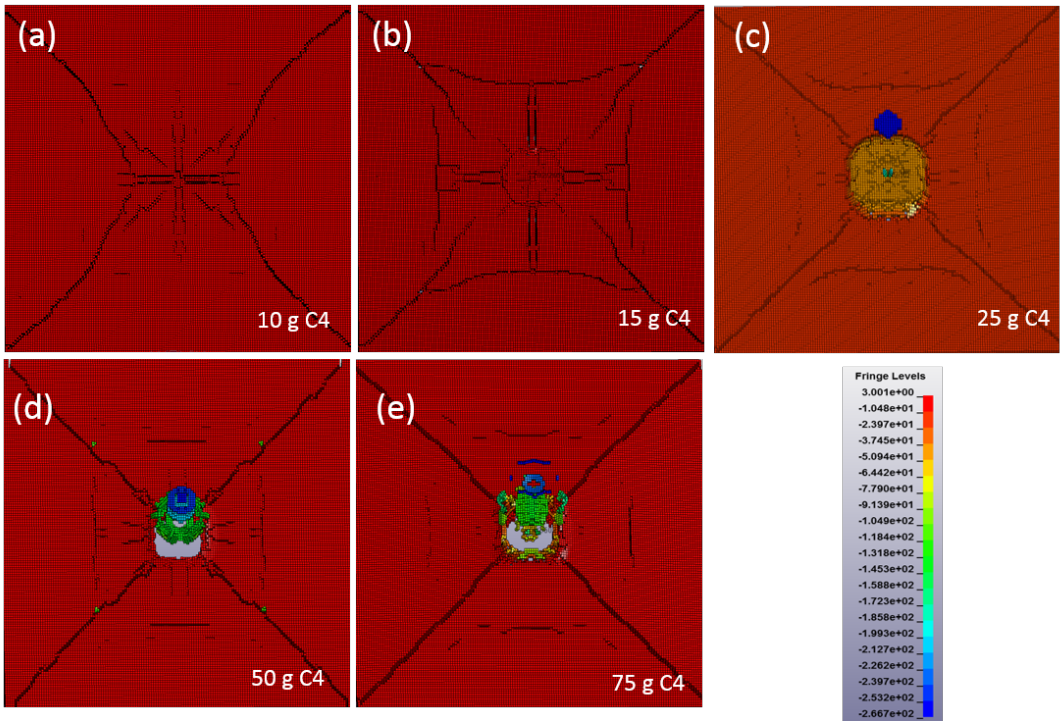

Figure 7.13: Damage at the back face of the tested slabs: (a) 10 g C4, (b) 15 g C4, (c) 25 g C4, (d) 50 g C4 and (e) 75 g C4.

From the discussion above, regarding the validation of the numerical model, the author will explore the pressures and impulses acting on the surface of RC structures, the conservation of energy as well as the response of the reinforced concrete slab as the distance from the impacted area increases.

7.2.1 Pressure and impulse on the surface of the concrete slabs

The pressures acting on the surface of the concrete slabs can be seen in Figure 7.14. Each pressure curve is the result of the average of all the individual pressure histories of the elements on the surface of the reinforced concrete slab. For all the tests, the time of arrival of the blast wave is zero, since the distance between the target and the explosive source (stand-off) is equal to zero as well. From this time, the incident pressure is evident and then increases rapidly to the peak pressure, which is the result

of the interaction both of the incident and the reflecting waves. The incident pressure wave hits the structure and is reflected directly to the opposite direction. As a result, the superposition of the two waves leads to the final peak pressure, which increases with the increase of the amount of the explosive. Two peaks of each pressure curve can be identified in the cases of 75, 50 and 25 g while in the cases of 15 and 10 g only the second peak can be clearly identified. Thus, in the last two amounts of C4, the change in the slope of the curves helped in order to estimate the first peak. Based on that, another outcome is also the fact that according to the experimental and numerical results of the damage, the 25 g of C4 apart from being the threshold of the total perforation of the concrete slabs, is also the amount of explosive whereafter the incident and peak pressures are clearly identified in the graph. A possible explanation is that in the cases of 15 and 10 g of C4, where the hole is not formed, the reflected pressure wave is a consequence of the incident pressure acting on intact concrete, while in the rest cases where the hole is evident, there is no material for direct reflection. The reflection, only takes place later.

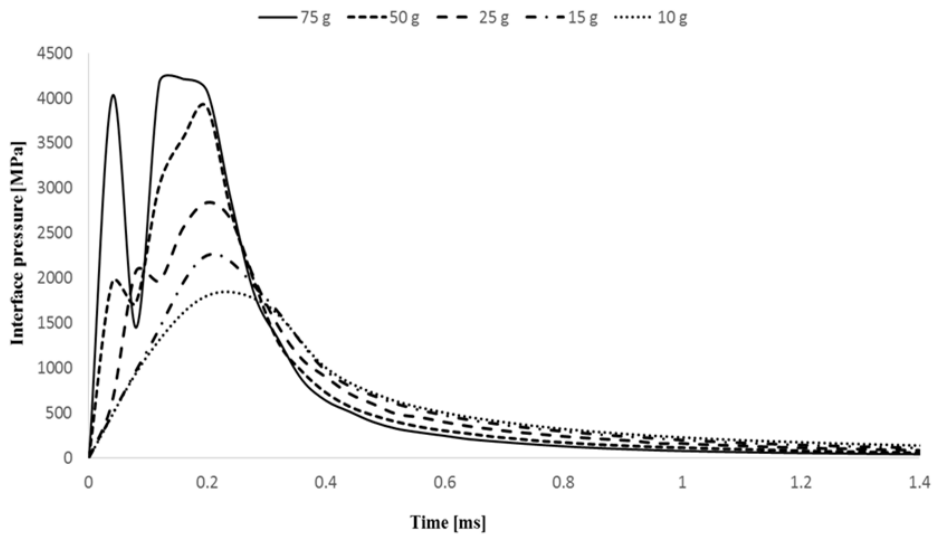

Figure 7.14: Pressure history for the different tests.

The incident and maximum peak pressure values are shown in Table 7.3. Under the effect of 75 and 50 g, the incident pressures are 4020 and 1940 MPa, respectively, happening at the same time (0.04 ms), while the incident pressures of the remaining tests (2070, 1420 and 922 MPa) are observed after twice that time. A possible explanation is that in the cases of detonation under 75 and 50 g of C4, the energy that is released and consequently the incident pressure is higher compared to other cases, hence reaches the target sooner. In terms of the peak pressures, as shown in Table 7.3, the obtained values, indicate that the increase in the mass of the explosive leads to an increase of the peak pressures. The aforementioned pressures take place at the same time (0.20 ms) except for the peak pressure produced by the 75 g of C4 which takes place slightly earlier (0.16 ms). Thus, it can be said that the increase of the mass of the explosive is not only responsible for affecting the magnitude of the peak pressure but also to speed up the time of the peak pressure. It is also evident from Figure 7.14 that the descending branch of the blast wave pressures exhibits a steeper slope as the mass of the explosive increases, until it returns to the conditions of pressures approximately equal to 0. The latter happens because, as the damage (hole) is progressing with the increase of C4 mass, the blast reflected pressure is free to attenuate without any barriers from concrete material that has eventually lost its strength.

Table 7.3: Incident and peak pressures maximum values during time.

C4 mass [g]	Incident Pressure [MPa]	Incident time [ms]	Peak pressure [MPa]	Peak time [ms]
75	4020	0.04	4210	0.16
50	1940	0.04	3900	0.20
25	2070	0.08	2830	0.20
15	1420	0.08	2250	0.20
10	922	0.08	1800	0.20

In addition, Figure 7.15 presents the variation of peak pressure as a function of the mass of explosive, showing that there is a logarithmic relationship between the mass and the peak pressure that causes the damage on the structure (within the tested range of masses).

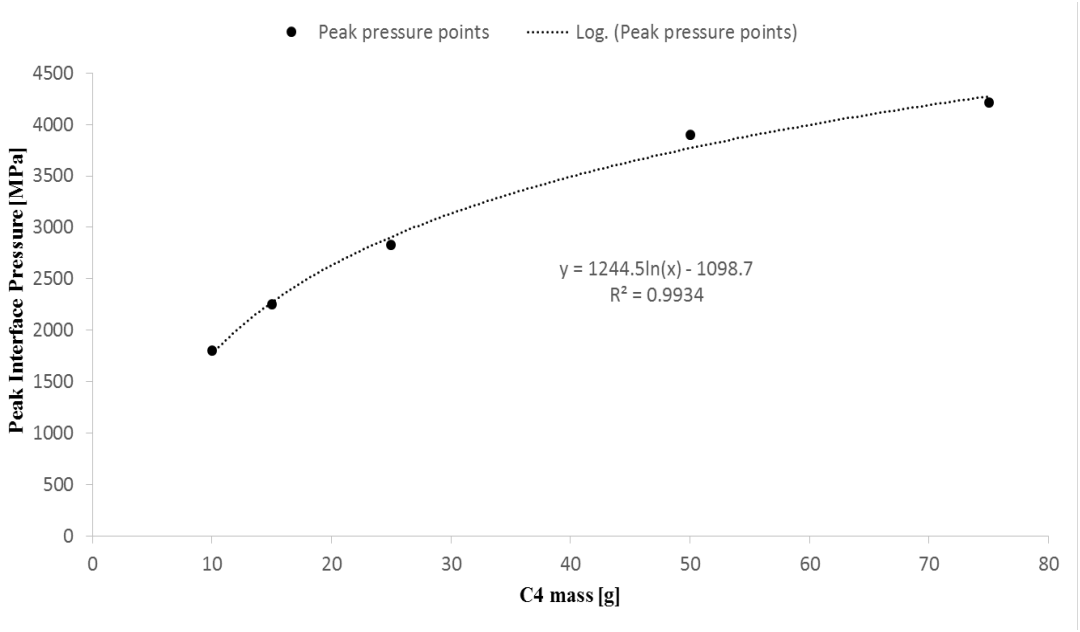

Figure 7.15: Variation of peak pressure as a function of the mass of explosive.

Furthermore, the impulses (see Figure 7.16) represent the area below the normal incident forces history that act on the structural surface due to the presence of the blast

wave force. Thus, for each test, the impulse is the resulting curve obtained both from the superposition of all the incident forces history acting on the elements that belong to the front face of the RC slab and the integration of this single curve (final incident force history curve) over time. Consequently, the curves shown on Figure 7.16 are important, since it is not only significant to mention the peak values of the incident pressures but also to mention how these loads are performing during time (area below the incidence force history curve). In other words, if in two different cases the incident pressures are equal in terms of magnitude but the first acts for a longer period, the impulse obtained from the former case is greater than the impulse obtained from the latter. Hence, in the first case the blast incident force is more severe for the structure as it acts for a longer period.

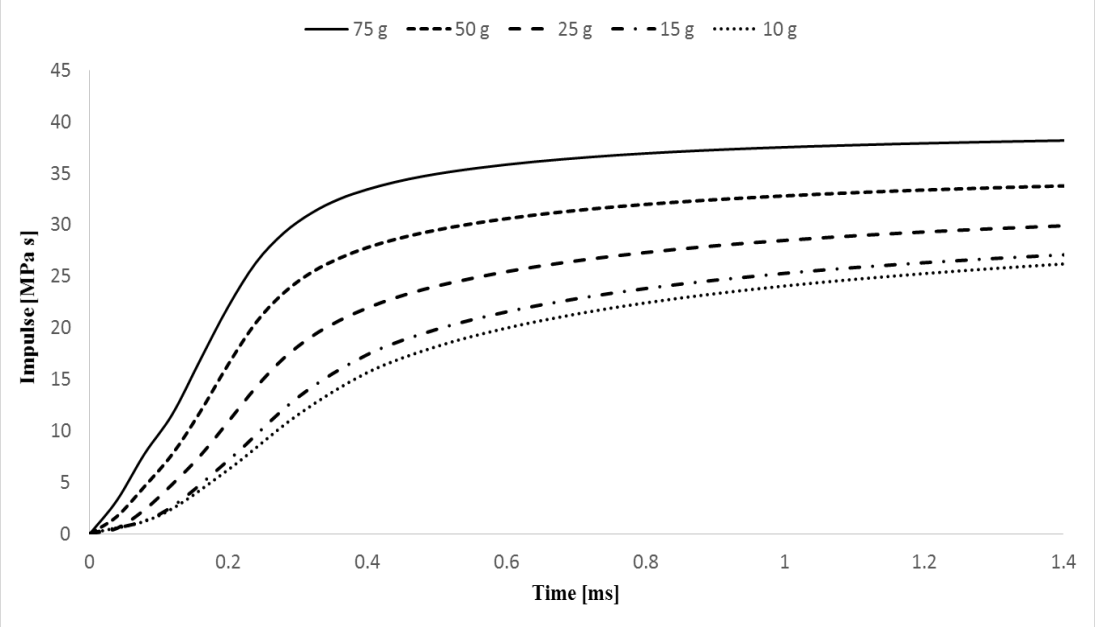

Figure 7.16: Impulse history for the different tests.

The maximum obtained impulses shown in Table 7.4 range from 28.9 to 39.1 MPa s and prove that there is a linear increase in the impulse value (within the tested range

of masses) as the explosive amount increases (see Figure 7.17). Observation of the pressures evolution, see Figure 7.14, also shows that impulses are affected only by the amount of the explosive and not from the duration of impact, since peak incident pressures obtained attenuate rapidly.

Table 7.4: Maximum impulse for the different tests.

C4 mass [g]	Maximum Impulse [Mpa s]
75	39.1
50	34.9
25	31.8
15	29.4
10	28.9

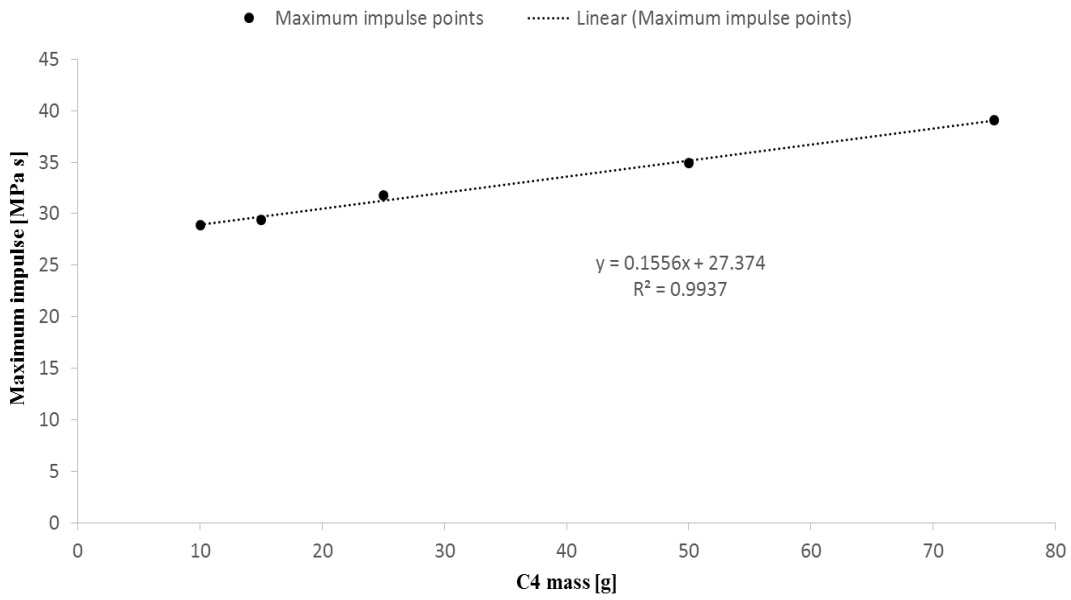

Figure 7.17: Variation of impulse as a function of the mass of explosive.

7.2.2 Energy analysis

Figure 7.18 to Figure 7.22 show the variation of the kinetic, internal, total and hourglass energy of the system for the models developed. A similar evolution of energy is observed among the different tests. The total energy is the sum of the hourglass, internal and kinetic energy. Moreover, the system is not conservative due to the heat loss during the detonation.

The internal and kinetic energies are the physical energies of the system of the slab that are respectively stored and possessed due to the change of the kinematic condition of the system. On the other hand, the hourglass energy is the numerical wasted energy of the system due to the work of the artificial forces that are applied to the elements in order to help them for overcoming the nonphysical deformation modes (hourglass modes).

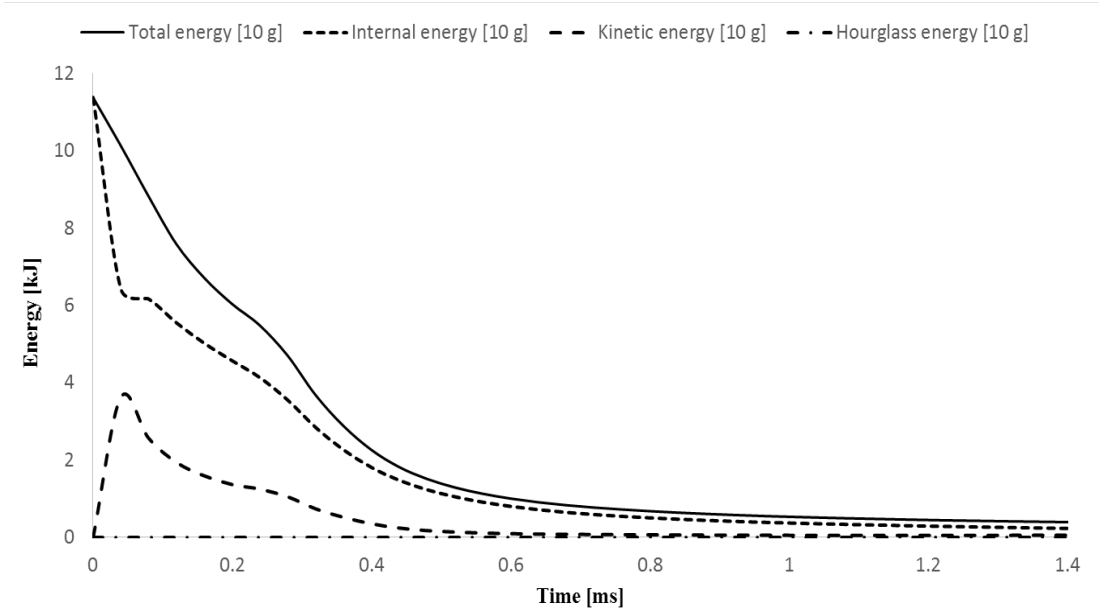

Figure 7.18: Energy balance for 10 g of C4.

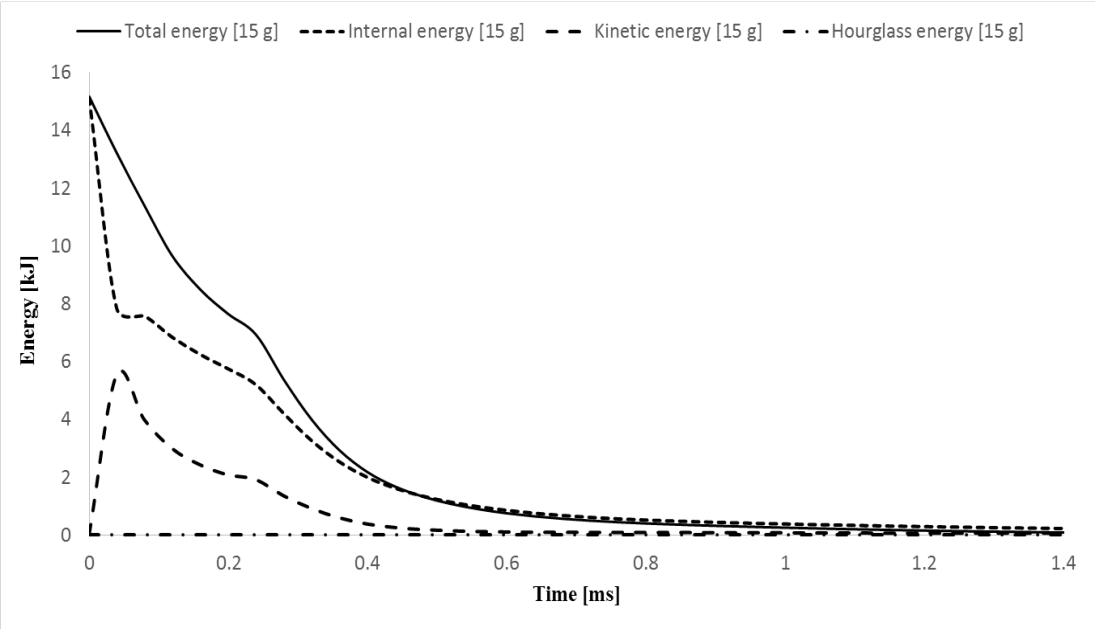

Figure 7.19: Energy balance for 15 g of C4.

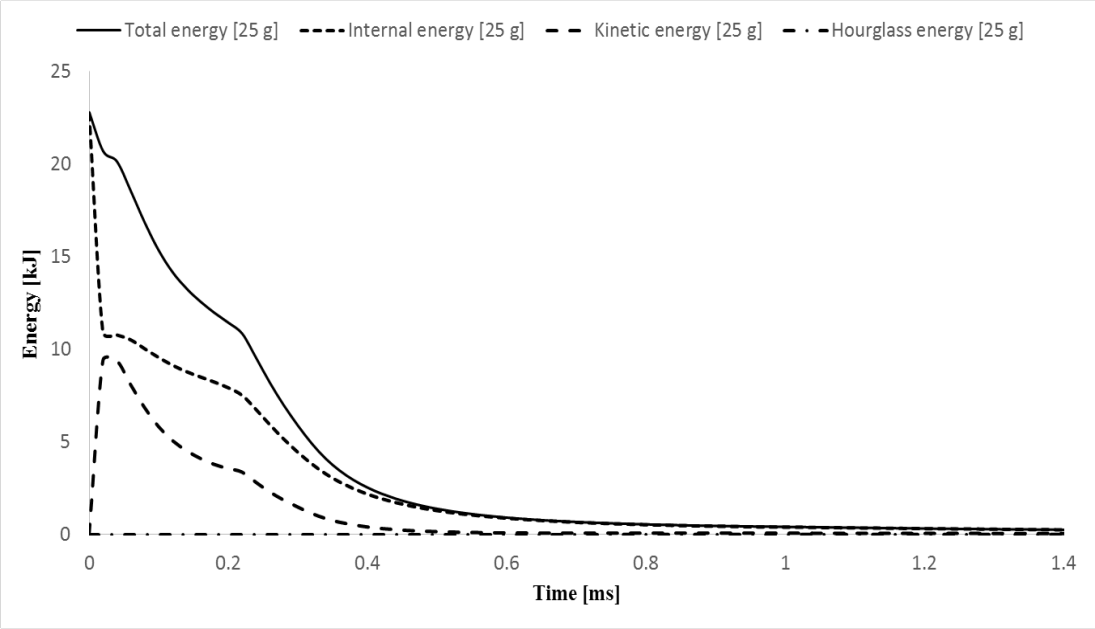

Figure 7.20: Energy balance for 25 g of C4.

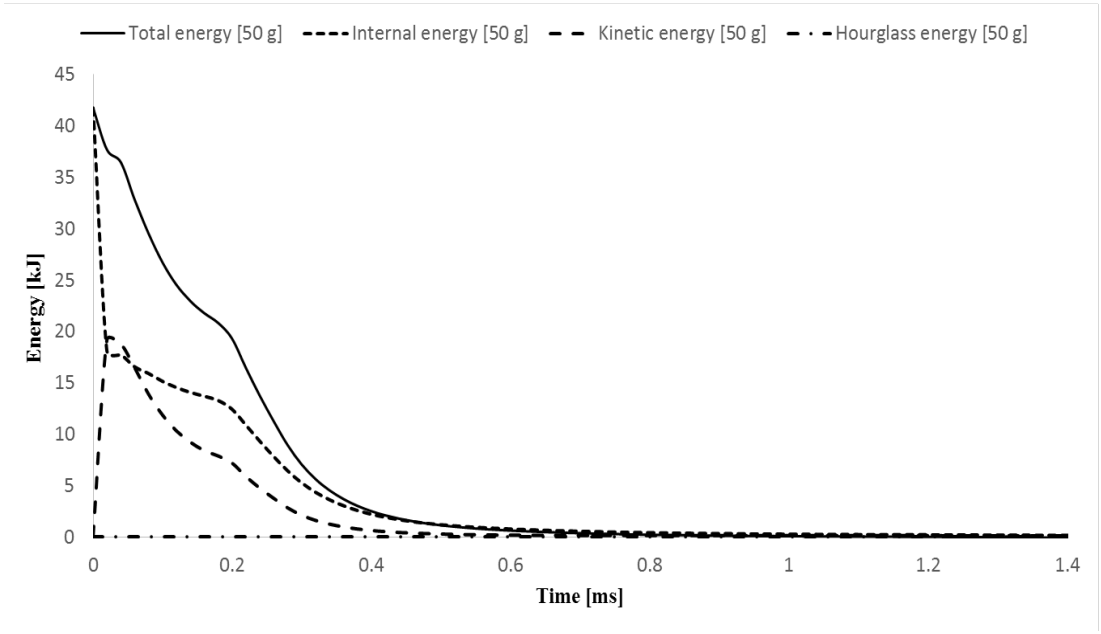

Figure 7.21: Energy balance for 50 g of C4.

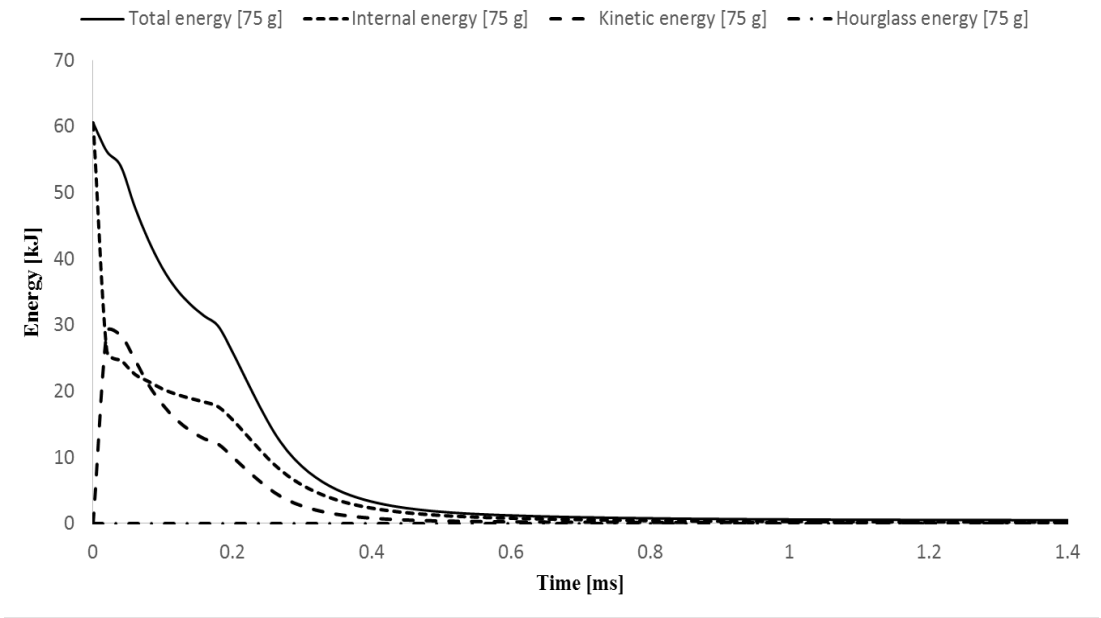

Figure 7.22: Energy balance for 75 g of C4.

Hourglass numerical energy

It is desirable to obtain a ratio ideally lower than 10 % [3] between hourglass and total energy. The hourglass energy is a very important check of the simulation outcomes, since it shows the adequacy and quality of the discretisation. This has been achieved, since the hourglass energy ranges from 5.13×10^{-3} to 1.52×10^{-2} kJ and increases with the increase of the mass of explosive, since the deformation becomes even greater and the elements are more vulnerable to hourglassing. Thus, to illustrate how small this ratio is (0.03 – 0.05 %), a separate hourglass energy ratio graph is created for each mass of C4 (see Figure 7.23). This graph presents the ratio between the hourglass energy and the total energy (hourglass energy history normalised by the maximum total energy of each case) in respect to the time.

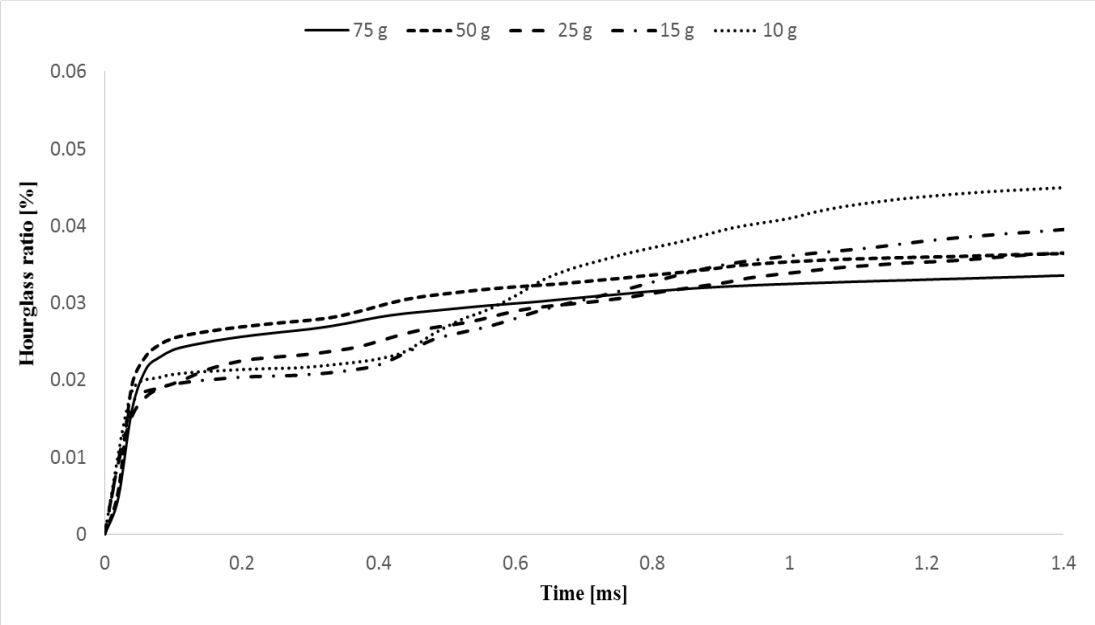

Figure 7.23: Hourglass energy ratio for the different tests.

Kinetic, internal and total physical energy

The kinetic energy of the whole system (see Figure 7.18 to Figure 7.22) shows a similar trend evolution for all the tests. The curves start from zero kinetic energy (before detonation) and rapidly reach the maximum value after detonation. At the detonation time, the chemical energy that is released is responsible for the applied pressure that results in the motion of the reinforced concrete slabs. Then, the kinetic energy quickly attenuates, since the chemical energy is dissipated. This energy is the result of the blast detonation energy and as expected, the greater the amount of the explosive is, the higher peak of kinetic energy is achieved (see Figure 7.24). According to the graph in Figure 7.25, there is an approximately linear relationship between the mass of explosive and the maximum kinetic energy.

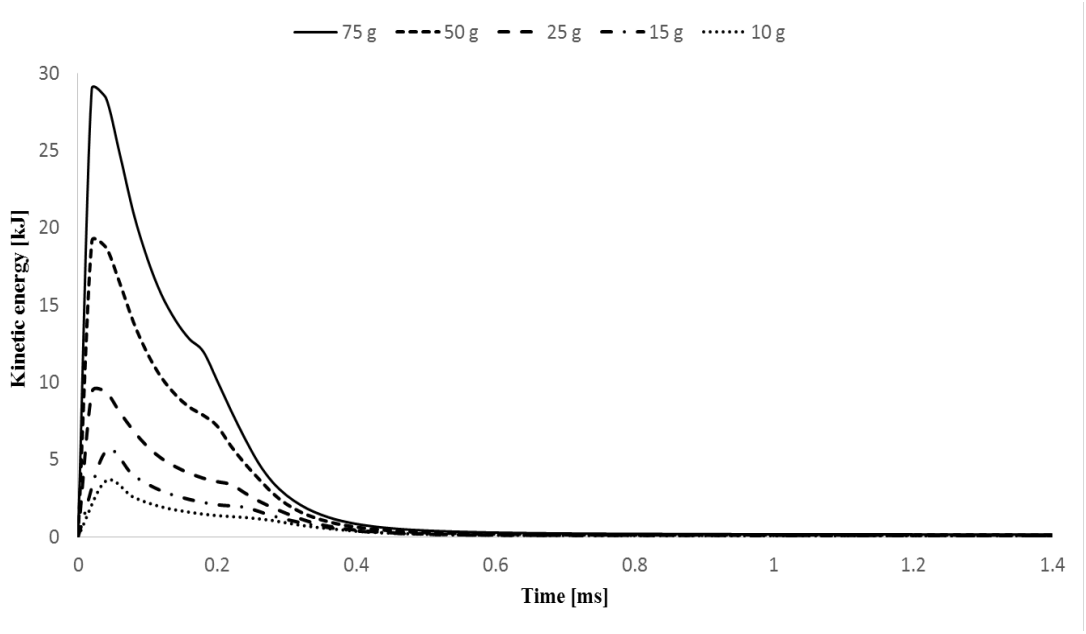

Figure 7.24: Kinetic energy history for the different tests.

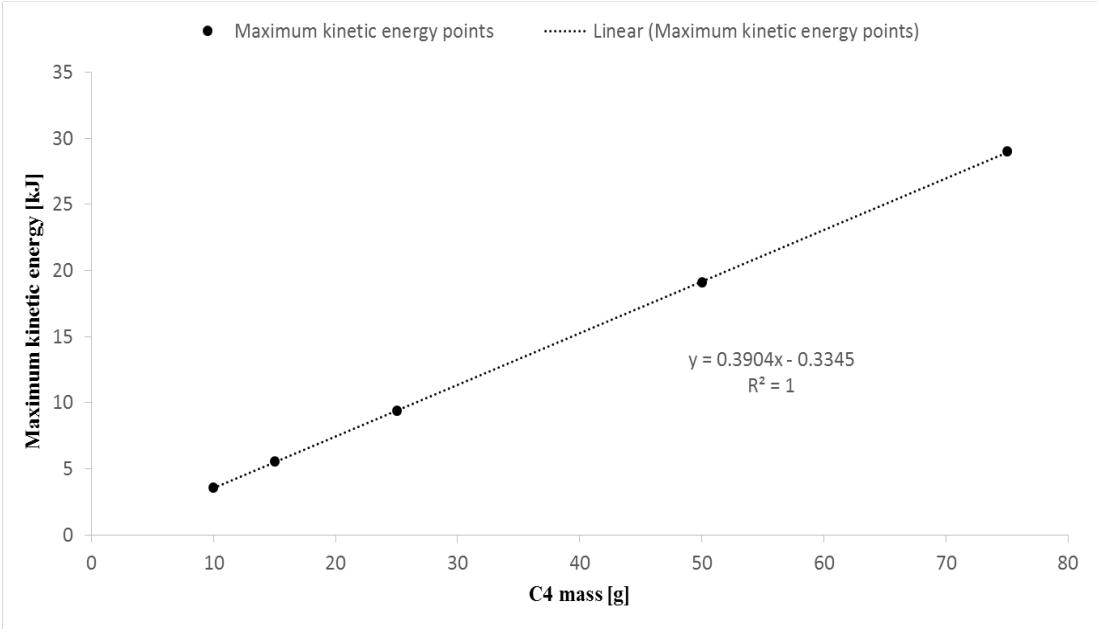

Figure 7.25: Variation of maximum kinetic energy as a function of the mass of explosive.

Furthermore, the internal energy of the system assumes its maximum values when the kinetic energy is at the lowest level. This is clearly shown in the graphs of Figure 7.18 to Figure 7.22. Prior to the detonation, when no kinetic energy is present on the system, the chemical energy of the explosive is stored in the form of internal energy. Then, when the detonation occurs, the internal stored energy is released and gradually starts to decrease since it is transformed to the kinetic energy of the system. In the end, the internal energy continues to attenuate because the system is not conservative and the energy is dissipated.

Table 7.5 summarises the peak values of the kinetic, internal, total energies and the hourglass ratio.

Table 7.5: Peak values of the energies (kinetic, internal, total) and hourglass ratio along with the correspondent time.

C4 [g]	Kinetic Energy [kJ]	Time [ms]	Internal Energy [kJ]	Time [ms]
10	3.61	0.04	11.40	0
15	5.54	0.04	15.20	0
25	9.39	0.02	22.80	0
50	19.10	0.02	41.70	0
75	29.00	0.02	60.60	0
C4 [g]	**Hourglass ratio [%]**	**Time [ms]**	**Total energy [kJ]**	**Time [ms]**
10	0.05	1.40	11.40	0
15	0.04	1.40	15.20	0
25	0.04	1.40	22.80	0
50	0.04	1.40	41.70	0
75	0.03	1.40	60.60	0

7.2.3 Kinematics of the reinforced concrete slab

The kinematic response of the RC slabs, as the mass of explosive increases, is assessed in terms of displacements and velocities of three nodes (A, B and C) at the front face of the tested structural members (see Figure 7.26). Node A (location A) is next to the hole obtained after the detonation. Thus, it is located just next to the damage caused by the 75 g of C4, since that element does not fail in any of the five tests. Node B is located in the middle of the distance between node A and the edge of the rigid support that is placed underneath the RC slab. Node C is located at the end of the reinforced concrete slab.

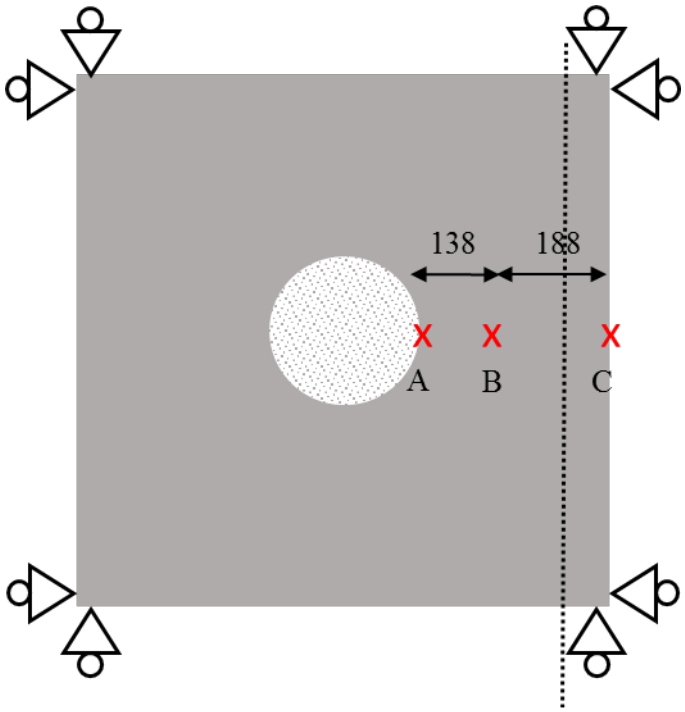

Figure 7.26: Location of nodes A, B and C for the kinematic analysis (top view, in mm).

Displacements for nodes A, B, and C

It is observed from the graph of the vertical displacements of node A (see Figure 7.27) that the increase of the mass of explosive leads to an increase of the maximum displacement achieved during the first stage of the dynamic oscillations of the RC concrete slabs.

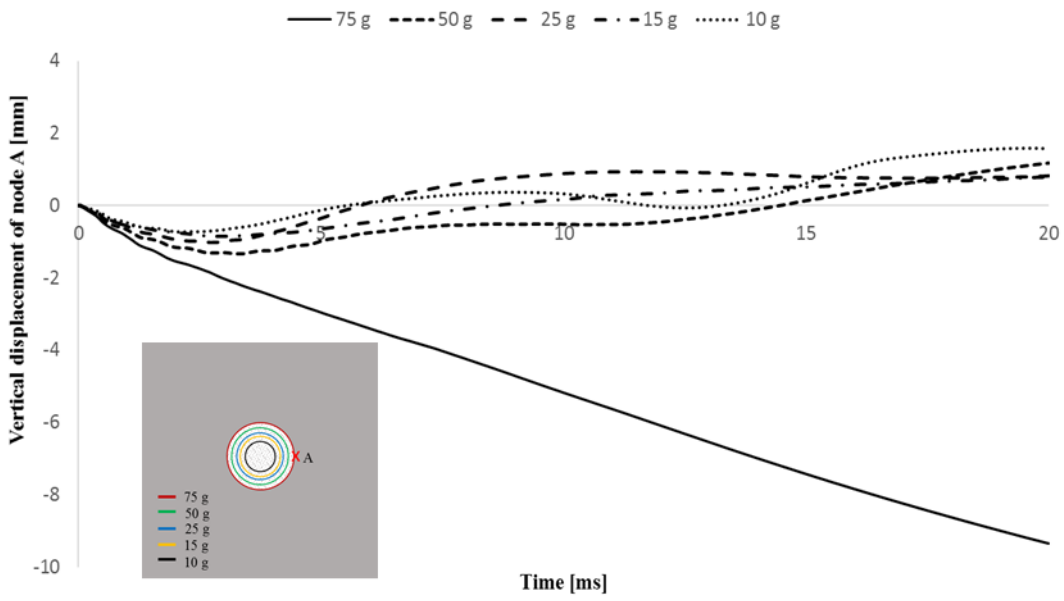

Figure 7.27: Displacement history of node A for the different tests.

It can be seen that point A at time 0 is at rest for all the masses of C4. When the detonation takes place, node A starts moving towards negative values of the vertical axis. As expected, the larger the mass of the explosive, the greater the displacement. The displacements reach their first maximum value at approximately the same time (2.9 ms) for the 50, 25, 15 and 10 g of C4. In the case of 75 g of C4 it is observed that node A keeps moving downwards during the simulation time. The former can be explained, if we realise that point A is placed exactly next to the damaged location caused by the 75 g of C4, thus larger displacements are expected and a different trend on the displacement response. It can be concluded also that not only the amount of the explosive, but also the distance away from the damaged zone, are responsible for the displacements of the nodes of the RC slab.

All the slabs, under the compressive detonation load caused by the several amounts of C4 (except for the 75 g of C4), are moving downwards (negative values of the vertical axis), oscillate and finally are moving upwards (positive values). This trend can be explained if it is realised that the amount of energy that is released under the detonation of 75 g of C4 is higher compared to the other cases. Hence, the node under such a strong shock wave is always compressed and not free to oscillate.

In Figure 7.28, the displacement history of node B is presented. It is observed that the trend of the response is similar to the response obtained by node A. It can be seen that the maximum displacements of node A, in the beginning of the oscillations, are around the double of the maximum displacements of node B, since node A is located closer to the damage area. Thus, when the distance from the damaged area increases (node B etc.) the displacements decrease as well.

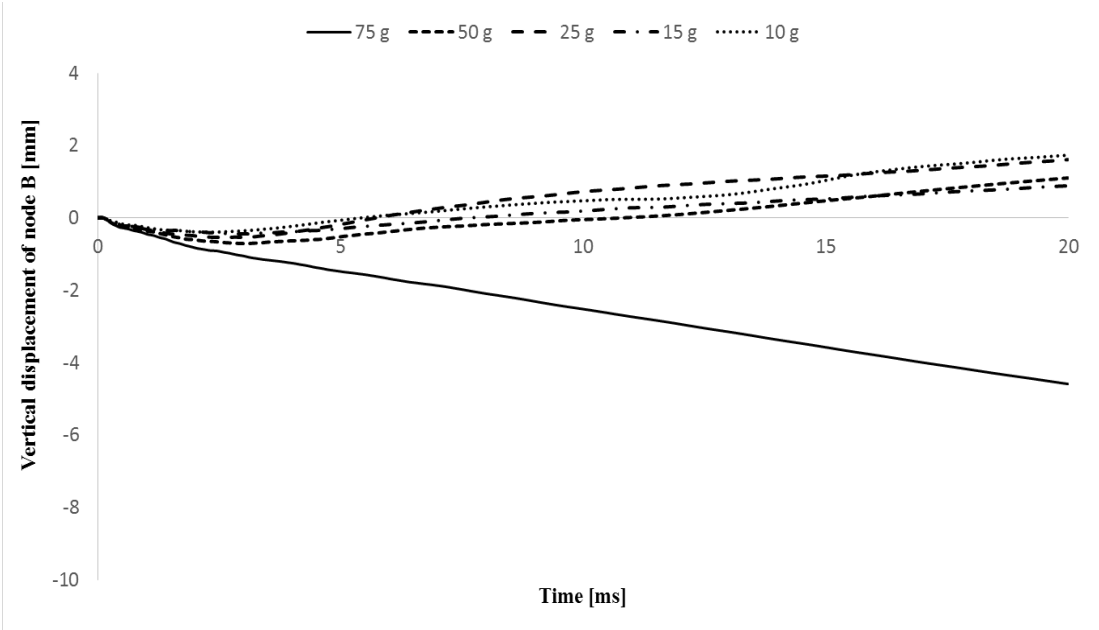

Figure 7.28: Displacement history of node B for the different tests.

The displacements of node C (rear end of concrete slabs) are presented in Figure 7.29. Point C is moving in the opposite direction to the rest of the slab, a fact that explains the flexural and rigid body response of the slab. The first peaks of the oscillations that are observed at time (1 ms) show the effect of the amount of the explosive in the increased flexural displacement response. Moreover, the obtained displacements are smaller (as expected), compared to the displacements of nodes A and B that are located closer to the damaged area.

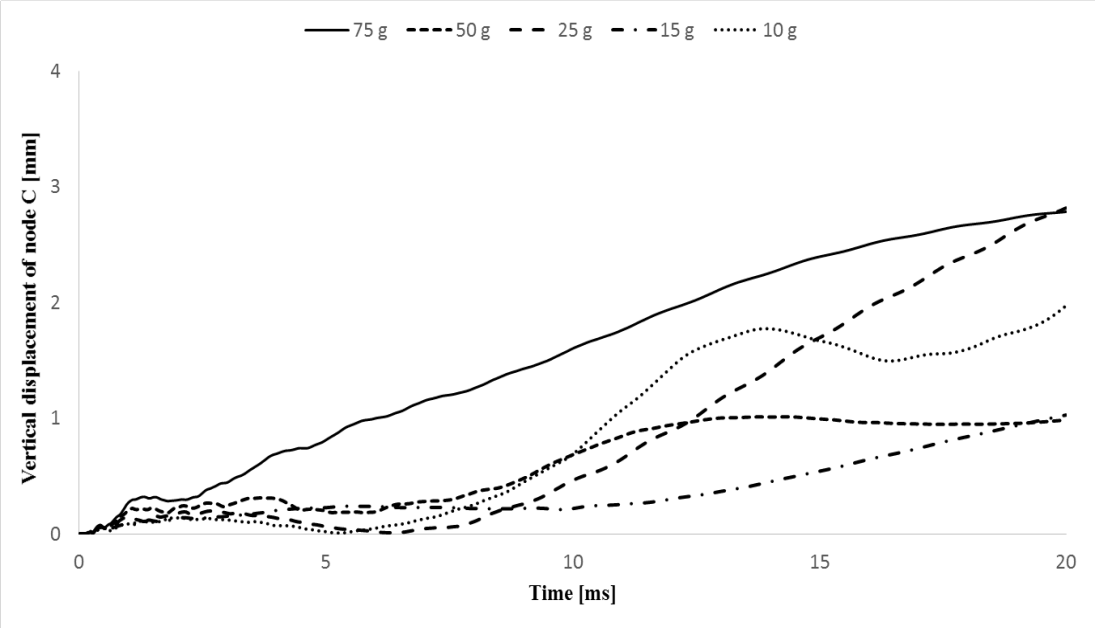

Figure 7.29: Displacement history of node C for the different tests.

Velocities of nodes A, B and C

The velocities of nodes A, B and C (see Figure 7.30 to Figure 7.32) are calculated numerically as the time derivatives of the displacements. This explains the oscillation (noise) that is evident. After the detonation event, the maximum vertical velocities of node A (motion downwards due to the presence of the compressive load), indicate that the increase of the mass of explosive leads to an increase of the nodal velocities as well

(see Table 7.6). This happens because the increase of the blast energy results in an increase of the kinetic energy of the system, hence the elements are moving faster. An approximately similar trend is observed for the nodal velocities of node B, with the velocities being increased with the increase of the explosive (same reason as before) but in a lower magnitude compared with node A. This can be explained if it is realised that node B is positioned further away from node A that is located next to the damaged location. Thus, as the distance from the damaged area increases, the response in terms of the magnitude of the velocity attenuates. In addition, the maximum velocities obtained from the location of node C, have a positive sign (movement upwards) with the velocities range between (0.86 -1.01 m/s). The latter explains the flexural – rigid body motion of the rear point of the slab, which has an enhanced velocity due to the presence of the undeformable rigid body frame support that is placed underneath.

Table 7.6, summarises the peak initial velocities (V_{max}) of points A, B and C for the different tests.

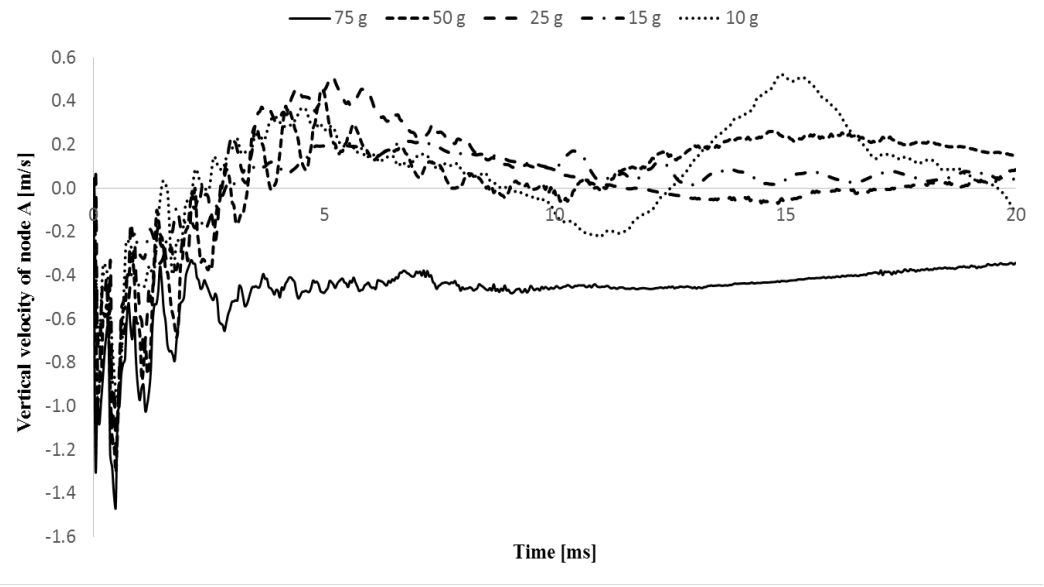

Figure 7.30: Velocity history of node A for the different tests.

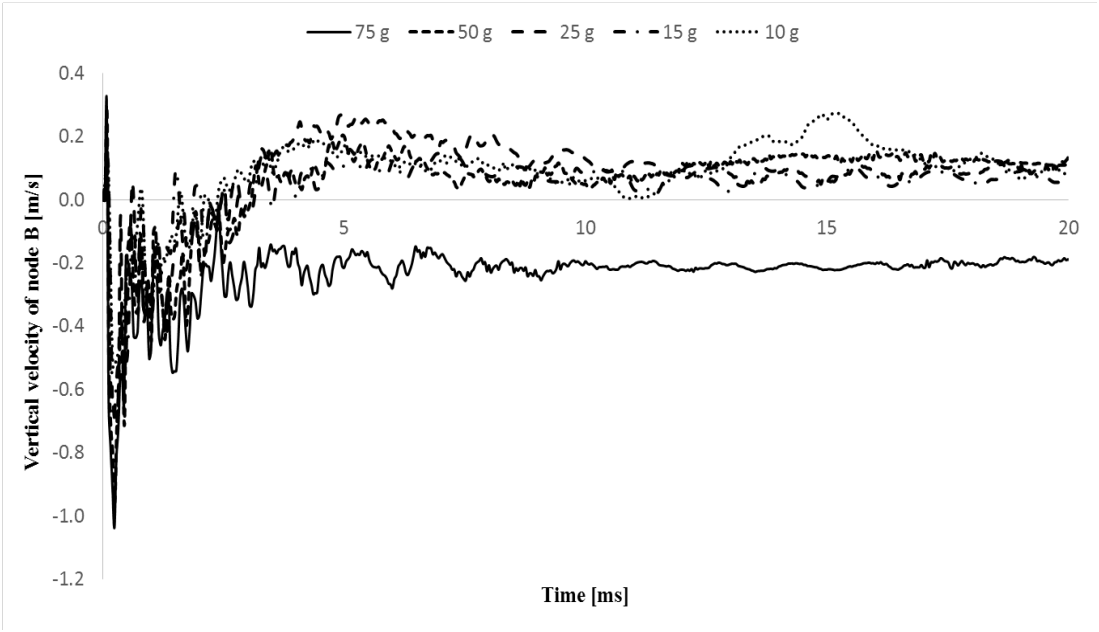

Figure 7.31: Velocity history of node B for the different tests.

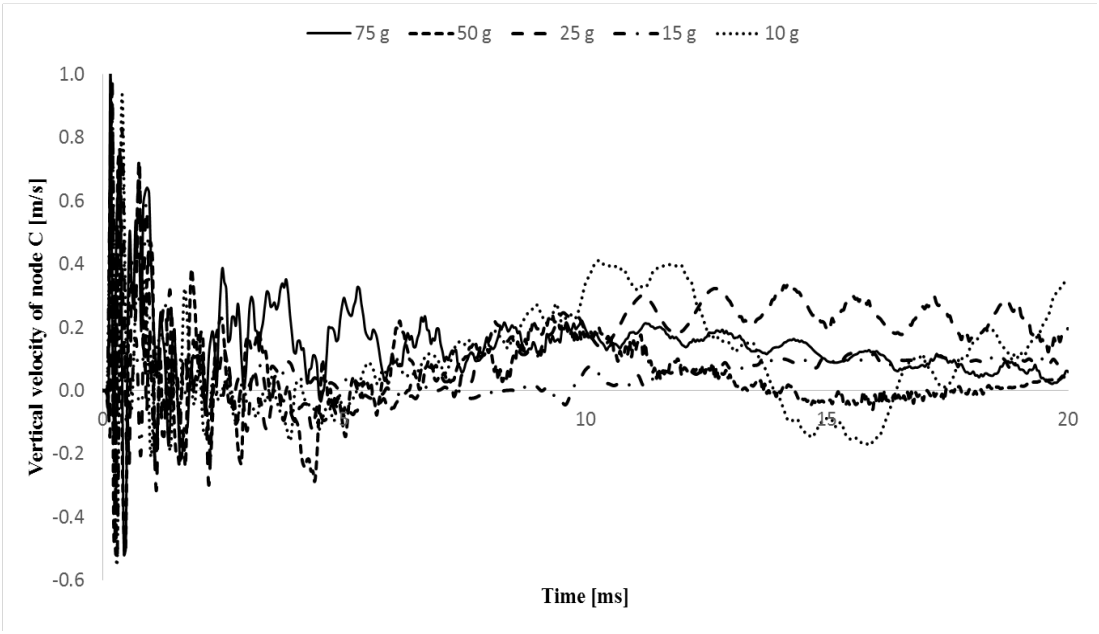

Figure 7.32: Velocity history of node C for the different tests.

Table 7.6: Maximum initial velocities (V_{max}) of nodes A, B and C for the different tests.

C4 mass [g]	V_{max} (node A) [m/s]	V_{max} (node B) [m/s]	V_{max} (node C) [m/s]
75	-1.27	-1.04	1.01
50	-0.98	-0.96	0.63
25	-0.89	-0.72	0.99
15	-0.74	-0.68	0.92
10	-0.71	-0.53	0.86

7.2.4 Rebar behavior analysis

The RC slabs are reinforced with a two layer rebar mesh of 469 MPa yield strength. After the detonation events, the experimental data does not show any damage of the reinforcement. In order to check if the numerical simulations are in accordance with the above results, the von Mises stress history of elements A (horizontal reinforcing

bar of the upper layer) and B (horizontal reinforcing bar of the lower layer) is calculated. These elements are the most stressed elements, located around the damaged area (see Figure 7.33).

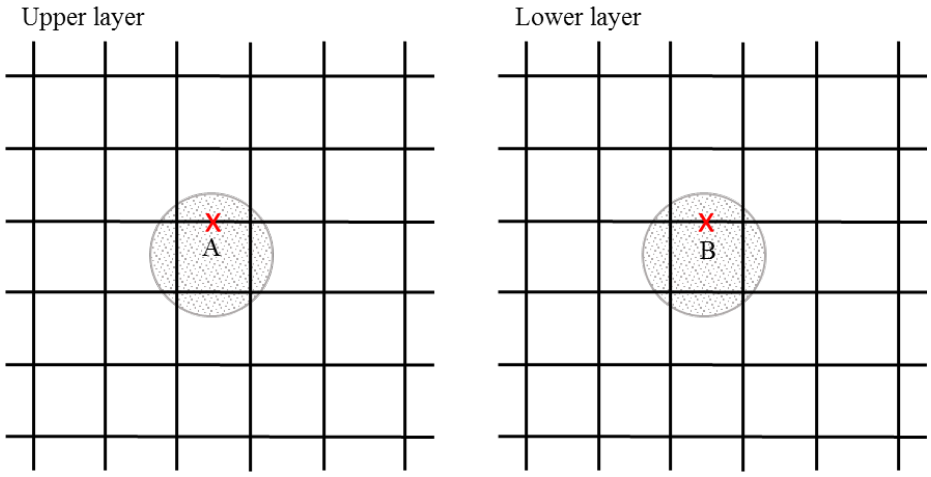

Figure 7.33: Elements A (upper layer) and B (lower layer) of the reinforcing bars (top view).

The obtained von Mises stress is compared with the yield strength of the steel used (469 MPa). Figure 7.34 and Figure 7.35, show that the reinforcing rebars have not yielded, behave elastically and can resist the external load. This outcome is in accordance with the experimental observations. All the stresses are lower than 55 MPa (element A), which is supposed to be the highest von Mises stress achieved among the simulations and is obtained from the detonation of 75 g of C4.

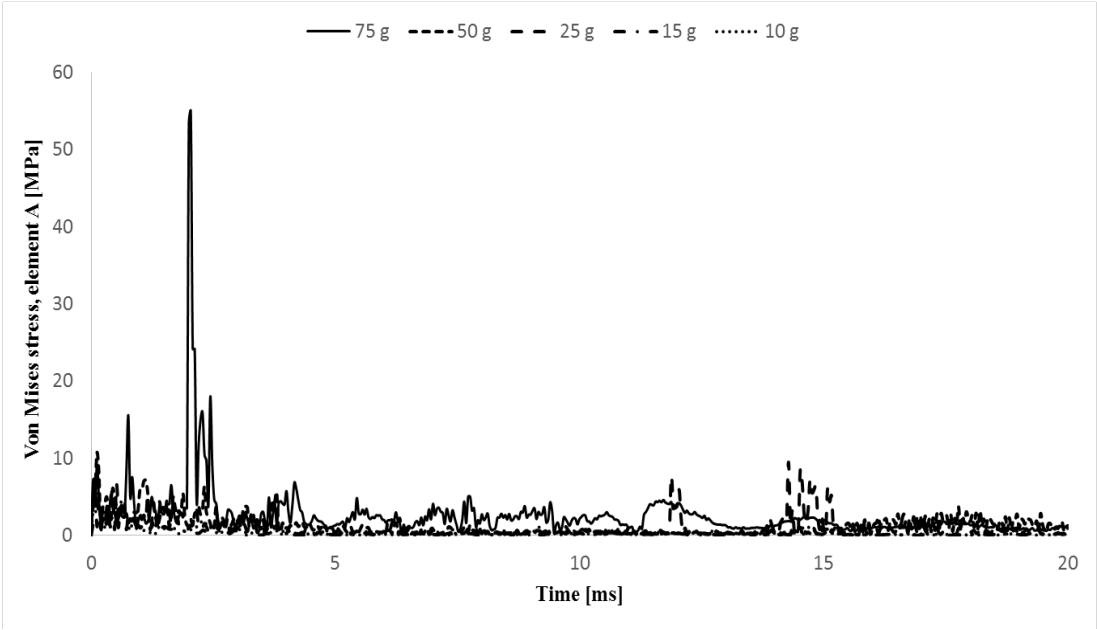

Figure 7.34: Von Mises stress history of element A.

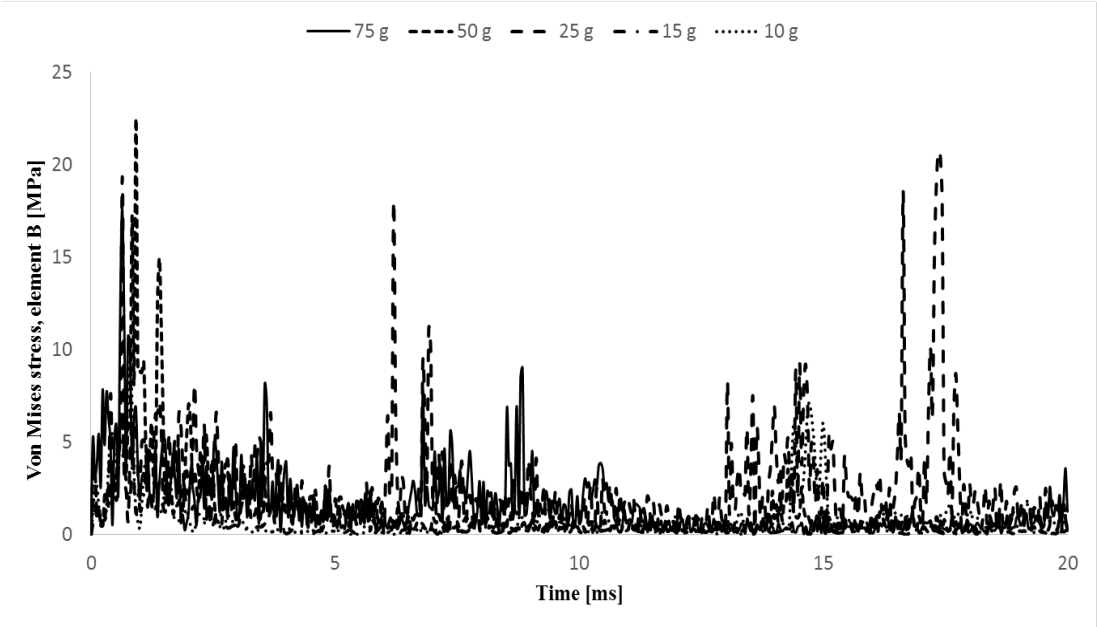

Figure 7.35: Von Mises stress history of element B.

Table 7.7 and Table 7.8, summarise the peak values of the von Mises stress extracted from elements A and B for all the tests. It is obvious from those tables, that the von

Mises stress peaks are not achieved at the same time during the five simulations. Figure 7.36 and Figure 7.37 show the evolution of the reinforcement stresses as the mass of explosive increases. The best possible fit between the von Mises stress of element A and the mass of the charge is the exponential (within the tested range of the masses). Moreover, it is not feasible to find a trend for the evolution of the stress of element B.

Table 7.7: Maximum von Mises stress of element A for the different tests.

C4 Mass [g]	Von Mises stress A [MPa]	Time [ms]
75	55	2
50	11	0.1
25	7.2	0.08
15	3.6	0.6
10	6.7	0.1

Table 7.8: Maximum von Mises stress of element B for the different tests.

C4 Mass [g]	Von Mises stress B [MPa]	Time [ms]
75	18	0.64
50	23	0.92
25	21	17.4
15	6.1	0.9
10	9.3	0.8

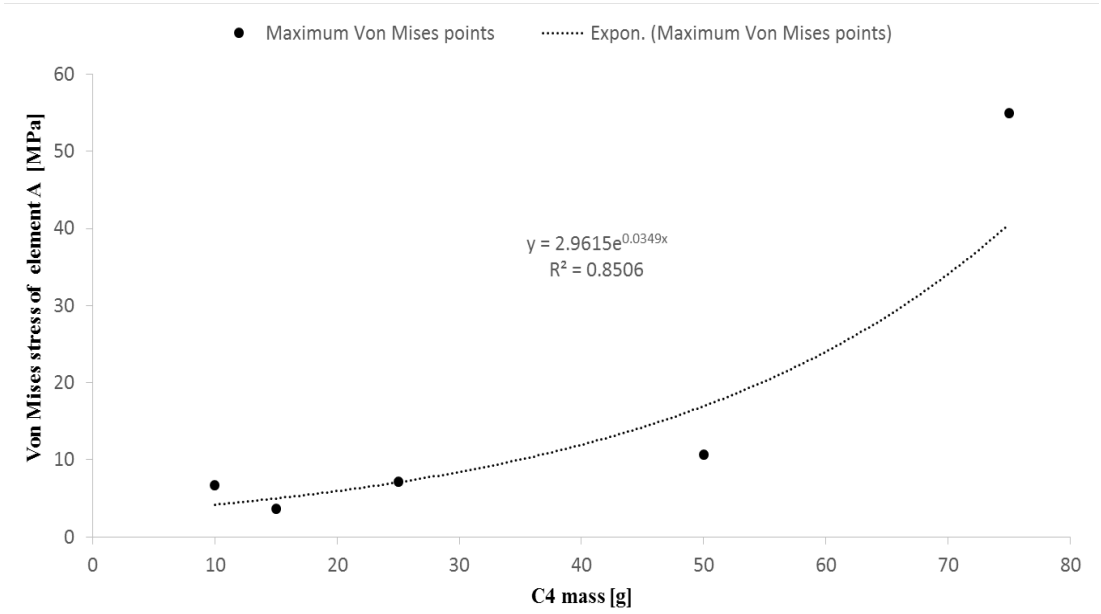

Figure 7.36: Variation of von Mises stress as a function of the mass of explosive (element A).

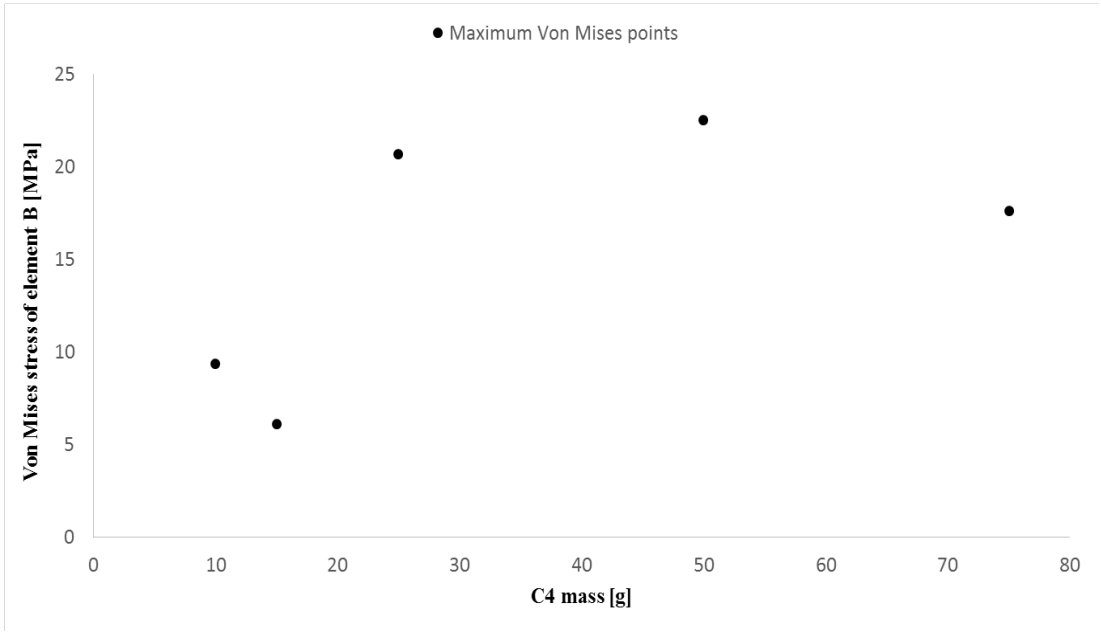

Figure 7.37: Variation of von Mises stress as a function of the mass of explosive (element B).

In addition, comparing the response of elements A and B under the same amount of explosive (see Figure 7.38 to Figure 7.42), it can be observed that in general, element B has higher stresses than element A, expect for the case of 75 g . This can be explained

if it is realised that element B is located on the lower layer of the reinforcing bars, hence it sustains tension while element A sustains compression. Concrete material has lost its strength (at the back side) due to its inability to withstand high in magnitude tensile loads and the reinforcing bars of the lower layer are aiming to resist the failure of concrete, hence are stressed in a greater level than the upper layer.

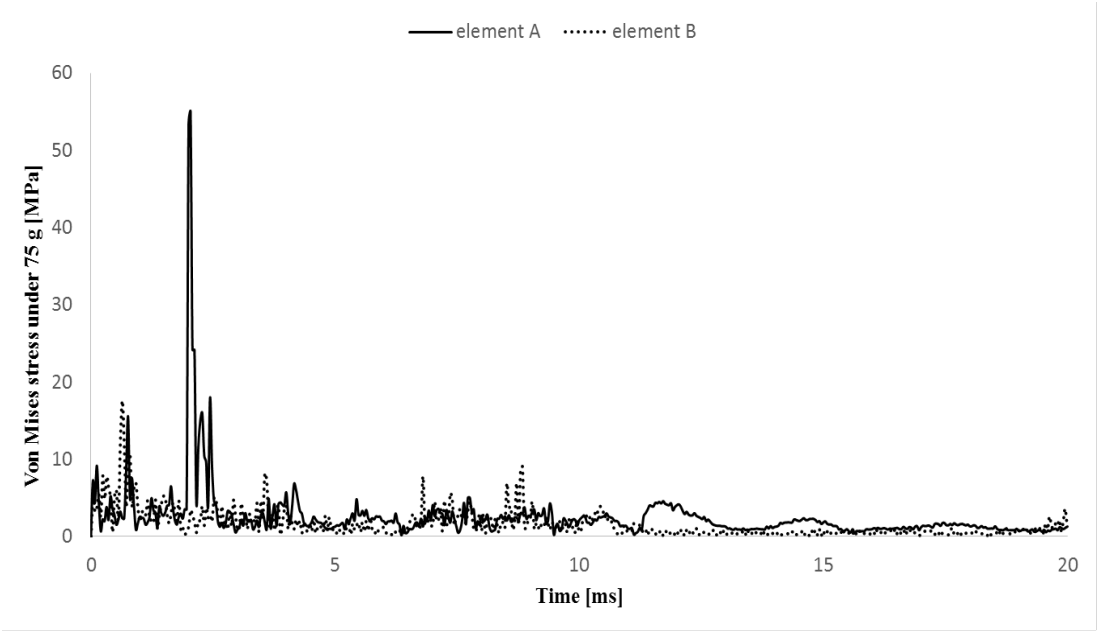

Figure 7.38: Von Mises stress history for the 75 g of C4.

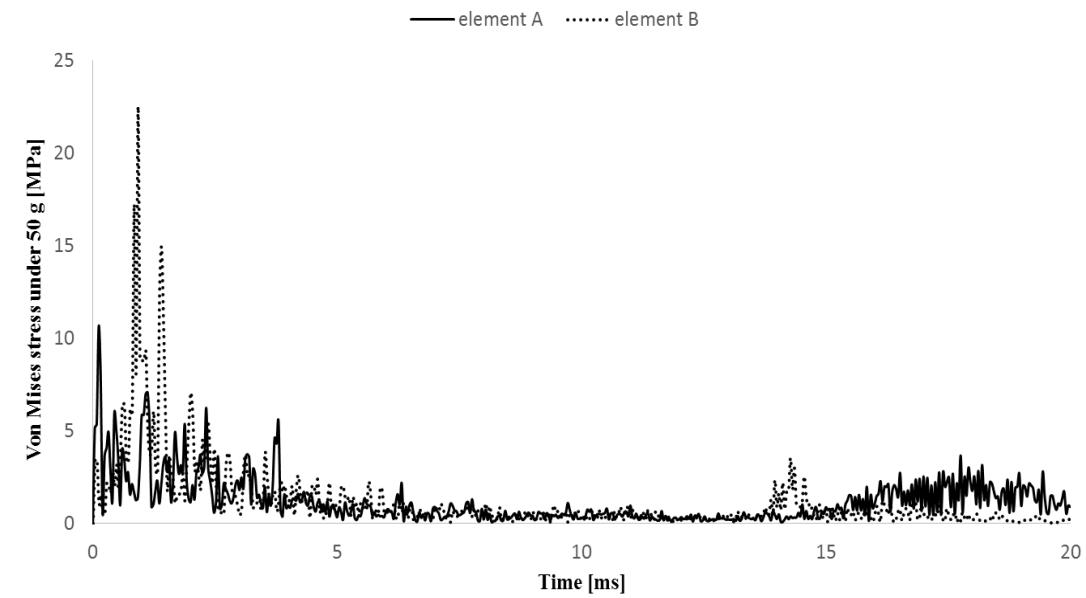

Figure 7.39: Von Mises stress history for the 50 g of C4.

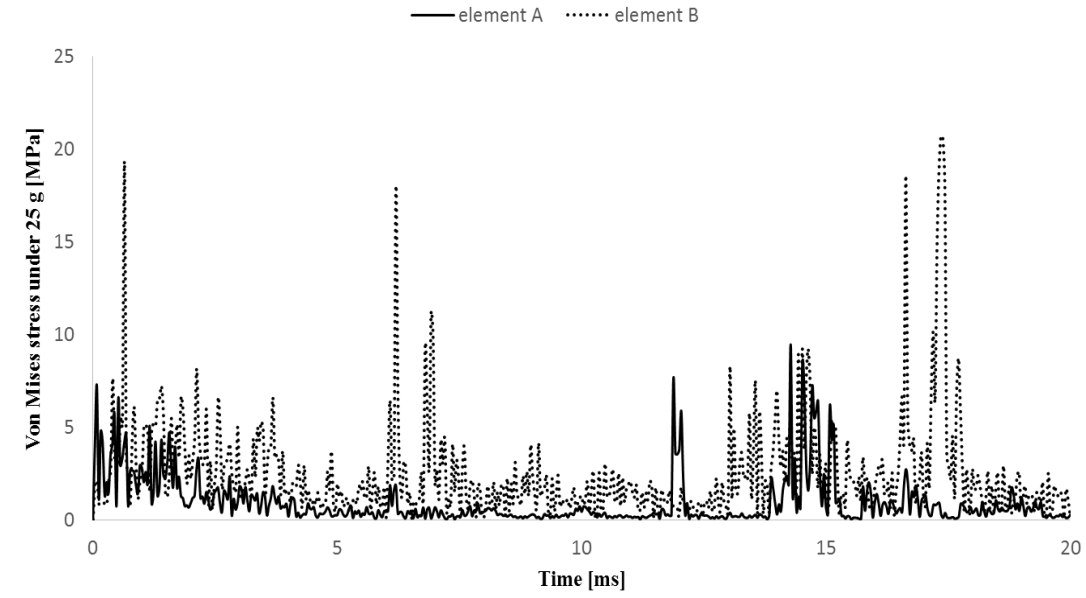

Figure 7.40: Von Mises stress history for the 25 g of C4.

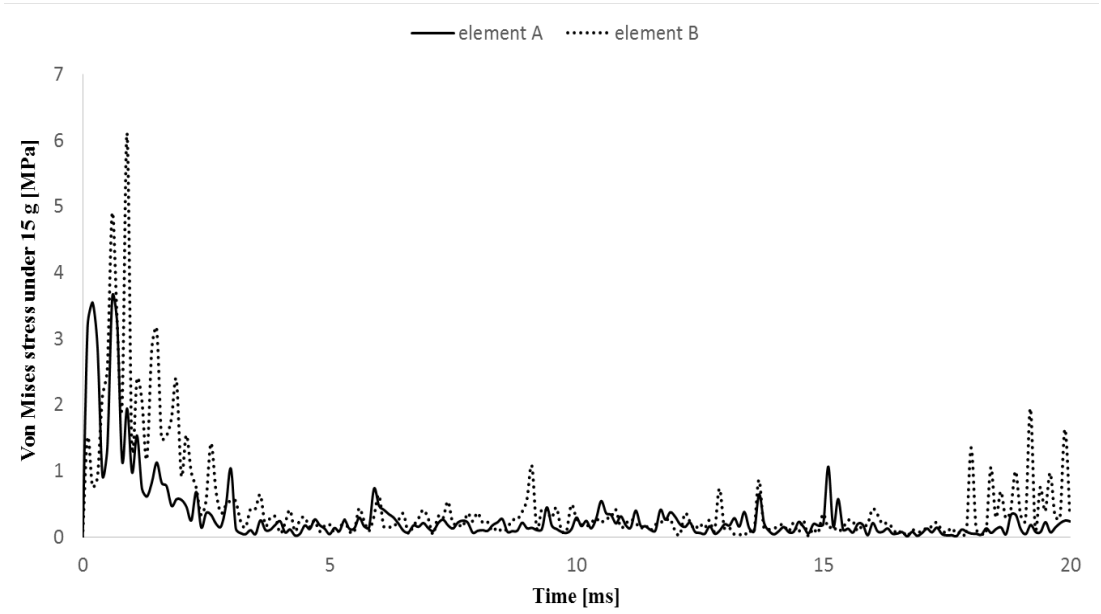

Figure 7.41: Von Mises stress history for the 15 g of C4.

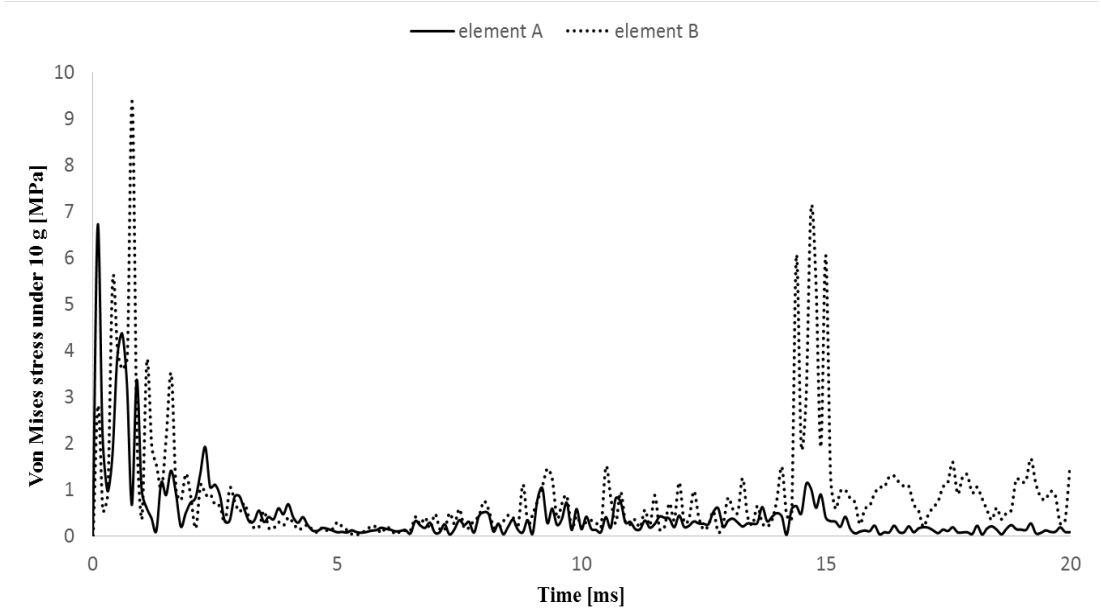

Figure 7.42: Von Mises stress history for the 10 g of C4.

7.3 Validation of the numerical damage observed on reinforced concrete walls under impact and contact detonation of a HESH

The two reinforced concrete walls (2464 × 2464 × 200 [mm^3]), with concrete material of 35 MPa compressive strength are tested under ballistic impact and detonation. The scope of this set of experiments is to assess the damage and investigate the response of those structural elements under the combined effect of the kinetic energy impact and contact detonation of a 90 mm MK8 HESH-T M691A2 projectile. These particular projectiles are fired from a distance of 70 m from the walls at three different velocities (600, 800 and 1000 m/s). Due to aerodynamic conditions, as was mentioned earlier, the actual impact velocities, are measured experimentally as 605, 802 and 988 m/s. The first and the last values are used also as input velocities during the numerical modelling. The tested concrete walls have identical mechanical properties and the only difference is the impact velocity. The validation of the experimental work using numerical simulations (LS-DYNA) includes only the cases of 605 and 988 m/s impact velocity, since the delayed detonation time for those two, was kept the same and equal to 0.15 ms.

The numerical modelling includes several challenges, due to the complex nature of the phenomenon. Since the mesh size affects the simulation quality, a mesh study is carried out in order to find the appropriate mesh that is able to depict the high impact velocity and detonation scenario. The reinforced concrete wall is initially discretised with solid hexahedra elements using a mesh bias and uniform meshes of 10 and 15 mm element size. For all the simulations, the air is modelled as a box with dimensions of 400 × 400 × 438 [mm^3] using elements of 5, 10 and 15 mm, respectively for the three simulation cases (bias, 10 mm mesh, 15 mm mesh). The configuration of the air

above the reinforced concrete wall (case of the uniform mesh of 15 mm as an example) is shown in Figure 7.43. The three mesh cases run with 605 m/s impact velocity and are compared with the relevant experimental damage obtained from the front face of the wall in order to choose the ideal mesh size for this study (see Figure 7.44).

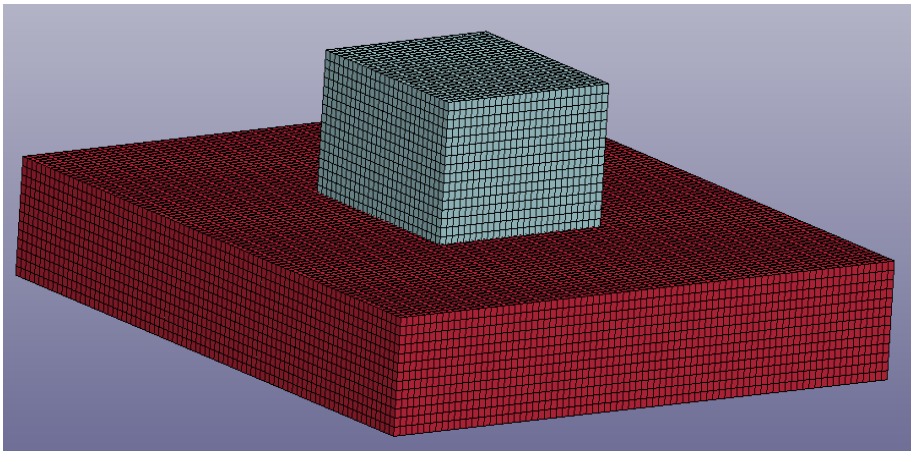

Figure 7.43: Initial mesh discretisation for the reinforced concrete wall and air (case of 15 mm mesh size).

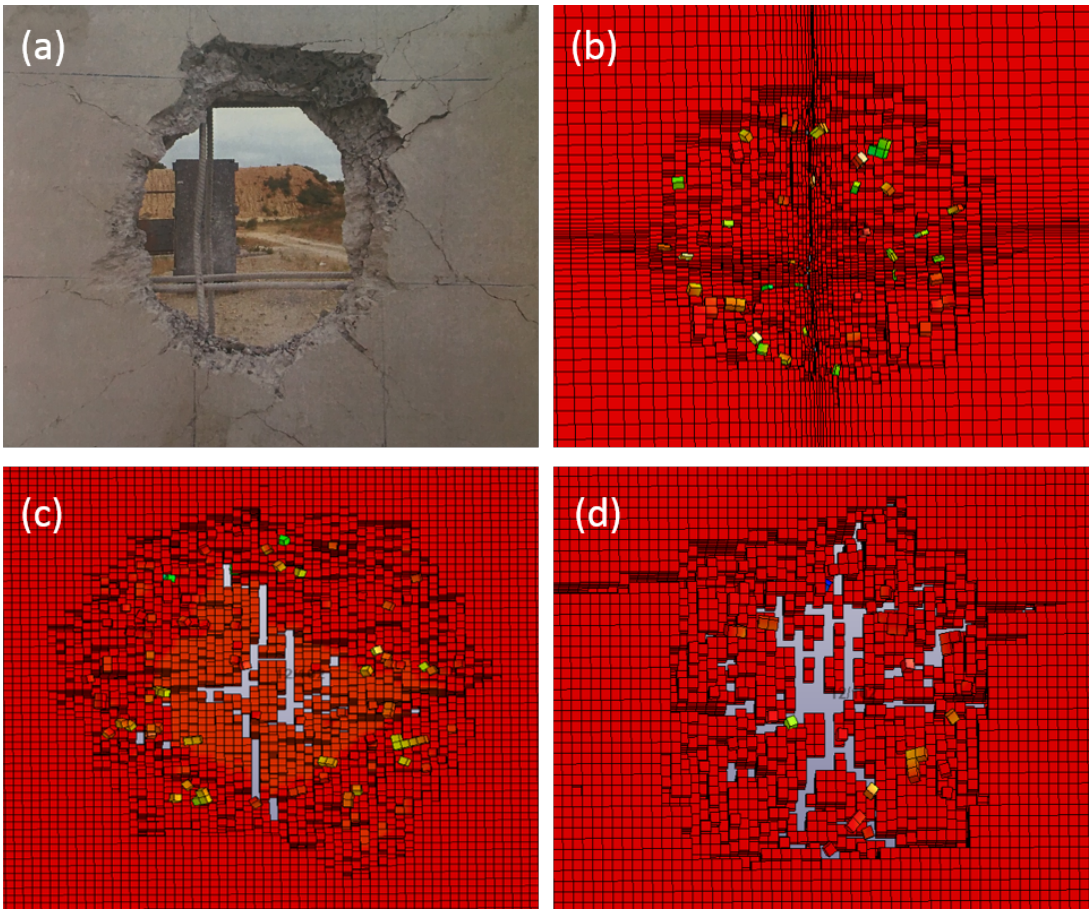

Figure 7.44: Damage caused on the front face by the impact velocity of 605 m/s: (a) experimental, (b) numerical: bias mesh, (c) numerical: 10 mm mesh, (d) numerical: 15 mm mesh.

Figure 7.44 (b) shows the obtained damage for a mesh with bias. Hence, the one quarter of the wall (1232 × 1232 × 200 [mm^3]) is modelled with 80 × 80 × 18 elements. The idea is to create a fine mesh around the impact area and a coarser one as the distance from the impact zone increases. The air is modelled with hexahedra elements of uniform size of 5 mm. This leads to a total number of 696,032 elements and a CPU time of 61.5 hrs. The number of elements used reaches approximately the limit of the available computational resources, leading to a very expensive model. Apart from that fact, the damage obtained numerically is not able to represent the hole that is observed from the on-site investigation. This happens because in situations where mesh

dependent erosion algorithms are being used, the erosion parameter is strongly affected by the element size. Thus, when a bias mesh is used, the erosion parameter is adequate for the deletion of some of the elements but may not work efficiently for others. Consequently, it was decided to model the impact event using a uniform mesh both for the wall and the air.

Figure 7.44 (c) and (d) show the damage observed when uniform meshes of 10 and 15 mm are chosen (respectively). In the case of the 10 mm mesh the model has 391,268 elements and a CPU time of 5 hrs, while in the case of the 15 mm mesh size the model has only 126,185 elements, a fact that decreases the computational time of the simulation considerably (1hr). Both simulations show that are struggling to depict the experimental hole, even though that there is evidence of the threshold of total perforation. On the one hand, the 15 mm mesh size performs better than the 10 mm mesh, since the initiation of the hole is clearer when the coarser mesh is used. On the other hand, in both cases the damage is located and concentrated around the boundaries of the air box. A fact that proves that the dimensions of the air domain are important in the numerical analysis. Thus, the air should be modelled and cover the whole structure in order to allow the detonation to develop without any constraints.

In Table 7.9 the three simulation scenaria along with the computational time and total number of elements are shown.

Table 7.9: Mesh and model parameters.

Mesh size [mm]	Number of elements	CPU time
15	126,185	1 hrs
10	391,268	5 hrs
Bias	696,032	61.5 hrs

Recall that in the case of the contact detonation of the reinforced concrete slabs (see Section 6.3.1), this was not an issue, since the dimensions of the RC slabs (1/4 model) were approximately the one third of the dimensions of the RC walls (1/4 model). Thus, it was possible to cover the whole structural element (slab) with air.

In the current situation, however, the confined air domain was necessary to be investigated in order to reduce the number of elements and save computational time.

Figure 7.44 of the damage showed that this approach (confined air domain) did not work effectively. This fact forced the modelling of the structural element (reinforced concrete wall) with a uniform mesh of 15 mm and an air domain that covers the whole structure (300,040 elements) as was presented in Section 6.5.1.

The scope of this mesh study is to prove the adequacy of the coarser (15mm) mesh since it was computationally demanding to use a finer mesh (10 mm) and cover the whole structure with the air. Both the numerical and experimental results (see Figure 7.45 and Figure 7.46) for impact velocities of 988 and 605 m/s, show the creation of a hole and a total perforation in the centre of the impacted target. The observed damage at the front and the back face of the RC walls is the result of the combined effect of the kinetic energy and the contact detonation of the HESH projectile. There is a favourable agreement between the experimental work and the numerical study. The obtained errors in terms of the diameter of the hole, for the two impact velocities, are lying slightly above 10 % and are listed in Table 7.10.

.

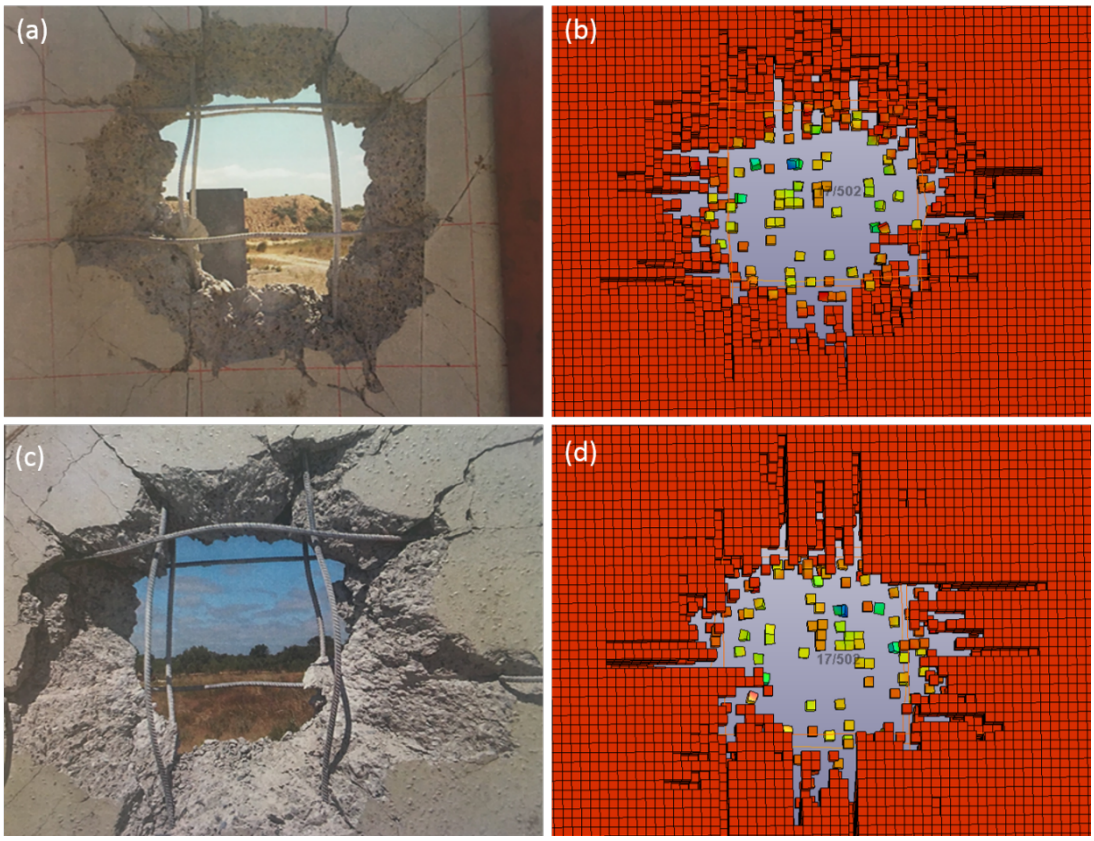

Figure 7.45: Damage caused by the 988 m/s impact velocity: (a) experimental: front face, (b) numerical: front face, (c) experimental: back face and (d) numerical: back face.

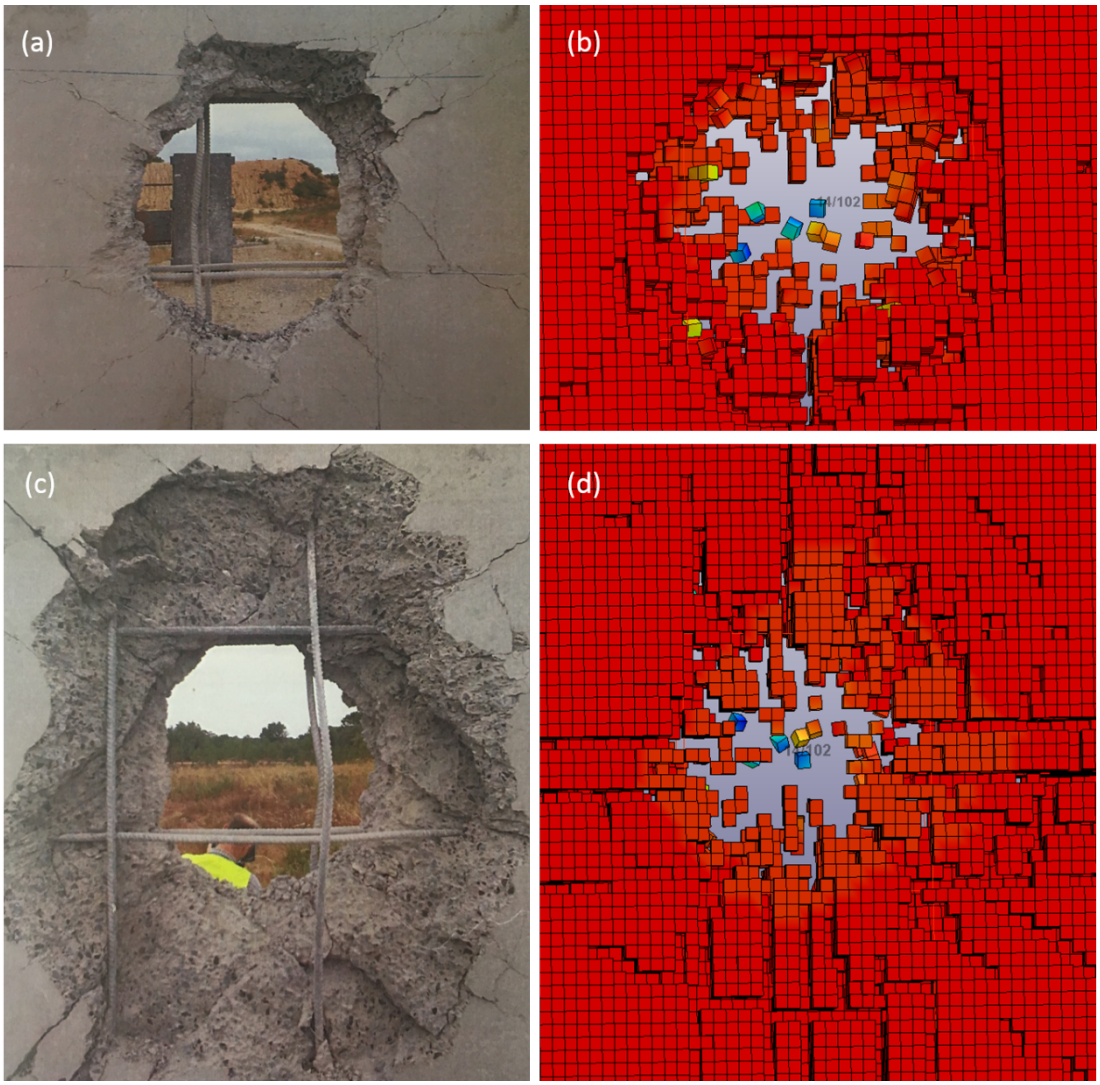

Figure 7.46: Damage caused by the 605 m/s impact velocity: (a) experimental: front face, (b) numerical: front face, (c) experimental: back face and (d) numerical: back face.

Table 7.10: Errors between experimental and numerical measurements.

t_{det} [ms]	V_{imp} [m/s]	Error [%]
0.15	988	12.0
0.15	605	13.5

In the case of 988 m/s impact velocity (see Figure 7.45), the numerical measurements estimate an average hole size of 436 mm. The error between the experiments (497 mm hole) and the numerical simulations is 12.0 %, which is considered to be good given all the complexities of the phenomena being modelled. In the case of the 605 m/s impact velocity (see Figure 7.46), the numerical evaluation of the hole is 300 mm. The latter gives an error of 13.5 % compared with the experimental measurements (347 mm hole), but again within an acceptable range. The perforation of the wall is the result of the action of the applied compressive load, resulting from the kinetic and blast energy, as well as the action of any reflected stress waves that cause bending failure. In addition, the cone shaped perforation and the diagonal cracks that are evident around the hole give the indication of local shear failure. Observing also the damage that is formed around the holes, for both impact velocities, it can be concluded that it has progressed in a similar manner for both the experimental and numerical studies.

Since the proposed numerical modelling is efficient and has already been validated for both impact velocities, the discussion on pressures, impulses, obtained numerical energies as well as the response of the RC wall and the behaviour of the reinforcing bars will follow. It is worth noting that even though the simulation time for both simulations is 10 ms, the graphs for the 988 and 605 m/s impact case will be investigated during the period of 0.3 ms, since after this time duration the response of the RC walls, in terms of damage, remains unchanged.

7.3.1 Pressure and impulse on the surface of the reinforced concrete walls

In Section 7.2.1, the variation of the maximum pressures and impulses was established with the changing mass of explosive. Using a TNT converting factor of 1.37 [4], the mass of C4 is modified into TNT equivalent mass. Hence, a more general graph is created, that can be used for any kind of high explosive, if the explosive is converted into a TNT equivalent mass. Figure 7.47 and Figure 7.48 show the variation of the peak blast interface pressure and impulse.

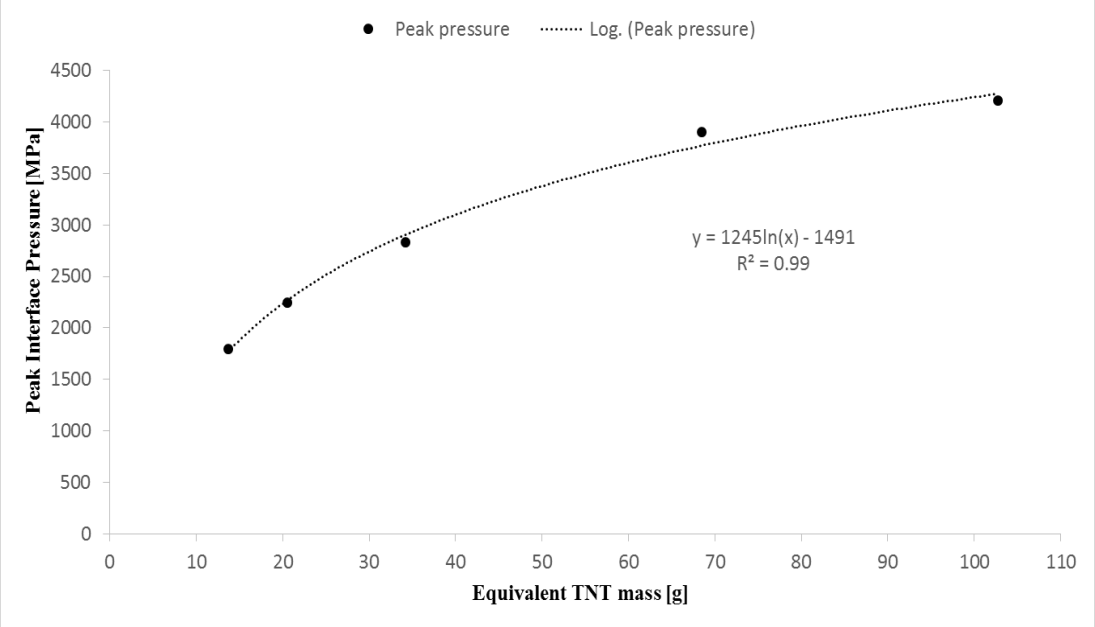

Figure 7.47: Variation of peak pressure as a function of the mass of explosive (in TNT).

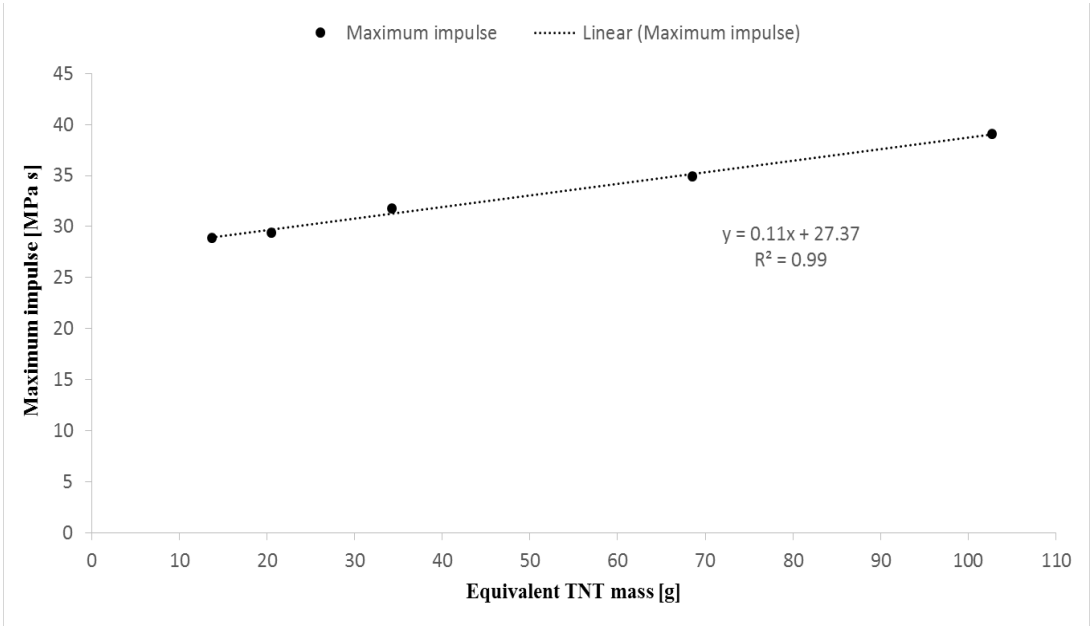

Figure 7.48: Variation of impulse as a function of the mass of explosive (in TNT).

The HESH projectile has 1220 g of A3 explosive. According to McVay [4], the TNT conversion factor for A3 is 1.09. Thus, the equivalent mass of TNT is 1330 g. The peak pressure p that is achieved after the contact detonation is 7458 MPa and can be derived from the following equation in which m is the mass of explosive:

$$p = 1245 \ln m - 1491 \qquad 7.1$$

In addition, the maximum obtained impulse in similar circumstances is equal to 178 [MPa s], calculated through the linear relationship:

$$i = 0.11m + 27.37 \qquad 7.2$$

7.3.2 Energy analysis

Figure 7.49 and Figure 7.50 present the energy balance of the numerical models under the effect of two impact velocities V_{ave} (988 and 605 m/s respectively).

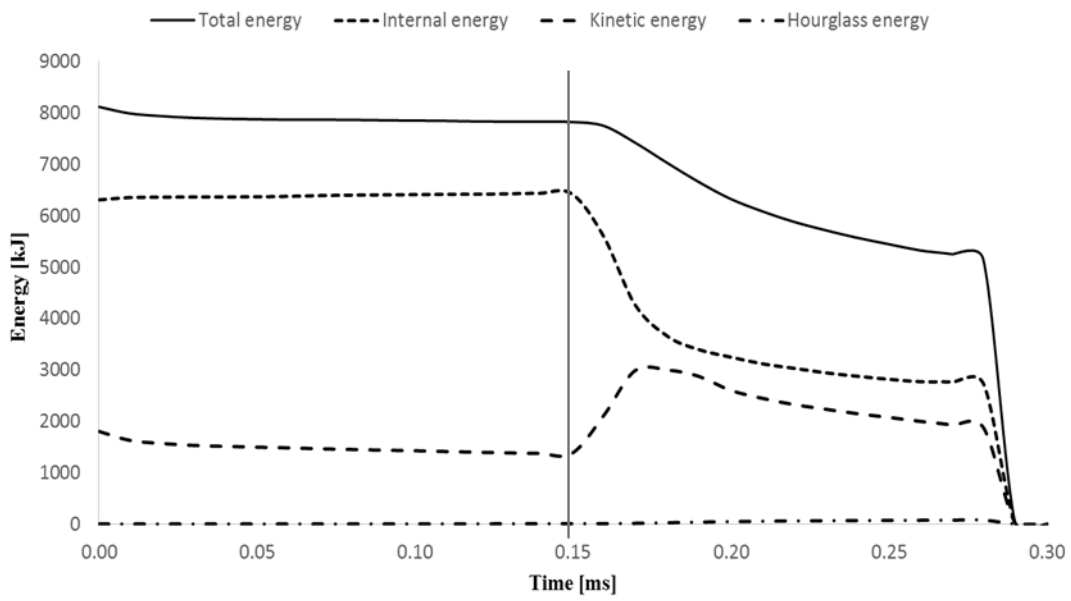

Figure 7.49: Energy histories for the impact case of 988 m/s.

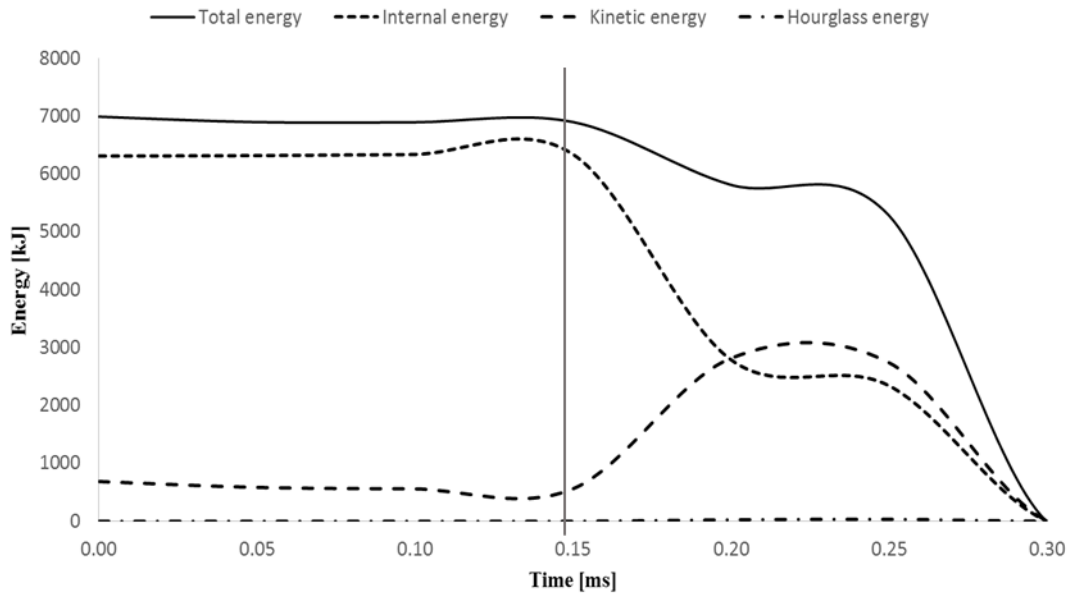

Figure 7.50: Energy histories for the impact case of 605 m/s.

These graphs show the time history of energies (total, internal, kinetic and hourglass energy). The grey vertical line represents the time (0.15 ms), that the contact

detonation takes place. In addition, Table 7.11 and Table 7.12 list the maximum energy values observed. As expected, the higher the impact velocity, the higher the maximum values of the energies are achieved. In addition, as the impact velocity increases, the kinetic energy due to the impact becomes as important as the kinetic energy coming from the detonation. However, in both cases, the contact detonation is still the dominant event.

Table 7.11: Peak values of the energies (kinetic, internal) and correspondent time for the contact blast and impact scenario.

V_{ave} [m/s]	Kinetic [kJ]	Time [ms]	Internal [kJ]	Time [ms]
988	3,010	0.18	6,440	0.15
605	2,800	0.20	6,350	0.15

Table 7.12: Hourglass ratio and peak values of total energy for the contact blast and impact scenario.

V_{ave} [m/s]	Hourglass [ratio %]	Time [ms]	Total [kJ]	Time [ms]
988	0.90	0.28	8,120	0
605	0.48	0.25	6,990	0

Total, kinetic and internal energy

In both models the total energy of the system is equal to the sum of the internal, kinetic and hourglass energy. More precisely, for the case of 988 m/s impact the maximum total energy observed at t =0 is 8,120 kJ with the rest of the energies being lower than this value. The same pattern is also followed for the impact at 605 m/s albeit with a lower total energy (6,990 kJ). Neglecting hourglass energy, there is a conservation of energy until detonation time is reached. Moreover, after detonation, the system is not

conservative and energy starts to decrease due to the dissipation of the chemical energy.

The results in Figure 7.49 show the history of the kinetic energy of the system for the impact velocity of 988 m/s. At the beginning of the simulation ($t = 0$) the kinetic energy (1,810 kJ) is the kinetic energy of the HESH projectile. This value is the same as the kinetic energy obtained analytically from the impact of a mass equal to 4 kg (mass of the projectile parts). Due to projectile impact, the kinetic energy of the system obtains a non-zero value at $t = 0$, while in the case of contact detonation of reinforced concrete slabs the kinetic energy at the same time was equal to zero. Then, the kinetic energy starts to decay until it reaches the value of 1,380 kJ at time $t = 0.15$ ms, where the detonation takes place. The consequent increase of kinetic energy is caused by the release of chemical energy from the detonation. The maximum energy of the model that is achieved is equal to 3,010 kJ. As a result, the combined effect of the kinetic and blast energy, after time 0.15 ms, is mostly dominated by the detonation event rather than the projectile impact.

The results in Figure 7.50 also show the variation of the kinetic energy for an impact at 605 m/s. This impact velocity results in a much lower initial kinetic energy of the system (676 kJ). It is also noted that the variation of the kinetic energy follows a similar pattern if compared with the case of the higher velocity. At $t = 0.15$ ms, where the detonation happens, the initial kinetic energy drops to 547 kJ. After this time, the kinetic increases in a slower rate than in the case of 988 m/s and needs roughly 0.05 ms in order to achieve the maximum value, which is 2,800 kJ.

The internal energy of the system for both impacts reaches its maximum value at the detonation time (0.15 ms), since at that stage the kinetic energy reaches its lowest value. The internal maximum energies are 6,440 and 6,350 kJ for the impacts at 988 and 605 m/s respectively.

Hourglass energy

The hourglass energy, as explained in the contact detonation scenario, is the undesirable wasted energy of the system and should be as low as possible (hourglass ratio less than 10% of the total energy). The results are found to be in accordance with the previous statement for both the impact velocities. This is shown in Figure 7.49 and Figure 7.50, but in a clearer manner in Figure 7.51. It is shown that both impact scenarios under only the effect of the kinetic energy (for $t < 0.15$ ms), exhibit a comparatively low hourglass ratio. This ratio increases steeply after detonation. Hence, the increase in the impact velocity in combination with the detonation results in the increase of the hourglass ratio. More precisely, the impact at 988 m/s exhibits an hourglass ratio (0.90 %) nearly the double of the ratio obtained at 605 m/s impact velocity (0.48 %). This happens because elements are starting to deform severely when the two events are combined.

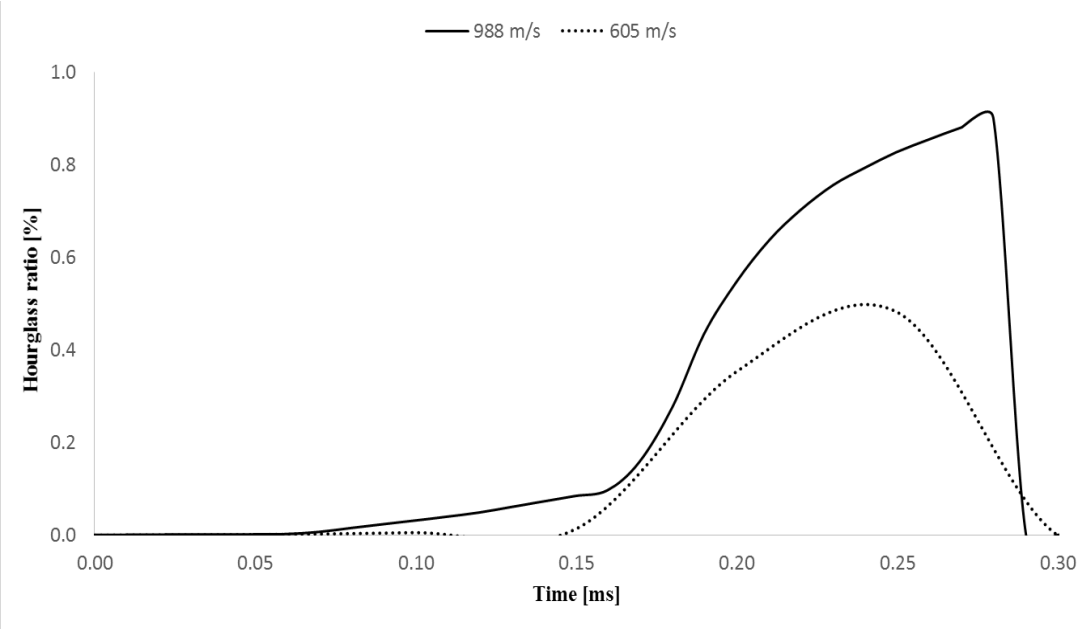

Figure 7.51: Hourglass energy ratio for the impact velocities.

7.3.3 Kinematics of the reinforced concrete wall

The displacements and velocities under the combined effect of contact detonation and impact, of nodes A and B, at the front face of the RC walls are collected and discussed (see Figure 7.52). Node A is located next to the damage caused by the HESH projectile impact of 988 m/s. The kinematic response of the same node is investigated in the case of 605 m/s, in order to assess the influence of impact velocity. Node B is located at the free end of the RC wall, in order to observe the kinematic response of a node away from the impacted area that does not belong to any of the symmetric or fixed boundaries.

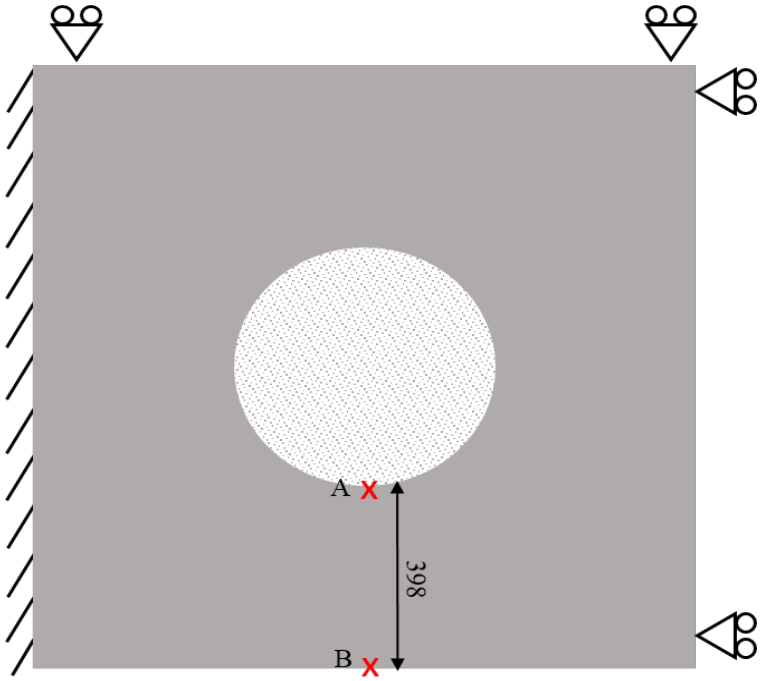

Figure 7.52: Nodes A and B for the kinematic analysis of the RC wall (top view, in mm).

Displacements for nodes A and B

The displacement histories of nodes A and B for both impact velocities are shown in Figure 7.53. It is observed that until t = 0.15 ms, when the delayed detonation of the projectile takes place, the displacement values are small compared to the displacements observed after the detonation of the projectile. Hence, the kinetic energy of the HESH is not capable of causing a significant displacement on the concrete structural element as long as the contact detonation on the wall enhances the "impact force".

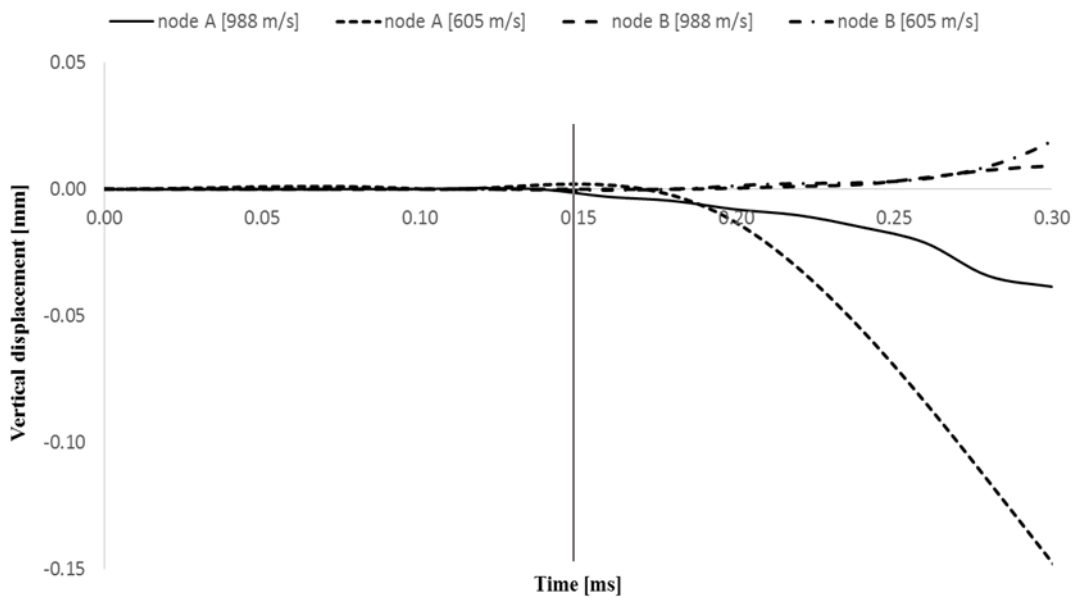

Figure 7.53: Displacement history of node A and B for the impact velocities.

Node A, which is located next to the damaged area, under 605 and 988 m/s impact velocity and contact detonation, is moving downwards following the impact direction. It should be noted that at t = 0.3 ms, node A for the impact at 605 m/s deforms approximately three times more (0.15 mm) compared to the displacement obtained for the impact velocity of 988 m/s (0.04 mm). This result can be explained due to the inertia. When an object (the wall for example) is forced with a higher impact velocity (case of 988 m/s), it resists every attempt in changing its initial configuration in a more intensive manner compared with a situation of a lower in magnitude impact (case of 605 m/s).

Node B for both impact velocities is moving upwards (opposite the impact direction). If compared with node A, node B after the detonation time (0.15 ms) is displaced on the opposite direction due to the bending response of the RC wall. The inertia is evident here as well, since point B in the case of the 988 m/s obtains at time 0.3 ms a

displacement equal to 0.01 mm, while the same node in the case of 605 m/s and at the same time reaches a displacement of 0.02 mm.

When comparing the absolute values of the same velocity and for both nodes A and B, it can be concluded that when the distance away from the damaged zone is increased the vertical displacements decrease. Table 7.13, summarises the displacements (*d*) achieved for the two impact velocities (V_{ave}).

Table 7.13: Displacements of nodes A and B and for both impact velocities.

Node	V_{ave} [m/s]	*d* [mm]	*t* [ms]
A	988	-0.04	0.3
B	988	+0.01	0.3
A	605	-0.15	0.3
B	605	+0.02	0.3

Velocities of nodes A and B

The velocities of nodes A and B are calculated numerically as the time derivatives of the displacements (see Figure 7.54). The nodes move slightly before the detonation time because of the impact of the HESH projectile. Moreover, higher velocities are achieved after the detonation, a fact that indicates that the motion is affected more by the detonation rather than the impact velocity. Table 7.14 summarises the obtained velocities of nodes A and B before the detonation event (V_{bb}, before blast), as well as the velocities achieved after the detonation (V_{ab}, after blast).

Node A for both the impact velocities is experiencing greater velocities compared to the velocities of node B, since it is located next to the damaged zone where the impact

and contact detonation take place. Hence, the velocities are decreasing as the distance from the damaged area increases.

In addition, node A, due to inertia, moves with a lower velocity when the higher impact velocity is considered (988 m/s). Node B as well, follows the same inertia rules in the evolution of velocities as previously did node A. Moreover, the node is moving on the opposite direction from node A, a fact that shows again the bending behaviour of the structural member.

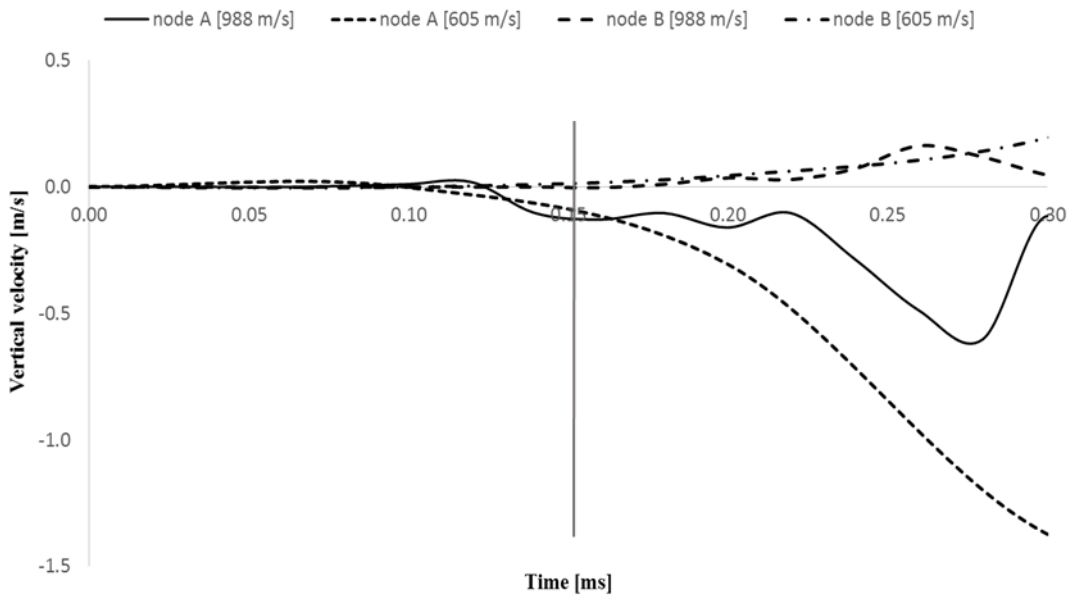

Figure 7.54: Velocity history of node A and B for the impact velocities.

Table 7.14: Velocities of node A and B before and after detonation.

Node	V_{ave} [m/s]	V_{bb} [m/s]	V_{ab} [m/s]	t_{ab} [ms]
A	988	0.13	0.603	0.28
B	988	0.003	0.163	0.26
A	605	0.3	1.37	0.3
B	605	0.04	0.194	0.3

7.3.4 Response of reinforcing bars

The reinforcing bars have a yield strength f_y = 275 MPa. The history of the von Mises stress (see Figure 7.55 and Figure 7.56) for both impact velocities is compared with the aforementioned value. It seems that the rebars deform in a similar manner both in experiments and in numerical observations. In addition, it was found that the elements that are stressed more, are the elements A and B which are located close to the impacted area and are in the upper layer of the reinforcing bars.

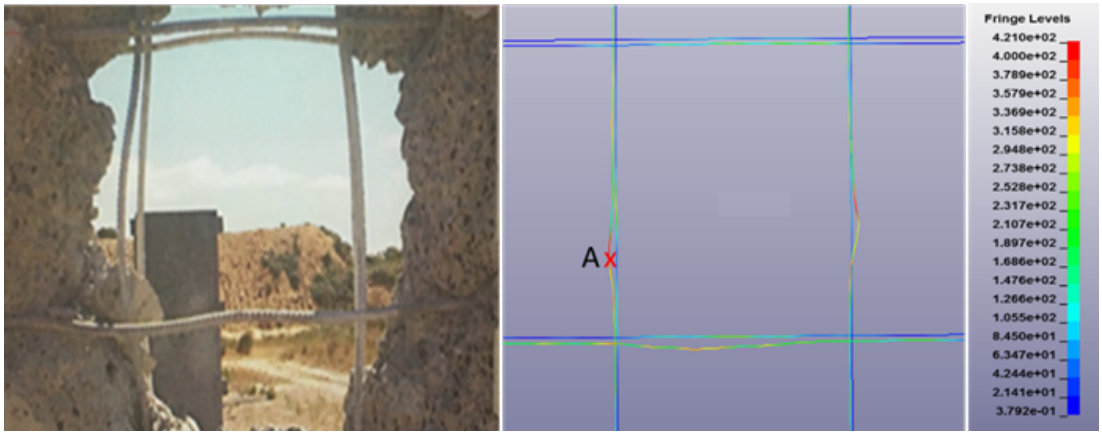

Figure 7.55: Levels of von Mises stress (MPa) for the case of 988 m/s impact velocity.

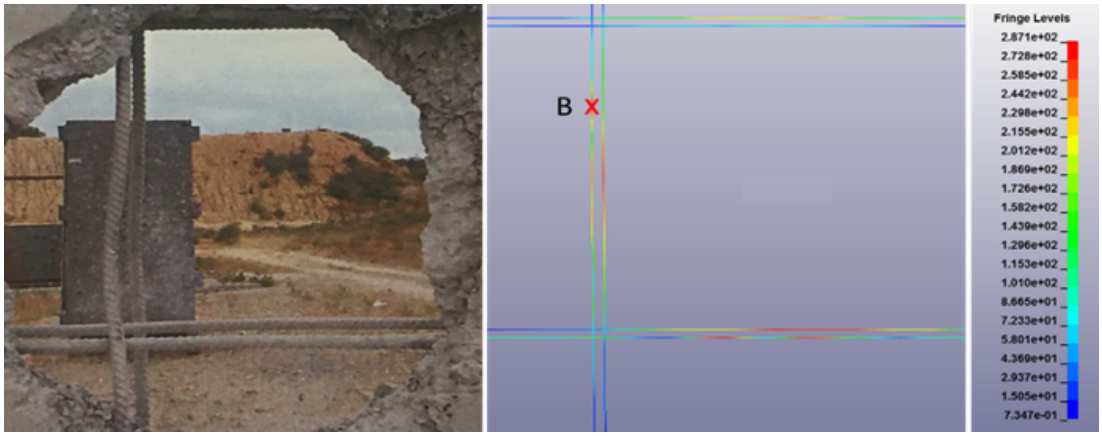

Figure 7.56: Levels of von Mises stress (MPa) for the case of 605 m/s impact velocity.

It is observed (Figure 7.57) that the rebars behave elastically during the impact stage, since the reinforcement is not affected directly by the impact (projectile is fired between the reinforcing bars). When the detonation takes place, there is a sharp increase of the von Mises stress for both impact velocities. At t = 0.3 ms, the rebars, for both the impact cases, exhibit plastic deformation. More precisely, element A reaches a stress of 421 MPa while element B reaches 287 MPa. This indicates, as expected, that the increase of the impact velocity in combination with the detonation, results in the increase of the stresses that are developed in the reinforcing bars. Steel bars are used in order to undertake the tensile forces that concrete is unable to undertake due to its low tensile strength. Thus, increasing the load on the RC structural element and consequently the stresses on the rebars, the plastic deformation and fracture of those results in a greater damage of the surrounding concrete. Hence, the damage that is expected in the case of the impact at 988 m/s is supposed to be higher than in the case of the lower velocity. This statement is in accordance with the experimental and numerical observations.

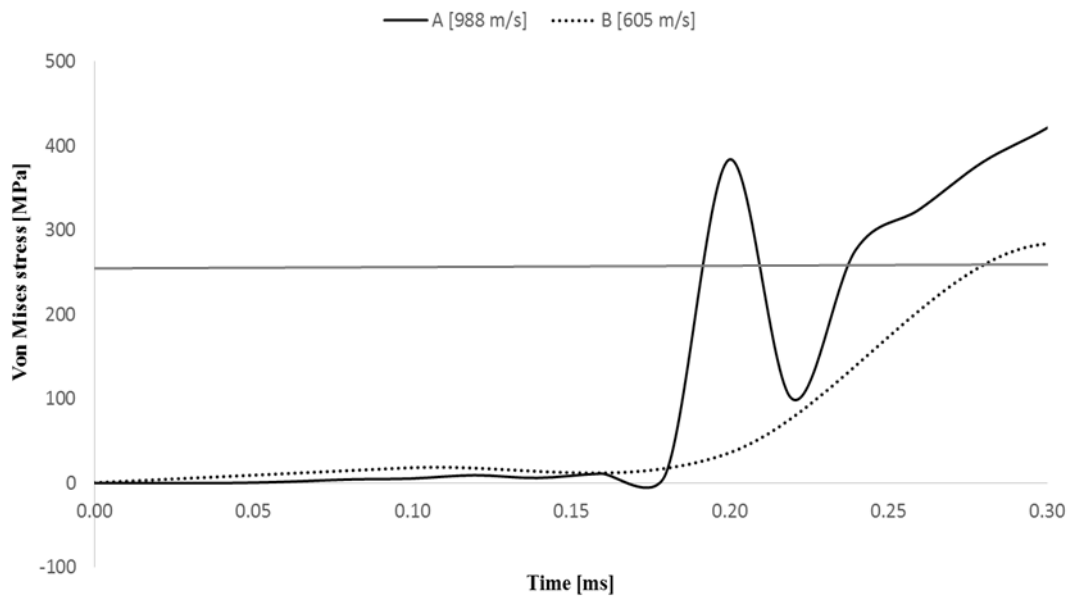

Figure 7.57: Von Mises stress history of elements A and B for the impact velocities.

7.3.5 Impact force and crushed length of the HESH

The recommended equations for calculating the force F that impacts the target and the crushed length $x(t)$, in the soft impact case (see Section 2.3.1), are used herein, in order to determine analytically those values in the current soft impact and blast scenario. Later, by using LS-DYNA, the crushed length is determined by subtracting the deformed length of the projectile (stage before the delayed detonation) from the initial length. In addition, the maximum force F is obtained numerically by multiplying the total mass of the projectile with the maximum average value of the nodal accelerations on the surface of the RC wall. The results (for both impact velocities), presented in Table 7.15, shown that the analytical equations established for the soft impact case are not valid in the current study. This is explained by considering the fact that those analytical equations were adopted using experimental data at impact velocities lower

than 500 m/s. In addition, another factor that affects the results is that the established equations assume a projectile with a uniform mass, consisting of one material only. Hence, in the current work that the soft projectile is an assembly of four different materials, the assumption of a uniform average density and yield stress is not adequate to capture the response.

Table 7.15: Analytical and numerical values of the impact force and crushed length.

	$F_{(605)}$ [kN]	$x(t)_{(605)}$ [mm]	$F_{(988)}$ [kN]	$x(t)_{(988)}$ [mm]
Analytically	7852	0	19678	0
Numerically	35	31	132	46

7.4 References

[1] N. J. Huffington Jr and W. O. Ewing, "Reflected impulse near spherical charges", Army Ballistic Research Lab, Aberdeen, 1985.

[2] C. N. Kingery and G. Bulmash, "Air blast parameters from TNT spherical air burst and hemispherical surface burst", Ballistic Research Laboratories, 1984.

[3] J. O. Hallquist, "LS-DYNA keyword user's manual", Livermore Software Technology Corporation, vol. 970., 2007.

[4] M. McVay, "Spall damage of concrete structures", U.S. Army Corps of Engineers, Waterways Experimental Station, 1988.

Chapter 8. Conclusions

8.1 Conclusions

In recent decades due to the threat of terrorist attacks there is an increasing interest on the safety of buildings of critical infrastructure. Those structures can be catastrophically affected by dynamic incidents of short duration and high magnitude of pressure, such as detonation and projectile impact events. Reinforced concrete (RC) slabs and walls are fundamental elements of the critical infrastructure. Thus, studying the behaviour of this material, widely used in military and civil sector, under high transient dynamic circumstances is an issue of great importance.

Although significant research studies have been carried on blast and hard projectile impact loading scenaria, a limited research has been conducted in order to investigate the detailed response of reinforced concrete structural members under contact detonation. There is also a lack of literature when contact blast is combined with the ballistic impact of a soft projectile. As a result, this doctoral thesis is focused on the aforementioned missing components and targets in the development of a three dimensional finite element model that is able to replicate the response of RC under such conditions. More specifically the contact detonation of C4 explosive on the surface of a RC slab and the contact detonation of a RC wall after the ballistic impact of a 90 mm High Explosive Squash Head, (HESH) projectile are investigated experimentally and numerically. The numerical tool that is used, is the finite element analysis software package LS-DYNA, since it has been proved very efficient when dealing with high transient dynamic loading conditions.

The main objectives were to verify the use of the Multi-Material-Arbitrary-Lagrangian-Eulerian (MMALE) approach in the near field regime by comparison with

the Lagrangian approach LBE and, most importantly, to validate the developed numerical model using MMALE and the Winfrith Concrete model [1] with the experimental results obtained by the Royal Military Academy of Belgium. Consequently, after the validation study, the author assesses the influence of the mass of explosive and impact velocity on pressures, impulses, energy balances, the kinematic response of the RC structural elements and the structural role of the reinforcing bars.

The understanding of the basic principles of detonations, soft/hard ballistic impact, governing equations of the Finite Element Method, techniques of modelling the blast loading, concrete material models implemented in LS-DYNA and research studies on the blast/ballistic field, led to the numerical modelling of the current doctoral thesis with the following main outcomes and conclusions:

Prior to the numerical modelling of the main impact events in this study, the comparison between the numerical results obtained through MMALE and LBE approach with experimental results in the near-field (scaled distances $0.079 < Z < 0.198$ [m/kg$^{1/3}$]), shows that for scaled distances lower than 0.17 m/kg$^{1/3}$, LBE gives more dispersion in the impulse values than the ALE approach and that the % error in the predictions is smaller and more stable when ALE is considered. In addition, the numerical results of the obtained pressures using both approaches reveal that the underestimation of the pressure using LBE increases with the decrease of the standoff distance. Hence, ALE is proved to be more accurate when dealing with the near-field and consequently is used for the modelling purposes of the current doctoral thesis.

Contact detonation scenario

Numerical simulations using MMALE approach and the Winfrith Concrete model [1], are carried out for five reinforced concrete slabs under the contact detonation of 75, 50, 25, 15, and 10 g of C4 explosive in order to replicate the experimental results obtained at the Royal Military Academy of Belgium. The experimental measurements used for validation purposes are analysed in terms of the obtained diameter of crater and spall, as well as the presence or absence of perforation.

The correspondent numerical measurements are in good agreement with the experimental data, since the majority of the average differences from the predicted diameters are lower than 10 %. It is also observed that the increase in the mass of explosive leads to a change of the damage mode from penetration to perforation. Also, the 25 g of C4 is the threshold of the total perforation of the concrete slabs. In addition, the diagonal cracks that are starting from the centre of the specimens and expanding to the corner, follow the yield lines of a simple supported two-way slab. At the time the incident wave hits the front face of each slab it acts as a compressive load. The compressive wave is reflected directly on the opposite side. Hence, the tensile reflected wave causes bending failure at the back face due to concrete's inability to withstand high tensile strengths. It is also noted that when the amount of explosive is increased, both the numerical and experimental response of the slab changes from bending failure to punching shear failure, since a cone shaped perforation is observed through the thickness of the concrete slabs.

The pressures acting on the surface of the concrete slabs follow a similar trend evolution for the different tests. For all the detonation cases, at $t = 0$, the incident blast

wave pressure increases rapidly up to the peak pressure. The latter peak pressure is the result of the superposition between the incident and reflecting waves. In addition, the increase of the detonating mass, raises the obtained pressures as well. A very interesting outcome that can be used in design, is the observation of a logarithmic relationship between the mass of explosive and the resultant peak pressure (within the tested range of masses).

The study of impulses is of great significance since it is not only important to mention the peak values of the incident pressures but also to observe in which way those loads are performing over time. By considering the pressure histories and observing, in particular, the evolution of the incident pressure, it can be concluded that impulses under contact detonation are only affected by the mass of explosive and not by the duration of the impact. The linear relation that is found between impulse and masses of explosive, is another very important outcome for design purposes.

The energy evolution (descending branch) shows that the system is not conservative, since the energy is dissipated in the air. The hourglass artificial energy, exhibited a ratio less than the 10% of the total energy (upper limit according to literature). This result does not contribute in the understanding of the physical mechanisms taking place during the contact detonation event. However, captures the adequacy of the mesh discretisation quality. The physical energies (total, kinetic and internal) follow a similar trend evolution among the several masses of explosive. Initially, the chemical energy of the explosive is stored within the charge in the form of the potential energy. When the detonation occurs, the internal energy starts to attenuate since it is converted into the kinetic energy of the system. It is worth noting that in the present case the

kinetic energy is the result of the blast detonation energy, hence a linear relationship is observed between this energy and the mass of explosive.

As expected, the amount of the explosive is responsible for the development of even greater nodal displacements in the area next to the damage. It is also found that not only the amount of the explosive, but the distance away from the damaged zone are affecting the displacement of the nodes of concrete material. More precisely, when the distance from the damaged location increases, the displacements decrease as well. In addition, a clear indication of the flexural/rigid body response is noticed, through the observation of the motion of the slab as the distance from the impact area is increased.

Numerical findings reveal that the velocities follow the same evolution pattern with displacements. That is expected since they are the first derivatives of the displacements. It should be noted that the rear node of the slab (node at the slab's free edge and above the rigid support) has an enhanced velocity compared to the velocities of the nodes that are closer to the impact due to the presence of the underformable rigid body support placed underneath.

In terms of the reinforcing bars, the numerical investigations confirm that their behaviour remains elastic and that can withstand without failure the external applied dynamic load, since the yield stress of the bars is 469 MPa and the maximum von Mises stress adopted around the impact area is 55 MPa. Furthermore, the layer of the reinforcing bars underneath the layer that faces the blast is stressed in a greater level than the upper layer, since it aims to withstand the spalling failure of concrete. In addition, the evolution of stresses of the upper layer follows an exponential relationship

(within the tested range of masses), while the stresses of the lower layer do not exhibit a clear trend.

Combined soft impact with detonation scenario

A similar numerical approach (MMALE) in combination with the same material model for concrete (Winfrith Concrete) is used in order to simulate the response of RC walls under the impact/contact detonation of the 90 mm HESH projectile. The projectile impacted the walls at two different velocities (605 and 988 m/s) and is detonated at the surface of the targets (A3 explosive). The detonation is delayed for both impacts and takes place after 0.15 ms. Hence, prior to that time there is the influence of the kinetic energy only and after that time there is the influence of both kinetic and blast energy. For validation purposes, the numerical models are compared with results from actual experiments.

A mesh study in the case of 605 m/s shows that the dimensions of the air domain affects the results considerably. Thus, the air domain should cover the whole structure that is under investigation.

The results obtained by the numerical models agree with the experimental findings. More precisely, the average obtained errors of the hole dimensions between the numerical and experimental measurements are equal to 12.0 and 13.5 % for the impacts at 988 and 605 m/s, respectively. The RC walls, under the impact of both velocities are totally perforated with clear indication of local shear failure.

Using the established relations (from the contact detonation scenario) between the mass of the explosive (in TNT equivalent) and the peak pressures / impulses, it is possible to calculate the blast pressure and the corresponding impulse on the surface

of the RC wall. That happens because the impact and the blast loading are acting together after the detonation time and it is not possible to isolate one event from the other. Hence, an estimation of the magnitude of the blast pressure is given, which is found to be the dominant event.

The hourglass artificial energy (ratio) is kept at low levels for both impact velocities, proving again the adequacy of the chosen mesh. The elements are even more deformed in the case of 988 m/s impact, thus greater artificial forces are necessary to be implemented in order to avoid hourglassing. The latter explains the reason of why the hourglass ratio value observed in the case of 988 m/s is much higher than the same ratio in the case of 605 m/s. Prior to the detonation (only ballistic impact), the system in terms of the physical energies (total, kinetic, internal) is conservative. The initial numerical kinetic energy agrees with the kinetic energy obtained analytically. This energy starts to attenuate due to the deceleration of the projectile's impact velocity within the concrete material, while at the same duration the internal energy is increasing due to the increase of the system's stored energy. When the detonation takes place, the chemical energy, stored as internal energy, is converted into the kinetic energy. In addition, similarly to the previous contact detonation scenario, the system does not remain conservative after detonation. The numerical results reveal that as the impact velocity increases, the kinetic energy due to the impact becomes as important as the kinetic energy coming from the detonation. Though, the most important finding from the energy analysis is that the combined effect of the kinetic and blast energy is dominated mostly by the detonation event, rather than the direct ballistic impact (kinetic energy).

The displacements of two nodes (one next to the impact area and the other at the free end of the 1/4 of the RC wall) show that prior to the detonation event, the kinetic energy of the projectile is unable to cause any significant displacements to the wall. After the detonation, the displacement are starting to increase. When the same node is considered, due to inertia conditions, the higher the impact velocity is, the smaller displacement is achieved. In addition, by comparing the direction of the motion between the two nodes, there is a clear indication of the bending response of the reinforced concrete wall. Furthermore, it is observed that for the same impact velocity, the displacements are decreased as moving away from the impact area. The obtained velocities at the same nodes follow the same evolution pattern with the displacements.

The response of the reinforcing bars is similar in both the experiments and the numerical simulations. It was found that the rebars have higher stresses around the impact area when compared to other locations on the reinforcement mesh. During the impact of the HESH, the rebars behave elastically because are not affected directly by the impact velocity. Right after the combination of the blast and impact event, the von Mises stress of the steel bars starts to increase sharply. Consequently, in both impact cases, the reinforcement fails to undertake the external load due to the combination of blast and impact. Also, the increase of the impact velocity affects the time that the failure starts to occur.

Furthermore, it was also found that the analytical equations (soft impact case), regarding the determination of the impact force and the crushed length of the projectile are not valid in the current study. A possible explanation is that those analytical

equations were derived from experimental work on projectiles with a uniform mass at impact velocities lower than 500 m/s.

Most important findings

The most important findings of this doctoral thesis study are mentioned below:

- The MMALE approach along with the use of the simple and user friendly Winfrith Concrete model proved efficient in predicting the dynamic response of RC structural elements under contact detonation and combined impact and detonation events.
- A set of design curves and equations, for the tested range of masses, is proposed to relate the mass of the explosive and the resulting pressures/impulses.
- The combined effect of the kinetic energy and contact blast is dominated mostly by the detonation event.
- Punching shear failure is observed in all the investigated situations (experimental and numerical) except for the case of the contact detonation under the lowest amount of the explosive.

8.2 Future work

Following the research work of the current doctoral study, the author would like to share some research ideas for future consideration:

In the case of the combined contact blast with ballistic impact scenario, to (numerically) increase the reinforcement ratio, the thickness of the wall and the compressive strength of concrete in order to observe the effect of those parameters in the dynamic response of the member, expecting that the increase of those will result in a better blast performance. Furthermore, in the existing blast/impact scenario, to

change the location of the impact. More specifically, moving from an impact location between the reinforcing bars (current study) to the impact directly on the reinforcing bars, it is not expected that will change the results considerably.

Perform the previous parametric study in the case of the contact detonation.

Perform experimental and numerical studies in the case of 605 and 988 m/s impact velocity with a delayed detonation at 0.25 ms, in order to investigate the effect of the delay in the evolution of damage.

Analytical solutions of the RC structure under contact blast, using the Single Degree of Freedom (SDOF) approach, which is the simplest dynamic system consisting of a mass attached to a spring.

Investigate the performance of strengthened concrete under contact detonation scenario. More precisely, based on experimental results of FRP strengthened concrete with carbon and aramid laminates conducted by Beppu et al. [2], to perform a numerical simulation using ALE approach. With the numerical model validated, perform parametric analysis in order to explore the parameters that affect the behaviour of the member under those conditions.

8.3 References

[1] B. J. Broadhouse, "The Winfrith concrete model in LS-DYNA3D", Structural Performance Department, AEA Technology, Winfrith Technology Centre, SPD/D(95)363, U.K1995.

[2] M. Beppu, T. Ohno, K. Ohkubo, B. Li, and K. Satoh, "Contact explosion resistance of concrete plates externally strengthened with FRP laminates", International Journal of Protective Structures, vol. 1, pp. 257-270, 2010.